Deciphering mantle contribution on surface uplift in the Atlas-Meseta system (Morocco)

Romano Clementucci

▶ To cite this version:

Romano Clementucci. Deciphering mantle contribution on surface uplift in the Atlas-Meseta system (Morocco). Earth Sciences. Università degli studi Roma Tre; Aix Marseille Univ., CEREGE, 2022. English. NNT : . tel-03630297

HAL Id: tel-03630297

https://theses.hal.science/tel-03630297v1

Submitted on 4 Apr 2022

Università degli Studi Roma Tre

Doctoral School in Earth Science

Curriculum Geodynamics and Volcanology

XXXIV cycle

Deciphering mantle contribution on surface uplift in the Atlas-Meseta system (Morocco)

Ph.D. candidate

Romano Clementucci

Discipline
Sciences de l'environnement

Spécialité
Geosciences

École doctorale
ED 251

Laboratoire/Partenaires de recherche
Università degli studi Roma TRE
Aix-Marseille Univesité

CEREGE (Centre de Recherche et d'Enseignement de Géosciences de l'Environnement)

Composition du jury

Sean Willett (Prof.) Institut Isotope Geology Mineral (ETH Zürich)	Rapporteur
Pierre-Henri Blard (Dir. Rech.) Université de Lorraine (CRPG)	Rapporteur
Lucilla Benedetti (Dir. Rech.) Université d'Aix-Marseille (CEREGE)	Examinatrice
Marta Della Seta (Prof.) Université de Rome 'Sapienza' (Italie)	Examinatrice
Prof. Paola Molin (Prof.) Université de Rome TRE (Italie)	Examinatrice
Olivier Bellier (Prof.) Aix-Marseille Université (CEREGE)	Président du jury
Lionel Siame (MCF, HDR) Aix-Marseille Université	Directeur de thèse
Paolo Ballato (MCF) Università degli studi Roma TRE	co-Directeur de thèse

Table of contents

Acknowledgment

This Ph.D. has been a fantastic experience that gave me the opportuny to explore new environments from geological, social and cultural point of views and to travel for the first time in Africa and in new localities in Europe.

I would like to really express my deep gratitude to Prof. Paolo Ballato for his guidance and support. He took care of each stage of the project stimulating my growth as researcher and human being. During this time, he really gave me continuous feedbacks and suggestions and sparked my curiosity toward new research directions. I really learned a lot from him.

I would like to deeply thank my supervisor Prof. Lionel Siame for the patience and support, especially during my time in France but more in general during this long path. He really supported and helped me during the thesis and lase gave me continues feedbacks to get better and better. We spent a really nice time together in the lab and not only.

I would also like to express my gratitude to Prof. Claudio Faccenna for helping me to understand and tackle the challenges of my project. He continuously stimulated my curiositis widening my research interests and sparking new ideas.

My gratitude is also for Ahmed Yaaquob, Abder Essaifi, Laëtitia Leanni, and Valery Guillou that supported me in the different steps of my reseach, providing continuous help during the fieldwork, the laboratory activities, and also in the daily life in Morocco and France.

A special thanks to Taylor Schildgen and Pierre-Henri Blard as reviewers of my thesis. They provided valuable comments that improved the clarity of the thesis very much. I really hope to meet them in person soon. I would also like to thank Sean Willett, Paola Molin, Olivier Bellier, Marta della Seta and Lucilla Benedetti, for accepting to be the jury commissioners of my PhD defence. I hope they will enjoy the thesis.

Many thanks to Riccardo Lanari, Riccardo Reitano, Simone Racano, Matthew Fox, Andrea Sembroni, Alex Boutoux, Adriano Goulart and Regis Braucher for the discussions and suggestions that stimulated my scientific interests and for they valuable help. The same for go to all my Ph.D. colleagues of Roma Tre, always ready with a cup of coffee or a beer after work to share the good but also the more difficult moments. I really spent a nice time with them during these last three and half years.

Finally, a special thanks tp my close friends from Orvieto and my family for the good times and for providing continuous moral support that helped me to face my PhD with enthusiasm.

Abstract

The interplay between uplift, which is mostly controlled by tectonics or deep-seated mechanisms and the efficiency of surface processes, which is primarly set by climate, modulates the growth and the decay of topography across diverse temporal and spatial scales. In active orogens, tectonic and climatic forcings are the dominant processes in controlling the landscape evolution and the creation of topographic relief, as largely demonstrated by numerical and quantitative investigations. Conversely, in tectonically quiescent settings, a few field-based studies have documented that the main control on topography is exerted by bedrock erodibility and to a minor extent by climate. Regions that experienced an increase in uplift rates (i.e., topographic rejuvenation) are in disequilibrium and are characterized by the coexistence of a transient landscape that is still recording the previous boundary conditions and a steep topography that has already adjusted to the new uplift rates. Consequently, the landscape of the renjuvineted regions contains at the same time information on present and past uplift (and erosion) conditions and hence represents a first-order geomorphological archive. To explore the landscape dynamics of a rejuvenated topography, we investigated the Atlas-Meseta system of Morocco, which represents a large-scale orographic system characterized by active orogens and quiescent domains. Particularly, it includes the High and the Middle Atlas, which represent active orogens, and the Anti-Atlas and the Western and Estern Meseta, which are tectonically incactive domains. The entire Atlas system has undergone a Cenozoic phase of topographic resurgence as testified by geological, geomorphological and volcanological contraints. However, the low amount of crustal shortening and the presence of an anomalous thinning of the lithosphere beneath suggest an important contribution of deep-seated processes in generating and supporting the topography of this orographic system.

Here I combine a quantitative analysis of regional and basin-scale topography, stream profiles analysis (knickpoints characterization, longitudinal profiles and χ-plot) and landscape modelling, with denudation rates inferred from ^{10}Be concentrations from bedrocks and watersheds in the quiescent Anti-Atlas and Western Meseta. The results of this study allow deciphering and quantifing the erosional dynamics that control the topographic relief production and the landscape uplift history for shorter and longer time scales. This approach further provides the possibility to dechiper, quantify, and differentiate the deep-seated, large wavelength signal, from the shallower contributions (i.e., tectonics and possibly magma injection) in the Atlas-Meseta system.

Riassunto

L’interazione tra sollevamento, principalmente controllato da tettonica e forzanti profonde, e processi superficiali, principalemente controllati dal clima, modula la crescita e l’erosione della topografia attraverso scale temporali e spaziali diverse. Negli orogeni attivi, le forze tettoniche e climatiche rappresentano processi dominanti sul controllo del paesaggio e del rilievo topografico, come ampiamente dimostrato da indagini numeriche e quantitative. Al contrario, in aree tettonicamente inattive, alcuni studi di campo hanno documentato il ruolo chiave dell’erodibilità della roccia e in misura minore dal clima, sulle dinamiche del paesaggio. Regioni che hanno subito un incremento recente del tasso di sollevamento (i.e., ringiovanimento topografico) sono in ondizione di disequilibrio e caratterizzati dalla coesistenza di un paesaggio transiente, ancora sottoposto alle condizioni precedenti al sollevamento, e una topografia piu acclive già in equilibrio con con il nuovo tasso di sollevamento. Conseguentemente, il paesaggio di regioni ringiovanite contiene allos stesso tempo informazioni sul sollevamento (e erosione) presente e passato, rappresentando un importante archivio geomorfologico di primo ordine. Per esplorare le dinamiche del paesaggio delle topografie ringiovanite, siamo andati a studiare il sistema dell’Atlante-Meseta in Marocco, che rappresenta un sistema orografico a grande scala caratterizzato da orogeni attivi e domini quiescenti. In particolare, esso racchiude l’Alto e Medio Atlante, che rappresentano i sistemi orogenici attivi, e dall’Anti-Atlante e Meseta occidentale e orientale, che sono i domini tettonicamente inattivi. Tutto il sistema è stato coinvolto in una fase cenozoica di ringiovanimento topografico testimoniato da varie evidenze geologiche, geomorfologiche e vulcanologiche. Tuttavia, il basso raccorciamento crostale calcolato e la presenza di un anomalo assottigliamento della litosfera al di sotto del sistema Atlante-Meseta suggerisce un importante contributo dei processi profondi nel processo di supporto della topografia del sistema orografico.

In questo contesto, ho combinato un’analisi quantitativa della topografia a scala regionale e di bacino, analisi dei profili fluviali (knickpoints, profili longitudinali e χ-plot), e modellizzazione del paesaggio con i tassi di denudazione derivanti dalla concentrazione di ^{10}Be nelle roccie sommitali e bacini di drenaggio dei domini quiescenti dell’Anti-Atlante e Meseta occidentale. I risultati di questo studio permettono di decifrare e quantificare le differenti dinamiche erosive e la storia del sollevamento a breve e lungo termine di questi domini del sistema orografico. Il nostro approccio fornisce la possibilità di decifrare,

quantificare e differenziare il segnale profondo a larga scala lunghezza d’onda, dai contributi piu superficiali (i.e., forze tettoniche e processi di risalita magmatica a livello crostale) nel sistema Atlante-Meseta.

Résumé

L'interaction entre le soulèvement, principalement contrôlé par la tectonique ou les mécanismes profonds liés à la dynamique du manteau, et l'efficacité des processus de surface, principalement déterminée par le climat, module la croissance et la décroissance de la topographie à diverses échelles temporelles et spatiales. Dans les orogènes actifs, les forçages tectoniques et climatiques sont les processus dominants dans le contrôle de l'évolution du paysage et de la création du relief topographique, comme le démontrent largement les études numériques et quantitatives. A l'inverse, dans les contextes tectoniquement calmes, quelques études de terrain ont montré que le contrôle principal de la topographie est exercé par l'érodabilité du substratum rocheux et, dans une moindre mesure, par le climat. Les régions qui ont connu une augmentation des taux de soulèvement (c'est-à-dire un rajeunissement topographique) sont en déséquilibre et sont caractérisées par la coexistence d'un paysage transitoire qui conserve encore les conditions aux limites précédentes et d'une topographie abrupte qui s'est déjà adaptée aux nouveaux taux de soulèvement. Par conséquent, le paysage des régions rajeunies contient en même temps des informations sur les conditions de soulèvement (et d'érosion) présentes et passées et représente donc une archive géomorphologique de premier ordre. Pour explorer la dynamique du paysage d'une topographie rajeunie, nous avons étudié le système Atlas-Meseta du Maroc, qui représente un système orographique à grande échelle caractérisé par des orogènes actifs et des domaines quiescents. En particulier, il comprend le Haut et le Moyen Atlas, qui représentent des orogènes actifs, et l'Anti-Atlas et la Meseta occidentale et orientale, qui sont des domaines tectoniquement inactifs. L'ensemble du système Atlas a subi une phase cénozoïque de résurgence topographique comme en témoignent les contraintes géologiques, géomorphologiques et volcanologiques. Cependant, la faible quantité de raccourcissement crustal et la présence d'un amincissement anormal de la lithosphère sous-jacente suggèrent une contribution importante des processus profonds dans la génération et le soutien de la topographie de ce système orographique.

Ici, nous combinons une analyse quantitative de la topographie régionale et à l'échelle du bassin, une analyse des profils de rivières (caractérisation des knickpoints, profils longitudinaux et χ-plot) et une modélisation du paysage, avec les taux de dénudation déduits des concentrations en nucléide cosmogénique ^{10}Be produit in situ dans les roches du substratum rocheux et les sédiments modernes transportés dans les bassins versants de l'Anti-Atlas et de la Meseta occidentale. Les résultats de cette étude permettent de déchiffrer et de

quantifier la dynamique érosive qui contrôle la production du relief topographique et l'histoire du soulèvement du paysage pour des échelles de temps courtes et longues. Cette approche offre en outre la possibilité de déchiffrer, de quantifier et de différencier le signal profond de grande longueur d'onde des contributions moins profondes (c'est-à-dire la tectonique et éventuellement l'injection de magma) dans le système Atlas-Meseta.

Chapter 1. Intoduction

1.1. The Atlas-Meseta orographic system: a geologic overview

The Atlas-Meseta system of Morocco is one of the most prominent topographic features in northwest Africa and it is bounded by the Central Atlantic passive continental margin to the west and the Alpine collision zone to the north (i.e., the Rif Mounatins of north Africa and and the Baetics of south Spain). It represents an intracontinental orographic system composed of different morpho-structural domains, including from north to south: the Moroccan Meseta (Western Moroccan Meseta and Eastern High Plateaus), the Middle Atlas, the High Atlas, the Siroua Massif, and the Anti-Atlas (Fig. 1.1).

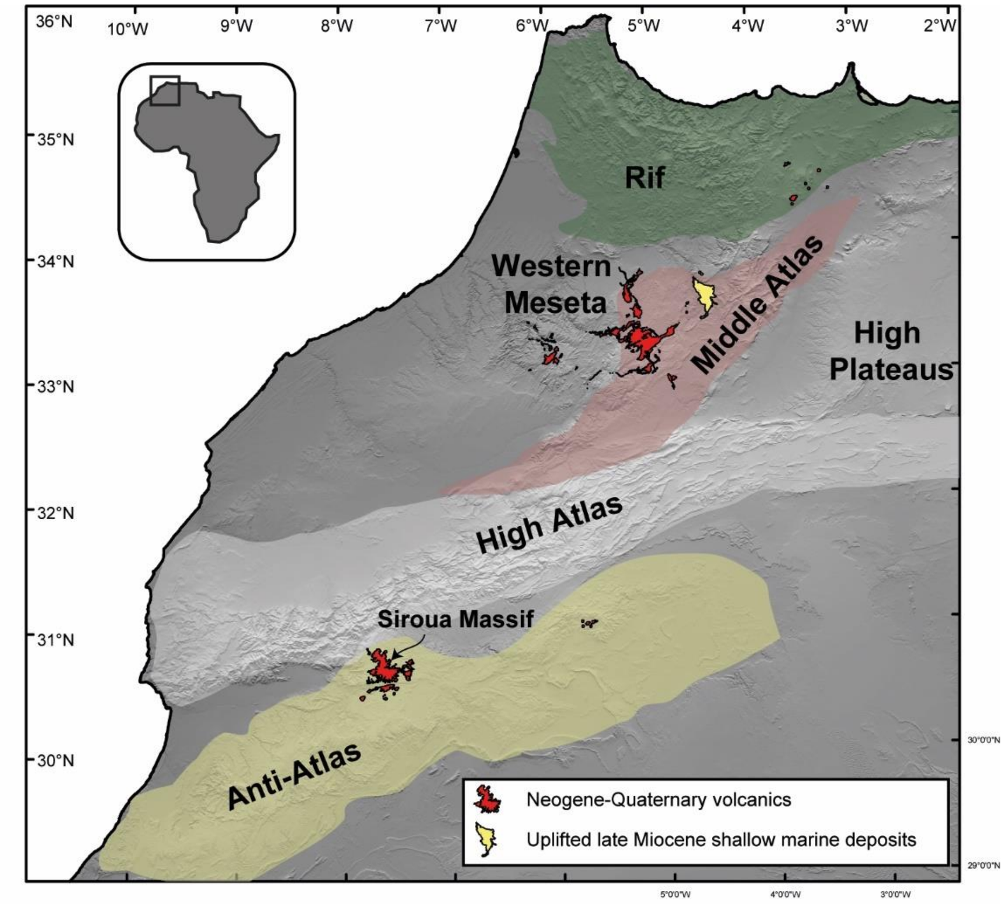

Figure 1.1. Topographic hillshade of the Atlas-Meseta system and his morpho-structural domains.

The E-NE striking Anti-Atlas belt represents the southernmost domain of the Atlas-Meseta system and consists of Precambrian basement and Paleozoic sedimentary rocks that experienced a complex geologic history including the Eburnean, Pan-African and the Variscan orogeny (Ait Malek et al., 1998; Soulaimani et al., 2003; Gasquet et al., 2008). The Eburnean (2.1 - 2 Ga) and Pan-African orogeny (685 – 660 Ma) are recorded in the development of a Precambrian basement consisting of magmatic, metamorphic and sedimentary rocks rocks, that are exposed in the axial sectors of the Anti-Atlas,

The Eburnean orogeny is thought to represent a major tectonic pulse of crustal growth related to the assembly of a pre-Rodinia, Paleo to Meso-Proterozoic supercontinent termed Columbia. The evolution of this accretionary event, however is still matter of debate because its preservation in the geological record is limited and discontinuos (Michard et al., 2008 and references therein). However, we can try to describe the long term history of the Anti-Atlas range.

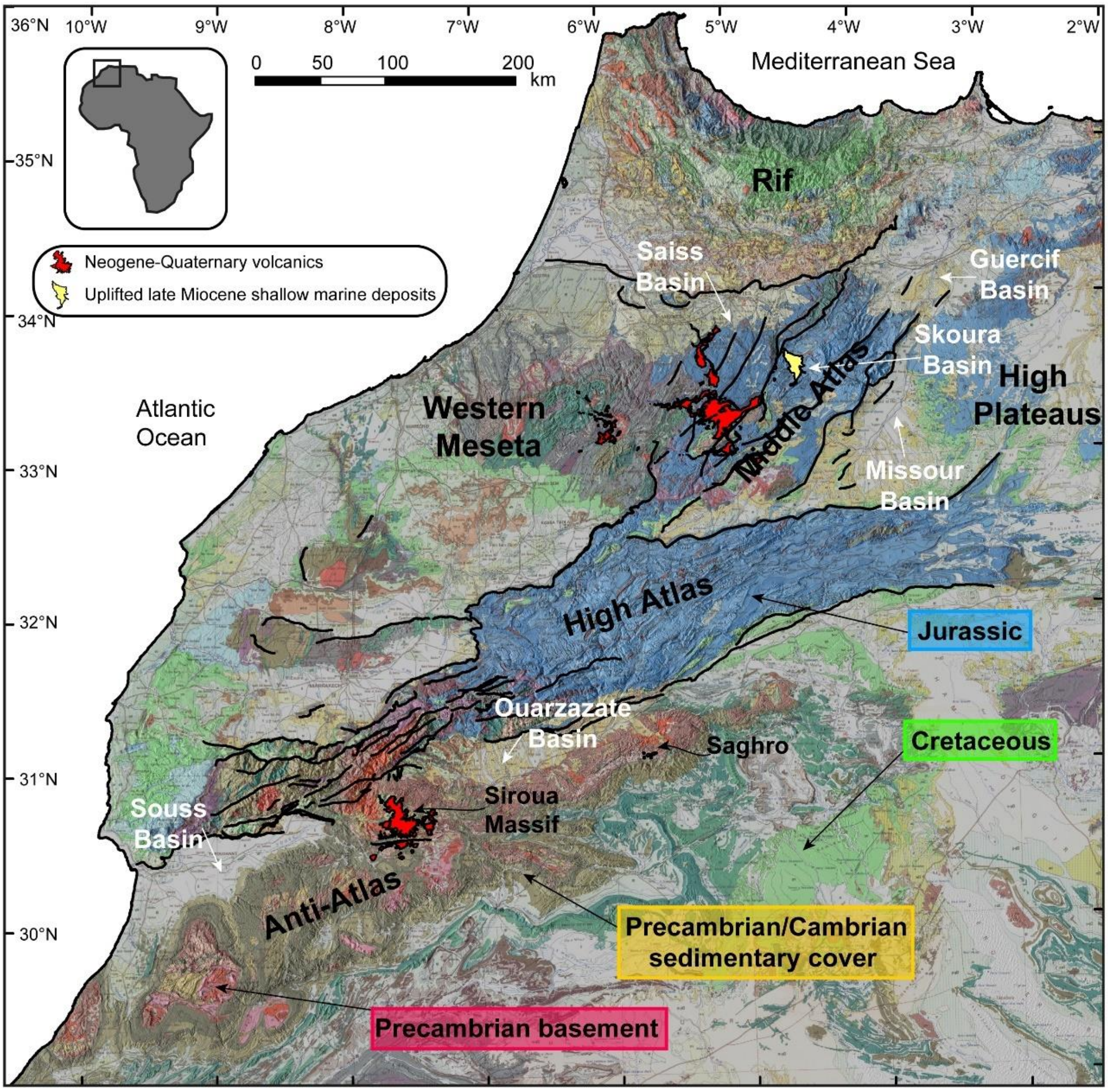

Figure 1.2. Semplified geological map of the Atlas-Meseta system and his morpho-structural domains (after Hollard et al., 1985).

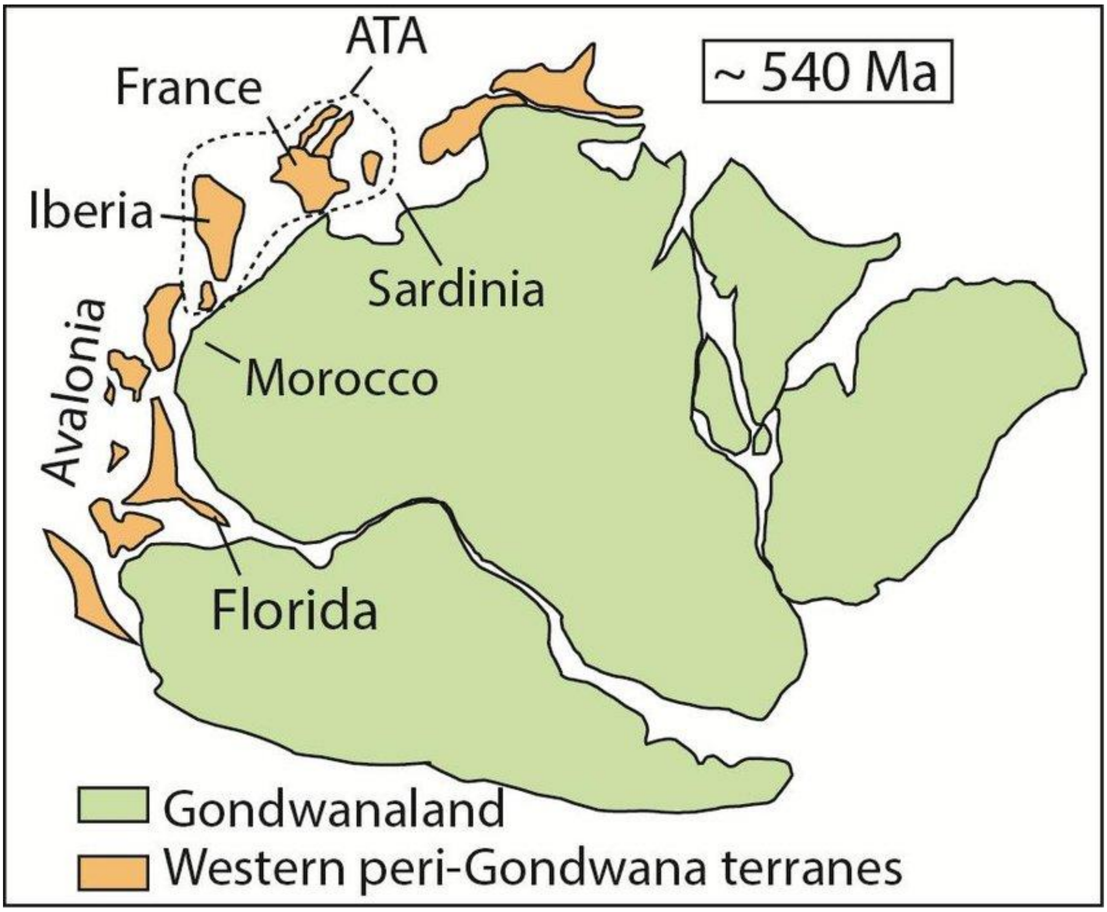

Figure 1.3. Palaeogeographic sketch of Northwestern Gondwana (from Padel, 2016).

The Pan-African events are responsible for the building of the supercontinent Godwana (Michard et al., 2008; Torsvik and Cocks, 2013; Fig. 1.3). Evidence of the Pan-African orogeny are exposed entirely in the surrounded areas of the Western-African Craton and Anti-Atlas. Here, the basement displays only low-pressure metamorphic units (Michard et al., 2008 and references therein).

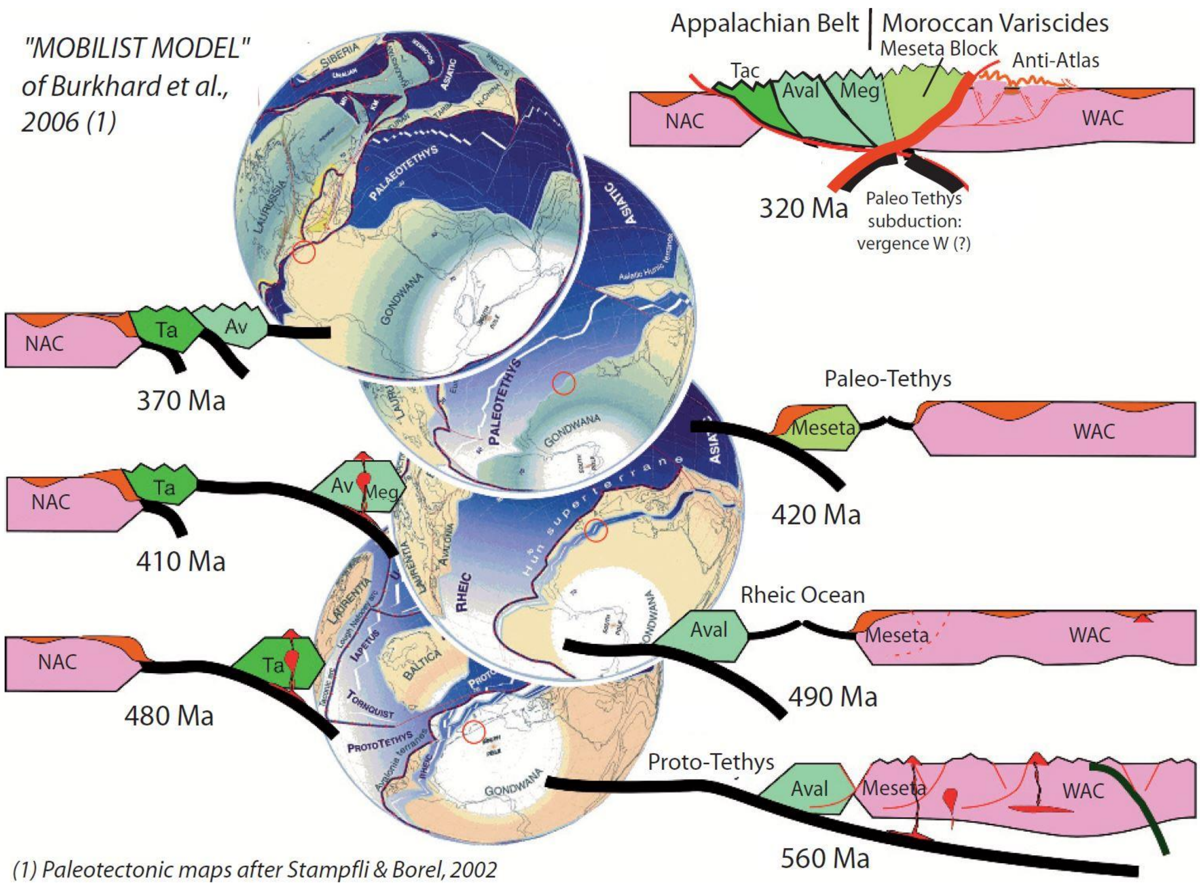

Figure 1.4. Evolution of Morocco during the Paleozoic, after Burkhard et al. (2006), based on the paleogeographic maps of Stampfli & Borel (2002). Here, the Meseta block is separated from the Gondwana supercontinent (Anti-Atlas) by a Devonian Ocean (Paleo-Tethys) (from Michard et al., 2013).

During the early Cambrian (560 Ma) the Anti-Atlas zone experienced an extensional event, which favored the accumulation of more than 10 km of clastic sediments (Fig. 1.4). Following the drift of Avalon toward America, the study area became a passive margin of the Rheic and Palaeo-Tethys oceans. During the late Devonian – late Carboniferous (320 Ma) the collision between northern Gondwana and Laurentina occurred (Fig. 1.4). This major and most pervasive Phanerozoic tectonic event is the Variscan orogeny (late Carboniferous – early Permian) as testified by thermocronological data and deformed Paleozoic rocks (Sebti et al., 2009; Sehrt et al., 2018), that are widely exposed across the entire Morocco (Fig. 1.4).

The Variscan Orogeny in Europe and northwest Africa (Morocco) and the Alleghanian orogeny in North America (Appalachian) occured during the early Permian and were caused by a kinematically and temporally identical shortening event as testified by the deformed Permian formations (Chopin et al., 2014). From the Triassic to the early Jurassic, the Anti-Atlas was eroded and represented a shoulder of the Mesozoic Atlantic rifting event. In particular, Charton et al. (2020) describes the Anti-Atlas as a topographic swell, that experienced slow exhumation during the entire Atlantic rifting and also afterward. The modern topography of the Anti-Atlas is mainly the result of Cenoizoic vertical movments following and possibly pre-dating the collision between Africa and Europe. Currently, such a topography is characterized by an extensive low-relief landscape knows as "high erosional surface" at elevation of 1800-1900 m, with localized mountain peaks up to 2500 m of elevation (Choubert, 1952; Missenard et al., 2008; Guimera et al., 2011).

The two Mesetas (Western and High Plateau in figure 1.1) are crustal blocks that underwent little Cenozoic deformation. The High Plateaus is a tabular region composed of sub-horizontal Jurassic and Cretaceous carbonare rocks. The Western Meseta is composed of a complex assemblage of Paleozoic rocks deformed during the Variscan orogeny (Hoepffner et al., 2005) and partially covered by underformed Mesozoic rocks (Fig. 1.2). The topography of these domains is higher than 1000 and 1500 m for the Meseta and High Plateaus, respectively.

The Siroua Massif has a dome-like morphology and includes a Mio-Pliocene strato-volcano with maximum elevation of 3304 m that overlies Precambrian basement rocks (Fig. 1.2).

The High and Middle Atlas are the highest domains of Morocco, with more than 4000 and 3000 m of elevation (the highest peak is Jebel Toubkal 4165 m), respectively. They consist of a fold and thrust belt, mainly composed of Precambrian, Paleozoic and Mesozoic rocks. The Mesozoic rocks are composed of carbonate syn-rift (Jurassic and Triassic) and post-rift deposits (Cretaceous), related to the opening of a rift basin during the breakup of Africa with an extension-oriented ca. NW-SE (blue and green lithologies in Figure 1.2; Arboleya et al., 2004; Baudon et al., 2009; Lanari et al., 2020b).

The whole orographic system has undergone a topographic resurgence during the Cenozoic most likely through the combination of crustal shortening and deep mantle processes possibly associated with the convergence between Africa and Eurasia (Frizon de Lamotte et al., 2009; Missenard et al., 2006). The recent Cenozoic uplift is also testified by the occurrence of Tortonian-Messinian shallow-water marine sediments (Skoura basin; Middle Atlas region) at an elevation of 1200 m (Babault et al., 2008), late Miocene deep-marine sediments (paleo-bathymetry of ~600 m) that started recording a shallowing-upward trend at ~7 Ma that culminated with terrestrial deposition from 6 Ma to the early Pliocene (Krijgsman et al., 1999) and high-standing river terraces in the eastern mountain front of the Middle Atlas (Pastor et al., 2015).

1.2. The Atlas-Meseta orographic system: open questions

The Atlas-Meseta orographic system is characterzed by a complex, long-term geological history with several tectonic events as described above. A large number of studies have deciphered these phases through time. For example, the main deformation and exhumation events have been constrained by means of low-temperature thermochronology data, especially for the High Atlas and Anti-Atlas. The High Atlas is characterized by a complex cooling history, with a more recent peak of exhumation in the late Miocene in response to collisional processes. Conversely, in the Anti-Atlas, the estimates of exhumation are rather low since the late Cretaceous (Sehrt et al., 2018; Charton et al., 2020; Lanari et al., 2020a). Crustal shortening in the High Atlas and Middle Atlas domains is thought to be limited to moderate, with estimates ranging between 12 and 25% (Gomez et al., 1998; Beauchamp et al., 1999; Teixell et al., 2003; Arboleya et al., 2004; Domènech et al., 2016; Fekkak et al., 2018; Lanari et al., 2020b). This is consistent with geophysical data showing that crustal thickening is limited, and hence isostasy can not explain the modern Atlas-Meseta topography (*e.g.*, Seber et al., 1996; Rimi et al., 1999; Ayarza et al., 2005; Missenard et al., 2006; Miller and Becker, 2014; Bezada et al., 2014; Miller et al., 2015). Moreover, the lithosphere astenoshpere boundary is unexpectedly shallow and this agrees with petrological data from the Sioua, Anti-Atlas and Middle Atlas domains indicating an alkaline affinity related to a sublithospheric mantle most likely caused by an asthenospheric uprise (El Azzouzi et al., 1999; De Beer et al., 2000; Missenard et al., 2006; Duggen et al., 2009; El Azzouzi et al., 2010).

The timing, cinematics and dynamics of the Cenozoic topographic evolution and the large scale of topographic resurgence of the entire orographic system is still a matter of debate. Neverthelss, geological evidence such as uplifted Messinian marine deposits in the Skoura Basin, shallowing upward trend of marine sediments in the Guercif Basin and the transient state of river network of the Atlas-Mesea domains, attest for a recent phase of topographic rejuvenation (Fig. 1.2; Krijgsman et al., 1999; Babault et a., 2008; Barbero et al., 2010; Pastor et al., 2015; Stokes et al., 2017).

Key and debated issues associated with this phase of uplift are the different contribution of short and long wavelength processes and hence the amount of uplift related to tectonic and mantle dynamic forces. To evaluate this dynamic component, we performed a geomorphic analysis using a combined approach of traditional and innovative techniques (*e.g.*, cosmogenic nuclides, linear inverse method, knickpoints, longitudinal profiles, χ-plot, celerity model, swath profiles) in the slowly eroding and exhuming domains of the Atlas-Meseta system. Particularly, we focused on the Anti-Atlas Mountains and Western Moroccan Meseta, which represent weakly deformed regions, where local tectonic and climatic conditions have been stable over geological time, thus providing the possibility to quantify the timing, magnitudes and rates of mantle-driven uplift.

1.3. Cosmogenic nuclides: an overview

In 1912 the Austrian physicist Victor Hess discovered the cosmic radiations, and in the 1934 A.V. Grosse suggested that they could produce radioactive nuclides at the surface of the Earth, thus generating "cosmic radio-elements". At the same time, Domenico Pacini, a professor at the University of Bari, made a series of measurements to determine the variation in the speed of discharge of an electroscope (and thus the intensity of the radiation) while the electroscope was immersed in a box in the sea near the Naval Academy in the Bay of Livorno. Pacini discovered that the discharge of the oscilloscope was significantly slower than at the surface. From that time, scientists started to think that this interaction between cosmic particles and rock materials could be used to solve geomorphic problems. Despite the efforts, until the mid-1980s the cosmogenic nuclide application remained just a theory without any natural appliction because available analytical instrumentation was not capable to measure the concentrations of most cosmogenic nuclides producted at the Earth-surface. In the meantime, a spatial model for production rates in the atmosphere was verified empiritically by Lal et al. (1960) at high elevation at 51°N latitude, providing the possibility to normalized production rates on the surface. A key step in the history has been played by the development of AMS (accelerator mass spectrometry) in the early 1980s, which allow to measure the isotopic ratios (^{10}Be/^{9}Be and ^{26}Al/^{27}Al), despite the presence of isobars. After that, the method has been refined by the development of a more reliably cosmogenic nuclide production scaling model that incorporate different physical processes, such as influence of geomagnetic field, temporal spatial variation in the paleo-atmosphere and surface elevation for different latitudes and altitudes of sampling sites (Lal, 1991; Stone et al., 2000; Gosse and Phillips, 2001).

Hence, the production of cosmogenic nuclides on Earth results from nuclear reactions initiated by primary and secondary energetic ray particles, by spallation process, that interact with atmosphere and surface rock. Spallation-produced nucleons, which in turn induce spallation in other target nuclides, producing a nuclear cascade composed of secondary nucleons (protons and neutrons) and mesons (kaons and muons) (Gosse and Phillips, 2001; Dunai, 2010). The most used cosmogenic isotopes such as ^{10}Be, ^{26}Al, ^{36}Cl, ^{14}C, ^{3}He and ^{21}Ne allow addressing a wide range of geomorphologic problems due to their surface production in commonly occurring minerals (for example quartz, in case of ^{10}Be, ^{26}Al; e.g., Gosse and Phillips, 2001; Dunai et al., 2010).

Table 1.1

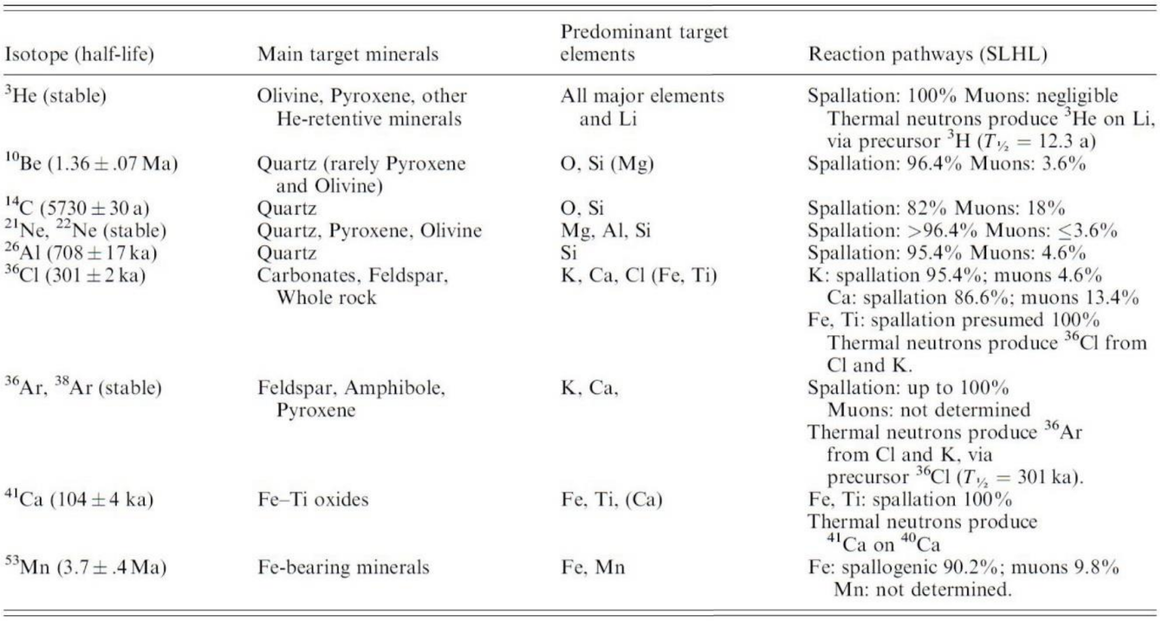

Isotope (half-life)	Main target minerals	Predominant target elements	Reaction pathways (SLHL)
^{3}He (stable)	Olivine, Pyroxene, other He-retentive minerals	All major elements and Li	Spallation: 100% Muons: negligible Thermal neutrons produce ^{3}He on Li, via precursor ^{3}H ($T_{½}$ = 12.3 a)
^{10}Be (1.36 ± .07 Ma)	Quartz (rarely Pyroxene and Olivine)	O, Si (Mg)	Spallation: 96.4% Muons: 3.6%
^{14}C (5730 ± 30 a)	Quartz	O, Si	Spallation: 82% Muons: 18%
^{21}Ne, ^{22}Ne (stable)	Quartz, Pyroxene, Olivine	Mg, Al, Si	Spallation: >96.4% Muons: ≤3.6%
^{26}Al (708 ± 17 ka)	Quartz	Si	Spallation: 95.4% Muons: 4.6%
^{36}Cl (301 ± 2 ka)	Carbonates, Feldspar, Whole rock	K, Ca, Cl (Fe, Ti)	K: spallation 95.4%; muons 4.6% Ca: spallation 86.6%; muons 13.4% Fe, Ti: spallation presumed 100% Thermal neutrons produce ^{36}Cl from Cl and K.
^{36}Ar, ^{38}Ar (stable)	Feldspar, Amphibole, Pyroxene	K, Ca,	Spallation: up to 100% Muons: not determined Thermal neutrons produce ^{36}Ar from Cl and K, via precursor ^{36}Cl ($T_{½}$ = 301 ka).
^{41}Ca (104 ± 4 ka)	Fe–Ti oxides	Fe, Ti, (Ca)	Fe, Ti: spallation 100% Thermal neutrons produce ^{41}Ca on ^{40}Ca
^{53}Mn (3.7 ± .4 Ma)	Fe-bearing minerals	Fe, Mn	Fe: spallogenic 90.2%; muons 9.8% Mn: not determined.

However, there are unstable and stable cosmogenic nuclides (Table 1.1). Assuming that the production rate is constant with time, and that a given target is continuously exposed, the concentration of “stable” cosmogenic nuclides increases monotonously at a constant rate (Fig. 1.5). Cosmogenic radionuclides decay with time and after 5-6 half-life, they can be considered extinct (Dunai et al., 2010). The cosmogenic nuclides become a widely used tool in geomorphology, in order to: (i) dating the exposure ages of geomorphic surfaces, (ii) burial dating, (iii) estimates of erosion/denudation rates (constrainingn uplift rates), (iv) study soil dynamics and sedimentary processes of fluvial catchments.

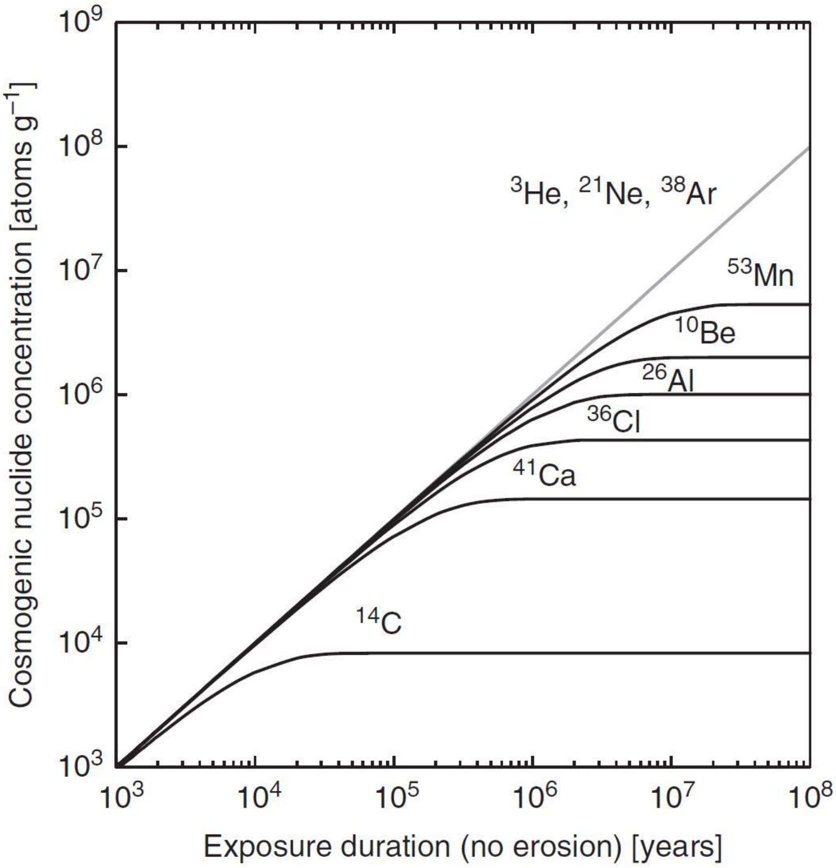

Figure 1.5. Accumulation of cosmogenic nuclides in a non-eroding surface. Radioactive nuclides approach a secular equilibrium between production and decay after 2–3 half-lives. The concentration of stable nuclides increases continuously (from Dunai, 2010).

In the thesis, we used the ^{10}Be concentratin in river-borne sediments to estimate the basin-wide denudation rates.

The nuclides can be used to infer denudation rates because their production rates within a mineral grain depend on their proximity to the surface, as then production rates decrease exponentially with the depth in rock (60 cm in rock of density 2.6 g cm^{3}). When studying basin-wide denudation rates the cosmogenic nuclide concentrations reflect how quickly the overlying mass went away (Granger et al., 2014). Thus, the concentration of cosmogenic nuclides is inversely proportional to the denudation rate (Lal, 1991).

The basin-wide denudation rates are usually calculated considering the three different categories of particles responsible for the in-situ production of ^{10}Be (Braucher et al., 2011).

$$C(\varepsilon,x,t)=\frac{P_n}{\lambda+\frac{\rho\cdot\varepsilon}{\Lambda_n}}\cdot e^{\frac{\rho\cdot x}{\Lambda_n}}\cdot\left(1-e^{-\left(\lambda+\frac{\rho\cdot\varepsilon}{\Lambda_n}\right)t}\right)+\frac{P_{\mu s}}{\lambda+\frac{\rho\cdot\varepsilon}{\Lambda_{\mu s}}}\cdot e^{\frac{\rho\cdot x}{\Lambda_{\mu s}}}\cdot\left(1-e^{-\left(\lambda+\frac{\rho\cdot\varepsilon}{\Lambda_{\mu s}}\right)t}\right)+$$

$$\frac{P_{\mu f}}{\lambda+\frac{\rho\cdot\varepsilon}{\Lambda_{\mu f}}}\cdot e^{\frac{\rho\cdot x}{\Lambda_{\mu f}}}\cdot\left(1-e^{-\left(\lambda+\frac{\rho\cdot\varepsilon}{\Lambda_{\mu f}}\right)t}\right) \qquad (5)$$

Where $C(x,t)$ corresponds to the nuclide concentration as a function of depth x (g/cm^2), e (g/cm^2/yr) represents the denudation rate and t (yr) the exposure time. P_n, P_{us}, P_{uf} and Λ_m, Λ_{us}, Λ_{uf} are the production rates and attenuation lengths of neutrons, slow muons and fast muons, respectively, and λ is the radioactive decay constant of ^{10}Be and ρ is the rock density.

To derive production rates several scaling and correction factors have to be considered. Not only the production rates change as a function of latitude and altitude, but also it depends on the local factors (topographic shielding), such as sloping surfaces of exposure and vicinity of topographic irregularities (Gosse and Phillips, 2001; Dunai et al., 2010).

Furthermore, the calculation of ^{10}Be-derived denudation rates requires several assumptions, such as:sediments are supplied at the rate that is proportional to the denudation rate, quartz (in case of ^{10}Be, ^{26}Al) is evenly distributed throughout the catchment and that the analyzed cosmogenic nuclide was absent before the rock approached the surface (Fig. 1.6). An additional constrain in case of unstable cosmogenic nuclides is that denudation is fast enough to neglet the radioactive decay. This is not an issue with stable nuclides.

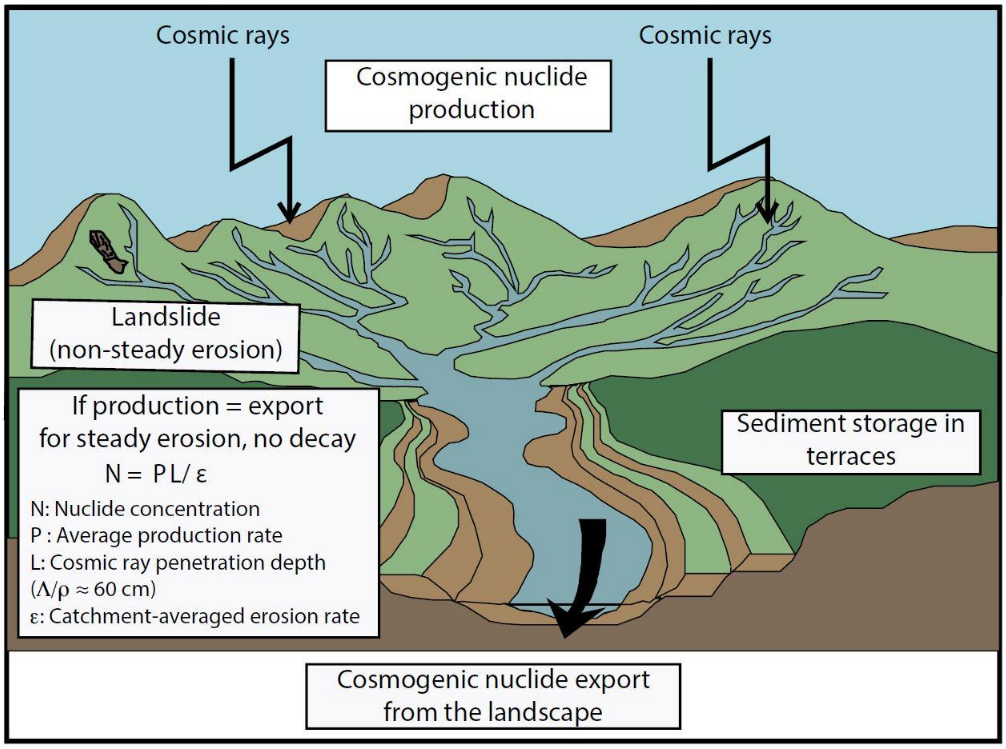

Figure 1.6. Schematich sketch of an eroding landscape and catchment dyanamics (from Granger et al., 2014).

However, some assumptions may not be representative for real case studies. For example, if it is likely true that the sampled sand in the active channels might be representative for the whole catchment, it is however important to consider that surface processes, such as landslides, can perturbate the supply system, and thus deliver an overwhelming load of sediment that can biases the estimates of basin-wide denudation rate (Fig. 1.6). Another important point to discuss is the timescale, which is equivalent to the time necessary to lower the landscape by 60 cm. However, an acceleration in denudation rate due to and increase in uplift or a climate change (more erodible conditions) will perturb the response time of cosmogenic nuclide concentration (“damped response time”). Despite these complications and assumptions, the method has been used over the past 30 years to estimate basin-wide denudation rates. The measurement of in-situ ^{10}Be produced in quartz is the most used method to infer the basin-wide denudation. An impressive amount of works has been done in active and inactive regions to quantify denudation rates (*e.g.,* Ouimet et al., 2009; Miller et al., 2013; Derrieux et al., 2014; Olivetti et al., 2016). A first conclusion from these studies indicates that usually a primary role in controlling the erosional dynamics of a landscape is played by climate and topographic steepening (only few studies suggest the main role of bedrock erodibility even in active ranges, i.e., Molliex et al., 2017; Zondervan et al., 2020), which is caused by rock uplift and drives river incision and hillslope erosion, in the active regions (e.g., Adams et al., 2020). Instead, in the quiescent areas, where tectonic and climate forces are stable and do not vary significantly in space, landscape dynamics seem mainly control by lithology and spatial variation of bedrock erodibility (e.g., Scharf et al., 2013; Piefer et al., 2021).

1.4. Motivations and descriptions of thesis chapters

The long-term tectonic evolution and the deformation style of the High Atlas and to a lesser extent the Middle Atlas are well described in literature as well as the geomorphic configurations of some domains of the Atlas-Meseta system. Nevertheless, there are still debated issues and open questions. For example, how can the Atlas-Meseta topography be so high without a significant crustal root? What are the rates and tha magnitude of the large wavelength surface uplift? How does tectonic deformation and large wavelength uplift interact? What are the main processes that causes Cenozoic topographic rejuvenation?

This Ph.D. project focuses on some of these questions, with the main goal of deciphering the mantle-driven contribution on uplift, for the domains of the Atlas-Meseta system that experienced limited tectonic deformation (Anti-Atlas and Western Meseta). To achieve this goal, I combined basin-wide and in situ denudation rates derived from cosmogenic nuclides with stream profiles, regional and basins geomorphic analysis using innovative and traditional geomorphic approaches. The results are subdivided into three manuscripts presented here in form of three chapters.

In chapter two, I characterized the topographic metrics and the erosion rates obtained from ^{10}Be cosmogenic concentrations, of the uplifted relict landscapes of the Anti-Atlas domain to assess the main controlling factors on the erosional dynamics. This allowed quantifying the bedrock erodibility of different rocks exposed in the sampled catchments. Through a comparison between the Anti-Atlas and similar ancient, tectonically inactive belt, I concluded that lithology plays a major role in lowering and creating topographic relief, without any dependence on climate and mean annual precipitation. This chapter has been submitted to *Earth and Planetary Science Letters*.

The third chapter is focused on the long-term topographic evolution of the Anti-Atlas Mountains in order to decipher the mechanisms of uplift that were responsible for the Cenozoic topographic resurgence. In particular, I extracted information from topography and channel networks for the entire landscape (i.e., upstream and downstream of the major non-lithological knickpoints) and calculated the timing, magnitude and rates of uplift during the Cenozoic. The results of this analysis suggest that the Anti-Atlas is characterized by an increase of surface uplift from 500 m, in the western sector of Anti-Atlas, to 1200 m in the Siroua Massif during the middle-late Miocene. The Anti-Atlas is only the result of deep-seated processes. Instead, Siroua Massif topography results from the contribution of different signals (long- and short-wavelength components), such as faulting activity and magma injection and deep-seated processes. Finally, the upwelling of hot asthenosphere seems the only possible mechanism to explain this long wavelength topographic swell. This chapter will be submitted to *Tectonics*.

The fourth chapter aimed to dechipere the long-term topographic evolution of the Western Moroccan Meseta, a quiescent tectonic region characterized by a transient adjustment of hillslope and channels in response to a Cenozoic increase in rock uplift rates. Here, I also quantified the erosional processes using the ^{10}Be-derived denudation rates, and the magnitude of dynamic uplift through a detailed topographic analysis. The main results let me conclude that Western Moroccan Meseta is characterized by a transient state, as documented by the linear correlation between denudation rates and topographic and channel metrics. The results highlight the importance of considering uneven distribution of quartz-bearing rocks in the sampled catchments, which represents a critical issue for deriving basin-wide denudation rates. Finally, the estimates of surface uplift from the different domains of Atlas-Meseta system describe a large wavelength positive feature, with a highest uplift recorded by the uplifted Messinian marine deposits in the Middle Atlas domain.

Overall, this thesis provides new insights into the topographic evolution and the erosional dynamics of two tectonically inactive regions of Morocco such as the Anti-Atlas and the Western Meseta. Specifically, it demonstrates that the morphologic signatures of transience can be used to understand the landscape dynamics and to assess the temporal and spatial scales of tectonic perturbations.

1.5. References

Adams, B. A., Whipple, K. X., Forte, A. M., Heimsath, A. M., & Hodges, K. V. (2020). Climate controls on erosion in tectonically active landscapes. *Science advances*, 6(42), eaaz3166.

Ait Malek, H. A., Gasquet, D., Bertrand, J. M., & Leterrier, J. (1998). Géochronologie U-Pb sur zircon de granitoïdes éburnéens et panafricains dans les boutonnières protérozoïques d'Igherm, du Kerdous et du Bas Drâa (Anti-Atlas occidental, Maroc). *Comptes Rendus de l'Académie des*

Sciences-Series IIA-Earth and Planetary Science, *327*(12), 819-826. https://doi.org/10.1016/S1251-8050(99)80056-1

Arboleya, M. L., Teixell, A., Charroud, M., & Julivert, M. (2004). A structural transect through the High and Middle Atlas of Morocco. *Journal of African Earth Sciences*, 39(3–5), 319–327. https://doi.org/10.1016/j.jafrearsci.2004.07.036

Arboleya, M.-L., Babault, J., Owen, L. A., Teixell, A., & Finkel, R. C. (2008). Timing and nature of Quaternary fluvial incision in the Ouarzazate foreland basin, Morocco. *Journal of the Geological Society*, 165(6), 1059–1073. https://doi.org/10.1144/0016-76492007-151

Ayarza, P., Alvarez-Lobato, F., Teixell, A., Arboleya, M. L., Teson, E., Julivert, M., & Charroud, M. (2005). Crustal structure under the central High Atlas Mountains (Morocco) from geological and gravity data. *Tectonophysics*, *400*(1-4), 67-84. https://doi.org/10.1016/j.tecto.2005.02.009

Babault, J., Teixell, A., Arboleya, M. L., & Charroud, M. (2008). A Late Cenozoic age for long-wavelength surface uplift of the Atlas Mountains of Morocco. *Terra nova*, *20*(2), 102-107. https://doi.org/10.1111/j.1365-3121.2008.00794.x

Barbero, L., Jabaloy, A., Gómez-Ortiz, D., Pérez-Peña, J. V., Rodríguez-Peces, M. J., Tejero, R., ... & Asebriy, L. (2011). Evidence for surface uplift of the Atlas Mountains and the surrounding peripheral plateaux: Combining apatite fission-track results and geomorphic indicators in the Western Moroccan Meseta (coastal Variscan Paleozoic basement). *Tectonophysics*, 502(1-2), 90-104.

Baudon, C., Fabuel-Perez, I., & Redfern, J. (2009). Structural style and evolution of a Late Triassic rift basin in the central High Atlas, Morocco: Controls on sediment deposition. *Geological Journal*, 44(6), 677–691. https://doi.org/10.1002/gj.1195

Beauchamp, W., Allmendinger, R. W., Barazangi, M., Demnati, A., El Alji, M., & Dahmani, M. (1999). Inversion tectonics and the evolution of the High Atlas Mountains, Morocco, based on a geological-geophysical transect. *Tectonics*, 18(2), 163–184. https://doi.org/10.1029/1998TC900015

Bezada, M. J., Humphreys, E. D., Davila, J. M., Carbonell, R., Harnafi, M., Palomeras, I., & Levander, A. (2014). Piecewise delamination of Moroccan lithosphere from beneath the Atlas Mountains. *Geochemistry, Geophysics, Geosystems*, *15*(4), 975-985. https://doi.org/10.1002/2013GC005059

Braucher, R., Merchel, S., Borgomano, J., Bourlès, D. L. (2011). Production of cosmogenic radionuclides at great depth: A multi element approach. *Earth Planet. Sci. Lett*. 309(1-2), 1-9. https://doi.org/10.1016/j.epsl.2011.06.036.

Burkhard, M., Caritg, S., Helg, U., Robert-Charrue, C., Soulaimani, A. (2006). Tectonics of the Anti-Atlas of Morocco. *C.R. Geosci*. 338(1-2), 11-24. https://doi.org/10.1016/j.crte.2005.11.012.

Charton, R., Bertotti, G., Arnould, A. D., Storms, J. E., & Redfern, J. (2021). Low-temperature thermochronology as a control on vertical movements for semi-quantitative source-to-sink analysis: A case study for the Permian to Neogene of Morocco and surroundings. *Basin Research*, *33*(2), 1337-1383. https://doi.org/10.1111/bre.12517

Choubert, G. (1952). Histoire géologique du domaine de l'Anti-Atlas. *Notes et Mém. Serv. Géol. Maroc*, (100), 77-172.

De Beer, C. H., Chevallier, L. P., De Kock, G. S., Gresse, P. G., & Thomas, R. J. (2000). Mémoire explicatif de la carte géologique du Maroc au 1/50 000, Feuille Sirwa. *Notes Mem. Serv. Geol. Maroc*, *395*, 86.

Derrieux, F., Siame, L. L., Bourlès, D. L., Chen, R. F., Braucher, R., Léanni, L., Lee, J.C., Chu, H.T., & Byrne, T. B. (2014). How fast is the denudation of the Taiwan mountain belt? Perspectives from in situ cosmogenic 10Be. *Journal of Asian Earth Sciences*, *88*, 230-245. https://doi.org/10.1016/j.jseaes.2014.03.012

Domènech, M., Teixell, A., & Stockli, D. F. (2016). Magnitude of rift-related burial and orogenic contraction in the Marrakech High Atlas revealed by zircon (U-Th)/He thermochronology and thermal modeling. *Tectonics*, 35(11), 2609–2635. https://doi.org/10.1002/2016TC004283

Duggen, S., Hoernle, K. A., Hauff, F., Kluegel, A., Bouabdellah, M., & Thirlwall, M. F. (2009). Flow of Canary mantle plume material through a subcontinental lithospheric corridor beneath Africa to the Mediterranean. *Geology*, *37*(3), 283-286. https://doi.org/10.1130/G25426A.1

Dunai, T. J. (2010). *Cosmogenic nuclides: principles, concepts and applications in the earth surface sciences*. Cambridge University Press.

El Azzouzi, M., Bellon, H., Maury, R. C., Pique, A., Cotten, J., Griffiths, J. B., ... & Hernandez, J. (1999). Evolution of the sources of Moroccan volcanism during the Neogene. *Comptes Rendus de l'Academie des Sciences. Serie 2, Sciences de la Terre et des Planetes*, 95-102.

El Azzouzi, M. H., Maury, R. C., Bellon, H., Youbi, N., Cotten, J., & Kharbouch, F. (2010). Petrology and K-Ar chronology of the Neogene-quaternary Middle Atlas basaltic province, Morocco. *Bulletin de la société géologique de France*, *181*(3), 243-257. https://doi.org/10.2113/gssgfbull.181.3.243

Fekkak, A., Ouanaimi, H., Michard, A., Soulaimani, A., Ettachfini, E. M., Berrada, I., et al. (2018). Thick-skinned tectonics in a Late Cretaceous-Neogene intracontinental belt (High Atlas Mountains, Morocco): The flat-ramp fault control on basement shortening and cover folding. *Journal of African Earth Sciences*, 140, 169–188. https://doi.org/10.1016/j.jafrearsci.2018.01.008

Gasquet, D., Ennih, N., Liégeois, J. P., Soulaimani, A., & Michard, A. (2008). The pan-african belt. In *Continental evolution: the geology of Morocco* (pp. 33-64). Springer, Berlin, Heidelberg. https://doi.org/10.1007/978-3-540-77076-3_2

Gomez, F., Allmendinger, R., Barazangi, M., Er-Raji, A., & Dahmani, M. (1998). Crustal shortening and vertical strain partitioning in the Middle Atlas Mountains of Morocco. *Tectonics*, *17*(4), 520-533. https://doi.org/10.1029/98TC01439

Gosse, J. C., & Phillips, F. M. (2001). Terrestrial in situ cosmogenic nuclides: theory and application. *Quaternary Science Reviews*, 20(14), 1475-1560.

Granger, D. E., & Schaller, M. (2014). Cosmogenic nuclides and erosion at the watershed scale. *Elements*, 10(5), 369-373.

Guimerà, J., Arboleya, M. L., & Teixell, A. (2011). Structural control on present-day topography of a basement massif: the Central and Eastern Anti-Atlas (Morocco). *Geologica Acta: an international earth science journal*, *9*(1), 55-65. https://doi.org/10.1344/105.00 0001643.

Hoepffner, C., Soulaimani, A., & Piqué, A. (2005). The moroccan hercynides. *Journal of African Earth Sciences*, *43*(1-3), 144-165. https://doi.org/10.1016/j.jafrearsci.2005.09.002

Frizon de Lamotte, D., Leturmy, P., Missenard, Y., Khomsi, S., Ruiz, G., Saddiqi, O., Guillocheau F., & Michard A. (2009). Mesozoic and Cenozoic vertical movements in the Atlas system (Algeria, Morocco, Tunisia). An overview: *Tectonophysics.* 475, 9–28. https://doi.org/10.1016/j.tecto.2008.10.024.

Hollard, H., Choubert, G., Bronner, G., Marchand, J., Sougy, J. (1985). Carte géologique du Maroc, scale 1: 1,000,000. Serv. Carte géol. Maroc. 260(2).

Krijgsman, W., Langereis, C. G., Zachariasse, W. J., Boccaletti, M., Moratti, G., Gelati, R., ... & Villa, G. (1999). Late Neogene evolution of the Taza–Guercif Basin (Rifian Corridor, Morocco) and implications for the Messinian salinity crisis. *Marine Geology*, 153(1-4), 147-160.

Lal, D., Arnold, J. R., & Honda, M. (1960). Cosmic-ray production rates of Be 7 in oxygen, and P 32, P 33, S 35 in argon at mountain altitudes. Physical Review, 118(6), 1626.

Lal, D. (1991). Cosmic ray labeling of erosion surfaces: in situ nuclide production rates and erosion models. *Earth and Planetary Science Letters*, 104(2-4), 424-439.

Lanari, R., Fellin, M. G., Faccenna, C., Balestrieri, M. L., Pazzaglia, F. J., Youbi, N., & Maden, C. (2020a). Exhumation and surface evolution of the western high atlas and surrounding regions as constrained by low-temperature thermochronology. *Tectonics*, *39*(3), e2019TC005562. https://doi.org/10.1029/2019TC005562

Lanari, R., Faccenna, C., Fellin, M. G., Essaifi, A., Nahid, A., Medina, F., & Youbi, N. (2020b). Tectonic evolution of the western high Atlas of Morocco: oblique convergence, reactivation, and transpression. *Tectonics*, *39*(3), e2019TC005563. https://doi.org/10.1029/2019TC005563

Michard, A., Saddiqi, O., Chalouan, A., & de Lamotte, D. F. (Eds.). (2008). Continental evolution: The geology of Morocco: Structure, stratigraphy, and tectonics of the Africa-Atlantic-Mediterranean triple junction (Vol. 116). Berlin: Springer.

Miller, S. R., Sak, P. B., Kirby, E., & Bierman, P. R. (2013). Neogene rejuvenation of central Appalachian topography: Evidence for differential rock uplift from stream profiles and erosion rates. Earth and Planetary Science Letters, 369, 1-12.

Miller, M. S., & Becker, T. W. (2014). Reactivated lithospheric-scale discontinuities localize dynamic uplift of the Moroccan Atlas Mountains. *Geology*, *42*(1), 35-38. https://doi.org/10.1130/G34959.1.

Miller, M. S., O'Driscoll, L. J., Butcher, A. J., & Thomas, C. (2015). Imaging Canary Island hotspot material beneath the lithosphere of Morocco and southern Spain. *Earth and Planetary Science Letters*, *431*, 186-194. https://doi.org/10.1016/j.epsl.2015.09.026

Missenard, Y., Zeyen, H., Frizon de Lamotte, D., Leturmy, P., Petit, C., Sébrier, M., & Saddiqi, O. (2006). Crustal versus asthenospheric origin of relief of the Atlas Mountains of Morocco. *Journal of Geophysical Research: Solid Earth*, *111*(B3). https://doi.org/10.1029/2005JB003708

Missenard, Y., Saddiqi, O., Barbarand, J., Leturmy, P., Ruiz, G., El Haimer, F. Z., & Frizon de Lamotte, D. (2008). Cenozoic denudation in the Marrakech High Atlas, Morocco: insight from apatite fission-track thermochronology. *Terra Nova*, *20*(3), 221-228. https://doi.org/10.1111/j.1365-3121.2008.00810.x.

Molliex, S., Jouet, G., Freslon, N., Bourles, D. L., Authemayou, C., Moreau, J., & Rabineau, M. (2017). Controls on Holocene denudation rates in mountainous environments under Mediterranean climate. Earth Surface Processes and Landforms, 42(2), 272-289. https://doi.org/10.1002/esp.3987

Olivetti, V., Godard, V., Bellier, O., & ASTER team. (2016). Cenozoic rejuvenation events of Massif Central topography (France): Insights from cosmogenic denudation rates and river profiles. *Earth and Planetary Science Letters*, 444, 179-191.

Ouimet, W. B., Whipple, K. X., & Granger, D. E. (2009). Beyond threshold hillslopes: Channel adjustment to base-level fall in tectonically active mountain ranges. Geology, 37(7), 579-582.

Pacini, D., & De Angelis, A. (2011). Penetrating radiation on the sea. *arXiv preprint arXiv:1101.3015*.

Padel, M. (2016). Influence cadomienne dans les séries présardes des Pyrénées Orientales: approche géochimique, stratigraphique et géochronologique. *Université de Lille*, 1.

Rimi, A. (1999). Mantle heat flow and geotherms for the main geologic domains in Morocco. *International Journal of Earth Sciences*, *88*(3), 458-466. https://doi.org/10.1007/s005310050278

Seber, D., Barazangi, M., Tadili, B. A., Ramdani, M., Ibenbrahim, A., & Ben Sari, D. (1996). Three-dimensional upper mantle structure beneath the intraplate Atlas and interplate Rif mountains of Morocco. *Journal of Geophysical Research: Solid Earth*, *101*(B2), 3125-3138. https://doi.org/10.1029/95JB03112

Sebti, S., Saddiqi, O., El Haimer, F. Z., Michard, A., Ruiz, G., Bousquet, R., Baidder, L., & de Lamotte, D. F. (2009). Vertical movements at the fringe of the West African Craton: First zircon fission track datings from the Anti-Atlas Precambrian basement, Morocco. *Comptes Rendus Geoscience*, *341*(1), 71-77. https://doi.org/10.1016/j.crte.2008.11.006

Sehrt, M., Glasmacher, U. A., Stockli, D. F., Jabour, H., & Kluth, O. (2018). The southern Moroccan passive continental margin: An example of differentiated long-term landscape evolution in Gondwana. *Gondwana Research*, *53*, 129-144. https://doi.org/10.1016/j.gr.2017.03.013

Soulaimani, A., Bouabdelli, M., & Piqué, A. (2003). L'extension continentale au Néo-Protérozoïque supérieur-Cambrien inférieur dans l'Anti-Atlas (Maroc). *Bulletin de la Société géologique de France*. http://hdl.handle.net/2042/244

Stokes, M., Mather, A. E., Belfoul, M., Faik, F., Bouzid, S., Geach, M. R., Cunha, P.P., & Thiel, C. (2017). Controls on dryland mountain landscape development along the NW Saharan desert margin: Insights from Quaternary river terrace sequences (Dadès River, south-central High Atlas, Morocco). *Quaternary Science Reviews*, *166*, 363-379.

Teixell, A., Arboleya, M. L., Julivert, M., & Charroud, M. (2003). Tectonic shortening and topography in the central High Atlas (Morocco). *Tectonics*, *22*(5). https://doi.org/10.1029/2002TC001460

Torsvik, T. H., & Cocks, L. R. M. (2013). Gondwana from top to base in space and time. *Gondwana Research*, 24(3-4), 999-1030. https://doi.org/10.1016/j.gr.2013.06.012

Zondervan, J. R., Stokes, M., Boulton, S. J., Telfer, M. W., Mather, A. E. (2020). Rock strength and structural controls on fluvial erodibility: Implications for drainage divide mobility in a collisional mountain belt. *Earth and Planet. Sci. Lett.*, 538, 116221. https://doi.org/10.1016/j.epsl.2020.116221.

Chapter 2. Lithological control on erosional dynamics in a tectonically inactive mountain belt (Anti-Atlas, Morocco)

Authors

Romano Clementucci[1,2*], Paolo Ballato[1], Lionel L. Siame[2], Claudio Faccenna[1,3], Ahmed Yaaqoub[4], Abderrahim Essaifi[4], Laëtitia Leanni[2], Valery Guillou[2]

Affiliations:

[1] Dipartimento di Scienze, Università Roma Tre, Largo San Leonardo Murialdo 1, 00146 Rome, Italy.

[2] Aix-Marseille Univ., CNRS, IRD, INRAE, Collège de France, CEREGE, Aix-en Provence, France.

[3] GFZ-German Research Centre for Geosciences, Potsdam, Germany.

[4] Département de Géologie, FSSM, B.P. 2390, Université Cadi Ayyad, Marrakech, Morocco.

*Corrisponding author : romano.clementucci@uniroma3.it

Keywords

cosmogenic nuclides, quantitative geomorphology, erodibility, landscape evolution, Atlas Mountains, topographic relief

2.1. Abstract

Topographic relief results from the complex interactions between tectonics and erosional surface processes. The efficiency of surface processes is a function of topographic slopes, bedrock erodibility and climatic conditions. Ancient orogens offers a favourable setting to isolate the contribution of lithology, as tectonically driven surface uplift is typically negligible and rock strength variability can exerts a critical role on the evolution of topographic relief. The Anti-Atlas in NW Africa is a late Paleozoic orogen that contains a well-preserved, uplifted, relict landscape that has been slowly eroding since the late Cretaceous. Here, we combine geomorphic analysis with ^{10}Be-derived denudation rates, to quantify the impact of bedrock erodibility and get insight into the surface evolution of the Anti-Atlas and the adjacent Siroua Massif. Specifically, we show that basin-wide denudation rates from the relict landscape range from 5 to 20 m/Myr, in agreement with the average long-term rates estimated from eroded volumes of Miocene volcanics and available thermochronometric data. This suggests that the regional relict topography has attained an erosional steady state and has been slowly decaying over geological time. Our results are comparable with data from other tectonically quiescent settings and demonstrate a positive linear correlation between denudation rates and normalized channel steepness indices. This allows us to constrain a narrow range of bedrock erodibility values for different rock-types (quartzite, granitic and sedimentary rocks), that are comparable with estimates from different stable settings. Finally, our compilation from tectonically inactive regions indicates that channel steepness, denudation rates and bedrock erodibility do not change significantly across different climatic zones and precipitation regimes highlighting the critical role of lithology in controlling the topographic relief.

2.2. Introduction

Numerical modelling studies, together with qualitative and quantitative investigations have largely demonstrated the role of tectonics and climate in controlling landscape characteristics of tectonically active regions (Kirby and Whipple, 2001; Kirby and Whipple, 2012; Adams et al., 2020). Conversely, in tectonically quiescent settings, the dominant mechanisms that sustain topographic relief over longer time scales (10^6-10^8 yr) are less understood. In these regions, the relationship between topographic metrics (*i.e.*, basin-averaged slope, local relief, and normalized steepness index) and erosion/rock-uplift rates suggests that climate and bedrock erodibility exert a major control on landscape evolution, channel morphology, and bedrock incision dynamics (Jansen et al., 2010; Scharf et al., 2013; Gallen, 2018; Peifer et al., 2021). The quantification of bedrock erodibility, however, is challenging given that erodibility may span several orders of magnitude (Hack, 1957; Stock and Montgomery, 1999; Kirby and Whipple, 2001; Jansen et al., 2010; Gallen et al., 2018; Zondervan et al., 2020; Piefer et al., 2021). Importantly, post-orogenic and tectonically inactive mountain ranges are usually characterized by steady and protracted low denudation rates, and hence offer the opportunity to isolate the impact of bedrock erodibility for different lithologies (Scharf et al., 2013; Gallen et al., 2018; Peifer et al., 2021).

The Anti-Atlas of NW Africa is a late Palaeozoic orogen that experienced concurrent surface uplift and topographic rejuvenation during the late Cenozoic (Missenard et al., 2008; Frizon de Lamotte et al., 2009; Guimera et al., 2011; Miller and Becker, 2014). Although the flanks of the Anti-Atlas are steeply dissected by fluvial erosion, the top of the range is characterized by a well-preserved, uplifted landscape consisting of crystalline basement and sedimentary rocks. Thermochronometric data suggest that such a basement has been slowly eroding since the late Cretaceous (few tens of meters per million years; Lanari et al., 2020). Furthermore, the Anti-Atlas has not been affected to any extensive tectonic drift across climatic zones during the Cenozoic that may have changed dramatically the erosional conditions (Burkhard et al., 2006). Rather, it has experienced an overall aridification associated with the establishment of the Sahara Desert since at least 2-3 Ma and possibly earlier (7-11 Ma) with alternating wetter phases (Zhang et al., 2014). These characteristics offer a favourable setting to study erosional dynamics and the main factors that control the short- and long-term evolution of topographic relief.

Here, we present ^{10}Be-derived basin-wide denudation rates in the relict landscape and we estimate erosion rates from the eroded volumes of Miocene volcanic flows emplaced along paleo-valleys on the same relict surface. Ths comparison demonstrates that erosion rates have been rather uniform over different time scales (i.e., at least since the late Cretaceous in agreement with thermochronomteric data). Furthermore, we show that the ^{10}Be-derived denudation rates exhibit a strong linear correlation with the topographic metrics, especially when the catchments are classified according to the quartz-bearing lithology exposed on the surface. This allows a reliable quantification of bedrock erodibility and suggests that lithology plays a key role in controlling the landscape evolution and generating topographic relief in a tectonically inactive setting as observed in slowly eroding settings where denudation rates and channel steepness are generally low and do not approached the transition to stochastic threshold of erosion, increasing monotonically through linear relationship (Ouimet et al., 2009; DiBiase and Whipple, 2011).

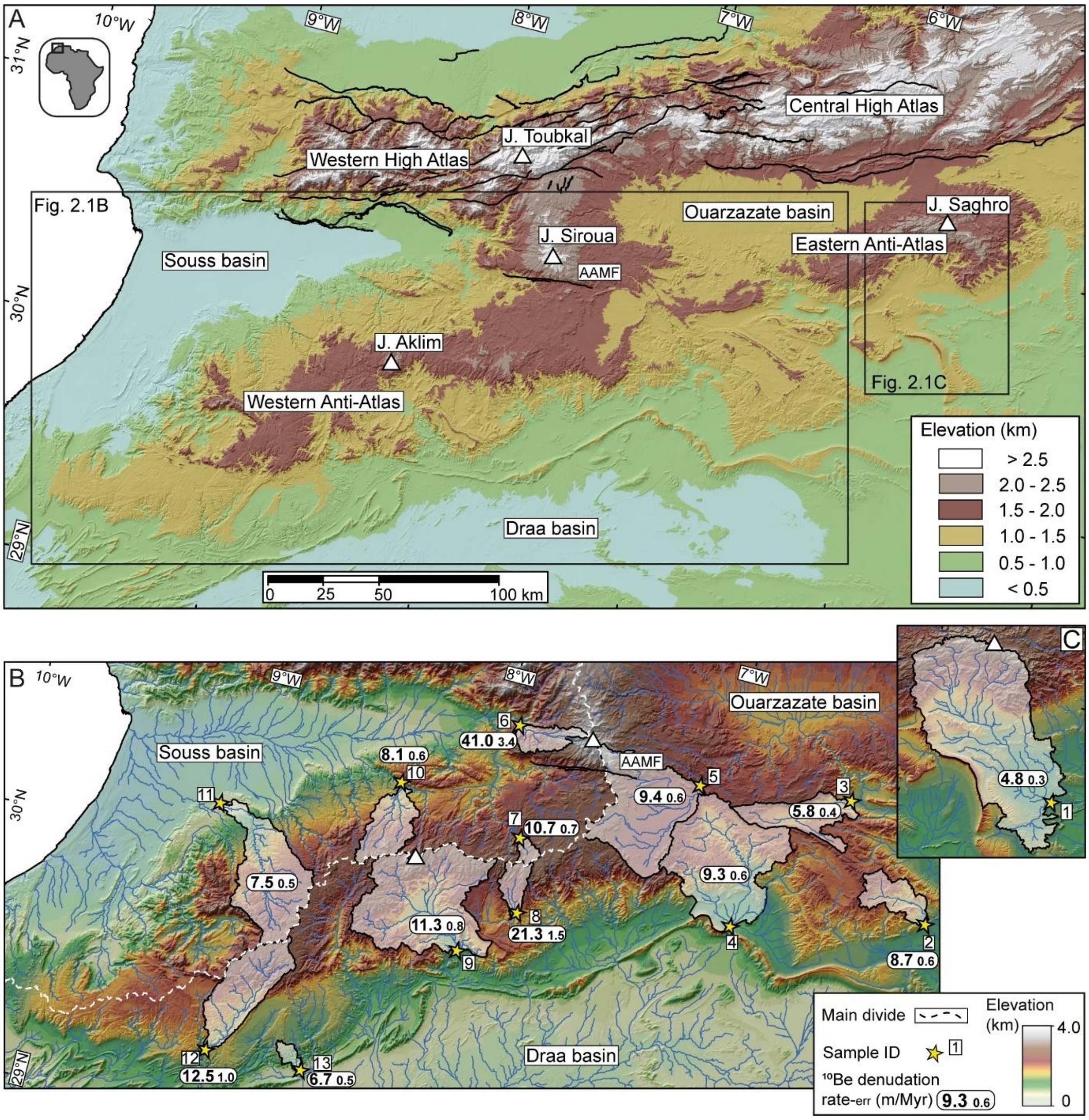

Figure 2.1. A) Digital Elevation Model of the High Atlas and Anti-Atlas Mountains (SRTM dem, pixel size 90 m). The black lines are the major tectonic lineaments. B-C) Topographic map of Anti-Atlas and Siroua Massif, with the ^{10}Be sampling locations. The white polygons are the limits of the sampled catchments. The sample ID is used in the Table S2.1 in supplementary material. AAMF: Anti-Atlas Major Fault.

2.3. Anti-Atlas and Siroua Massif

The Anti-Atlas is the southern extent of the Atlas orogenic system of Morocco (North Africa) (Fig. 2.1). Basement rocks of the region were formed during the Eburnean (~2000 Ma) and the Pan-African (~600 Ma) orogenesis, and comprise granitic, metamorphic, and sedimentary rocks. These rocks are unconformably overlain by Upper Precambrian marine carbonates, Lower Cambrian carbonates and marls, and Middle Cambrian to Middle Devonian sandstone and shales (Fig. 2.2A; Burkhard et al., 2006), that were deformed during the Variscan orogeny (~300 Ma; Burkhard et al., 2006; Soulaimani et al., 2014). Currently, the Anti-Atlas forms an elongated (~ 600 km), WSW-ENE oriented topographic ridge, with a mean elevation of ~2 km, resulting from a regional late Cenozoic topographic rejuvenation, likely attribute to mantle dynamics (Sebrier et al., 2006; Frizon de Lamotte et al., 2009). The elevated axial zone of the belt is characterized by an area of low-topographic relief known as the “high erosional surface” (Choubert, 1952; Missenard et al., 2008; Guimera et al., 2011). This morphotectonic feature is mostly composed of Precambrian basement and Upper Precambrian to Paleozoic sedimentary rocks (Fig. 2.2A). A similar erosional feature has been observed in the Appalachians, the north American counterpart of the Variscan orogens in Africa and Europe (Burkhard et al., 2006; Gallen et al., 2013; Miller et al., 2013). There, the persistence of high topography is supported by isostasy or rock uplift processes and the relict highlands haves been slowly eroding over at least since the Miocene and likely much longer (Gallen et al., 2013; Miller et al., 2013). The Siroua Massif is located between the Anti-Atlas and the High-Atlas and consists of a Mio-Pliocene strato-volcano (Berrahma and Delaloye, 1989) built up over the same high erosional surface, which here is mostly sculpted on Precambrian granites (Missenard et al., 2008; Guimera et al., 2011).

2.4. Methods

2.4.1. Stream profiles, network and topographic analysis

The stream power incision model can describe the variation of channel elevation in time (*dz/dt*), as a function of upstream contributing drainage area and channel slope (Howard and Kerby, 1983; Whipple and Tucker, 1999):

$$\frac{dz}{dt} = U - KA^{m}S^{n} \tag{1}$$

where , *U* is the rock uplift rate, *K* is the erodibility coefficient controlled by bedrock lithology, climate and sediment load, *A* is drainage area, *S* is local channel slope and *m* and *n* are constants, that depend on basin hydrology, channel geometry, and erosion processes (Whipple and Tucker, 1999). Under steady state conditions, the erosion rate (*E*) and rock uplift rate (*U*) are balanced (Kirby and Whipple, 2012), and hence there are no changes in the elevation of the channel bed in time (*dz/dt* = 0). Accordingly, equation (1) can be written as:

$$S = \left(\frac{U}{K}\right)^{\frac{1}{n}} A^{-\left(\frac{m}{n}\right)} \qquad (2)$$

where $(U/K)^{1/n}$ is the channel steepness index (ks) and m/n is the concavity index (θ). Equation (2) can be integrated, assuming steady state condition and spatially invariant uplift and erodibility (Perron and Royden, 2013):

$$z(x) = z(x_b) + \left(\frac{U}{KA_0^m}\right)^{\frac{1}{n}} \int_{xb}^{x} \left(\frac{A_0}{A(x)}\right)^{\frac{m}{n}} dx = z(x_b) + k_s\, A_0^{-\left(\frac{m}{n}\right)} \chi \qquad (3)$$

$$\chi = \int_{xb}^{x} \left(\frac{A_0}{A(x)}\right)^{m/n} dx \qquad (4)$$

Where the integral quantity χ is the independent variable, $z(x_b)$ is the intercept, ks (becomes k_{sn} assuming a reference value of concavity index) is the slope and A_0 is the reference drainage area, usually assumed to be 1 km^2 (Perron and Royden, 2013). Thus, to constrain the topographic evolution of the study area, we analysed the spatial variations of the topographic slope (Supplementary Fig. S2.1), normalized channel steepness index (k_{sn}) and the spatial distribution of knickpoints in order to explore the possible spatial changes in rock uplift (Fig. 2.2B). We used a Shuttle Radar Topography Mission Digital Elevation Model (SRTM DEM, pixel size of 90 m) for the Anti-Atlas and the Siroua Massif to extract the drainage network. Stream profiles were extracted and analyzed using MATLAB scripts. Particularly, we used a MATLAB software package TopoToolbox (Schwanghart and Scherler, 2014) and Topographic Analysis Kit (Forte and Whipple, 2019). The k_{sn} and concavity indices, upstream and downstream of the non-lithological knickpoints, have been extracted from DEMs by the use of integral approach,(Perron and Royden, 2013; Forte and Whipple, 2019), considering a critical drainage area for channel head initiation of 1 km^2. To allow the effective comparison among longitudinal profiles with different drainage area, and to compare value of k_{sn} from different regions a reference value of reference concavity (θ_{ref}) of 0.45 is applied, as commonly used (Kirby and Whipple, 2012). This value of θ_{ref} falls in the range of values covering the estimates of θ upstream and downstream of non-lithological knickpoints, from single stream profiles analysis in the study area (Supplementary Table S2.2). The non-lithological knickpoints were identified using available geological maps and satellite imagery and also based on their distribution in the χ-elevation plot (Fig. 2.3A). In fact, rivers that have experienced a similar rock uplift history should have similar slopes with knickpoints clustering around similar χ values (Perron and Royden, 2013), and usually separate stream segments with different k_{sn} (Kirby and Whipple, 2012; Olivetti et al., 2016). Finally, we extracted basin-averaged precipitation rates (as a proxy for the spatial climate variation), slope, local relief and k_{sn} for the portions of the sampled catchment that include quartz-bearing lithologies, in order to compare them with ^{10}Be-derived denudation rate (see next section; Supplementary Table S2.5). Estimates of bedrock erodibility (K) were performed using the stream power river incision model (for n =1). Furthermore, basin-averaged denudation and normalized channel steepness for different lithologies (mainly granitic rocks and quartzites) of our study area are then integrated into a global compilation of regions characterized by slow tectonic activity (section 2.6.3). Here, we calculated the normalised K for n=1 and 2, to test the best-fit model that describes the relationship between denudation and channel steepness in the tectonically inactive settings.

2.4.2. ^{10}Be-derived denudation rates

To investigate the role of bedrock erodibility in shaping the landscape we measured the concentration of in situ-produced cosmogenic ^{10}Be of river-borne quartz from sands samples collected in active channels of 13 catchments covering most of the western and central Anti-Atlas (Fig. 1 and Table S1). The sampled catchments drain different quartz-bearing rocks including basement (mainly granite, quartzite, and conglomerate), Pre-Cambrian carbonate, and Cambrian-Ordovician sedimentary rocks. The denudation rates are relative to the portions of the landscape providing quartz grains, hence they were extracted excluding carbonates and classifying the rest of the catchment according to the most abundant quartz-bearing lithology exposed on the surface (see similar approaches in Safran et al., 2005 and Carretier et al., 2015 among others). Specifically, we defined three quartzite, four granite and six sedimentary dominated basins (for details see supplementary material Tables S4 and S5). Most of the sampled catchments are in disequilibrium conditions (Figs. 3A) with non-lithological knickpoints delimiting an relict landscape (Fig. 2). Samples were collected upstream and downstream of these major knickpoints. Granites and quartzites, however, are mainly exposed in the highest portions of the catchments (upstream of the knickpoints; Figs. 2A and S2), therefore, most of the measured denudation rates are only representative of the relict landscape. Sample 6, located in the Siroua Massif, represents the unique case where a wide contributing area composed of granitic basement occurs downstream the major knickpoint (Figs. 1 and 2A).

Samples were analyzed following a protocol including: (1) sieving of river sand to extract the 250 – 1000 μm fraction. (2) Magnetic separation with the Frantz magnetic separator (three steps: 0.5 - 1 – 1.5 Ampere). (3) Decarbonation of carbonate-rich samples through the reaction with HCl. (4) Leaching with HCl and H_2SiF_6 solution to remove all remaining minerals except quartz. (5) Decontamination from atmospheric ^{10}Be in the quartz grains by means of a three sequential leaching in HF. (6) Total dissolution of quartz grains, after addition of 150 μl spike of an in-house carrier of ^{9}Be carrier solution (3025 ±9 μg/g), from deep-mined phenakite crystal (Merchel et al., 2008). (7) Extraction of the final amount of Be using hydrofluoric and perchloric fuming to remove fluorides; cation and anion exchange chromatography was used to eliminate iron, aluminum, manganese and other elements. (8) Mixing of beryllium oxide with a 325-mesh niobium powder. Measurements of in situ-produced ^{10}Be concentrations were performed at the French Accelerator mass spectrometry (AMS) national facility ASTER (Aix-en Provence). The obtained ^{10}Be/^{9}Be ratios were corrected for procedural blanks and calibrated directly against the in-house STD-11 standard (^{10}Be/^{9}Be = (1.191±0.013) x 10^{-11}; Braucher et al., 2015). Analytical uncertainties (1σ) are related to external uncertainties, variation of isotopic ratios of standards during the runs and to AMS counting statistics.

Finally, the basin-wide denudation rates were calculated considering the three different categories of particles responsible for the in-situ production of ^{10}Be (Braucher et al., 2011).

$$C(x,t) = \frac{P_n}{\lambda + \frac{\rho \cdot \varepsilon}{\Lambda_n}} \cdot e^{\frac{\rho \cdot x}{\Lambda_n}} \cdot \left(1 - e^{-\left(\lambda + \frac{\rho \cdot \varepsilon}{\Lambda_n}\right)t}\right) + \frac{P_{\mu s}}{\lambda + \frac{\rho \cdot \varepsilon}{\Lambda_{\mu s}}} \cdot e^{\frac{\rho \cdot x}{\Lambda_{\mu s}}} \cdot \left(1 - e^{-\left(\lambda + \frac{\rho \cdot \varepsilon}{\Lambda_{\mu s}}\right)t}\right) +$$

$$\frac{P_{\mu f}}{\lambda + \frac{\rho \cdot \varepsilon}{\Lambda_{\mu f}}} \cdot e^{\frac{\rho \cdot x}{\Lambda_{\mu f}}} \cdot \left(1 - e^{-\left(\lambda + \frac{\rho \cdot \varepsilon}{\Lambda_{\mu f}}\right)t}\right) \tag{5}$$

Where *C(x,t)* corresponds to the nuclide concentration as a function of depth (g/cm^2), ε (g/cm^2/yr) represents the denudation rate and *t* (yr) the exposure time. P_n, P_{us}, P_{uf} and Λ_m, Λ_{us}, Λ_{uf} are the production rates and attenuation lengths of neutrons, slow muons and fast muons, respectively. Λ_n, $\Lambda_{\mu s}$, $\Lambda_{\mu f}$ values used in this paper are 160, 1500 and 4320 g/cm^2, respectively (Braucher et al., 2011) and λ is the radioactive decay constant of ^{10}Be and ρ is the rock density.

To determine basin averaged production rates, scaling factors for latitude and altitude corrections were calculated according to Stone (2000), for each pixel of a 90 m-resolution digital elevation model (DEM) using Matlab scripts and following by Balco et al. (2008). Geomorphic shielding factors were also calculated for each pixel of the DEM using a 15° azimuth step following formulations by Dunne et al. (1999). At cosmogenic steady-state, the cosmogenic 10Be in river-borne quartz mineral record a time integrated, spatially averaged denudation rates, which represents fluvially mixed denudation products of all the processes occurring in each watershed (Granger et al., 1996). This integration occurs over the time needed to remove one attenuation length (e.g., roughly 60 cm; Lal, 1991). This integration time depends on the denudation rates and is typically on the order of 10^5 yrs in southern Morocco (Table S2.1).

2.4.3. Erosion rates from incised lava flows

The Siroua Massif comprises several late Miocene to Pliocene lava flows that were emplaced along paleo-valleys on top of the relict landscape, covering an area of approximately of 500 km2 and reaching maximum elevation of ~3300 m (Figs. 2.2A and 2.4). These lava flows were subsequently incised mostly below the former, local, channel base at the time of eruption. These lavas represent a key temporal and geometrical benchmark (Fig. 2.4B; Table S2.3) and offer the opportunity to estimate the longer-term denudation rates (Nereson et al., 2013; Ferrier et al., 2013). To do that, we mapped the lava flows deposited between 7 and 4 Ma (Berrahma and Delaloye, 1989; De Beer et al., 2000) (Fig. 2.4B, 2.4C). Subsequently, we reconstructed the paleo-topography by connecting the highest points of the remnant lava flows and we subtracted it from the present-day topography to obtain the eroded volume (Fig. 2.4B and 2.4C). Finally, we divided it by the relative drainage area of the associated catchment. The ratio between volume and area was further divided by the lava flow age to determine basin-wide denudation rates (Supplementary Table S2.3). This approach allows to estimate the long-term averaged denudation rates, assuming a negligible the uncertainties in drainage area, erosion and erodibility variation over time (Ferrier et al., 2013).

2.5. Results

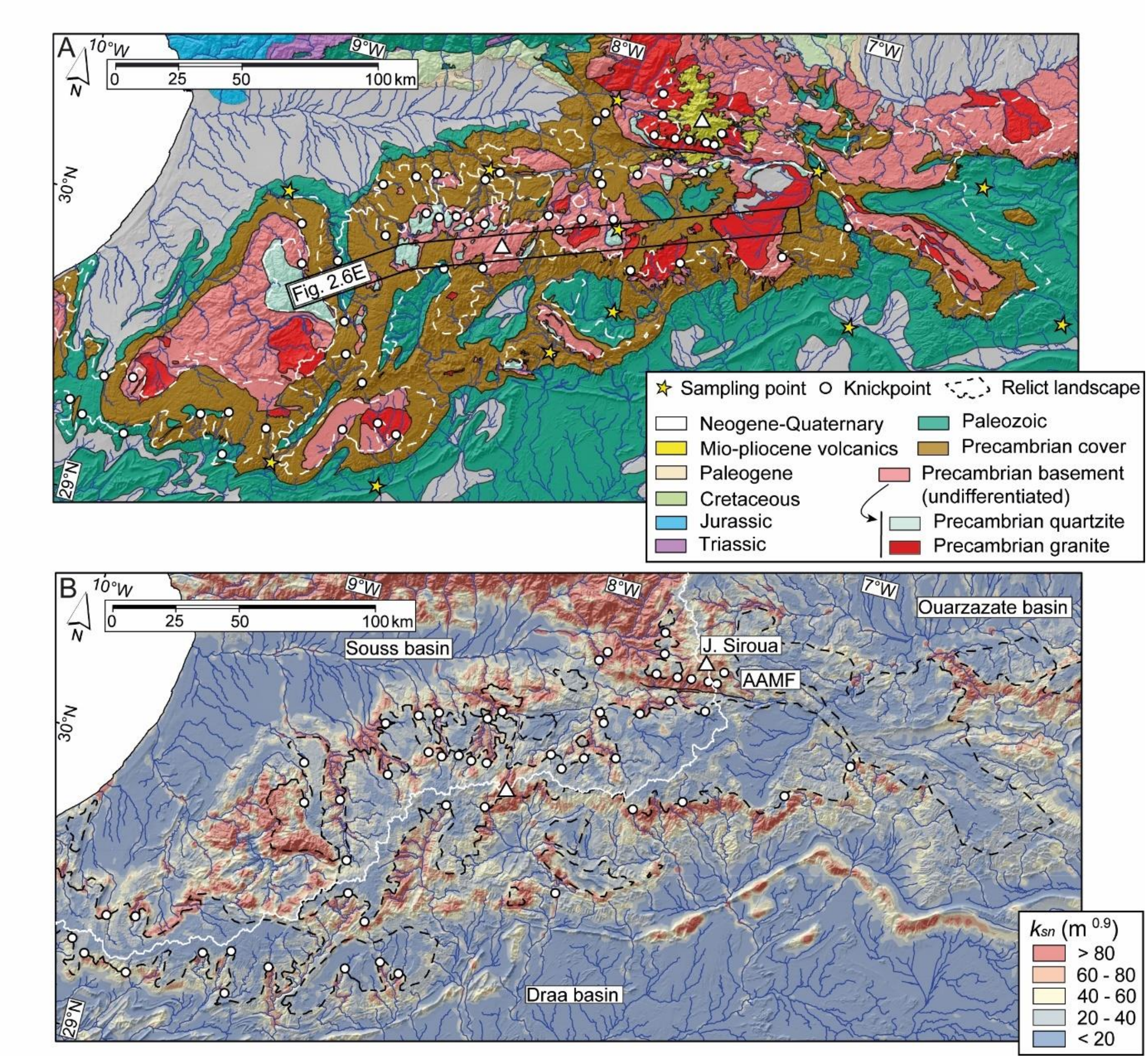

Figure 2.2. A) Geological map of the Anti-Atlas and the Siroua Massif (after Hollard et al., 1985) and B) interpolated map of k_{sn} values. The white line and triangle indicate the main drainage divide and topographic peaks, respectively.

2.5.1. Regional topographic analysis

The Anti-Atlas is characterized by high-standing topography rising to more than 2 km, while the Siroua Massif represents the highest local topographic peak (3.3 km). The lowest k_{sn} and slope values are observed in the Souss and Draa basins and the elevated axial zone of the Anti-Atlas (Figs. 2.2B and S2.1). Conversely, the highest k_{sn} and topographic slope values are in the lower portions of the Anti-Atlas and along the flanks of the Siroua Massif (Figs. 2.2B and S2.1). A regionally widespread, series of non-lithological knickpoints mark a sharp separation from the lowest and highest k_{sn} and slope portions of the Anti-Atlas landscape (dashed line in Figs. 2.2 and S2.1).

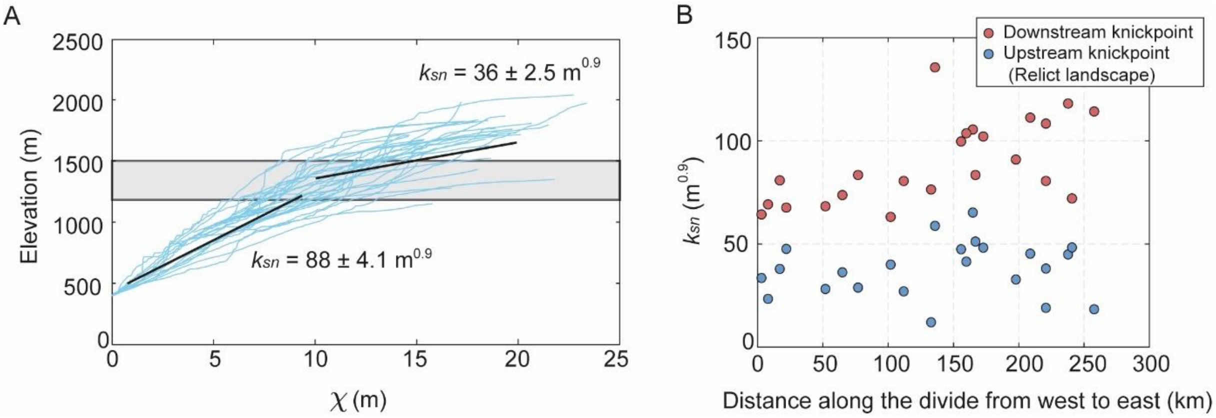

Figure 2.3. A) χ- transformed profiles of the main streams draining the central Anti-Atlas. All rivers are extracted from the bedrock-alluvial transition, which is at about 400 m (in order to consider only the bedrock part of the rivers). The non-lithological knickpoints are located between 1200 and 1500 m (see grey band) and separate segments with different k_{sn} value (see Table S2.2 for details). The numbers in the plot represent the mean k_{sn} and associated standard deviation upstream and downstream the grey band. B) k_{sn} values upstream and downstream of major non-lithological knickpoints from the main river trunks.

The non-lithological knickpoints are positioned on the slope break changes in the χ-transformed stream profiles and cluster in a narrow range of χ (Fig. 2.3A). The high-standing relict landscape has a mean k_{sn} of 36 ± 2.5 $m^{0.9}$ and a θ of 0.12 ± 0.07, whereas the landscape portion downstream of the non-lithological knickpoints has a mean k_{sn} of 88 ± 4.1 $m^{0.9}$ and a θ of 0.47 ± 0.02 (Fig. 2.3B and Table S2.2). Locally, within the relict landscape, an increase in topographic slope, relief and k_{sn} values occurs for quartzites and conglomerates, while a decrease in topographic slope, relief and k_{sn} values is observed in areas dominated by granites (Figs. 2.2, 2.6E and S2.3, S2.4).

.

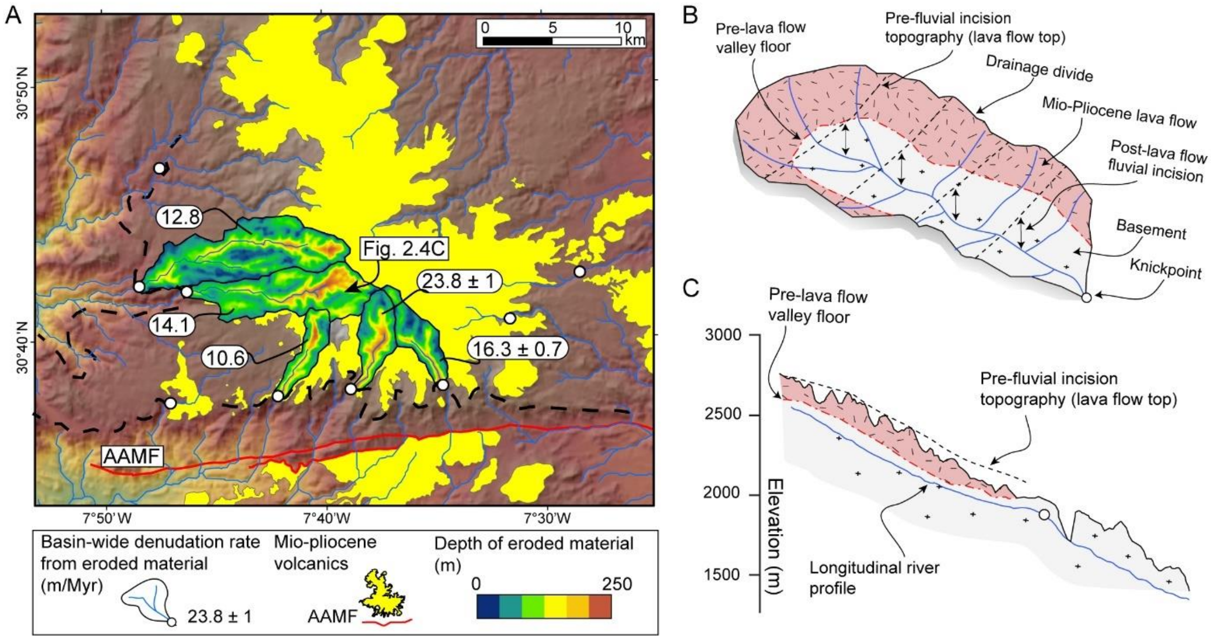

Figure 2.4. A) Digital elevation model of the Siroua Massif with the depth of eroded rock volumes and associated denudation rates (see results in Table S2.3). The dashed black line and the white circles demark the uplifted relict landscape and non-lithological knickpoints, respectively. B) Schematic 3D sketch of the Siroua landscape. The eroded rock volume is calculated from the highest point of the lava flows upstream of non-lithological knickpoint. Based on the age of the lavas, the eroded volume estimate is translated into denudation rate. C) Simplified geological cross section and river profile of a selected catchment.

2.5.2. Denudation rates across time scales

Long-term, basin-wide denudation rates from the relict landscape of the Siroua Massif indicate a topographic lowering between 10 and 20 m/Myr, over the last 7 to 4 Myrs (Fig. 2.5 and Table S2.3). ^{10}Be-derived basin-wide denudation rates range from 5 to 12 m/Myr, with local maximum values of 20 and 40 m/Myr for the Anti-Atlas and the Siroua, respectively (basin 8 and 6, Fig. 2.1). Importantly, these rates are valid for the relict portion of the landscape upstream of the major non-lithological knickpoints and are comparable with the mean erosion rates averaged over a longer time scale obtained through low temperature thermochronology (Lanari et al., 2020; Fig. 2.5). Particularly, estimates of erosions derived from fission track ages on apatite range between 50 and 130 m/Myr and yielding an average value of 70 m/Myr; estimates form AHe range between 10 and 50 m/Myr, with an average of 30 m/Myr.

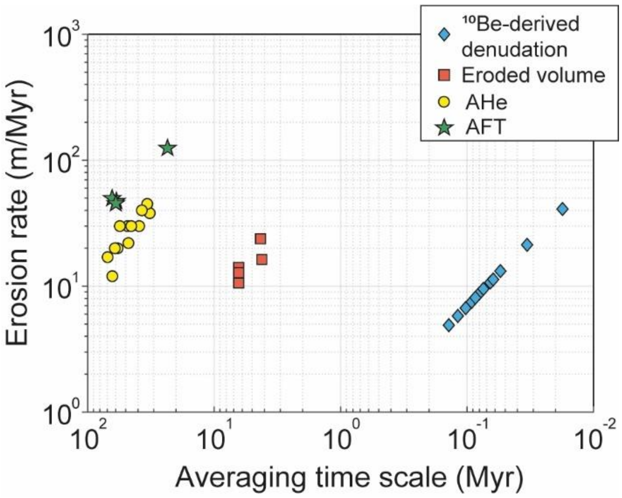

Figure 2.5. Erosion rates for the Anti-Atlas and the Siroua Massif for different time scales. Long-term erosion rates (AFT and AHe) are from thermochronologic ages (Lanari et al., 2020a) and eroded volumes of Mio-Pliocene volcanics exposed in the Siroua Massif (this study; see Table S2.3 for details). Short-term denudation rates are from ^{10}Be data (this study; see Table S2.1 for details).

2.5.3. Basin-scale topographic analysis

Basin-wide denudation rates were plotted against the basin-averaged topographic metrics, k_{sn} and averaged annual precipitations for the main quartz-bearing lithologies exposed in the sampled catchments to assess the potential controls on denudation at basin-scale (Fig. 2.6A, 2.6B, 2.6C, 2.6D). Basin-averaged k_{sn} ranges from 20 to 105 m$^{0.9}$ with maximum values in the Siroua (Fig. 2.6A and Table S2.5). Basin-averaged slopes in the sampled basins range from 4 to 14° showing highest value in the Siroua Massif (Fig. 2.6B and Table S2.5). Basin-averaged local relief in the sampled basins range from 200 m to 600 m reaching the maximum value in the Siroua Massif (Fig. 2.6C and Table S2.5). Overall, the basin-averaged k_{sn}, slope and local relief are poorly correlated with basin-wide denudation rates, showing an R2 of 0.64, 0.26 and 0.21, respectively (grey best-fit in Fig. 2.6A, 2.6B, 2.6C).

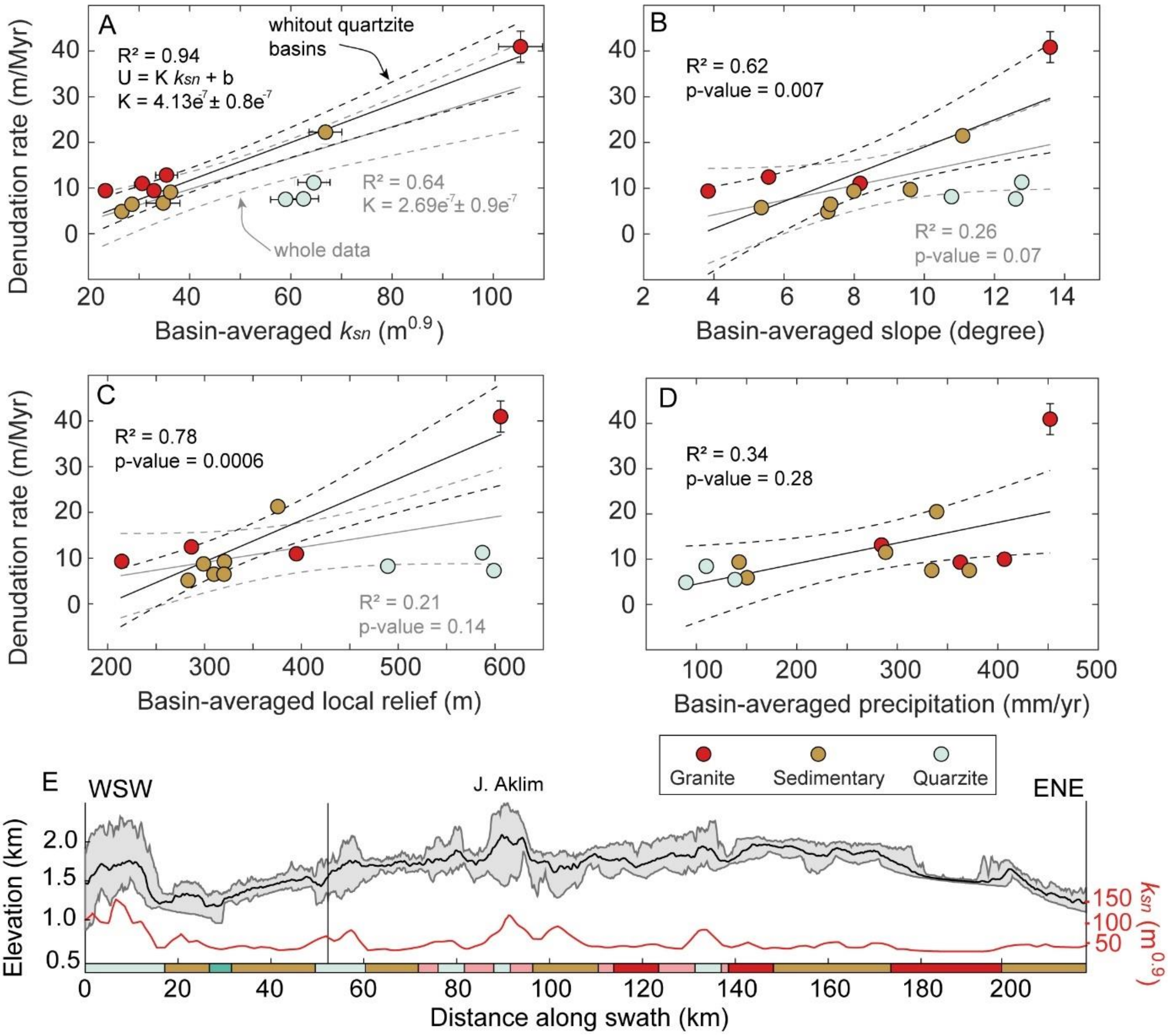

Figure 2.6. A) Basin-wide denudation rate vs basin-averaged A) k_{sn}, B) slope, C) local relief (2.5 km radius), and D) precipitation rate for different rock types exposed in the sampled basins. The solid line represents the forced linear best-fit, while the dashed black line delimits the bootstrapped 95% confidence interval considering only basins composed of granite and sedimentary rocks. The grey line denotes the best-fit considering all sampled basins, while the dashed grey line is the associated bootstrapped 95% confidence interval. E) Topographic swath profile along the main divide of Anti-Atlas (see Figure 2.2A for details).

A strongest correlation between basin-wide denudation rates and topographic metrics is found when we exclude the quartzite bearing basins, and we consider only the granite and sedimentary dominated basins. In this case, we observe R^2 values of 0.94, 0.62 and 0.78 for basin-averaged k_{sn}, slope and local relief, respectively (black best-fit in Fig. 2.6A, 2.6B, 2.6C). The highest k_{sn}, topographic slope and local relief values are about 60-65 $m^{0.9}$, 10-13° and 450-600 m, respectively, and are associated with quartzite bearing basins. In contrast, the lowest k_{sn}, slope and local relief values are about 20-40 $m^{0.9}$, 4-8° and 200-400 m, respectively, and are found in granite bearing basins, except for basin 6 in the Siroua Massif

(Fig. 2.6A, 2.6B, 2.6C and S2.4, Table S2.5). Similarly, to what observe for the catchments dominated by Paleozoic sedimentary rock. Overall, the basin-wide denudation rates are constant between the sampled catchments of the Anti-Atlas relict landscape. Whereas it should be noted that the highest denudation rate corresponds to the incised portion of Siroua Massif catchment (basin 6), where a large area of the quartz-contributing lithology (mostly granite) is exposed downstream of non-lithological knickpoint (Figs. 1 and 2.2A). Finally, basin-wide denudation and averaged annual precipitation rates do not show a significant correlation across the sampled catchments (Fig. 2.6D).

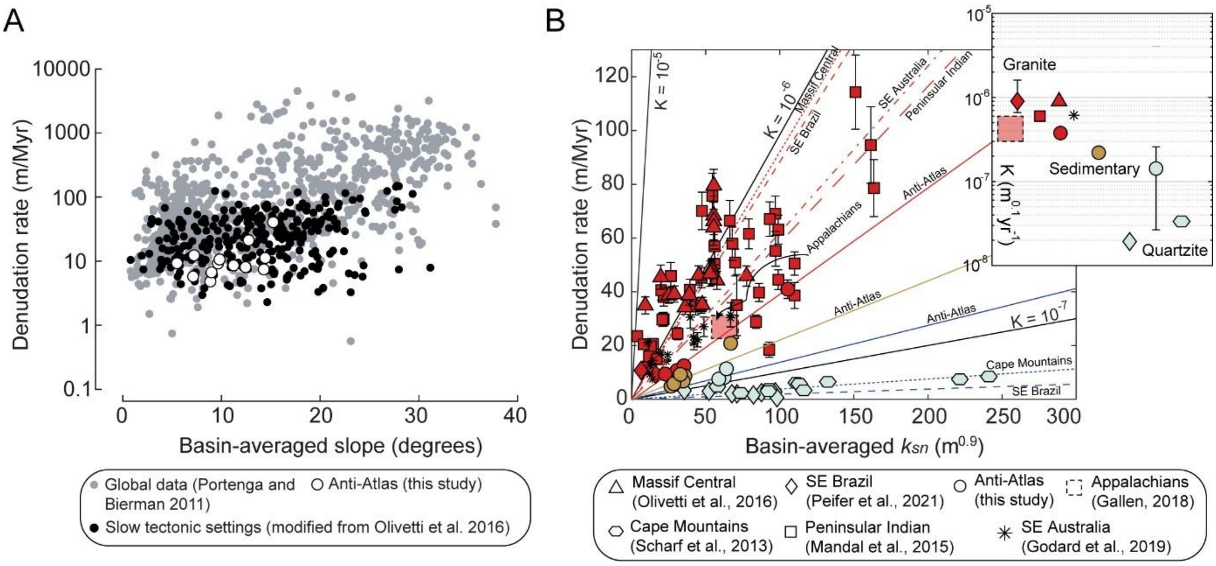

Figure 2.7. A) Global compilation of slope versus basin-wide denudation rate. B) Comparison of basin-averaged k_{sn} value versus denudation rate for different rock-types (red: granitic rocks, brown: sedimentary rocks, light blue: quartzite) in tectonically inactive settings. The solid lines show the forced linear best-fit (see Table S2.6 for details).

2.6. Discussion

2.6.1. Erosional steady state landscape

The regional spatial variation of k_{sn} and slope delimit a low-topographic relief, high-standing region upstream of the non-lithological knickpoints from a downstream steep portion of the landscape (Figs. 2.2B, 2.3 and S2.1). This configuration reflects a phase of topographic rejuvenation that has occurred during the late Cenozoic (Missenard et al., 2008; Frizon de Lamotte et al., 2009; Guimera et al., 2011; Miller and Becker, 2014). The causes of the recent surface uplift are still poorly constrained, however the proposed mechanisms are mainly related to mantle dynamics, which seems compatible with non-isostatic topography (Frizon de Lamotte et al., 2009; Miller and Becker, 2014). Overall, the main quartz contributing lithologies within the sampled catchments are in the relict landscape where basin-wide denudation rates range from 5 to 20 m/Myr. Whereas, the sharp increase in denudation rates recorded in the Siroua Massif (40 m/Myr) is due to the presence of quartz-rich lithologies (granitic rocks) located in the steep slopes downstream of the non-lithological knickpoints (Figs. 2.1 and 2.2A). There, the slopes are steeper in response to a local increase in uplift rates, associated with Miocene magmatism (i.e., magmatic addition) and/or to faulting along a main tectonic lineament (AAMF; Missenard et al., 2008; Giumera et al., 2011).

Importantly, in situ-produced cosmogenic 10Be-derived denudation rates (timescales of 10^4 -10^5 yr) agree with long-term estimates from the eroded lava flows (timescales of few 10^6 yr) and thermochronometric data (timescales of 107 yr; Lanari et al., 2020 and references therein) (Fig. 2.5). The persistence of spatial uniform erosion rates of the relict landscape since at least the late Cretaceous, suggests a long-term balance between slow rock uplift, that characterized the pre-rejuvenation condition, and hillslope lowering. This is further corroborated by the occurrence of uniform k_{sn} values (except for areas dominated by quartzite, see next section) and equilibrated river profiles upstream of the non-lithological knickpoints (Figs. 2.2B, 2.3 and S2.5). These considerations suggest that the uplifted relict landscape has attained an erosional steady state (Hack, 1957; Willet and Brandon, 2002; Scharf et al., 2013; Mandal et al., 2015), as typically observed in slow decay of post-orogenic topography and tectonically inactive ranges. Despite, this slow and protracted process of topographic lowering and the low denudation rates, rivers are in bare bedrock channels and keeps the detachment-limited erosion condition (Whipple and Tucker, 2002; Baldwin et al., 2003), as observed in other inactive settings (Scharf et al., 2013; Mandal et al., 2015; Piefer et al., 2021), where denudation rates and exposed lithologies are comparable (Fig. 2.7B).

Finally, within a trend of rather uniform erosion rates, we observe a smooth decrease in the mean value over contrasting time scales (from a mean of 70 and 30 to 12 m/Myr, for AFT, AHe and 10Be respectively; Fig. 2.5). This overall decrease may be related to the recent Sahara desertification from the late Miocene - Quaternary (Zhang et al., 2014).

2.6.2. Lithological control on erosional dynamics

The decline of tectonic activity and consequently of rock uplift rates is thought to generate topographic relief mostly controlled by lithological and climatic variations (Jansen et al., 2010; Scharf et al., 2013; Gallen et al., 2018). The effect of modern climate does not affect the erosional dynamics of the Anti-Atlas because the mean annual precipitation rates among different catchments show a poor correlation with the basin-wide denudation rates (Fig. 2.6D). Conversely, the topographic metrics correlate with the basin-wide denudation rates especially when the drainage basins are classified according to the dominant quartz-bearing lithology exposed on the surface (Figs. 2.6A, 2.6B, 2.6C and 2.7B). This indicates that local variations in k_{sn} values reflect the non-uniform rock strength distribution over the study area, and thus different values of bedrock erodibility (K; Jansen et al., 2010; Peifer et al., 2021). For a given range of denudation rates, basins dominated by quartzite have higher k_{sn}, slope and local relief values than the other lithologies (Fig. 2.6A, 2.6B, 2.6C). The linear correlation between k_{sn} values and our denudation rates suggests that the n parameter of the stream power law (equation (1)), can be approximated to 1 (Fig. 2.6A), despite the low variability of the dataset. Although this appears to be inconsistent with the expected power - law function, it should be noted that $n > 1$ has been observed in regions with high denudation rates and steep topography approaching an threshold of erosion (Ouimet et al., 2009; DiBiase and Whipple, 2011; Kirby and Whipple, 2012; Adams et al., 2020). Thus, for low ranges of denudation rates and channel steepness the linear and the power law relationships are practically indistinguishable (Ouimet et al., 2009; Scharf et al., 2013; Mandal et al., 2015; Olivetti et al., 2016). This is the case for tectonically inactive settings as documented by our data (see area of figure 7A with slopes lower than ca. 20° and 7B where channel steepness is generally lower than 200 $m^{0.9}$). In these settings, we further demonstrated that linear fit ($n = 1$) better explain the variability of denudation and channel steepness respect to power-law fit, using $n = 2$, showing a higher R^2 (Figs. 2.7B and S2.8, Tables S2.6 and S2.7). These observations suggest that the approximation of n = 1 could allow one to effectively constrain bedrock erodibilities for our setting.

Similarly to channel steepness, the correlation between denudation rates and topographic slope is generally poorly sensitive in stable and relict regions (Figs. 2.7A and S2.6), usually due to the decoupling between hillslope and river incision processes or to the lithological control (Olivetti et al., 2016; Peifer et al., 2021). In the Anti-Atlas, the poor sensitivity of basin-wide denudation rate to the basin-averaged slope for the whole, lithologically undifferentiated dataset (Fig. 2.6B) is due to the drastically difference in erodibility of lithologies within the catchments, representing a further evidence of the critical role of rock strength variability in controlling the topographic evolution.

2.6.3. Quantification of the bedrock erodibility parameter (K)

The approximation of the stream power river incision model to a linear equation offers the possibility to easily quantify the bedrock erodibility parameter (K). Specifically, K values range from 1.4 ± 0.9 x 10^{-7} to 3.8 ± 0.4 x 10^{-7} $m^{0.1}$/ yr for quartzite and granitic dominated basins, respectively (Fig. 2.7B and Table S2.6). This is consistent with estimates from the Appalachians and other slow tectonic regions (SE Brazil, Cape Mountains, Peninsular Indian, Massif Central) (Fig. 2.7B) where similar lithologies occur (Scharf et al., 2013; Mandal et al., 2015; Olivetti et al., 2016; Gallen, 2018; Peifer et al., 2021). Specifically, in granite dominated catchments from different stable regions and with variable climate conditions erodibility values are distributed in a narrow range mainly between 10^{-7} and 10^{-6} $m^{0.1}$/yr (3.8± 0.4 x 10^{-7} $m^{0.1}$/ yr in the Anti-Atlas relict landscape; 5.8 ± 0.1 x 10^{-7} $m^{0.1}$/ yr in the Peninsular Indian, Mandal et al., (2015); 8.8 ± 1.9 x 10^{-7} $m^{0.1}$/ yr in south-eastern Brazil, Peifer et al., (2021); 9.2 ± 0.5 x 10^{-7} $m^{0.1}$/ yr in the Massif Central, Olivetti et al., (2016); ~5 x 10^{-7} $m^{0.1}$/ yr in the Appalachians, Gallen et al., (2018); Fig. 2.7B and Table S2.6). Conversely, in quartzite dominated catchments K values range usually from 10^{-7} to 10^{-8} $m^{0.1}$/ yr (1.4 ± 0.9 x 10^{-7} $m^{0.1}$/ yr in the Anti-Atlas; 0.3 ± 0.04 x 10^{-7} $m^{0.1}$/ yr for the Cape Mountains; 0.2 ± 0.05 x 10^{-7} $m^{0.1}$/ yr in south-eastern Brazil; Fig. 2.7B and Table S2.6). Indeed, the presence of physically robust and chemically inert quartzite in the sampled catchments strongly decreases the catchment-averaged value of K in the study area (Fig. 2.6A).

Overall, the erodibility values from tectonically inactive regions vary between 10^{-8} and 10^{-6} $m^{0.1}$/yr and are generally lower than those estimated in tectonically active orogens, where usually range between 10^{-6} and 10^{-3} $m^{0.1}$/ yr (Stock and Montgomery, 1999; Kirby and Whipple, 2001; see also the discuss in Peifer et al., 2021). There, tectonic deformation leads to the creation of fractures resulting in a general increase in bedrock erodibility (Molnar et al., 2007; Portenga and Bierman, 2011). Matters, however, may be more complex. For example, estimates of the mechanical rock strength erodibility derived from UCS and channel steepness values (Schmidt hammer) in the High Atlas, indicate that granitoid rocks from the basement are more resistant than the Paleozoic sedimentary cover (Zondervan et al., 2020). These results are clearly in contrast with our findings. However, the High Atlas is an active mountain belt with high rates of rock uplift and exhumation (estimates from low-T thermochronology are mostly > 100 m/Myr; Lanari et al., 2020), with granitoids exposed in the axial zone where topographic relief is high (k_{sn} values range from 90 to 200 $m^{0.9}$; Zondervan et al., 2020). Conversely, in the inactive Anti-Atlas, exhumation and denudation rates from the relict topography are two of order of magnitudes lower while the associated granitic rocks have a lower topographic relief (k_{sn} values range from 20 to 40 $m^{0.9}$, Fig. 2.6A). This means that in the Anti-Atlas the exposure time to physical and chemical weathering processes is much higher than in the High Atlas. Consequently, the granitic rocks in the Anti-Atlas are likely more weathered and present higher erodibility values, with respect to the granites exposed in the High Atlas (Kanamaru et al., 2018).

Finally, although the overall topographic lowering and the relative steady erosion rates (section 2.6.1), there is a strong variation of local topographic relief among different lithotypes (Fig. 2.6E). Quartzite dominated catchments have higher k_{sn} values and topographic relief, while bedrock erodibility (K) is more than one order of magnitude lower than in granitic bearing catchments (Fig. 2.7B). This applies also at global scale (Fig. 2.7B). Overall, these results suggest that the process of passive exhumation of lithologies with variable rock strength plays a dominant role in producing topographic relief over time scales longer than the integration timescale of ^{10}Be cosmogenic nuclides despite the lack of tectonic activity. Therefore, even if the relict landscape is in erosional steady state, it has not achieved the topographic steady state because the continuous exhumation of rocks with different erodibility critically influences the process of surface lowering leading to the development of localized topographic relief (Piefer et al., 2020 and references therein).

2.6.4. Possible impact of climate on K values in tectonically inactive settings

The role of climate can be evaluate by quantifying the annual precipitation rates, runoff and discharge variability (DiBiase and Whipple, 2011). In dry climate, such as Anti-Atlas, the discharge variability can represent a key issue in controlling the transport dynamics at short timescale. Despite that, as observe for the precipitation rates, it should not vary critically enough to influence the local denudation and channel steepness between the selected catchments. We can explore the climatic sensitivity on estimates of bedrock erodibility, expanding the analysis to other settings. Thus, we grouped data selecting catchments from inactive regions characterized by similar rock composition that span different climatic zones. For the granitic-dominated catchments, the Peninsular India is characterized by a wet, tropical climate with mean annual precipitation rates as high as 5000 mm/yr. It falls approximately in the same range of denudation and channel steepness of the Massif Central and SE Brazil, where maximum annual precipitation is 1700 mm/yr, or the Anti-Atlas where precipitation is even lower (> 600 mm/yr; Supplementary Fig. S2.7). The same erodibility for granitic-rock is estimated from the South Eastern Australia Escarpment and the Appalachians, which are temperate settings, where precipitation rates range from 1000 mm to up to 2000 mm (Fig. 2.7B). Similarly, is observed for erodibility of quartzite-dominated catchments from SE Brazil, Cape Mountains and Anti-Atlas (Fig. 2.7B). This suggests that in these settings climatic conditions do not have a major impact on erodibility (Fig. 2.7B) as also suggested by the week correlation between denudation and averaged annual precipitation rates for all these areas (Scharf et al., 2013; Mandal et al., 2015; Godard et al., 2019; Peifer et al., 2021). These observations seem to indicate that in tectonically inactive settings, climate might not play a primary role on the long-term evolution of topographic relief, channel steepness and on the denudation rates at the integration timescale of ^{10}Be cosmogenic nuclides.

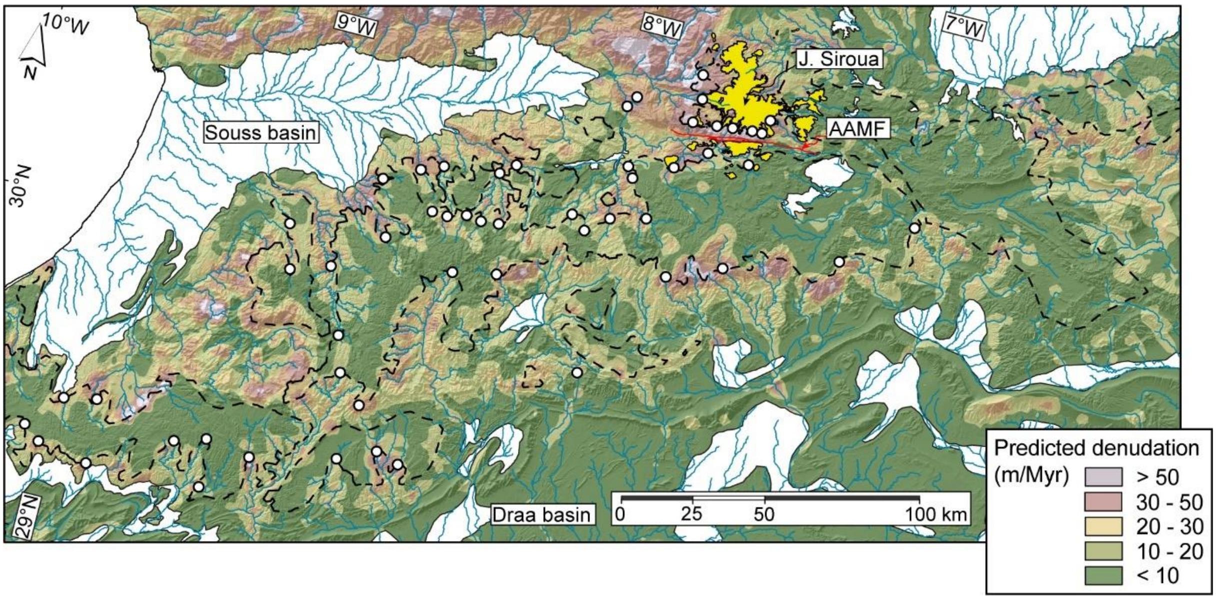

Figure 2.8. Predicted denudation rates based on the distribution of normalized channel steepness (k_{sn}), using different erodibility values for each lithology and n =1.

2.6.5. Predicted denudation of adjusted topography

^{10}Be-derived denudation rates were accurately determined for the relict portions of the Anti-Atlas landscape. There, the spatial variation of channel steepness is well correlated to the difference in erodibility of different rocks, which span a wide variety of lithologies (granitic, sedimentary and quartzite rocks). Conversely, downstream of non-lithological knickpoints, the outcropping lithologies are uniform, composed of mainly carbonates and sandstones (Fig. 2.2A). Therefore, the erosional dynamics and denudation rates from the adjusted topography are not well constrained and no ^{10}Be-derived denudation rates were estimated due to the lack of bearing-quartz lithologies. However, the modern topography, channel steepness and estimates of erodibility parameters allow to predict the denudation of landscape portions where no data are available (Adams et al., 2020). Using the stream power incision model with $n = 1$ and the different bedrock erodibility parameters, we can predict the denudation on the adjusted topography (downstream of non-lithological knickpoints), with values between 40-50 m/Myr (Fig. 2.8). These magnitudes of denudation can be directly interpreted as reflecting modern rock uplift, testified the Cenozoic rejuvenation of Anti-Atlas, which have been mainly based only on geophysical evidence until now (Missenard et al., 2008; Frizon de Lamotte et al., 2009; Miller and Becker, 2014).

The predicted denudation rates in the Anti-Atlas Mountains should be significant also at longer timescale than ^{10}Be cosmogenic nuclides, given that the range has not been subjected to any tectonic drift across climatic zones during the Cenozoic (Burkhard et al., 2006). Furthermore, these rejuvenated portions of the landscape are characterized by rather uniform lithology, overcoming the common problematic of the susceptibility of channel steepness to spatial variation of lithologies and/or precipitations (Scharf et al., 2013; Mandal et al., 2015; Adams et al., 2020). Interestingly, our estimates from the adjusted landscape are roughly equal to ^{10}Be-denudation rates estimates from quasi-equilibrium landscape of Appalachians by Miller et al. (2013), which represent the American counterpart of the Variscan orogens, characterized by the similar lithologies. Here, not only the adjusted topography but also the upstream relict topography is slowly eroding at the same rates of Anti-Atlas relict catchments. The model allows to quantify the predicted denudation, in term of rock uplift, along the fluvial landscapes, showing how landscape can record the time and space change of tectonic a long timescale.

2.7. Conclusions

Our analysis indicates that Anti-Atlas underwent a late-Cenozoic rejuvenation as documented by the transient state of the stream networks. The persistence of an uplifted, relict landscape upstream of non-lithological knickpoints documents the pre-uplift stage of the mountain range. This uplifted topography is characterized by low value of channel steepness and denudation as typically observed in tectonically inactive regions. The close agreement between short- and long-term erosion rates for the relict landscape supports the idea of erosional steady state conditions for the Anti-Atlas relict landscape, where topography is slowly decaying (section 2.6.1). Lithology plays a major role in lowering and creating topographic relief as testified by the relationships between basin-wide denudation rates and topographic metrics, especially when considering different rock-types (section 2.6.2). In particular, the linear correlation between k_{sn} values and the denudation rates of catchments classified according to the dominant exposed lithology is consistent in regions characterized by slow tectonic regime. This allows estimating a range of bedrock erodibility for different lithologies. Despite the uniform denudation between rock-types, a key process could also be played by the degree of chemical and physical weathering, function of rock exposure time, in turn depending on the regional denudation/ exhumation rates, as the case of granitic rocks of the Atlas Mountains (section 5.3). Conversely, climate and mean annual precipitation rates do not appear to have a major impact the estimates of erodibility (section 2.6.4). Our estimates of erodibility for different lithologies allow to predict the denudation in the downstream portions of the landscape. There, strongly increase of denudation rates, testified the recent topographic rejuvenation (section 2.6.5). Although, the complex interactions between surface dynamics and relief production processes are difficult to determine, the Anti-Atlas and other quiescent tectonic regions offer unique conditions to isolate and quantify the impact of lithology on shaping the landscape and creating topographic relief.

2.8. Acknowledgments

This study is part of the PhD thesis of RC at the University of Roma Tre (PhD Cycle XXXIV). It was supported by the PhD School of Roma Tre and grant “Vinci 2020” awarded to RC (Number : C2- 1403). PB was supported by the MIUR (Ministry of Education University and Research), Excellence Department Initiative, Art. 1, com. 314-337, Low 232/2016. The ASTER (CEREGE, Aix-en-Provence) AMS national facility, is supported by the INSU/CNRS, the ANR (Projets thématiques d’excellence programme for the Equipements d’Excellence) and the IRD. We thank G. Aumaître and K. Keddadouche for their support in

AMS measurements, R. Lanari, S. Racano, N. Youbi and R. Braucher for the stimulating discussions.

2.9. References

Adams, B. A., Whipple, K. X., Forte, A. M., Heimsath, A. M., Hodges, K. V. 2020. Climate controls on erosion in tectonically active landscapes. Sci. adv. *6*(42), eaaz3166. https://www.science.org/doi/10.1126/sciadv.aaz3166.

Balco, G., Stone, J. O., Lifton, N. A., Dunai, T. J., 2008. A complete and easily accessible means of calculating surface exposure ages or erosion rates from ^{10}Be and ^{26}Al measurements. Quat. Geochronol. 3(3), 174-195. https://doi.org/10.1016/j.quageo.2007.12.001.

Baldwin, J. A., Whipple, K. X., Tucker, G. E., 2003. Implications of the shear stress river incision model for the timescale of postorogenic decay of topography. J. Geophys. Res., Solid Earth. 108(B3). https://doi.org/10.1029/2001JB000550.

Berrahma, M., Delaloye, M., 1989. Données géochronologiques nouvelles sur le massif volcanique du Siroua (Anti-Atlas, Maroc). J. Afr. Earth. Sci. 9(3-4), 651-656. https://doi.org/10.1016/0899-5362(89)90049-3.

Braucher, R., Merchel, S., Borgomano, J., Bourlès, D. L., 2011. Production of cosmogenic radionuclides at great depth: A multi element approach. Earth Planet. Sci. Lett. 309(1-2), 1-9. https://doi.org/10.1016/j.epsl.2011.06.036.

Braucher, R., Guillou, V., Bourlès, D. L., Arnold, M., Aumaître, G., Keddadouche, K., Nottoli, E., 2015. Preparation of ASTER in-house ^{10}Be/^{9}Be standard solutions. Nucl. Instrum. Methods Phys. Res., Sect. Beam Interactions with Materials and Atoms. 361, 335-340. https://doi.org/10.1016/j.nimb.2015.06.012.

Burkhard, M., Caritg, S., Helg, U., Robert-Charrue, C., Soulaimani, A., 2006. Tectonics of the Anti-Atlas of Morocco. C.R. Geosci. 338(1-2), 11-24. https://doi.org/10.1016/j.crte.2005.11.012.

Carretier, S., Regard, V., Vassallo, R., Martinod, J., Christophoul, F., Gayer, E., Audin L., Lagane, C., 2015. A note on ^{10}Be-derived mean erosion rates in catchments with heterogeneous lithology: Examples from the western Central Andes. Earth Surf. Processes Landforms. 40(13), 1719-1729. https://doi.org/10.1002/esp.3748.

Choubert, G., 1952. Histoire géologique du domaine de l'Anti-Atlas: Notes Mém. Serv. Géol. Maroc. 100, 77-194.

De Beer, C. H., Chevallier, L. P., De Kock, G. S., Gresse, P. G., Thomas, R. J., 2000. Mémoire explicatif de la carte géologique du Maroc au 1/50 000, Feuille Sirwa. Notes Mem. Serv. Geol. Maroc. 395, 86.

DiBiase, R.A., Whipple, K.X., 2011. The influence of erosion thresholds and runoff variability on the relationships among topography, climate, and erosion rate. J.Geophys. Res. 116 (F4). http://dx.doi.org/10.1029/2011JF002095.

Dunne, J., Elmore, D., Muzikar, P., 1999. Scaling factors for the rates of production of cosmogenic nuclides for geometric shielding and attenuation at depth on sloped surfaces. Geomorphology. 27(1-2), 3-11. https://doi.org/10.1016/S0169-555X(98)00086-5.

Ferrier, K. L., Perron, J. T., Mukhopadhyay, S., Rosener, M., Stock, J. D., Huppert, K. L., Slosberg, M., 2013. Covariation of climate and long-term erosion rates across a steep rainfall gradient on the Hawaiian island of Kaua 'i. Bulletin, 125(7-8), 1146-1163. https://doi.org/10.1130/B30726.1.

Frizon de Lamotte, D., Leturmy, P., Missenard, Y., Khomsi, S., Ruiz, G., Saddiqi, O., Guillocheau F., Michard A., 2009. Mesozoic and Cenozoic vertical movements in the Atlas system (Algeria, Morocco, Tunisia). An overview: Tectonophysics. 475, 9–28. https://doi.org/10.1016/j.tecto.2008.10.024.

Forte, A.M., Whipple, K.X., 2019. Short communication: the Topographic Analysis Kit (TAK) for TopoToolbox. Earth Surf. Dyn.7, 87–95. https://doi.org/10.5194/esurf-7-87-2019.

Gallen, S. F., Wegmann, K. W., Bohnenstiehl, D. R., 2013. Miocene rejuvenation of topographic relief in the southern Appalachians. GSA Today. 23(2), 4-10. https://doi.org/10.1130/GSATG163A.1.

Gallen, S. F., 2018. Lithologic controls on landscape dynamics and aquatic species evolution in post-orogenic mountains. Earth and Planet. Sci. Lett. 493, 150-160. https://doi.org/10.1016/j.epsl.2018.04.029.

Godard, V., Dosseto, A., Fleury, J., Bellier, O., Siame, L., ASTER Team., 2019. Transient landscape dynamics across the Southeastern Australian Escarpment. Earth and Planet. Sci. Lett. 506, 397-406. https://doi.org/10.1016/j.epsl.2018.11.017

Granger, D. E., Kirchner, J. W., & Finkel, R., 1996. Spatially averaged long-term erosion rates measured from in situ-produced cosmogenic nuclides in alluvial sediment. J. Geol. 104(3), 249-257. https://doi.org/10.1086/629823

Guimerà, J., Arboleya, M. L., Teixell, A., 2011. Structural control on present-day topography of a basement massif: the Central and Eastern Anti-Atlas (Morocco). Geologica Acta. 9(1), 55-65. https://doi.org/10.1344/105.00 0001643.

Hack, J. T., 1957. Studies of longitudinal stream profiles in Virginia and Maryland (Vol. 294). US Government Printing Office.

Hollard, H., Choubert, G., Bronner, G., Marchand, J., Sougy, J., 1985. Carte géologique du Maroc, scale 1: 1,000,000. Serv. Carte géol. Maroc. 260(2).

Howard, A.D., Kerby, G., 1983. Channel changes in badlands. Geol. Soc. Am. Bull.94, 739–752. http://dx.doi.org/10.1130/0016-7606(1983)94<739:CCIB>2.0.CO;2.

Jansen, J. D., Codilean, A. T., Bishop, P., Hoey, T. B., 2010. Scale dependence of lithological control on topography: Bedrock channel geometry and catchment morphometry in western Scotland. J. Geol. 118(3), 223-246. https://doi.org/10.1086/651273.

Kanamaru, T., Suganuma, Y., Oiwane, H., Miura, H., Miura, M., Okuno, J. I., Hayakawa, H., 2018. The weathering of granitic rocks in a hyper-arid and hypothermal environment: A case study from the Sør-Rondane Mountains, East Antarctica. Geomorphology. 317, 62-74. https://doi.org/10.1016/j.geomorph.2018.05.015.

Kirby, E., Whipple, K. X., 2001. Quantifying differential rock-uplift rates via stream profile analysis. Geology. 29(5), 415-418. https://doi.org/10.1130/0091-7613(2001)029<0415:QDRURV>2.0.CO;2.

Kirby, E., Whipple, K. X., 2012. Expression of active tectonics in erosional landscapes. J. Struct. Geol. 44, 54-75. https://doi.org/10.1016/j.jsg.2012.07.009.

Lal, D., 1991. Cosmic ray labeling of erosion surfaces: in situ nuclide production rates and erosion models. Earth Planet. Sci. Lett.104, 424–439. http://dx.doi.org/10.1016/0012-821X(91)90220-C.

Lanari, R., Fellin, M. V., Faccenna, C., Balestrieri, M. L., Pazzaglia, F. J., Youbi, N., Maden, C., 2020. Exhumation and surface evolution of the western high atlas and surrounding regions as constrained by low-temperature thermochronology. Tectonics. 39(3), e2019TC005562. https://doi.org/10.1029/2019TC005562

Mandal, S. K., Lupker, M., Burg, J. P., Valla, P. G., Haghipour, N., Christl, M., 2015. Spatial variability of ^{10}Be-derived erosion rates across the southern Peninsular Indian escarpment: A key to landscape evolution across passive margins. Earth and Planet. Sci. Lett. 425, 154-167. https://doi.org/10.1016/j.epsl.2015.05.050.

.

Merchel, S., Arnold, M., Aumaître, G., Benedetti, L., Bourlès, D. L., Braucher, R., Alfimov V., Freeman S.P.H.T., Steier P., Wallner, A., 2008. Towards more precise ^{10}Be and ^{36}Cl data from measurements at the 10− 14 level: Influence of sample preparation. Nucl. Instrum. Methods Phys. Res., Sect. Beam Interactions with Materials and Atoms. 266(22), 4921-4926. https://doi.org/10.1016/j.nimb.2008.07.031.

Miller, S. R., Sak, P. B., Kirby, E., & Bierman, P. R., 2013. Neogene rejuvenation of central Appalachian topography: Evidence for differential rock uplift from stream profiles and erosion rates. Earth and Planet. Sci. Lett. 369, 1-12. https://doi.org/10.1016/j.epsl.2013.04.007

Miller, M. S., Becker, T. W., 2014. Reactivated lithospheric-scale discontinuities localize dynamic uplift of the Moroccan Atlas Mountains. Geology. 42(1), 35-38. https://doi.org/10.1130/G34959.1.

Missenard, Y., Saddiqi, O., Barbarand, J., Leturmy, P., Ruiz, G., El Haimer, F. Z., Frizon de Lamotte, D., 2008. Cenozoic denudation in the Marrakech High Atlas, Morocco: insight from apatite fission-track thermochronology. Terra Nova. 20(3), 221-228. https://doi.org/10.1111/j.1365-3121.2008.00810.x.

Molnar, P., Anderson, R.S., Anderson, S., 2007. Tectonics, fracturing of rock, and erosion. J. Geophys. Res. v. 112, F03014. https://doi.org/10.1029/2005JF000433.

Nereson, A., Stroud, J., Karlstrom, K., Heizler, M., McIntosh, W., 2013. Dynamic topography of the western Great Plains: Geomorphic and ^{40}Ar/^{39}Ar evidence for mantle-driven uplift associated with the Jemez lineament of NE New Mexico and SE Colorado. Geosphere. 9(3), 521-545. https://doi.org/10.1130/GES00837.1.

Olivetti, V., Godard, V., Bellier, O., ASTER team., 2016. Cenozoic rejuvenation events of Massif Central topography (France): Insights from cosmogenic denudation rates and river profiles. Earth and Planet. Sci. Lett. 444, 179-191. https://doi.org/10.1016/j.epsl.2016.03.049.

Ouimet, W.B., Whipple, K.X., Granger, D.E., 2009. Beyond threshold hillslopes: chan-nel adjustment to base-level fall in tectonically active mountain ranges. Geology. 37, 579–582. http://dx.doi.org/10.1130/G30013A.1.

Peifer, D., Persano, C., Hurst, M. D., Bishop, P., Fabel, D., 2021. Growing topography due to contrasting rock types in a tectonically dead landscape. Earth Surf. Dyn. 9(2), 167-181. https://doi.org/10.5194/esurf-9-167-2021.

Perron, J.T., Royden, L., 2013. An integral approach to bedrock river profile analysis. Earth Surf. Process. Landf. 38, 570–576. https://doi.org/10.1002/esp.3302.

Portenga, E. W., Bierman, P. R., 2011. Understanding Earth's eroding surface with ^{10}Be. GSA today. 21(8), 4-10. http://dx.doi.org/10.1130/G111A.1.

Safran, E. B., Bierman, P. R., Aalto, R., Dunne, T., Whipple, K. X., Caffee, M., 2005. Erosion rates driven by channel network incision in the Bolivian Andes. Earth Surf. Processes Landforms. 30(8), 1007-1024. https://doi.org/10.1002/esp.1259.

Scharf, T. E., Codilean, A. T., De Wit, M., Jansen, J. D., Kubik, P. W., 2013. Strong rocks sustain ancient postorogenic topography in southern Africa. Geology. 41(3), 331-334. https://doi.org/10.1130/G33806.1.

Schwanghart, W., Scherler, D., 2014. Short communication: TopoToolbox 2 – MATLAB-based software for topographic analysis and modeling in Earth surface sciences. Earth Surf. Dyn.2, 1–7. https://doi.org/10.5194/esurf-2-1-2014.

Sébrier, M., Siame, L., Zouine, E. M., Winter, T., Missenard, Y., Leturmy, P., 2006. Active tectonics in the moroccan high atlas. C.R. Geosci. 338(1-2), 65-79. https://doi.org/10.1016/j.crte.2005.12.001.

Soulaimani, A., Michard, A., Ouanaimi, H., Baidder, L., Raddi, Y., Saddiqi, O., Rjimati, E. C., 2014. Late Ediacaran–Cambrian structures and their reactivation during the Variscan and Alpine cycles in the Anti-Atlas (Morocco). J. Afr. Earth. Sci. 98, 94-112. https://doi.org/10.1016/j.jafrearsci.2014.04.025.

Stock, J. D., Montgomery, D. R., 1999. Geologic constraints on bedrock river incision using the stream power law. J. Geophys. Res., Solid Earth. 104(B3), 4983-4993. https://doi.org/10.1029/98JB02139.

Stone, J. O., 2000. Air pressure and cosmogenic isotope production. J. Geophys. Res., Solid Earth. 105(B10), 23753-23759. https://doi.org/10.1029/2000JB900181.

Whipple, K.X., Tucker, G.E., 1999. Dynamics of the stream-power river incision model: implications for height limits of mountain ranges, landscape response timescales, and research needs. J. Geophys. Res., Solid Earth. 104, 17661–17674. https://doi.org/10.1029/1999JB900120.

https://doi.org/10.1029/2000JB000044.

Willett, S. D., & Brandon, M. T., 2002. On steady states in mountain belts. Geology. 30(2), 175-178. https://doi.org/10.1130/0091-7613(2002)030<0175:OSSIMB>2.0.CO;2.

Zhang, Z., Ramstein, G., Schuster, M., Li, C., Contoux, C., Yan, Q., 2014. Aridification of the Sahara desert caused by Tethys Sea shrinkage during the Late Miocene. Nature. 513(7518), 401-404. https://doi.org/10.1038/nature13705.

Zondervan, J. R., Stokes, M., Boulton, S. J., Telfer, M. W., Mather, A. E., 2020. Rock strength and structural controls on fluvial erodibility: Implications for drainage divide mobility in a collisional mountain belt. Earth and Planet. Sci. Lett. 538, 116221. https://doi.org/10.1016/j.epsl.2020.116221.

Chapter 3. Large wavelength surface uplift in the Anti-Atlas and the Siroua Massif (Morocco): Insights into topographic rejuvenation of a tectonically inactive mountan belt

Authors

Romano Clementucci[1,2*], Paolo Ballato[1], Lionel L. Siame[2], Matthew Fox[3], Riccardo Lanari[1,4], Andrea Sembroni[1], Claudio Faccenna[1,5], Ahmed Yaaqoub[6], Abderrahim Essaifi[6]

Affiliations:

[1] Dipartimento di Scienze, Università Roma Tre, Largo San Leonardo Murialdo 1, 00146 Rome, Italy.

[2] Aix-Marseille Univ., CNRS, IRD, INRAE, Collège de France, CEREGE, Aix-en Provence, France.

[3] Department of Earth Sciences, University College London, Gower Street, London, WC1E 6BT, United Kingdom.

[4] Dipertimento di scienze, Università di Firenze, Italia

[5] GFZ-German Research Centre for Geosciences, Potsdam, Germany.

[6] Département de Géologie, FSSM, B.P. 2390, Universite´ Cadi Ayyad, Marrakech, Morocco.

*Corrisponding author : romano.clementucci@uniroma3.it

Keywords

Atlas-Meseta system, transient topography, knickpoints, landscape evolution, quantitative geomorphology, topographic swell

3.1. Abstract

The Atlas-Meseta system of Morocco experienced a late Cenozoic topographic rejuvenation most likely related to deep dynamic processes. This recent, large-scale surface-uplift is documented by a few geological evidence such as uplifted, late Miocene, shallow-water marine deposits exposed in the Middle Atlas Mountains. Conversely, the Anti-Atlas Mountains do not present any stratigraphic records that may allow documenting this uplift history. The presence of a high-standing, erosional surface and the transient state of river networks, however, can be used to reconstruct its recent uplift history and to obtain new insights into the mechanisms that drove such an uplift. In this study, we combined geomorphic and stream profiles analyses, celerity of knickpoints and linear inverse landscape modelling with available geological evidence, to decipher the spatial and temporal variations of surface uplift in the Anti-Atlas and the Siroua Massif. Our results highlight the presence of a transient landscape and associated river network in a state of adjustment, and document a surface uplift of ~ 1100 m in the central Anti-Atlas decreasing westward to ~ 500 m. This uplift started most likely in the middle-late Miocene (9.9 ± 4.1 Ma) and was associated with magmatism in the Siroua Massif. There, the erosional surface is ~350 m higher than in the Anti-Atlas, most likely in response to the activity of the Anti-Atlas Major Fault and possibly for the injection of magma in the crust, recording a maximum uplift of ~ 1150 m. Maximum uplift rate estimates for the central Anti-Atlas, of ~200 m/Myr, fall within the same range of the rates obtained from the uplifted shallow marine deposits in the Middle Atlas sector, suggesting a similar mechanism of uplift. Overall, our approach allows to quantitatively constrain the transient state of the landscape and the contribution of regional, large wavelength surface uplift on mountain building processes. In particular, we examine all possible uplift causes and we conclude that the observed topographic swell was most likely generated by asthenospheric upwelling.

3.2. Introduction

Interplay between exogenic and endogenic processes controls the growth and decay of topography over diverse temporal and spatial scales. Topographic development is generated by different mechanisms, such as crustal shortening and thickening, magmatic addition, flexural rebound, and asthenospheric flow, where each process is associated with a typical wavelength (10^{-1} to 10^{3} km) and amplitude (10 to 10^{3} m; *e.g.*, England and Molnar, 1990; De Celles et al., 2009; Faccenna and Becker, 2020). Topographic decay results from geomorphic erosion, which is primarily set by climate, topographic gradients, and rock strength (*i.e.*, Jansen et al., 2010; Scharf et al., 2013; Chapter 2). When topographic decay prevails, extensive low-gradient, low-topographic relief landscapes may form (Baldwin et al., 2003; Tucker and van der Beek, 2013). These geomorphic features can be also found at the summit of mountains areas (Miller et al., 2013; West et al., 2013; Calvet et al., 2015), where they have been interpreted to have formed either in situ at high elevation (*e.g.*, Yang et al., 2015; Fox et al., 2020), or to be part of a less elevated and extensive low-relief landscape that has undergone recent surface uplift (*e.g.*, Calvet et al., 2015; Whipple et al., 2017). In the case of surface uplift, such an elevated paleo-topography is called relict landscape or paleo-surface and represents a transient geomorphic marker that provides a reference frame for quantifying the spatial distribution of surface uplift (Calvet et al., 2015; Fox, 2019). Relict landscapes, thus, represent a unique opportunity to decipher the wavelength and the amplitude of surface uplift, and consequently the mechanisms that created such a topography, especially in areas devoid of stratigraphic constraints.

The Atlas-Meseta intracontinental orographic system of Morocco is composed of different structural and topographic domains that from north to south include: the Moroccan Meseta (Western Meseta and Eastern High Plateaus), the Middle Atlas, the High Atlas, the Siroua Massif, and the Anti-Atlas. The High and Middle Atlas are the main active orogen (*e.g.*, Sebrier et al., 2006), while the other regions are characterized by a relatively high topography that formed without significant crustal deformation (Teixell et al., 2003; Frizon de Lamotte et al., 2009; Pastor et al., 2015). This configuration offers the opportunity to investigate rates, wavelength, magnitudes and causes of topographic growth.

In this study, we focused on the Anti-Atlas Mountains, a Variscan orogen characterized by a complex assemblage of intrusive, metamorphic, and sedimentary rocks representing the African counterpart of the Appalachian Valley and Ridge province (Miller et al., 2013; Gallen et al., 2018). Similarly to the Appalachian, the topography of the Anti-Atlas results from a relatively recent phase of surface uplift associated with erosion of a wide relict landscape (Choubert, 1952; Malusà et al., 2007; Missenard et al., 2008; Guimera et al., 2011; Chapter 2). The causes of this topographic rejuvenation are still poorly understood. Some authors suggested that the uplift may be related to Cenozoic shortening (Giumera et al., 2011), whereas other suggested the occurrence of a deep, dynamic process (Missenard et al., 2006; Sebrier et al., 2006; Frizon de Lamotte et al., 2009). Receiver function analysis indicating that the topography of the Moroccan orographic system is not isostatically balanced by significant crustal roots (Miller and Becker, 2014). In this context, the absence of tectonic activity, the steady protracted low denudation rates, and the preserved relict landscape offer the possibility to quantify the regional uplift in the Anti-Atlas and the Siroua Massif. This setting offers the possibility to quantify the regional uplift studying the present-day topographic configuration without available geological evidence. These questions can be addressed by a combination of traditional geomorphologic applications with, terrestrial cosmogenic nuclides and numerical models, which allow the topographic evolution at different timescales to be investigated.

In this study, we combined quantitative analysis of regional and basin-scale topography with stream profiles analysis (knickpoints characterization, longitudinal profiles and χ–z plot) and published basin-wide denudation rates inferred from ^{10}Be concentrations (Chapter 2). Furthermore, we performed stream projections from the upper relict channel profiles and reconstruct a paleo-landscape to constrain the amount of relative base level fall following the increase in Cenozoic rock uplift rates. Finally, we constrained the timing of this geomorphic rejuvenation to the middle-late Miocene by applying a knickpoints celerity model. This approach provides a framework for discussing the contribution of large-scale deep signals and shallower processes in generating the regional topographic relief in areas where large wavelength uplift occurs.

3.3. Geological background

3.3.1. Geological setting

The intracontinental Atlas-Meseta orographic system of Morocco is composed of two WSW-ENE oriented mountain belts, High Atlas (HA) and the Anti-Atlas (AA), and two elevated regions with low-topographic relief, named Western and Eastern (or High Plateaus) Meseta, which are separated by the SW-NE striking Middle Atlas belt (MA). This system of mountain belts experienced a complex geologic history including multiple episodes of contractional deformation and rifting (Froitzheim et al., 1988; Hafid, 2000; Frizon de Lamotte et al. 2000; Domènech et al., 2015). Currently, active deformation is controlled by the plate convergence between Africa and Eurasia (Froitzheim et al., 1988; Hafid, 2000; Frizon de Lamotte et al. 2000; Gomez et al. 2000; Teixell et al., 2003; Lanari et al., 2020b). In the following, we briefly summarized the evolution of the HA, the AA, the Siroua Massif, and the adjacents Souss and Ouarzazate basins.

The HA is the highest domain of the Atlas system (with a few mountain peaks above 4 km of elevation) and strikes for approximately 600 km, with a width of 50 to 100 km. The belt consists of a fold and thrust belt composed of Precambrian, Paleozoic, and Mesozoic rocks (Figure 3.1). Mesozoic rocks are mostly composed of carbonate syn-rift (Jurassic and Triassic) and post-rift deposits (Cretaceous), related to the opening of a rift basin during the breakup of Africa with an extension oriented NW-SE (Arboleya et al., 2004; Baudon et al., 2009; Lanari et al., 2020b). Based on thermochronological and structural data the main exhumation episode started in the middle/late Miocene and led to 4-6 km of exhumation

(Balestrieri et al., 2009; Barbero et al., 2007; Domènech, 2015; 2016; Ghorbal, 2009; Lanari et al., 2020a; 2020b; Leprêtre et al., 2018; Missenard et al., 2008).

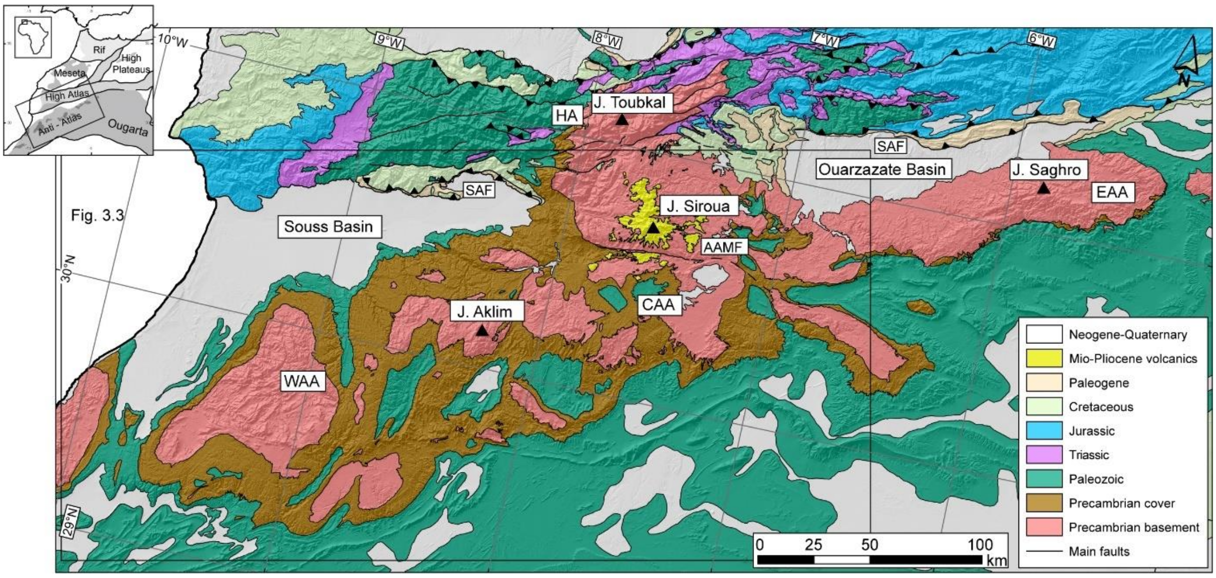

Figure 3.1. Simplified geological map of High and Anti-Atlas Mountains based on the 1:1.000.000 geological map of Morocco (modified from Maroc Service Géologique, 1985). EAA: Eastern Anti-Atlas, CAA: Central Anti-Atlas, WAA: Western Anti-Atlas, HA: High Atlas, AAMF: Anti-Atlas Major Fault, SAF: South Atlas Fault. The main mountain peaks are shown with black triangles.

The HA and AA belts are separated by the Souss and the Ouarzazate basins, which have been commonly interpreted as the southern Neogene foreland basins of the HA (Figure 3.1; Sebrier et al., 2006; Arboleya et al., 2008). The Souss Basin has an eastward wedging geometry and is characterized by a longitudinal, E-W oriented, drainage system flowing directly into the Atlantic Ocean (Figure 3.2A). The basin has a rather flat, low-topographic relief morphology that increases progressively toward the basin interior up to ~700 m of elevation. It extends for a length of more than 150 km and has been filled by Pliocene to Quaternary fluvial, fluvio-lacustrine and aeolian sediments derived from the uplifting HA and AA belts (Hssaine and Bridgland, 2009). The northern sectors of the Souss Basin are characterized by steeper margins, with high-standing Quaternary fluvial terraces and dissected alluvial fans that originated during faulting along the HA orogenic front (i.e., South Atlas Fault, SAF; Figure 3.1) (Sebrier et al., 2006). Conversely, the southern margin is characterized by a gently, uniformly north-dipping slope that do not show evidence of tectonic deformation (Sebrier et al., 2006; Lanari et al., 2022).

The Ouarzazate Basin is sandwiched between the Siroua Massif to the west and the Saghro Massif to the east, and follows the same WSW-ENE trend of the HA and the AA belt (Figure 3.1). It lies between 1200 and 1800 m of elevation and extends over a length of more than 150 km. The basin filling consists of a < 1-km-thick-succession including Middle Eocene marine deposits unconformably overlain by Mio-Pliocene terrestrial sediments marking the development of an endorheic stage (Fraissinet et al. 1988; Gorler et al. 1988; El Harfi et al., 2001; Teson & Teixell 2006; Teson et al., 2010). The basin is currently drained by the Draa River a southward draining system that crosses the AA through a narrow bedrock gorge and then flows parallel to the AA before entering in the Atlantic Ocean (Figure 3.2A). The transition from endorheic to exoreic conditions occurred most likely in the Plio-Pleistocene, either through the regressive erosion of rivers draining the southern AA flank (Stablein, 1988) or lake overspill (Arboleya et al., 2008).

The Siroua Massif represents a strato-volcano covering an area of approximately of 500 km2 and reaching maximum elevation of ~3300 m. Here, the Mio-Pliocene volcanic deposits directly overlie the Precambrian basement, which is characterized by an elongated, dome-like morphology with a low-topographic relief landscape (Missenard et al., 2008; Giumera et al. 2011).

The AA belt extends over approximately 600 km of length, has a width of 100 to 150 km, and rises ~2 km above sea level. It was structured during a series of collisional events starting from the Eburnean orogeny at around 2000 Ma (Ait Malek et al., 1998; Thomas et al., 2002; Walsh et al., 2002). Afterward, it experienced two main orogenic events: the Neoproterozoic Pan-African orogeny (Leblanc, 1975; Saquaque et al., 1989; Hefferan et al., 2000; Gasquet et al., 2008) with a subsequent extensional event during the Late Neoproterozoic (Piqué et al., 1999; Doblas et al., 2002; Soulaimani et al., 2003) and the late Carboniferous Variscan orogeny (Sebti et al., 2009; Soulaimani et al., 2014; Sehrt et al., 2018). Low-temperature thermochronology and stratigraphic data indicate that the AA was not subjected to major Mesozoic vertical movements, while erosion and exhumation have been rather uniform at rates of ~20 m/Myr since at least the late Cretaceous (Lanari et al., 2020a; Charton et al., 2021; Chapter 2). The basement is composed of magmatic, metamorphic, and sedimentary rocks assembled during the Eburnean and Pan-African orogenesis. These rocks are widely exposed along the axial sectors of the range (Figure 3.1) and are overlain by a late Precambrian and Paleozoic sedimentary sequence with a thickness of almost 10 km in the Western AA decreasing to less than 6 km in the eastern sectors of the belt (Piqué and Michard, 1989; Helg et al., 2004; Burkhard et al., 2006). This sedimentary cover was predominantly deposited in a shallow-water marine environment during the post Pan-African extensional event (Azizi Samir et al., 1990; Thomas et al., 2002; Soulaimani et al., 2003), and includes Lower Cambrian carbonates, siltstone and marls as well as Middle

Cambrian to Middle Devonian sandstones and shales. These strata were subsequently deformed during the Variscan orogeny and covered by marine (mainly Cretaceous) sediments that are locally preserved (Figure 3.1).

3.3.2. Geophysical and petrological data

The peculiarity of the Atlas-Meseta orographic system is characterized by the lack of orogenic roots generated through crustal shortening and thickening processes that would isostatically support the modern topography. This applies to the HA (Beauchamp et al., 1999; Gomez et al., 2000; Teixell et al., 2003; Domènech et al., 2016; Fekkak et al., 2018; Lanari et al., 2020b) and MA (Gomez et al., 1998; Arboleya et al., 2004; Pastor et al., 2015), where contractional structures can be observed in the field, and to the tectonically inactive AA, western and eastern Meseta (Babault et al., 2008; Frizon de Lamotte et al., 2009; Pastor et al., 2015). Several geophysical and petrological studies indicate an anomalous thinning of the lithosphere and a shallow and hot asthenosphere beneath the entire Atlas-Meseta orographic system (El Azzouzi et al., 1999; Missenard et al., 2006; Duggen et al., 2009; Miller et al., 2015). This includes geophysical modelling of gravity data, S-received function (Ayarza et al., 2005; Missenard et al., 2006; Miller and Becker, 2014; Miller et al., 2015), heat flow measurements, deep electrical resistivity (Rimi et al., 1999; Zeyen et al., 2005) and seismic tomography (Seber et al., 1996; Palomeras et al., 2014; Bezada et al., 2014). This configuration is thought to support the present-day topography of the Atlas-Meseta system, which should have been generated, at least in part, by deep-seated, mantle driven processes. For example, a maximum of 2000 m of residual topography has been estimated in the HA and MA considering a crustal thickness of ca. 35 km (Miller and Becker, 2014), while more than 1000 m of elevation has been attributed to dynamic topography (Frizon de Lamotte et al., 2009; Spieker et al., 2014). Magmatic activity in the Siroua, Saghro and MA Mountains present an alkaline affinity indicating a partial melting of sublithospheric mantle caused by asthenospheric flow (El Azzouzi et al., 1999; De Beer et al., 2000; Missenard et al., 2006). The geochemical signature and trace element patterns of the MA lavas are very similar to those observed in the Canary Islands, suggesting a possible link between the Canary mantle plume and continental intraplate volcanism in the Atlas-Meseta system (Duggen et al., 2009). Interestingly, magmatism occurred in different pulses, in the Eocene and middle-late Miocene in association with renewed tectonic activity as documented by thermochronological data (Lanari et al., 2021a). A more recent phase of magmatism, however, has occurred in the MA and Western Meseta during the last 2 Ma, apparently without major acceleration in tectonic deformation (El Azzouzi et al., 2010; Missenard et al., 2012).

3.4. Methods

3.4.1. River profile and topographic analysis

River networks represent a powerful reconnaissance tool to investigate the impact of rock uplift and climate changes on landscape evolution (Hack, 1957; Kirby and Whipple, 2001; Wobus et al., 2006; Kirby and Whipple, 2012; Whittaker, 2012). This is possible because channel steepness and erosion rates along river profiles adjust to rock uplift, climatic conditions and bedrock erodibility (Duvall et al., 2004; DiBiase and Whipple, 2011). The relationship between steepness and erosion of bedrock river channels has been empirically defined in a large variety of geological settings and orogens (Kirby and Whipple, 2012, reference therein). Channel slopes along the stream course commonly exhibit an inverse power-law scaling relationship with upstream contributing drainage area (Flint, 1974). Hence, the stream power model describes the variation of channel elevation in time (*dz/dt*) (Howard and Kerby, 1993; Whipple and Tucker, 1999):

$$\frac{dz}{dt} = U - KA^m S^n \qquad (1)$$

where U is the rock uplift rate, K is the fluvial erodibility coefficient controlled by bedrock lithology, climate and sediment load, A is the upstream drainage area, S is the local channel slope and m and n are constants that depend on basin hydrology, channel geometry and erosional processes (Howard, 1994; Whipple and Tucker, 1999). Under steady state conditions erosion (E) and rock uplift rates (U) are balanced (Willet and Brandon, 2002; Kirby and Whipple, 2012), and there is no change in elevation of the channel bed over time ($dz/dt = 0$). Therefore, eq. 1 can be rearranged as:

$$S = \left(\frac{U}{K}\right)^{\frac{1}{n}} A^{-\left(\frac{m}{n}\right)} \qquad (2)$$

where $(U/K)^{1/n}$ and m/n are the channel steepness index (ks) is the concavity index (θ), respectively (Flint, 1974). The relationship in eq. 2 is only valid above a critical upstream drainage area of 0.1 to 5 km^2, where fluvial processes dominate over debris flow processes (Montgomery and Foufoula, 1993; Stock and Dietrich, 2003; Wobus et al., 2006). Channel steepness and concavity indices can be extracted from DEMs by a logarithmic regression of the local channel slope versus the contributing drainage area (Whipple, 2004; Wobus et al., 2006) or through an integral approach (Perron and Royden, 2013). Small variations in the concavity index can, however, lead to wide variations in the channel steepness index (Kirby and Whipple, 2012). To allow the effective comparison among longitudinal profiles with greatly varying drainage areas and counteract the influence of DEM-noise, a typical reference concavity index (θ_{ref}) of 0.45 is generally used to calculate the normalized channel steepness index (k_{sn}) (Snyder et al., 2000; Wobus et al., 2006). This θ_{ref} value falls in the range of θ estimates upstream and downstream of non-lithological knickpoints. The validity of the selected reference concavity index has been tested using the criteria proposed by Perron and Royden (2013), as discussed in Chapter 2.

The k_{sn} value is sensitive to variations in bedrock erodibility, climate conditions and rock uplift (Snyder et al., 2000; Kirby and Whipple, 2001; Wobus et al., 2006). An effective approach to extract information and define landscape scenarios is to reconstruct the spatial distribution of k_{sn} across the landscape (Harkins et al., 2007; Olivetti et al., 2016; Gallen and Wegmann, 2017; Fox, 2020). Here, we performed a regional scale analytical and statistical analyses, using the integral approach calculating χ along the main river segments. A linear regression though χ allows estimating θ and k_{sn} (Chapter 2). These results are comparable with values estimated from the log slope-log area method of the same river network (Tables S3.1, S3.2 and Figure S3.3 in supporting informations).

Moreover, the integral approach allows visualizing k_{sn} variation along the stream segments and to discretize the knickpoints. The method is based on the transformation of the horizontal coordinates of a river profile to the χ reference frame assuming steady state conditions and spatially invariant uplift rates and bedrock erodibility (Perron and Royden, 2013):

$$z(x) = z(x_b) + \left(\frac{U}{KA_0^{m}}\right)^{\frac{1}{n}} \int_{xb}^{x} \left(\frac{A_0}{A(x)}\right)^{\frac{m}{n}} dx = z(x_b) + k_s\, A_0^{-\left(\frac{m}{n}\right)} \chi \qquad (3)$$

$$\chi = \int_{xb}^{x} \left(\frac{A_0}{A(x')}\right)^{\frac{m}{n}} dx \qquad (4)$$

where x_b is the base level, χ is the independent variable of integral quantity, z is the elevation along the channel, ks (or k_{sn} assuming a reference concavity) is the steepness index and A_0 is the reference drainage area, usually assumed to be 1 (Perron and Royden, 2013). In the χ–z plot the slope is proportional to the channel steepness index (k_{sn}). This transformation of the system of coordinates allows detecting spatial variations in rock uplift rates and bedrock erodibility among rivers from different drainage basins, as well as changes in the drainage area through time (Willett et al., 2014). In areas where erodibility and climate variability is marginal, the river network analysis can be used to infer and visualize the pattern of relative rock uplift rate across the region. Usually, variation of rock uplift rate is identified by the presence of "consuming knickpoints" which separate portions of the landscape eroding at different rates (Kirby and Whipple, 2012; Royden and Perron, 2013; Mudd et al., 2014). A detailed analysis of these features is fundamental to understand the state of a landscape.

A Shuttle Radar Topography Mission Digital Elevation Model (SRTM DEM, pixel size of 90 m) was used to perform the topographic and the river network analysis. All steps were conducted using ArcGIS tools, TopoToolbox (Schwanghart and Scherler, 2014), TAK (Forte and Whipple, 2019) and a series of MATLAB functions for analyzing river profiles (Gallen, 2017; Fox, 2019).

3.4.2. Knickpoints discretization and celerity model

Knickpoints can be divided in two categories, transient and stable knickpoints (Kirby and Whipple, 2012). Both features mark changes in the channel gradient, but transient knickpoints are characterized by an abrupt downstream increase in the channel steepness index reflecting a relative increase in the rate of rock uplift. Conversely, stable knickpoints are anchored in space, and are usually associated with landslides (Korup, 2006) and heterogeneities along the profile related to lithological contrasts (Kirby et al., 2003). The transient knickpoints represent a mobile boundary between the downstream portion of the landscape that has already adjusted to the new imposed rock uplift rate and the upstream part which is still recording an earlier rock uplift stage. This portion of the landscape represents the perched relict landscape that is usually bounded by migrating knickpoints (Miller et al., 2013; Olivetti et al., 2016; Gallen and Wegmann, 2017). The generation and migration of transient knickpoints can be related to changes in tectonic rates (Safran et al., 2005; Kirby and Whipple, 2012; Miller et al., 2013; Chapter 2), drainage pattern reorganization associated with river capture processes (Clark et al., 2004; Willet et al., 2014; Gallen, 2018; Fox et al., 2020), base-level fall (Berlin and Anderson, 2007; Ballato et al., 2015) and/or climate changes. Distinguishing the nature of the knickpoints requires a detailed analysis of the geological and geomorphic characteristics (Kirby and Whipple, 2012). Transient from lithological knickpoints were differentiated by looking at: (1) their position and distribution in the χ–z plot (*i.e.*, rivers that experienced a similar rock uplift history should cluster in the χ–z plot; Gallen and Wegmann, 2017; Ma et al., 2020; Figure S3.2 in supporting informations); (2) available geological maps (1: 200.000, 100.000 and 50.000, Service Géologique du Maroc); and (3) satellite imageries on Google Earth.

Subsequently, a celerity model was applied to calculate the onset of knickpoints upward migration. By using the stream model shown in Equation 1, considering plucking the primary erosion mechanism (n = 1) and assuming a constant knickpoints celerity through time, the horizontal migration of knickpoints along the river profiles in response to a relative base-level drop can be described as:

$$\frac{dx}{dt} = KA^{m} \tag{5}$$

where, $dx/\ dt$ is the knickpoint celerity, K is a dimensional coefficient of erosion (Whipple and Tucker, 1999; Whipple, 2004), A is upstream drainage area and m is a non-dimensional parameter that depends on basin hydrology, channel geometry, and erosion process (Whipple and Tucker, 1999). To constrain the K and m parameters, a brute force two-parameter search was used (Stock and Montgomery, 1999; Crosby and Whipple, 2006; Berlin and Anderson, 2007; Miller et al., 2013; Gallen et al., 2013; Sembroni et al., 2016), which allow finding the best combination of parameters that predict the knickpoints' location. The celerity prediction has been applied over a wide range of settings and scenarios and using a large variety of constrains for K and m to minimize the misfit between the observed and modelled knickpoint positions (Berlin and Anderson, 2007; Miller et al., 2013; Gallen et al., 2013; Ballato et al., 2015; Sembroni et al., 2016; Heidarzadeh et al., 2017). Specifically, m was allowed to vary linearly between 0 and 0.75, as suggested by the present-day topography (Tables S3.1, S3.2 and Figure S3.3 in supporting information), while K was allowed to vary between 10^{-7} and 10^{-4} (Figure S3.5), in agreement with the relationship between ^{10}Be denudation rates and k_{sn}, using a linear version of the stream power model (Chapter 2). Finally, we set the onset of knickpoints migration between 3.8 and 18.6 Ma (details in chapter 4.4). This timing was estimated by using the maximum excavation time required to erode the missing rock volume from the river catchments (Table S4). Although the landscape is characterized by disequilibrium condition, the estimates of denudation rate are relative only to the upper relict portion of the landscape, which is eroding at lower rates (Chapter 2). Similarly to previous studies (Norton et al. 2008; Schildgen et al., 2012; Gallen et al., 2013; Siame et al., 2015), the excavation time is expressed as:

$$T = \left(\frac{V}{A}\right) E^{-1} \tag{6}$$

where T is the time required to erode the missing rock volume in the catchments, V is the rock volume, A is the drainage area of the catchments and E is the basin-wide denudation rate. V can be estimated by the difference between a surface connecting the highest points in the current landscape and the current topography itself.

3.4.3. River projections and linear inverse method

The mechanisms of topographic relief growth can be deciphered by studying the present-day river incision and studying the modern topography. The magnitude of fluvial incision, associated with changes in rock uplift, can be estimated from the relict topography upstream of major non-lithological knickpoints (Berlin and Anderson, 2007; Schildgen et al., 2012; Gallen et al., 2013). In particular, the reconstructed river projection from the relict landscape allows determining the paleo-base level (either due to a base level variation and/or an increase in rock uplift rates) and hence the magnitude of minimum surface uplift and paleo-relief before the development of the knickpoints (Perron and Royden, 2013; Olivetti et al., 2016; Heidarzadeh et al., 2017; Fox et al., 2019). This projection was carried out in χ space with $\theta_{ref} = 0.45$. To do this a linear model is regressed through the χ-elevation data from the relict part of the landscape. Projecting this model across the incised part of the landscape provides an estimate of the incision and the intercept with the y-axis (*i.e.*, where χ=0) provides the elevation of the paleo-baselevel. This approach relies on several assumptions: that the paleo-river network has remained approximately the same through time; erosion rates across the relict landscape have remained constant; that the channel steepness in the paleolandscape was spatially uniform; and that the change in baselevel due to surface uplift is spatially uniform. The assumption that the erosion rates have remained constant across the Anti-Atlas relict landscape is justified by the close match between short and long-term erosion rates throughout the Cenozoic (Chapter 2), suggesting erosional steady-state conditions (*i.e.*, balance between long- and short-term erosion rates; *e.g.*, Willet and Brandon, 2002). The assumption that the channel steepness was relatively uniform, and that surface uplift is uniform can be tested by comparing predictions from different tributaries within the same catchment. The method has been already applied in different tectonic and geological settings showing the importance of channel morphology to infer the uplift and topographic history (Schildgen et al., 2012). This method can only be applied to individual rivers and there is no guarantee that the projected rivers within the same catchment will predict the same amount of surface uplift. This has the benefit of providing a test of the underlying assumptions, however, the resulting landscape may be unrealistic because predicted elevations at confluences may be very different.

A new approach proposed by Fox (2019) allows reconstructing the paleo-topography in two dimensions by means of a linear inverse method that interpolates the river profiles of the relict topography and ensures that confluences share the same elevation. A discrete version of the stream power model can be written using a series of nodes along the main trunk river:

$$z_{i} - B.L. = \sum_{j=1}^{i} (\Delta\chi_j) u_j^* + S.U._i \tag{7}$$

where the *i*th pixel is the upstream of the *j*th pixel and the lowest most pixel has the elevation of B.L. (baselevel), *S.U.i* is the surface uplift that the relict landscape has experienced following fluvial dissection, $u*$ is the normalized rock uplift rate, which is proportional to the normalized channel steepness that is preserved across the relict landscape. This expression provides a prediction of elevation as a function of channel steepness and surface uplift. Provided both vary smoothly in space over long length scales, the elevation of pixels within the DEM can be used to recover these values using inverse methods. This inversion provides a reconstructed pre-incision landscape and allows quantifying the amount of surface uplift for each node (Fox, 2019; Fox et al., 2020). Maps of $u*$ and *S.U.* can be calculated to minimize the misfit between predicted and observed topography of the relict landscape and the roughness of the $u*$ and *S.U.* maps. For a single channel, if the $u*$ and *S.U.* values are invariant with space (*i.e.*, there is roughness), the approach reduces to the simple projection method described above. In this case, the χ values were calculated for the entire drainage network of the Anti-Atlas but only the upstream knickpoints on the relict landscape were used to estimate the $u*$ and *S.U.*. Values of m = 0.45 and A_0 = 1 m^2 and damping parameters, λ and α equal to 10 and the grid size to 5 km, were used for the inversion method. Importantly, the main assumptions of the method are that the shape of the river network has remained constant in time, there was no major drainage reorganization, and the erodibility coefficient (*K*) is considered constant. Importantly, these are the same assumptions used in the analysis presented above. The reconstructed paleo-topography is also based on these assumptions and is forced by the interpolation scheme based on the steady state stream power model.

3.5. Results

3.5.1. Topographic analysis

The AA is characterized by an extensive, high-standing (~2000 m), axial zone with low-topographic relief together with steep and dissected flanks (Figure 3.2). The westernmost sectors of the belt have a dome-shape geometry with a rather symmetric topography across the drainage divide (Figure 3.2B). The central sectors of the western AA have an asymmetric topography with a gentle southern and a steep northern flank grading toward the Draa and the Souss basins, respectively (Figure 3.2C). The central AA has also a flat top but is bounded to the north by the Siroua plateau through a topographic step in proximity of the Anti-Atlas Major Fault (AAMF; Figure 3.2D). The along-strike swath profile highlights the geometry and the extent of the elevated axial surface, which exhibits local variations in topographic relief, with a few mountain peaks (*e.g.*, Mt. Jebel Aklim, 2531 m and Mt. Jebel Saghro, 2592 m) and deeply incised valley (the Draa gorge; Figures 3.2A and 3.2E). The high-standing landscape is mostly composed of Paleozoic limestones and Precambrian basement rocks (volcano-clastics, granites and quartzites; Figure 3.3A) and is located upstream of non-lithological knickpoints.

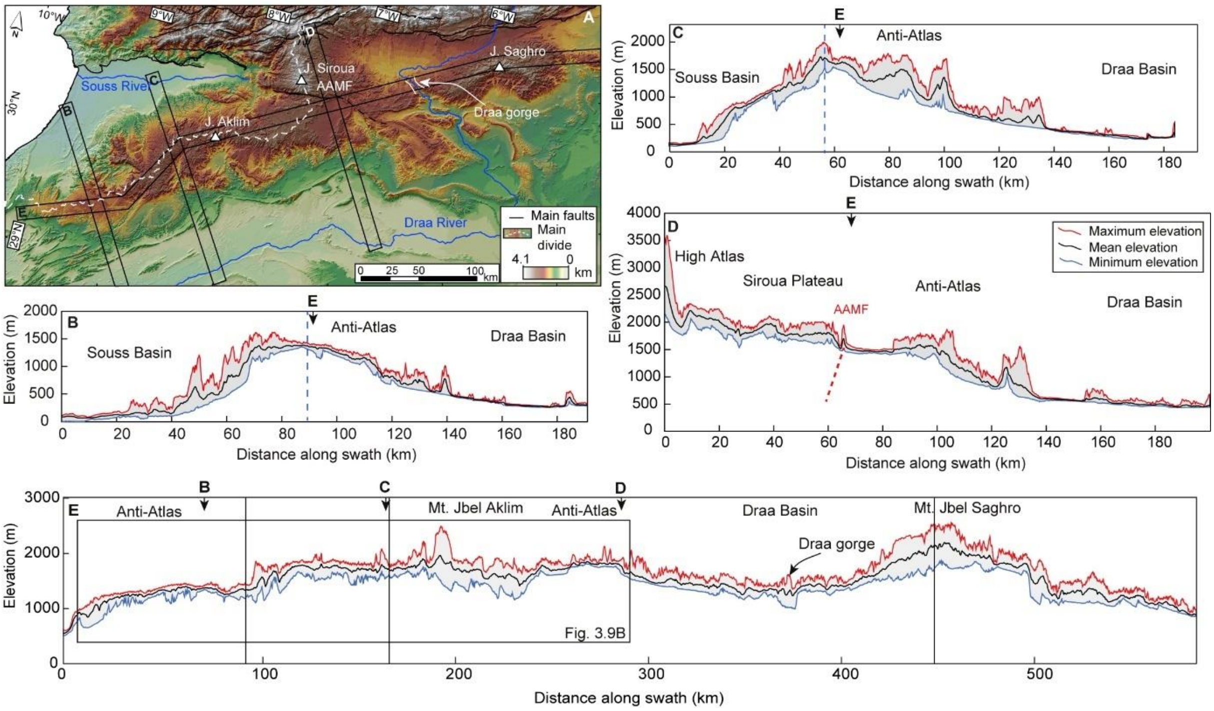

Figure 3.2. (A) Topographic map of the Anti-Atlas and the Siroua Massif (SRTM DEM database) with location of the swath profiles. The dashed white line indicates the position of the main drainage divide. (B, C, D) are swath profiles orthogonal to the main drainage divide of the Anti-Atlas, while (E) is parallel to the main drainage divide. The dashed blue line indicates the position of main drainage divide on swath profiles B, C.

Downstream of these knickpoints, below 1500 m of elevation, the topography has steeper slopes sculptured on late Precambrian and Paleozoic sedimentary rocks (Figures 3.3A, 3.3B, 3.3C). In more detail, the northern flank has a slope that is sub-parallel to the bedding of the late Precambrian carbonates and includes narrow and deep valleys perpendicular to the bedding (Figure 3.4, profile A-A’). Conversely, the southern flank consists of wide valleys mostly located along the core of the Paleozoic synclines (Soulaimani and Burkhard, 2008; Figure 3.4, profile B-B’). Finally, the swath profiles indicate that the high-standing, elevated surface plunges along the strike of the orogen (Figure 3.2E) and also perpendicularly to it (Figures 3.2B, 3.2C).

3.5.2. River morphology

Seventeen stream profiles from the northern flank of the central Anti-Atlas (NCAA) together with 17 profiles from its southern flank (SCAA) and 14 from the western side of the orogen (WAA) were analysed individually. Specifically, we extracted the main knickpoints, the concavity values (θ) and the normalized channel steepness indices (k_{sn}) for the main river trunks using the log S-log A approach and the integral method. In the AA, most of the rivers are characterized by transient conditions with mean k_{sn} values of 84 ($\sigma_m = 3.8$) and 30 ($\sigma_m = 2.9$) in the downstream and the upstream stream segments, respectively (Table S3.1 in the supporting information).

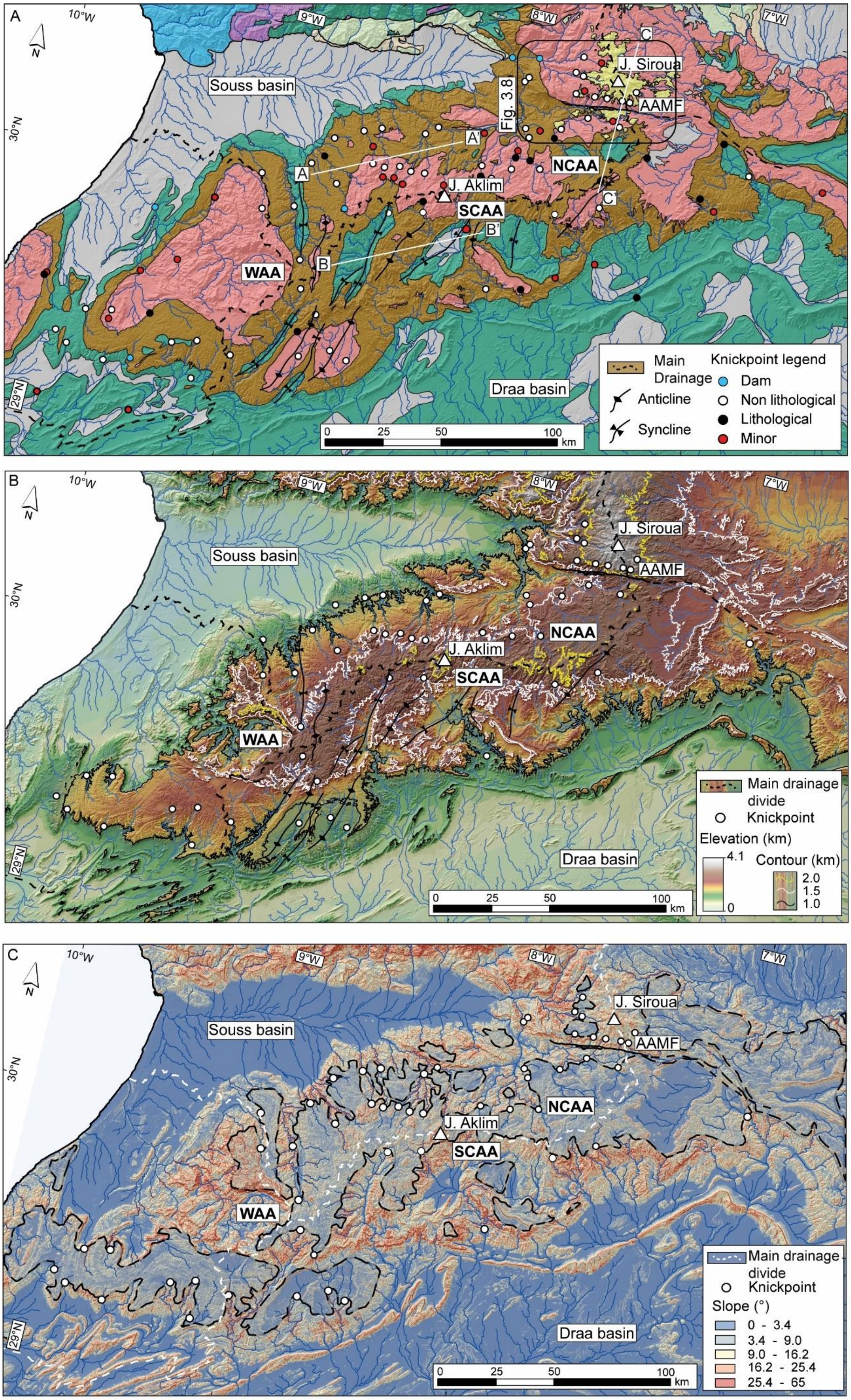
A
10°W
9°W
8°W
7°W
N
30°N
29°N
Souss basin
Fig. 3.8
J. Siroua
AAMF
C
C'
A
A'
B
B'
J. Aklim
NCAA
SCAA
WAA
Draa basin
Main Drainage
Anticline
Syncline
Knickpoint legend
Dam
Non lithological
Lithological
Minor
0
25
50
100
km
B
Main drainage divide
Knickpoint
Elevation (km)
4.1
0
Contour (km)
2.0
1.5
1.0
C
Slope (°)
0 - 3.4
3.4 - 9.0
9.0 - 16.2
16.2 - 25.4
25.4 - 65

Figure 3.3. (A) Geological map of the study area with a detailed analysis of the knickpoints for the northern flank of the central Anti-Atlas (NCAA), western (WAA), and southern flank of central Anti-Atlas (SCAA) and the Siroua Massif. The main fold axes are associated with the Variscan orogeny and are shown with black lines (from Soulaimani and Burkhard, 2008). (B) Topographic map (SRTM DEM database) of the study area with the non-lithological knickpoints and the fold axes. The black, white and yellow dashed lines demark the 1000, 1500 and 2000 m contours, respectively. (C) Slope map of the study area with non-lithological knickpoints. The dashed line indicates the low-slope area of the axial zone of the Anti-Atlas (after Chapter 2). Location of the maps is shown in figure 3.1.

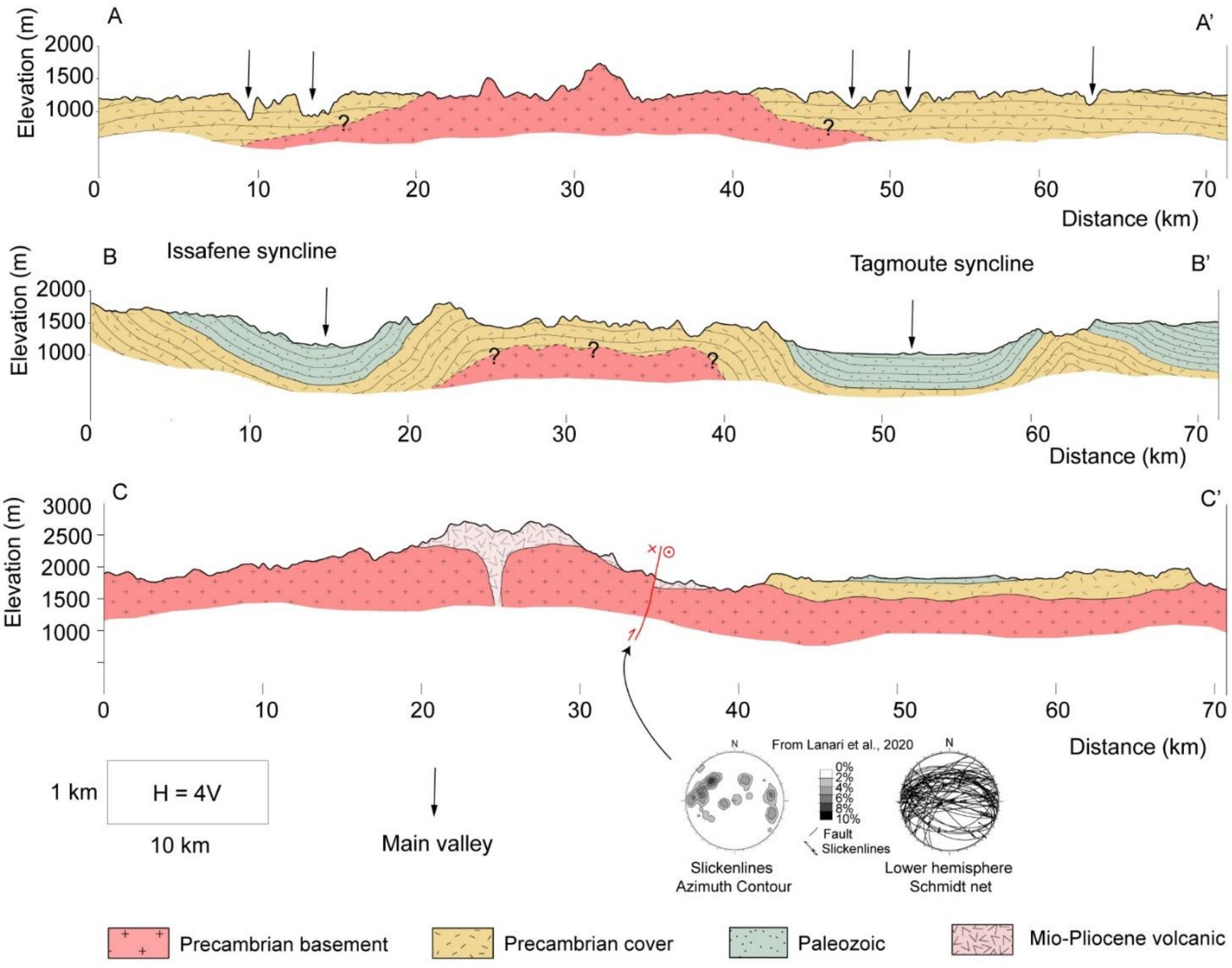

Figure 3.4. A-A' geological cross section of the northern flank of the Anti-Atlas. B-B' geological cross section of the southern flank of Anti-Atlas. C-C' geological cross section in the Siroua Massif. Location of the cross-sections is indicated in figure 3.3A.

The NCAA is mostly characterized by transient longitudinal river profiles. Overall, we recognized 51 knickpoints with two main patterns of non-lithological knickpoints standing between 700 and 1000 m and 1300 and 1500 m of elevation and several minor lithological knickpoints (Figures 3.3A, 3.3B and 3.5A). The two patterns of non-lithological knickpoints cluster approximately at values of χ of 3-5 and 9–11, respectively (Figure 3.5B). The steepest and concave up segments of the NCAA rivers are downstream of the highest knickpoints (Figures 3.5A, 3.5B), whereas, the upstream segments are mostly rectilinear, have a shallow gradient and contain minor knickpoints (Figures 3.3A and 3.5A, 3.5B). The θ values of the segments downstream of the highest knickpoints range from 0.28 to 0.53, with an average of 0.44 ($\sigma_m = 0.02$) while the k_{sn} varies between 76.5 and 135, with an average of 102.6 ($\sigma_m = 4.7$; Table S3.1, Figure 3.5B). The θ values of the segments upstream of the highest knickpoints range from -0.08 to 0.38, yielding an average of 0.18 ($\sigma_m = 0.04$), whereas the k_{sn}, values vary between 11.5 and 50.7 with an average of 33.2 ($\sigma_m = 3.5$; Table S3.1, Figure 3.5B). Another minor group of knickpoints separating gentle upstream river segments from steeper downstream portions is in the Siroua Massif, over 2000 m of elevation (see red profiles in figures 3.5A and 3.5B), upstream of the Anti-Atlas Major Fault (AAMF, Figures 3.6A, 3.6B, 3.6C).

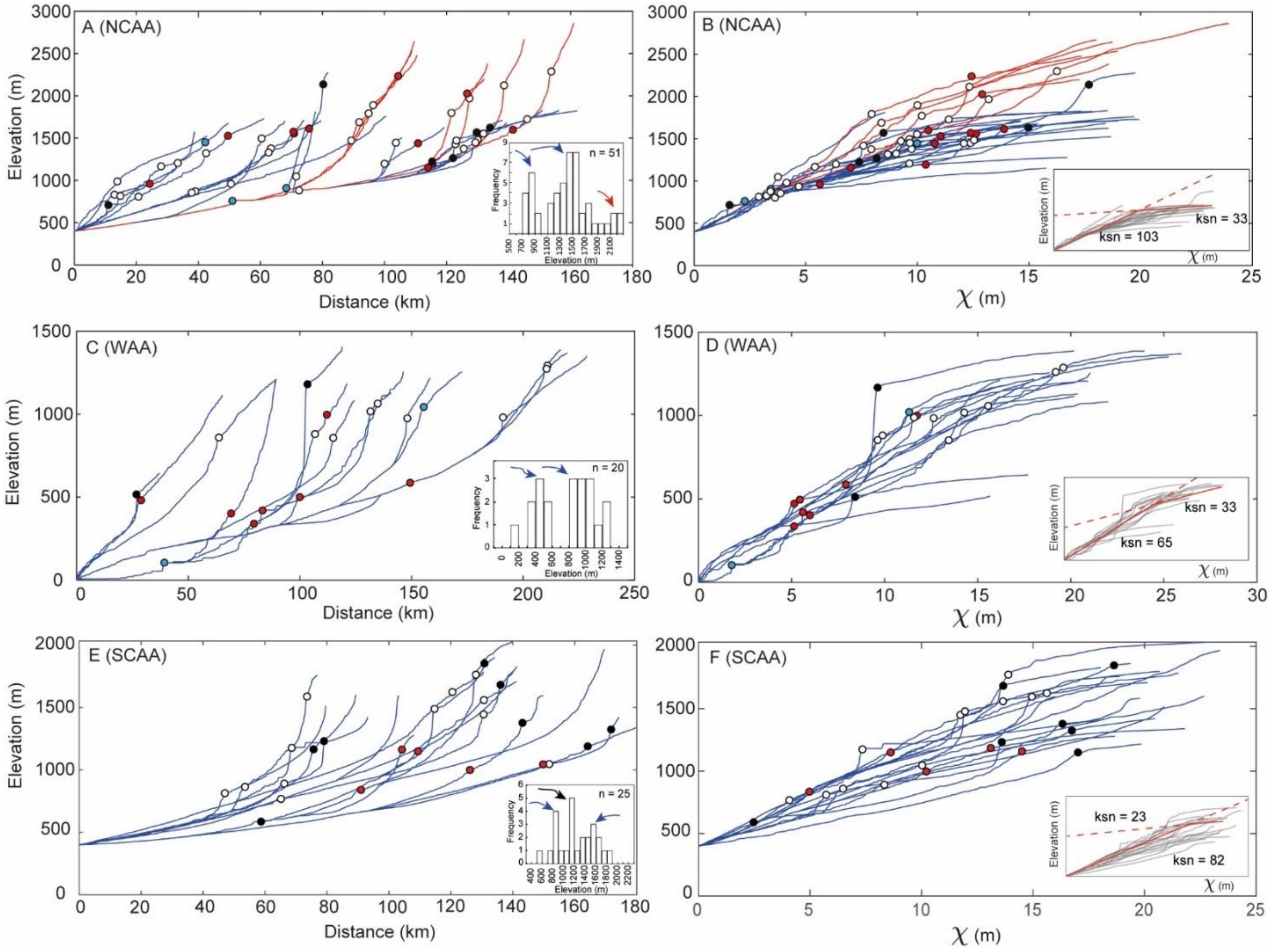

Figure 3.5. Longitudinal river profiles and χ plots with major knickpoints for (A-B) NCAA, (C-D) WAA, and (E-F) SCAA. The rivers of NCAA and SCAA sectors are extracted from the bedrock-alluvial transition, which in the study area is around 400 m. The red profiles indicate the rivers flowing from the Siroua Massif. The knickpoints legend is in figure 3.3A. The inset plots in the χ space show the mean regional k_{sn} values upstream and downstream of the highest knickpoints. The inset histogram in the longitudinal profiles show the frequency distribution of the elevation of the knickpoints.

The WAA sector also has transient river profiles with approximately 20 knickpoints. Most of the non-lithological knickpoints are located within a relatively narrow elevation band, of about 800 to 1100 m while the minor knickpoints are at about 400 to 500 m (Figures 3.5C, 3.5D). The steeper downstream portion of the major non-lithological knickpoints exhibit a concave-up geometry with a few minor knickpoints (Figures 3.5C, 3.5D). The upstream segments are mostly rectilinear with a typical equilibrium profile (straight segment in χ space; Figure 3.5D). Here, the two patterns of knickpoints at ~500 m and ~1000 m, occur approximately at χ values of 5-6 and 10–15, respectively (Figure 3.5D). The θ and k_{sn} values of the segments downstream of the highest knickpoints range from 0.41 to 1.1, yielding an average of 0.75 ($\sigma_m = 0.1$) and from 49.8 to 78.6 with an average of 65.1 ($\sigma_m = 3.1$), respectively (Table S3.1, Figure 3.5D). Instead, upstream of the highest knickpoints, θ and k_{sn} values vary between -0.25 and 0.55, with an average of 0.14 ($\sigma_m = 0.07$) and between 12.9 and 75.6 with an average of 33.2 ($\sigma_m = 6.1$), respectively (Table S3.1, Figure 3.5D).

The SCAA sector is characterized by both, equilibrated and transient longitudinal river profiles containing at least 25 knickpoints distributed across a wide range of elevation (Figure 3.5E). Most of the non-lithological knickpoints stand at about 800 to 1000 m of elevation and over 1500 m of elevation, while the lithological knickpoints are at an elevation range of 1000 to 1500 m (Figures 3.5E, 3.5F). The equilibrated rivers present a straight trend in the chi space with mean values of 82.2 ($\sigma_m = 2.7$) and 0.57 ($\sigma_m = 0.03$) of k_{sn} and θ, respectively (Table S3.1, Figure 3.5F). The transient longitudinal profiles upstream of the highest knickpoints are characterized by θ and k_{sn} values ranging from 0.04 to 0.5 with an average of 0.17 ($\sigma_m = 0.07$) and 8.44 to 43.7 with an average of 22.7 ($\sigma_m = 5.1$), respectively (Table S3.1, Figure 3.5F).

Furthermore, the k_{sn} and θ values obtained with the χ method were compared with those estimated with the logS-logA method (Tables S3.1 and S3.2 in the supporting information). k_{sn} values lie mostly on the 1:1 trend (Figure S3.3A), while the θ values show a higher dispersion (Figure S3.3B in the supporting information). The entire dataset of knickpoints also present a correlation between the drainage area and the distance from the drainage divide in agreement with the scaling relationship of the Hack’s law (Figure S3.4A). The elevation and distance from the mouth show a positive correlation with the drainage area of catchments (Figures S3.4B and S3.4C).

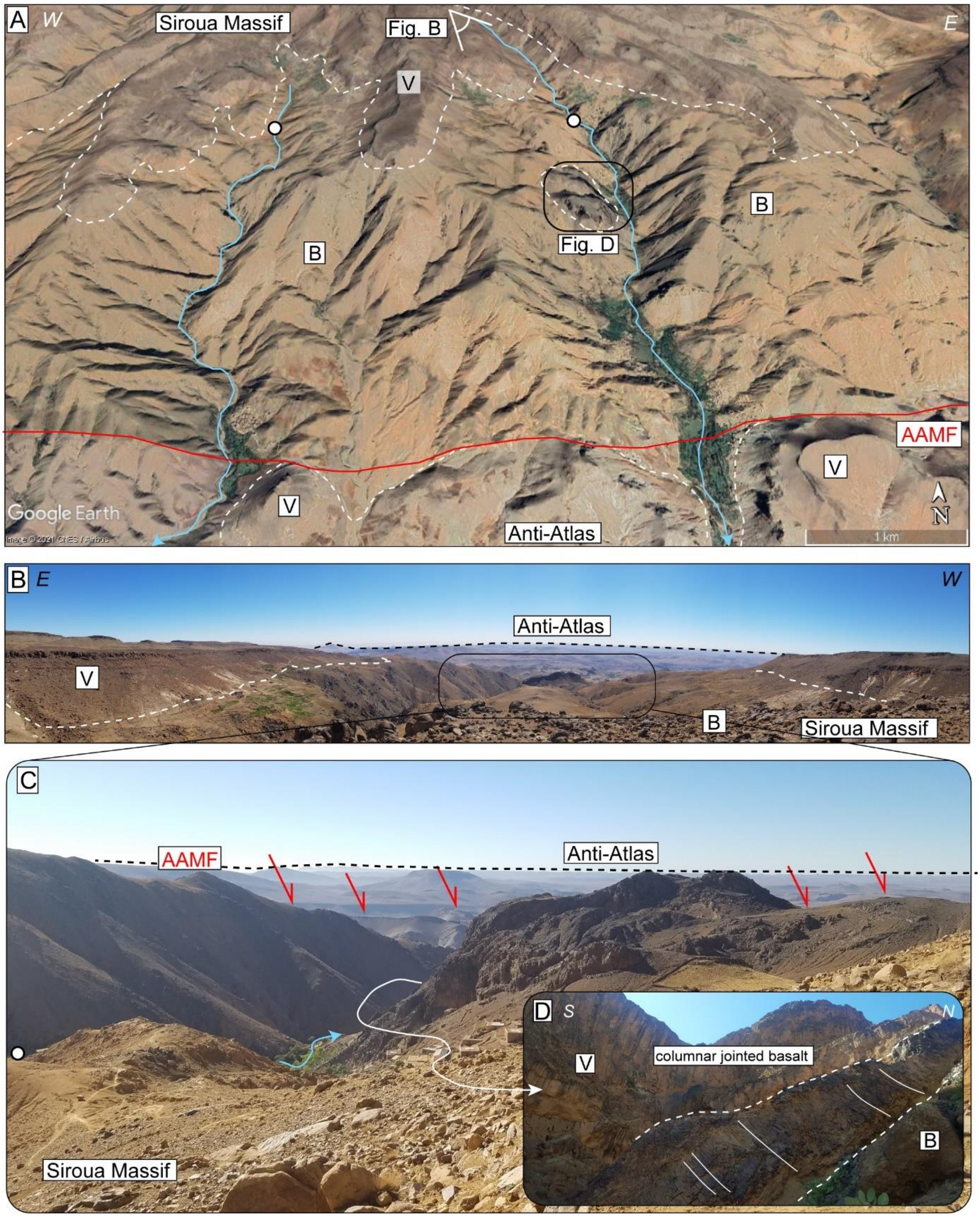

Figure 3.6. (A) Prospective Google Earth view of the southern flank of the Siroua Massif. Note the volcanic edifice composed of lava flows demarked by the dashed white line (see V

symbol) resting unconformably over the Precambrian basement (see B symbol), the north-dipping Anti-Atlas Major Fault (AAMF), the non-lithological knickpoints shown with a white dot, the deep incisions and the remanence of the lava flows downstream of the non-lithological knickpoints. (B) Panoramic view from the Siroua Massif showing in the background the summit erosional surface (i.e., relict landscape) of the Anti-Atlas (see dashed black line) and in the foreground the contact between the basement (B) and the lava flows (V). (C) Detail of figure B showing the basalt flow preserved in the deeply incised valley of figure A. (D) Field picture of the basalt of figure C with high angle columnar joint (white lines) perpendicular to the valley bottom (dashed white lines).

3.5.3. Magnitude of fluvial incision

The presence of transient stream profiles allows quantifying the total magnitude of fluvial incision (*e.g.*, Schildgen et al., 2012; Miller et al., 2013). Here incision represents the incision into a specific surface which may be undergoing continued erosion itself. Therefore, incision may not represent total erosion but the difference between the erosion across the low-relief landscape and that within the incising part of the landscape. Similar estimates can be obtained by reconstructing the paleo-topography from the entire drainage network by means of the linear inversion approach proposed by Fox (2019).

3.5.3.1. River projection

The magnitude of fluvial incision is represented by the difference between the reconstructed river profiles projected from the relict landscape (*i.e.*, upstream of the highest non-lithological knickpoints) and the channel elevation at the modern base level assuming that the modern level is representative of the paleo-base level (Figure 3.7 and Table S3.3).

The Souss and Draa outlets represent the present-day base level for the NCAA and SCAA rivers, respectively, whereas the WAA rivers flow directly into the Atlantic Ocean. To a first approximation we can consider that all rivers of the Anti-Atlas drained toward the Atlantic before the relative base level fall that initialized the most elevated non-lithological knickpoints (Figure 3.5), because the opening of the South Atlantic Ocean occurred in the early Cretaceous (Torsviket al., 2009) and hence earlier than any Cenozoic topographic growth of the Atlas System. Estimated values of fluvial incision for the NCAA based on 10 stream profiles range from 822 ($2\sigma = 36$) to 1162 m ($2\sigma = 18$), with an average of 930 m ($\sigma_m = 40$) (Figure 3.7 and Table S3.3). In the WAA sectors, 7 transient profiles yielded fluvial incision values ranging from 459 ($2\sigma = 9$) to 872 m ($2\sigma = 29$), with an average of 630 m ($\sigma_m = 50$) (Figure 3.7 and Table S3.3). Finally, in the SCAA where most of the rivers are in equilibrium, the fluvial incision based on 6 stream profiles ranges from 811 ($2\sigma = 117$) to 1117 m ($2\sigma = 18$), with an average of 1000 m ($\sigma_m = 50$) (Figure 3.7 and Table S3.3).

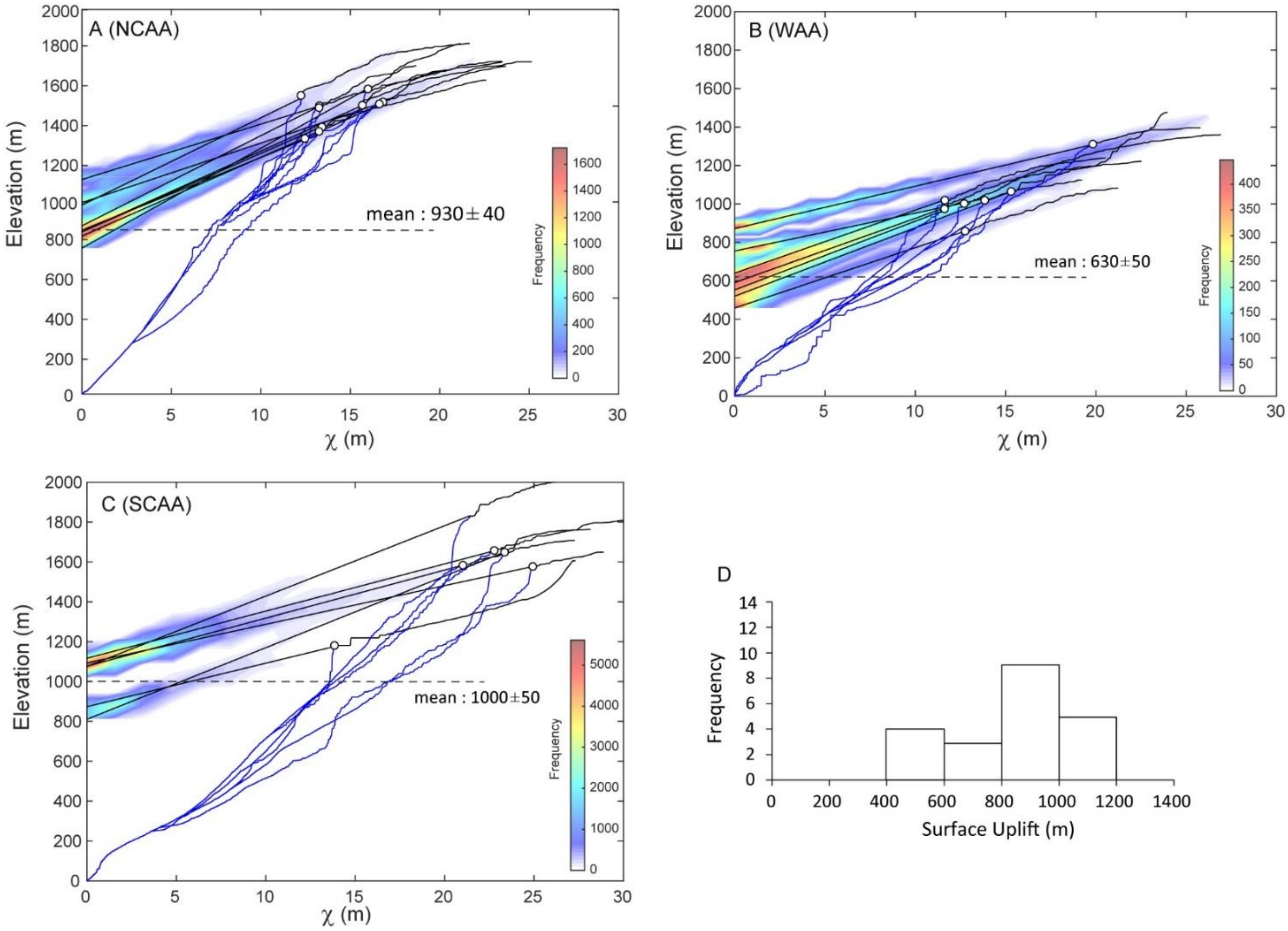

Figure 3.7. Modern longitudinal profiles and projections of the relict landscape (red segments) upstream of the highest knickpoints using $\theta_{ref} = 0.45$ and the k_{sn} of the relict portion for the (A) NCAA, (B) WAA, and (C) SCAA sectors. Major knickpoints are marked with white circles. (D) Frequency diagrams of the magnitude of surface uplift for the different sectors.

Furthermore, this approach allows estimating the first-order paleo-topographic relief as the difference between the modern mean drainage divide elevation and the elevation of the outlet of the reconstructed river profiles. Our results indicate a mean elevation difference of 970, 890 and 750 m for the NCAA, SCAA and WAA sectors, respectively (Table S3.3 in the supporting information).

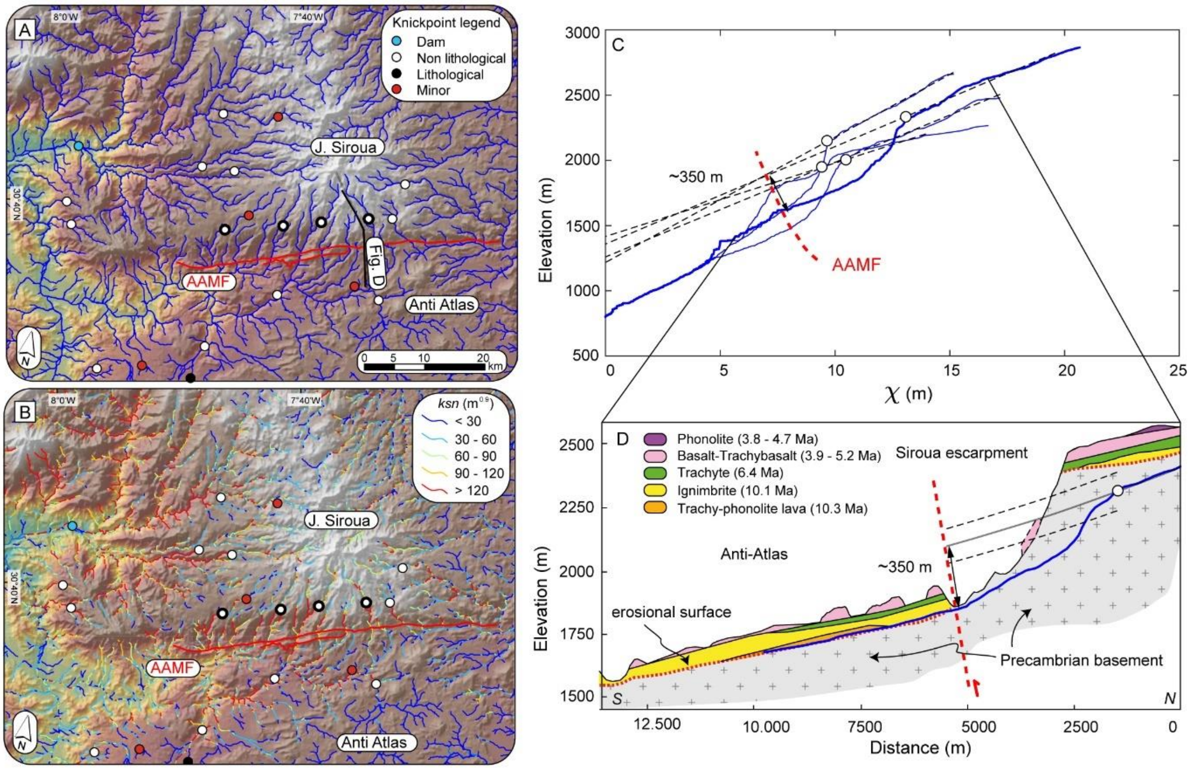

Figure 3.8. (A)Topographic map (SRTM DEM database) of study area with the main knickpoints. Bold blue rivers and associated knickpoints (thick black circles) are projected in figure 3.8C. (B) k_{sn} map of the stream network in the Siroua area. Location of the maps is shown in figure 3.3A. (C) Modern longitudinal profiles and projections from the Siroua relict landscape (dashed black segments) upstream of the highest knickpoints using θ_{ref} = 0.45 and the k_{sn} of the relict portion. Note, the reconstructed river projections intersect each other between 5 and 10 of χ. (D) Geological profile of the Siroua escarpment (after De Beer et al., 2000). The minimum value of incision is 350 m.

In the Siroua Massif, rivers are characterized by strong disequilibrium profiles with high-standing non-lithological knickpoints lying at the margin of a low-topographic relief area and delimiting streams with high k_{sn} from those with low k_{sn} values, in the downstream and upstream portion of the fluvial channel, respectively (Figures 3.6A, 3.8A, 3.8B). The magnitude of fluvial incision along the Siroua escarpment was obtained by projecting the upstream portions of the rivers up to the AAMF and is ~350 m (Figures 3.8C, 3.8D). This value represents only the amount of incision between the Siroua Massif and the central sector of AA.

Overall, the distribution of the highest knickpoints and of the estimated values of fluvial incision indicate a progressive increase in the magnitude from the WAA to the central sector of AA with a culmination in the Siroua Massif (Figure 3.9B). This is also associated with a regional increase in k_{sn} values downstream of the major knickpoints (red dots in figure

3.9A). Conversely, k_{sn} values upstream of the major non-lithological knickpoints are characterized by limited variability within the entire study area (blue dots in figure 3.9A).

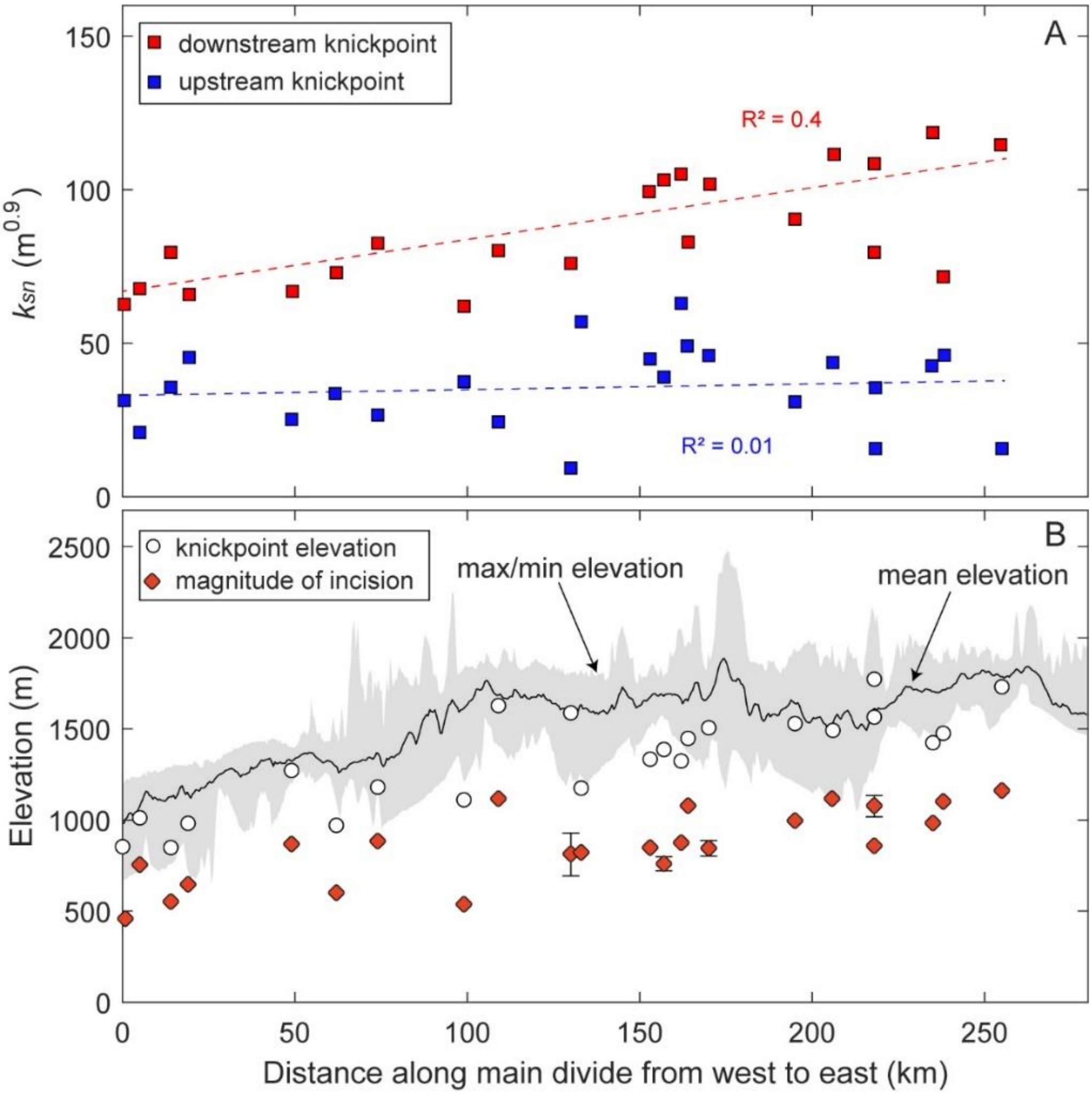

Figure 3.9. (A) Distance along the main drainage divide versus k_{sn} down and upstream of the non-lithological knickpoints. (B) Distance along the main drainage divide versus knickpoint elevation and estimated surface uplift values. The location of the swath profile is indicated in figure 3.2D.

3.5.3.2. Linear inverse method

The linear inverse method allows estimating the paleo-base level and the distribution of rock uplift rates, u^* proportional to k_{sn}, as a function of the elevations and the χ values from the relict river network (in the portion of landscape demarks by white polygon in figure 3.10D). Due to the increased spatial variability provided by this approach, multiple solutions which pass through the χ and elevation data are expected, and results are non-unique. Damping forces smooth maps and provides a means to choose a preferred result.

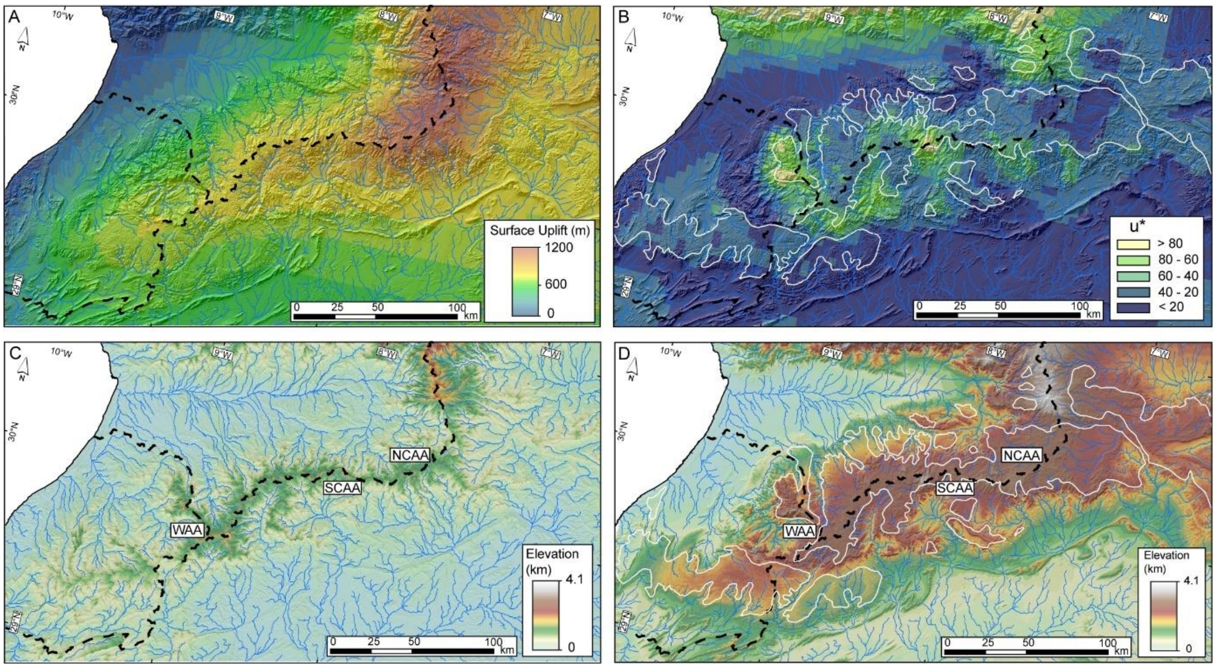

Figure 3.10. (A) Surface uplift (*S.U.*) map. (B) Normalized rock uplift rate (u^* or k_{sn}, using $\theta_{ref} = 0.45$) map relative to the high-standing relict landscape (white polygons). The base level is defined at the relict landscape boundary; values of $m = 0.45$ and $A_0 = 1$ m^2 were used to calculate χ and u^*. (C) Paleo-topographic reconstruction of the Anti-Atlas. (D) Present-day topography of Anti-Atlas.

Here damping parameters are chosen to ensure that results are consistent with the estimates obtained from projecting the information preserved in the upper reaches of the transient river profiles. Results suggest an incision associated with a base level fall in the order of ~1200 m in the Siroua Massif, that decreases gradually to ~500 m in the WAA (Figure 3.10A). The u^* values in the upstream relict landscape at the maximum elevation are rather uniform with major variations coinciding with the highest mountain peaks composed mostly of quartzites (Figure 3.10B). Conversely, lower u^* values occur in the central sector of AA and correlate with granite lithologies (Figure 3.10B), as discussed in Chapter 2. Finally, the reconstructed paleo-topography indicates a maximum elevation of ~1000 and ~500 m in the central sector of AA and the WAA, respectively before the onset of uplift (Figure 3.10C). Overall, these results are consistent with those obtained from the river projections but with increase spatial resolution (Figures 3.10A, 3.10C).

Finally, it should be noted that the fitting surface through the relict topography above the incised landscape is less constrained in the Souss and, Draa basins and in the Siroua Massif.

In the two basins, the aggradation/deposition process recorded by Plio-Quaternary sedimentary sequences (Hssaine and Bridgland, 2009) is not take into consideration. Moreover, the maximum elevation obtained for the Siroua Massif represents a maximum estimate because the construction of the volcanic edifice may be coeval or younger than the timing of the fluvial incision, as testified by preserved lava flows along the Siroua escarpment (Figures 3.6D and 3.8D).

3.5.4. Timescales of knickpoint migration

The time that the highest non-lithological knickpoints of the Ant-Atlas Mountains took to travel from the base level to their present-day position is in the same range of time required to erode the volume of rocks in a catchment between the high-standing preserved landscape and minimum topography (*e.g.*, Gallen et al., 2013; Siame et al., 2015). This is called "excavation time" and is generally calculated assuming that erosion took place at constant rates, which can be derived from ^{10}Be concentrations of river sand or other methods. Denudation rates derived from ^{10}Be concentrations for the Anti-Atlas, however, are representative mainly for the relict landscape, as discussed in Chapter 2. This because the sampled catchments are not representative for the portions of landscape downstream of non-lithological knickpoints, which are mostly composed of carbonate rocks. Hence, denudation rates of 5.8 to 12.5 m/My (Table S3.4) provide a maximum age for the onset of relief production in the Anti-Atlas (8.8 to 18.6 Myr in Table S3.4). Conversely, the highest value of denudation rate (21.3 m/Myr in Table S3.4) from the Anti-Atlas flank provides a minimum age ~3.8 Myr (Table S3.4).

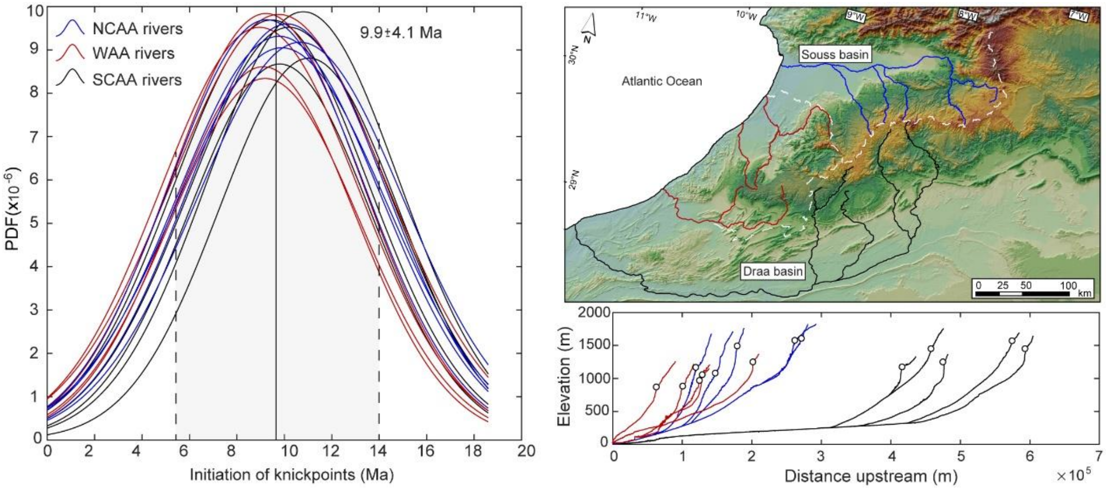

Figure 3.11. Initiation time of knickpoints propagation in the north, western and southern Anti-Atlas sectors (NCAA, WAA, SCAA). For further information see the table S3.5 in the supplementary materials.

To constrain the erodibility parameter (*K*), we used the basin-wide k_{sn} and denudation rates assuming a linear function for the stream power river incision model ($n \approx 1$). This assumption is justified by the relationships between topographic metrics and normalized channel steepness for tectonically stable regions, as discussed in Chapter 2. We considered the present-day river outlets to model the initiation point of the knickpoint propagation. We calculated the basin-averaged k_{sn}, assuming θ_{ref} ranging from 0.45 and 0.17 (Figure S3.5 in the supporting information). These θ reference values for the Anti-Atlas relict landscape represent a realistic range of values to constrain the erodibility *(K)* in the study area. In particular, most of the values in the relict landscape (upstream knickpoints) are lower than 0.45 (Tables S3.1 and S3.2 in the supporting information) and hence we decided to use a reference value of 0.45 to be more conservative. Conversely, 0.17 represents the mean of the concavity estimates for the river sectors of the relict landscape (*i.e.*, upstream the non-lithological knickpoints; Table S3.1). The results and misfits of the modelled knickpoints show that the onset of propagation of the base level fall is at 9.9 ± 4.3, 9.2 ± 4.1 and 10.4 ± 4.0 Myr for NCAA, WAA and SCAA sectors, respectively (averaged value 9.9 ± 4.1 Myr; Figure 3.11 and Table S3.5). The Siroua Massif also shows a pattern of knickpoints at the edge of the relict landscape (Figure 3.8A). Here, the volcanic deposits exposed in the Siroua plateau are also preserved along the steep valleys in the Siroua escarpment (Figures 3.6C, 3.6D, 3.8D) and consists of ~4-My-old columnar jointed basalts (Berrahma et al., 1995; De Beer et al., 2000). The volcanic flows at the valley bottom provide evidence for the minimum time of knickpoints migration from the AAMF.

3.6. Discussion

Our analyses pointed out that the Anti-Atlas (AA) topography is characterized by a high-standing relict surface demarked by non-lithological knickpoints. Similar features have been observed in a large variety of settings, from infracratonic regions to plate margins, and in many tectonically inactive (*e.g.*, French Massif, Appalachians) and active mountain ranges (*e.g.*, High Atlas, Andes, Himalaya; Calvet et al., 2015 and reference therein). In slowly eroding landscapes like the AA (e.g., Gouiza et al., 2017; Lanari et al., 2020a, Charton et al., 2021; Chapter 2), the low relief topography can be preserved easily due to the lower rates of rock uplift and denudation. In the following, we discuss the significance of the transient state of the Anti-Atlas topography, the magnitude, timing and rates of surface uplift, and finally we highlight the implications of our results in terms of mechanisms that may have caused such a topographic rejuvenation.

3.6.1. Significance of the transient topography

The strong variation in the normalized channel steepness indices, concavity values, topographic slope, elevation, and fluvial incision between the portions of the landscape downstream and upstream of the highest non-lithological knickpoints (Figures 3.3 and 3.5) combined with the occurrence of low and uniform erosion rates averaged over different time scales (from late Cretaceous to Quaternary; Chapter 2) document a transient condition of the AA topography. This transient state could be attributed to several processes, such as drainage reorganization, climate change, eustatic sea level fall and tectonic uplift (Hancock and Kirwan, 2007; Kirby and Whipple, 2012; Miller et al., 2013, Ballato et al., 2015). Drainage reorganization does not appear to be the cause because there is limited evidence of knickpoints, and wind gaps formation related to river capture processes (Miller et al., 2013). An increase in erosion rates due to climate variations (*i.e.*, increase in precipitation rates) is also unlikely, because such a change is expected to produce a decrease in the channel slopes rather than a steepening (Figure 3.5; Molnar et al., 2004; Wobus et al., 2010) . The abrupt break in the river longitudinal profiles and χ–z plots at the highest non-lithological knickpoints and the position of the same knickpoints in the χ space (Figures 3.5B, 3.5D, 3.5F, 3.8A and S3.2) indicate that the two portions of the landscape upstream and downstream of these knickpoints erode at different rates (Schildgen et al., 2012; Miller et al., 2012; 2013; Olivetti et al., 2016). This is consistent with an increase in erosion and rock uplift rates propagating from the river outlet to the uppermost river segments (Miller et al., 2013; Gallen and Wegmann, 2017; Racano et al., 2021). Consequently, the highest knickpoints represent a response of the fluvial system to an increase in rock uplift rates and hence mark a phase of topographic rejuvenation, while the uplifted relict landscape records the previous erosional conditions predating such an increase. This implies that the magnitudes of fluvial incision documented through the river projection approach and the topographic linear inverse modelling represent minimum estimates of the total amount of surface uplift (*e.g.,* Kirby and Whipple, 2012). A similar scenario has been described in the Appalachian Mountains (Miller et al., 2013) and in other ancient orogens (Olivetti et al., 2012; Scharf et al., 2013; Mandal et al., 2015; Calvet et al., 2015).

Conversely, the minor and non-lithological knickpoints located in the lower segments of the fluvial network, at 700 to 1000 m and from 400 to 500 m in the NCAA, SCAA, and WAA sectors, respectively, can be attributed to a Quaternary climate forcing (Molnar and England, 1990; Hancock and Kirwan, 2007). This pattern of knickpoints is spatially consistent and does not show any channel steepness variation across the knickpoints in both the longitudinal profiles and the χ–z plot (Figures 3.5B, 3.5D, 3.5F and S3.2).

3.6.2. Topographic evolution and surface uplift history of Anti-Atlas

A peculiarity of the Anti-Atlas topography is the occurrence of a low-relief topography at its maximum elevation plunging along the mountain flanks to the NNE and the SSE with a wavelength of ~ 100 km (*i.e.*, across strike; Figures 3.2B, 3.2C and 3.13A). This is associated with a large wavelength topographic swell of ~ 600 km plunging to the WSW and the ENE (*i.e.*, along-strike; Figures 3.2E and 3.13A). It follows, that the high-standing surface forming the relict landscape represents a warped geomorphic marker that can be used to document the spatial distribution of the recent increase in surface uplift, but also the morphological characteristics of the paleo-landscape predating it. This landscape must have been characterized by a low-topographic relief with localized ~1000- to 700-m-high mountain peaks in the central Anti-Atlas (NCAA, SCAA) and the WAA, respectively (Figure 3.10C and Table S3.3).

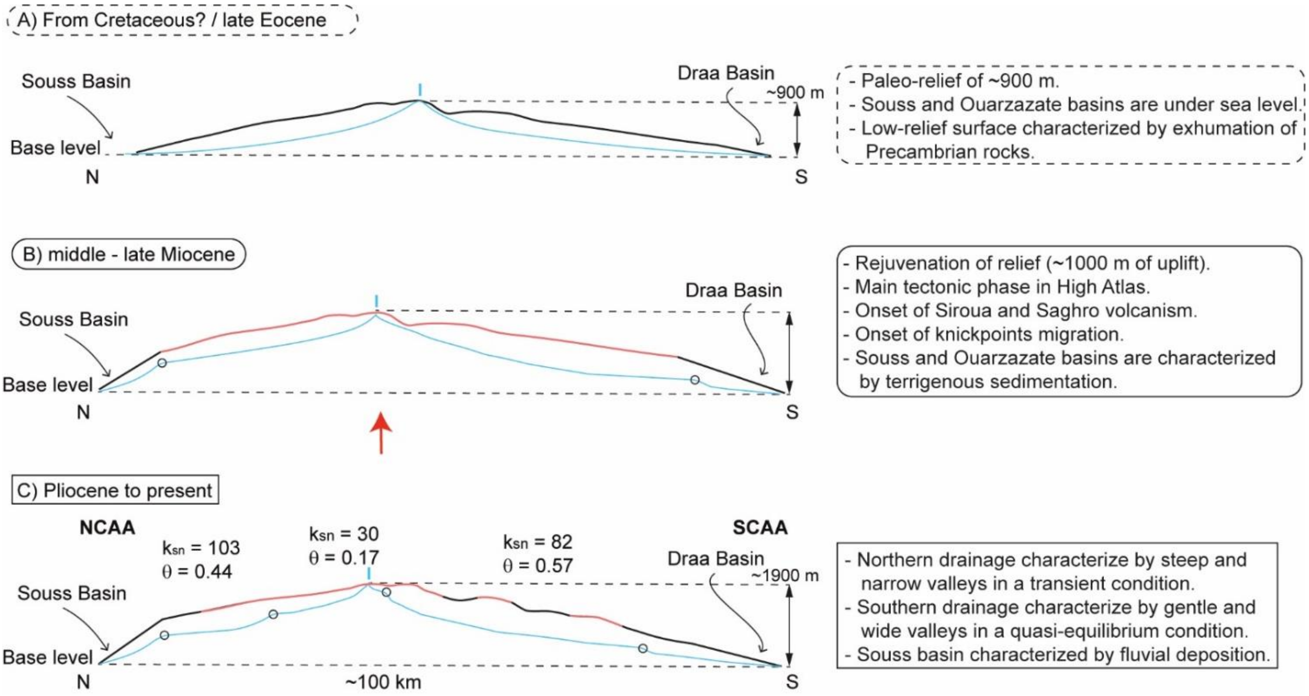

Figure 3.12. Conceptual model depicting the Anti-Atlas topographic evolution across the central Anti-Atlas. (A) Paleo-topography inferred until the late Eocene. (B) Topographic rejuvenation during the middle-late Miocene associated with the initiation of river incision and knickpoints upstream propagation. (C) Present-day configuration. Pink area describes the preserved relict landscape not yet rejuvenated.

These paleo-topographic heights correlate with high normalized channel steepness values observed in the low erodibility values, such as quartzite (Figure 3.10B; Chapter 2). The along strike pattern of uplift is further documented by variations in k_{sn} values downstream of the highest knickpoints, the elevation of the highest knickpoints, and the estimates of surface uplift inferred from the projected transient stream profiles ranging from ~500 to 1100 m from the western to the central sector of AA (Figure 3.9).

The presence of cooling ages older than 70 Ma, the low magnitude of exhumation (~1.5 km) over the same time interval suggest that the paleo-topography of the relict landscape has been developing since at least the late Cretaceous (Figure 3.12A; Gouiza et al., 2017; Lanari et al., 2020a; Charton et al., 2021; Chapter 2), as also testified by lack of sediments younger than the Cretaceous within the axial topographic zone Furthermore, the Ouarzazate and the Souss basins recorded marine sedimentation at least until the late Eocene, suggesting that part of the study area must have been under sea level until 44 - 42 Ma (Figure 3.12A; El Harfi et al., 2001; Teson et al., 2010; Hssaine and Bridgland, 2009). However,, no Meso-Cenozoic stratigraphic record is observed on the relict landscape, suggesting protracted subaerial conditions for the AA. Subsequently, the regional phase of surface uplift should have started with the initiation of the headward migration of the highest knickpoints. According to our celerity model calculations, this could have occurred in the middle-late Miocene (9.9 ± 4.1 Ma; Figures 3.11 and 3.12B). This agrees with the onset of volcanic activity in the Siroua Massif with more than 500 km^2 of crystalline basement covered by lava flows between 11 and 3 Ma (Figure 3.12B; Berrahma and Delaoye, 1989; Missenard et al., 2008). Moreover, this is consistent with the onset of clastic continental sedimentation in the Ouarzazate Basin from the Langhian to the Tortonian/Messinian after an Oligocene to early Miocene hiatus (El Harfi et al., 2001; Teson et al., 2010). Finally, the estimated time of topographic rejuvenation is also consistent with the onset of contractional deformation in the HA Mountains (Figure 3.12B; Lanari et al., 2020a). Overall, our new time constraints suggest average uplift rates ranging from 40 to 110 m/Myr (western sector) and from 70 to 180 m/My (central sector), gradually increase along strike from the western to the central sector of AA. These rates are based on the celerity model (9.9 ± 4.1 Ma) and averaged over time scales of 14 and 5.8 Ma, using the mean uplift values (Table S3.3). A maximum rate of 200 m/Myr could be reached close to the Siroua Massif, where the maximum amplitude of the topographic swell is observed (Fig. 3.13). Similar magnitudes of surface uplift have also been estimated from the uplifted Messinian shallow marine deposits located in a poor deformed sector of the Middle Atlas Mountains (170 – 220 m/Myr, Babault et al., 2008).

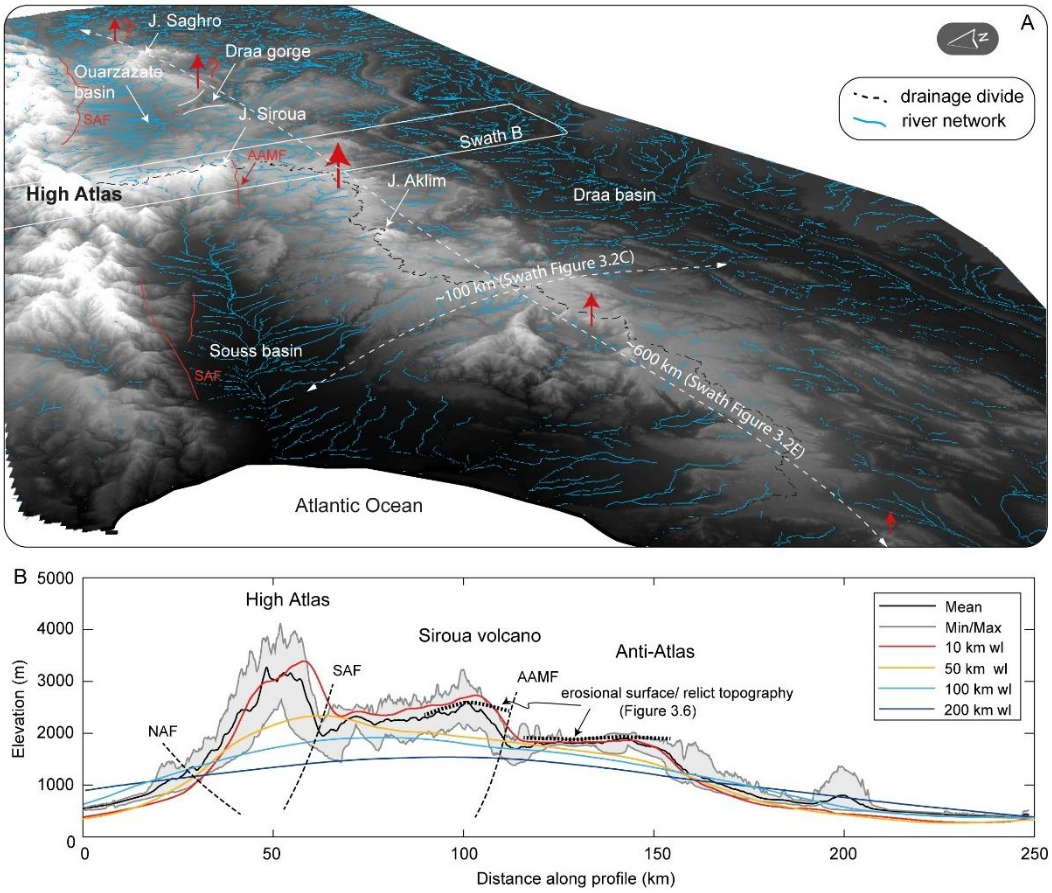

Figure 3.13. (A) Tridimensional view of the Anti-Atlas region. **(**B) Swath profile from north to south, showing the local relief and maximum elevation of High Atlas, Siroua Massif and Anti-Atlas. Note that the erosional surface of the Siroua Massif and the Anti-Atlas is standing at more than 2000 m and predated the onset of uplift in the Anti-Atlas and Siroua regions.

The asymmetry of the AA flanks and the different locations of the highest knickpoints between the southern (SCAA) and northern flanks (NCAA) can be attributed to a faster knickpoints migration in the SCAA sector, as also suggested by the occurrence of quasi-equilibrium stream profiles (Figures 3.5E, 3.5F). Here, the presence of wide synclines sculptured onto a more erodible Paleozoic substrate may have promoted an increase in the contributing drainage area and a faster knickpoint retreat (Figures 3.4B and S3.4B, S3.4C; Crosby and Whippe, 2006; Berlin and Anderson, 2007; Schwanghart and Scherler, 2020). Conversely, in the northern flank, the knickpoint' celerity is lower due to narrower and deeper valleys combined with less erodible late Precambrian carbonates (Figures 3.4A and 3.12C). This highlights the key role of rock strength plays in controlling the valley morphology, and in turn the location of genetically linked knickpoints (*e.g.*, Stokes et al., 2015). Importantly, for the NCAA and SCAA rivers, the migrating wave of transient erosion propagated for several kilometres within the Souss and Draa basins. These regions were likely characterized by erosional processes, before the onset of regional uplift (*e.g.*, Hssaine and Bridgland, 2009). This, allow to dismiss a complex scenario with different erodibility parameters within the Neogene-Quaternary sediments in the basins. However, this would not represent an issue because the knickpoint would travel quickly in the mainstream of the Souss and Draa rivers due to the large drainage areas. The knickpoints propagation rate would have decreased one reached the upstream portions of the main mountain front (Crosby and Whipple, 2006; Schwanghart and Scherler, 2020). Hence, the time of residence in the Draa and Souss basins would be negligible. Finally, it should be noted that the occurrence of recent fluvial conglomerates, at high elevation in the major valleys of the northern flank (~700 m) and in the Souss alluvial plain, has been interpreted as an indication that uplift has decreased during the Quaternary (Lanari et al., 2022).

3.6.3. Topographic evolution and surface uplift history of Siroua Massif

The Siroua Massif is also characterized by a transient topography as documented by the high-standing basement representing the substratum of the Mio-Pliocene volcanic edifice (Figure 3.8; Missenard et al., 2008). Along the southern margin of the massif, this transient topography is delimited by a pattern of non-lithological knickpoints lying over 2000 m of elevation that on map view are subparallel to the AAMF and cluster along similar χ values (Figure 3.8C). The projection of the stream profiles against the AAMF documents about 350 m of surface uplift in the hanging wall of the fault in response to fault activity (Figures 3.6A, 3.8C, 3.8D and 3.13B). This configuration suggests that the summit erosional surface of the AA must be the same surface that lies underneath the Siroua volcanic edifice that has been uplifted by the AAMF (Figures 3.8D and 3.13B). These conclusions are also consistent with the occurrence of the same volcanic units at different elevations, in the hanging wall and the footwall of the AAMF. Some of these lava flows are also exposed along the steep landscape of the hanging wall of the AAMF downstream of the non-lithological knickpoints. There, they present columnar jointed basalts orthogonal to the valley bottom, suggesting that the valley must have been a reference cooling surface at ~ 4 Ma when the lava was emplaced (Figure 3.6D). Consequently, the transient fluvial incision associated with the activity of the AAMF must have started earlier than 4 Ma.

These data allow estimating the contribution of the different mechanisms that produced the modern elevation of ~ 3300 m. Specifically the initial landscape could have been ~ 1000 m of elevation, like the AA (see previous section), while the occurrence of basement rocks beneath the volcano at ~ 2500 m of elevation indicates that volcanic edifice contribute for ~ 800 m high. By subtracting to the modern elevation, 1000 (paleo-topography) and 800 m (volcanic building), we can estimate a surface uplift for the Siroua Massif of ~ 1500 m, where at least 350 meters result from the activity of the AAMF. A fraction of this ~ 350 m, however, may be associated with the injection of magma at depth as suggested by the dome-like geometry (~ 50 x 100 km) of the metamorphic basement beneath the Siroua volcano (Missenard et al., 2008). In conclusion, if we exclude the ~ 350 m described above, the regional surface uplift in the Siroua Massif will be ~1150 m in agreement with estimates from the central sectors of the Anti-Atlas.

3.6.4. Causes of surface uplift and topographic expression of the Anti-Atlas and Siroua Massif

The intracontinental orographic system of the Atlas Mountains represents a natural laboratory for studying the interaction between deep-seated, crustal, and surface processes. The amount of tectonic (crustal) shortening and thickening is limited and in the order of 12 to 35% in the central HA (Beauchamp et al., 1999; Gomez et al., 2000; Teixell et al., 2003; Domènech et al., 2016; Fekkak et al., 2018; Lanari et al., 2020b) and less than 10% in the MA (Gomez et al., 1998; Arboleya et al., 2004). Geophysical evidences, such as heat flow (Rimi et al., 1999; Teixell et al., 2005; Zeyen et al., 2005), gravity anomalies (Ayarza et al., 2005; Missenard et al., 2006), seismological constraints (Seber et al., 1996; Palomeras et al., 2013; Bezada et al., 2013; Miller and Becker, 2014; Spieker et al., 2014) and seismic reflection data (Ayarza et al., 2014) point toward an insufficient thickness of the crust to explain the observed high topography and the anomalously thin lithosphere (~65 km). Geological and geomorphological constraints are consistent with these observations suggesting a contribution of deep-seated processes to the recent regional uplift (Babault et al., 2008; Benabdellouahed et al., 2017; Chapter 2). Moreover, the intraplate volcanism of the AA (Siroua and Saghro Massif) and MA is coeval with the main phase of regional uplift inferred in this study for the AA and from thermochronological data in the HA, indicating the occurrence of magmatism during mountain building processes (Berrahma & Delaloye, 1989; El Azzouzi et al., 1999; 2010).

The Atlas system displays short wavelength (10 – 50 km) topographic signals most likely linked to processes operating at crustal scale such as shortening and thickening (Teixell et al., 2003; Missenard et al., 2006; Faccenna and Becker, 2020) and long wavelength (> 100 km) signals associated with deeper processes (Figure 3.13B). Examples of the former and the latter include the HA Mountains and the Meseta, respectively, although multiple processes may concur to produce the observed topographic signal (Teixell et al., 2003; Lanari et al., 2020a). Our study documents that the AA Mountains presents a topography with a regional uplift signal that has an along- and across-strike wavelength of ~ 600 and 100 km, respectively and a maximum amplitude of ~1100 m (Figures 3.9B, 3.10A and 3.13). This is well underlined by the high-standing surface, which is warped along these two major directions (Figure 3.13A). The maximum values of surface uplift are observed in the central sector of the AA and appear to be slightly lower than those extracted from the adjacent Siroua Massif where surface uplift results from the sum of a long wavelength, regional uplift, and multiple crustal-scale signals such as faulting along the AAMF and possibly local magma injection. The occurrence of magma intrusions may be testified by the occurrence of a localized topographic bulge on the somital erosional surface of the Siroua that stands beneath the volcano. This would explain the short-wavelength topographic signal observed in figure 3.13B (Missenard et al., 2008). Similar geomorphic expressions have been described in different settings where magma injection at variable depth in the crust generated a few hundred meters of uplift over different timescale (Singer et al., 2018; Townsend, 2022). This process could have also occurred in the Saghro mountain peak of the eastern Anti-Atlas where a localized maximum topography associated with a few volcanic eruptions is observed (Figure 3.2E). In any case surface uplift rates for the central Anti-Atlas and the Siroua Massif are similar to the long-term rates inferred from uplifted, Messinian marine deposits exposed in the MA (Babault et al., 2008).

The long wavelength topographic swell (600 x 100 km) of the AA, however, needs still to be explained (Figure 3.13A). Tectonic uplift associated with displacement along a 600-km-long (along strike) crustal scale ramp appears to be unlikely because the AA domain has probably been tectonically quiescent throughout the entire Cenozoic (Frizon de Lamotte et al., 2009; Lanari et al., 2020a; Chapter 2), and because we did not observe any indications of recent faulting along the northern or southern mountain fronts. Furthermore, to explain the ~100-km-long across strike wavelength, one would need a fault-bend-fold mechanisms with a deep flat rooted into the basement, a ramp, and a shallower flat accommodating at least 100 km of horizontal displacement. This appears to be quite unlikely, especially if one considers that the AA is a Variscan orogen and not an undisturbed sedimentary multi-layer that may have been detached along weaker stratigraphic horizons. Furthermore, there are no evaporite layers in the pre Variscan sedimentary sequence that could accommodate such an amount of displacement, as observed in the adjacent HA (Lanari et al., 2020b). These observations suggest that the ~ 600 x 100 km topographic swell could be explained only through deeper processes associated with mantle activity. A possible mechanism that has already been invoked as a main contributor in the construction of orogenic plateaus is the delamination of the lithospheric mantle and possibly of the lower crust (*e.g.*, Garzione et al., 2006; Hatzfeld and Molnar, 2010). This would change the density structure of lithosphere through the sinking of a relatively dense lithospheric mantle and the rise of a hotter and less dense asthenosphere. This hypothesis requires the occurrence of a previously thickened lithosphere, which does not appear to be the case for the AA where crustal shortening and thickening processes following the Variscan orogeny have been very limited (Burkhard et al., 2006). Moreover, the occurrence of a thickened lithosphere would have produced a large-scale subsidence with associated marine sedimentation before the onset of uplift, and this is not supported by stratigraphic data, which suggest subaerial erosional conditions at least since the late Cretaceous (Gouiza et al., 2017; Chapter 2). In intracontinental areas, another possible mechanism is the upwelling of asthenospheric mantle (Duggen et al., 2009; Faccenna et al., 2013; Miller et al., 2013; Olivetti et al., 2016; Faccenna and Becker, 2020). Independently from the geodynamic setting and the main reasons for such a rise, the upward movement of hot asthenospheric mantle generates a deflection of the lithosphere in association with adiabatic melting and production of a magma with an alkaline signature (*e.g.*,Wilson and Downes, 1991; Gibson et al., 2006). This process will generate a strong positive free air anomaly (Faccenna and Becker, 2020). This appears to be the case for the AA, where all observations are met (Berrahma and Delaloye, 1989; Spieker et al., 2014). Moreover, the wavelength recorded in the topography of the AA is compatible with other examples from the oceanic floor, where larger-scale swell signals have also been observed (Cserepes et al., 2000). Tomography analysis also suggest mantle upwelling in NW Africa, which may be associated with plume activity recorded in the Atlantic Ocean in the Canary Islands (Duggen et al., 2009; Civiero et al., 2019). In conclusion, our topographic analysis allows attributing the topography of the Anti-Atlas to asthenospheric upwelling processes although the cause of these deep-seated mechanism remains still poorly understood.

3.7. Conclusion

Our study allows characterizing modern and past topography of the Anti-Atlas Mountains and inferring its surface uplift history. In particular, we show that:

1) The landscape is in a transient state and exhibits a main pattern of elevated non-lithological knickpoints that mark a regional transition, from high to low values of topographic and channel metrics. The topography upstream of the non-lithological knickpoints can be described as an erosional surface (relict landscape) that plunges along and across strike. Our paleo-topographic reconstruction suggests that such an erosional surface formed a subdued topography with a few local peaks in the order of ~ 1000 m of elevation that started to develop from the late Cretaceous.

2) The magnitude of surface uplift increases along-strike from the western Anti-Atlas (500 m) to the central Anti-Atlas (1100 m) and the Siroua Massif (1500 m), where the latter represents a main Mio-Pliocene regional volcanic centre. Geometrically, the surface uplift can be described as ~ 600 x 100 km swell. The initiation of knickpoints migration marks the onset of topographic rejuvenation and is estimated to be middle-late Miocene (9.9 ± 4.1 Ma). This is coeval with the initiation of a main tectonic phase in the High Atlas and with volcanism in the Siroua and the Saghro Massifs. Surface uplift occurred at rates of 40 to 110 m/Myr and 70 to 180 m/My, with maximum values of 200 m/Myr, (averaged over time scales of 14 and 5.8 Ma) gradually increase from the western to the central Anti-Atlas, respectively. Our estimates fall within the same range of values inferred from Messinian shallow marine deposits of the Middle Atlas.

3) Surface uplift in Siroua Massif is higher than the Anti-Atlas because results from the contribution of different signals, such as the long-wavelength regional component (i.e., the topographic swell; ~ 1150 m), the growth of a volcanic edifice (~ 800 m), faulting along the Anti-Atlas Major Fault (~ 350 m) and magma injection processes which cannot be easily quantified but may be included in the contribution ascribed to faulting.

4) The long wavelength (~ 600 x 100 km) topographic swell documented through the topographic analysis can be explained by upwelling of hot asthenosphere, which is also responsible for the generation of magmatism in the Siroua and Saghro area. Although the genesis of such a rise is unknown, it appears to be the only feasible mechanisms.

In conclusion, our data provide new constrains for deciphering the complex history of mountain belts, which topographic growth results from the interplay between shallow and deep-seated processes.

3.8. Acknowledgments

This study is part of the PhD thesis of RC at the University of Roma Tre (PhD Cycle XXXIV). It was supported by the PhD School of Roma Tre and grant “Vinci 2020” awarded to RC (Number: C2-1403). PB was supported by the MIUR (Ministry of Education University and Research), Excellence Department Initiative, Art. 1, com. 314-337, Low 232/2016. The ASTER (CEREGE, Aix-en-Provence) AMS national facility, is supported by the INSU/CNRS, and the IRD.

3.9. References

Ait Malek, H. A., Gasquet, D., Bertrand, J. M., & Leterrier, J. (1998). Géochronologie U-Pb sur zircon de granitoïdes éburnéens et panafricains dans les boutonnières protérozoïques d'Igherm, du Kerdous et du Bas Drâa (Anti-Atlas occidental, Maroc). *Comptes Rendus de l'Académie des Sciences-Series IIA-Earth and Planetary Science*, *327*(12), 819-826. https://doi.org/10.1016/S1251-8050(99)80056-1

Arboleya, M. L., Teixell, A., Charroud, M., & Julivert, M. (2004). A structural transect through the High and Middle Atlas of Morocco. *Journal of African Earth Sciences*, 39(3‐5), 319‐327. https://doi.org/10.1016/j.jafrearsci.2004.07.036

Arboleya, M. ‐ L., Babault, J., Owen, L. A., Teixell, A., & Finkel, R. C. (2008). Timing and nature of Quaternary fluvial incision in the Ouarzazate foreland basin, Morocco. *Journal of the Geological Society*, 165(6), 1059‐1073. https://doi.org/10.1144/0016 ‐ 76492007 ‐ 151

Ayarza, P., Alvarez-Lobato, F., Teixell, A., Arboleya, M. L., Teson, E., Julivert, M., & Charroud, M. (2005). Crustal structure under the central High Atlas Mountains (Morocco) from geological and gravity data. *Tectonophysics*, *400*(1-4), 67-84. https://doi.org/10.1016/j.tecto.2005.02.009

Azizi Samir, M. R., Ferrandini, J., & Tane, J. L. (1990). Tectonique et volcanisme tardi-Pan Africains (580-560 Ma) dans l'Anti-Atlas Central (Maroc): interprétation géodynamique à l'échelle du NW de l'Afrique. *Journal of African Earth Sciences*, *10*(3), 549-563. https://doi.org/10.1016/0899-5362(90)90105-N

Babault, J., Teixell, A., Arboleya, M. L., & Charroud, M. (2008). A Late Cenozoic age for long-wavelength surface uplift of the Atlas Mountains of Morocco. *Terra nova*, *20*(2), 102-107. https://doi.org/10.1111/j.1365-3121.2008.00794.x

Baldwin, J. A., Whipple, K. X., & Tucker, G. E. (2003). Implications of the shear stress river incision model for the timescale of postorogenic decay of topography. *Journal of Geophysical Research: Solid Earth*, 108(B3). https://doi.org/10.1029/2001JB000550.

Balestrieri, M. L., Moratti, G., Bigazzi, G., & Algouti, A. (2009). Neogene exhumation of the Marrakech High Atlas (Morocco) recorded by apatite fission ‐ track analysis. Terra Nova, 21(2), 75‐82. https://doi.org/10.1111/j.1365 ‐ 3121.2008.00857.x

Ballato, P., Landgraf, A., Schildgen, T. F., Stockli, D. F., Fox, M., Ghassemi, M. R., Kirby, E., & Strecker, M. R. (2015). The growth of a mountain belt forced by base-level fall: Tectonics and surface processes during the evolution of the Alborz Mountains, N Iran. *Earth and Planetary Science Letters*, *425*, 204-218. https://doi.org/10.1016/j.epsl.2015.05.051

Barbero, L., Teixell, A., Arboleya, M. L., del Río, P., Reiners, P. W., & Bougadir, B. (2007). Jurassic ‐ to ‐ present thermal history of the central High Atlas (Morocco) assessed by low ‐ temperature thermochronology. *Terra Nova*, 19(1), 58‐64. https://doi.org/10.1111/j.1365 ‐ 3121.2006.00715.x

Baudon, C., Fabuel ‐ Perez, I., & Redfern, J. (2009). Structural style and evolution of a Late Triassic rift basin in the central High Atlas, Morocco: Controls on sediment deposition. *Geological Journal*, 44(6), 677‐691. https://doi.org/10.1002/gj.1195

Beauchamp, W., Allmendinger, R. W., Barazangi, M., Demnati, A., El Alji, M., & Dahmani, M. (1999). Inversion tectonics and the evolution of the High Atlas Mountains, Morocco, based on a geological‐geophysical transect. *Tectonics*, 18(2), 163‐184. https://doi.org/10.1029/1998TC900015

Benabdellouahed, M., Klingelhoefer, F., Gutscher, M. A., Rabineau, M., Biari, Y., Hafid, M., ... & Sahabi, M. (2017). Recent uplift of the Atlantic Atlas (offshore West Morocco): Tectonic arch and submarine terraces. *Tectonophysics*, *706*, 46-58. https://doi.org/10.1016/j.tecto.2017.03.024

Berlin, M. M., & Anderson, R. S. (2007). Modeling of knickpoint retreat on the Roan Plateau, western Colorado. *Journal of Geophysical Research: Earth Surface*, *112*(F3). https://doi.org/10.1029/2006JF000553

Berrahma, M., & Delaloye, M. (1989). Données géochronologiques nouvelles sur le massif volcanique du Siroua (Anti-Atlas, Maroc). *Journal of African Earth Sciences (and the Middle East)*, 9(3-4), 651-656.https://doi.org/10.1016/0899-5362(89)90049-3.

Berrahma, M. (1995). Etudes pétrologiques des laves récentes du massif du Siroua (Anti-Atlas, Maroc). Éd. du Service Géologique du Maroc.

Bezada, M. J., Humphreys, E. D., Davila, J. M., Carbonell, R., Harnafi, M., Palomeras, I., & Levander, A. (2014). Piecewise delamination of Moroccan lithosphere from beneath the Atlas Mountains. *Geochemistry, Geophysics, Geosystems*, *15*(4), 975-985. https://doi.org/10.1002/2013GC005059

Burkhard, M., Caritg, S., Helg, U., Robert-Charrue, C., & Soulaimani, A. (2006). Tectonics of the anti-Atlas of Morocco. *Comptes Rendus Geoscience*, *338*(1-2), 11-24. https://doi.org/10.1016/j.crte.2005.11.012.

Calvet, M., Gunnell, Y., & Farines, B. (2015). Flat-topped mountain ranges: Their global distribution and value for understanding the evolution of mountain topography. *Geomorphology*, *241*, 255-291. https://doi.org/10.1016/j.geomorph.2015.04.015

Charton, R., Bertotti, G., Arnould, A. D., Storms, J. E., & Redfern, J. (2021). Low-temperature thermochronology as a control on vertical movements for semi-quantitative source-to-sink analysis: A case study for the Permian to Neogene of Morocco and surroundings. *Basin Research*, *33*(2), 1337-1383. https://doi.org/10.1111/bre.12517

Choubert, G. (1952). Histoire géologique du domaine de l’Anti-Atlas. *Notes et Mém. Serv. Géol. Maroc*, (100), 77-172.

Civiero, C., Custódio, S., Rawlinson, N., Strak, V., Silveira, G., Arroucau, P., & Corela, C. (2019). Thermal nature of mantle upwellings below the Ibero-western Maghreb region inferred from teleseismic tomography. *Journal of Geophysical Research: Solid Earth*, *124*(2), 1781-1801. https://doi.org/10.1029/2018JB016531

Clark, M. K., Schoenbohm, L. M., Royden, L. H., Whipple, K. X., Burchfiel, B. C., Zhang, X., ... & Chen, L. (2004). Surface uplift, tectonics, and erosion of eastern Tibet from large-scale drainage patterns. *Tectonics*, 23(1). https://doi.org/10.1029/2002TC001402

Crosby, B. T., & Whipple, K. X. (2006). Knickpoint initiation and distribution within fluvial networks: 236 waterfalls in the Waipaoa River, North Island, New Zealand. *Geomorphology*, *82*(1-2), 16-38. https://doi.org/10.1016/j.geomorph.2005.08.023

Cserepes, L., Christensen, U. R., & Ribe, N. M. (2000). Geoid height versus topography for a plume model of the Hawaiian swell. *Earth and Planetary Science Letters*, *178*(1-2), 29-38. https://doi.org/10.1016/S0012-821X(00)00065-0

De Beer, C. H., Chevallier, L. P., De Kock, G. S., Gresse, P. G., & Thomas, R. J. (2000). Mémoire explicatif de la carte géologique du Maroc au 1/50 000, Feuille Sirwa. *Notes Mem. Serv. Geol. Maroc*, *395*, 86.

DeCelles, P. G., Ducea, M. N., Kapp, P., & Zandt, G. (2009). Cyclicity in Cordilleran orogenic systems. *Nature Geoscience*, *2*(4), 251-257. https://doi.org/10.1038/ngeo469

DiBiase, R. A., & Whipple, K. X. (2011). The influence of erosion thresholds and runoff variability on the relationships among topography, climate, and erosion rate. *Journal of Geophysical Research: Earth Surface*, *116*(F4). http://dx.doi.org/10.1029/2011JF002095.

Doblas, M., López-Ruiz, J., Cebriá, J. M., Youbi, N., & Degroote, E. (2002). Mantle insulation beneath the West African craton during the Precambrian-Cambrian transition. *Geology*, *30*(9), 839-842.

Domènech, M., Teixell, A., Babault, J., & Arboleya, M. L. (2015). The inverted Triassic rift of the Marrakech High Atlas: A reappraisal of basin geometries and faulting histories. *Tectonophysics*, 663, 177‐191. https://doi.org/10.1016/j.tecto.2015.03.017

Domènech, M., Teixell, A., & Stockli, D. F. (2016). Magnitude of rift ‐ related burial and orogenic contraction in the Marrakech High Atlas revealed by zircon (U ‐ Th)/He thermochronology and thermal modeling. *Tectonics*, 35(11), 2609‐2635. https://doi.org/10.1002/2016TC004283

Duggen, S., Hoernle, K. A., Hauff, F., Kluegel, A., Bouabdellah, M., & Thirlwall, M. F. (2009). Flow of Canary mantle plume material through a subcontinental lithospheric corridor beneath Africa to the Mediterranean. *Geology*, *37*(3), 283-286. https://doi.org/10.1130/G25426A.1

Duvall, A., Kirby, E., & Burbank, D. (2004). Tectonic and lithologic controls on bedrock channel profiles and processes in coastal California. *Journal of Geophysical Research: Earth Surface*, 109(F3). https://doi.org/10.1029/2003JF000086

El Azzouzi, M., Bellon, H., Maury, R. C., Pique, A., Cotten, J., Griffiths, J. B., ... & Hernandez, J. (1999). Evolution of the sources of Moroccan volcanism during the Neogene. *Comptes Rendus de l'Academie des Sciences. Serie 2, Sciences de la Terre et des Planetes*, 95-102.

El Azzouzi, M. H., Maury, R. C., Bellon, H., Youbi, N., Cotten, J., & Kharbouch, F. (2010). Petrology and K-Ar chronology of the Neogene-quaternary Middle Atlas basaltic province, Morocco. *Bulletin de la société géologique de France*, *181*(3), 243-257. https://doi.org/10.2113/gssgfbull.181.3.243

El Harfi, A., Lang, J., Salomon, J., & Chellai, E. H. (2001). Cenozoic sedimentary dynamics of the ouarzazate foreland basin (Central High Atlas Mountains, Morocco). *International Journal of Earth Sciences*, 90, 393‐411. https://doi.org/10.1007/s005310000115

England, P., & Molnar, P. (1990). Surface uplift, uplift of rocks, and exhumation of rocks. *Geology*, *18*(12), 1173-1177. https://doi.org/10.1130/0091-7613(1990)018<1173:SUUORA>2.3.CO;2

Faccenna, C., Becker, T. W., Conrad, C. P., & Husson, L. (2013). Mountain building and mantle dynamics. *Tectonics*, *32*(1), 80-93. https://doi.org/10.1029/2012TC003176

Faccenna, C., & Becker, T. W. (2020). Topographic expressions of mantle dynamics in the Mediterranean. *Earth-Science Reviews*, 103327. https://doi.org/10.1016/j.earscirev.2020.103327

Fekkak, A., Ouanaimi, H., Michard, A., Soulaimani, A., Ettachfini, E. M., Berrada, I., et al. (2018). Thick ‐ skinned tectonics in a Late Cretaceous ‐ Neogene intracontinental belt (High Atlas Mountains, Morocco): The flat ‐ ramp fault control on basement shortening and cover folding. Journal of African Earth Sciences, 140, 169‐188. https://doi.org/10.1016/j.jafrearsci.2018.01.008

Flint, J. J. (1974). Stream gradient as a function of order, magnitude, and discharge. *Water Resources Research*, 10, 969‐973.

Forte, A. M., & Whipple, K. X. (2019). Short communication: The Topographic Analysis Kit (TAK) for TopoToolbox, *Earth Surface Dynamics*. 7, 87–95. https://doi.org/10.5194/esurf-7-87-2019.

Fox, M. (2019). A linear inverse method to reconstruct paleo-topography. *Geomorphology*, *337*, 151-164. https://doi.org/10.1016/j.geomorph.2019.03.034

Fox, M., & Carter, A. (2020). How continuous are the “Relict” landscapes of Southeastern Tibet?. *Frontiers in Earth Science*, *8*(587597). https://doi.org/10.3389/feart.2020.587597

Fraissinet, C., El Zouine, M., Morel, J. L., Poisson, A., Andrieux, J., & Faure-Muret, A. (1988). Structural evolution of the southern and northern central High Atlas in Paleogene and Mio-Pliocene times. In *The Atlas System of Morocco* (pp. 273-291). Springer, Berlin, Heidelberg.

Frizon de Lamotte, D., Saint Bezar, B., Bracène, R., & Mercier, E. (2000). The two main steps of the Atlas building and geodynamics of the western Mediterranean. *Tectonics*, 19, 740‐761. https://doi.org/10.1029/2000TC900003

Frizon de Lamotte, D., Leturmy, P., Missenard, Y., Khomsi, S., Ruiz, G., Saddiqi, O., Guillocheau F., & Michard A. (2009). Mesozoic and Cenozoic vertical movements in the Atlas system

(Algeria, Morocco, Tunisia). An overview: *Tectonophysics*. 475, 9-28. https://doi.org/10.1016/j.tecto.2008.10.024.

Froitzheim, N., Stets, J., & Wurster, P. (1988). Aspects of western High Atlas tectonics. *In The Atlas System of Morocco*, (pp. 219-244). Berlin: Springer.

Gallen, S. F., Wegmann, K. W., & Bohnenstiehl, D. R. (2013). Miocene rejuvenation of topographic relief in the southern Appalachians. *GSA Today*, *23*(2), 4-10. https://doi.org/10.1130/GSATG163A.1.

Gallen, S. F., & Wegmann, K. W. (2017). River profile response to normal fault growth and linkage: An example from the Hellenic forearc of south-central Crete, Greece. *Earth Surface Dynamics*, *5*(1), 161-186. https://doi.org/10.5194/esurf-5-161-2017

Gallen, S. F. (2018). Lithologic controls on landscape dynamics and aquatic species evolution in post-orogenic mountains. *Earth and Planetary Science Letters*, *493*, 150-160. https://doi.org/10.1016/j.epsl.2018.04.029.

Garzione, C. N., Molnar, P., Libarkin, J. C., & MacFadden, B. J. (2006). Rapid late Miocene rise of the Bolivian Altiplano: Evidence for removal of mantle lithosphere. *Earth and Planetary Science Letters*, *241*(3-4), 543-556. https://doi.org/10.1016/j.epsl.2005.11.026

Gasquet, D., Ennih, N., Liégeois, J. P., Soulaimani, A., & Michard, A. (2008). The pan-african belt. In *Continental evolution: the geology of Morocco* (pp. 33-64). Springer, Berlin, Heidelberg. https://doi.org/10.1007/978-3-540-77076-3_2

Ghorbal, B., Bertotti, G., Foeken, J., & Andriessen, P. (2008). Unexpected Jurassic to Neogene vertical movements in ‘stable’parts of NW Africa revealed by low temperature geochronology. *Terra Nova*, *20*(5), 355-363. https://doi.org/10.1111/j.1365-3121.2008.00828.x

Gibson, S. A., Thompson, R. N., & Day, J. A. (2006). Timescales and mechanisms of plume–lithosphere interactions: 40Ar/39Ar geochronology and geochemistry of alkaline igneous rocks from the Paraná–Etendeka large igneous province. *Earth and Planetary Science Letters*, *251*(1-2), 1-17. https://doi.org/10.1016/j.epsl.2006.08.004

Gomez, F., Allmendinger, R., Barazangi, M., Er-Raji, A., & Dahmani, M. (1998). Crustal shortening and vertical strain partitioning in the Middle Atlas Mountains of Morocco. *Tectonics*, *17*(4), 520-533. https://doi.org/10.1029/98TC01439

Gomez, F., Beauchamp, W., & Barazangi, M. (2000). Role of the Atlas Mountains (northwest Africa) within the African - Eurasian plate-boundary zone. *Geology*, 28(9), 775-778. https://doi.org/10.1130/0091-7613(2000)28<775:ROTAMN>2.0.CO;2

Görler, K., Helmdach, F. - F., Gaemers, P., Heißig, K., Hinsch, W., Mädler, K., et al. (1988). The uplift of the central High Atlas as deduced from Neogene continental sediments of the Ouarzazate province, Morocco. In *The Atlas System of Morocco*, (pp. 359-404). Berlin: Springer. https://doi.org/10.1007/s00531-016-1325-0

Gouiza, M., Charton, R., Bertotti, G., Andriessen, P., & Storms, J. E. A. (2017). Post-Variscan evolution of the Anti-Atlas belt of Morocco constrained from low-temperature geochronology. *International Journal of Earth Sciences*, *106*(2), 593-616.

Guimerà, J., Arboleya, M. L., & Teixell, A. (2011). Structural control on present-day topography of a basement massif: the Central and Eastern Anti-Atlas (Morocco). *Geologica Acta: an international earth science journal*, *9*(1), 55-65. https://doi.org/10.1344/105.00 0001643.

Hack, J. T. (1957). *Studies of longitudinal stream profiles in Virginia and Maryland* (Vol. 294). US Government Printing Office.

Hafid, M. (2000). Triassic - early Liassic extensional systems and their Tertiary inversion, Essaouira Basin (Morocco). *Marine and Petroleum Geology*, 17, 409-429. https://doi.org/10.1016/S0264 - 8172(98)00081 - 6

Hancock, G., & Kirwan, M. (2007). Summit erosion rates deduced from 10Be: Implications for relief production in the central Appalachians. *Geology*, *35*(1), 89-92. https://doi.org/10.1130/G23147A.1

Harkins, N., Kirby, E., Heimsath, A., Robinson, R., & Reiser, U. (2007). Transient fluvial incision in the headwaters of the Yellow River, northeastern Tibet, China. *Journal of Geophysical Research: Earth Surface*, *112*(F3). https://doi.org/10.1029/2006JF000570

Hatzfeld, D., & Molnar, P. (2010). Comparisons of the kinematics and deep structures of the Zagros and Himalaya and of the Iranian and Tibetan plateaus and geodynamic implications. *Reviews of Geophysics*, *48*(2). https://doi.org/10.1029/2009RG000304

Hefferan, K. P., Admou, H., Karson, J. A., & Saquaque, A. (2000). Anti-atlas (Morocco) role in neoproterozoic western Gondwana reconstruction. *Precambrian Research*, 103(1-2), 89-96. https://doi.org/10.1016/S0301-9268(00)00078-4

Heidarzadeh, G., Ballato, P., Hassanzadeh, J., Ghassemi, M. R., & Strecker, M. R. (2017). Lake overspill and onset of fluvial incision in the Iranian Plateau: Insights from the Mianeh Basin. *Earth and Planetary Science Letters*, 469, 135-147. https://doi.org/10.1016/j.epsl.2017.04.019

Helg, U., Burkhard, M., Caritg, S., & Robert-Charrue, C. (2004). Folding and inversion tectonics in the anti-Atlas of Morocco. *Tectonics*, *23*(4). https://doi.org/10.1029/2003TC001576

Hollard, H., Choubert, G., Bronner, G., Marchand, J., Sougy, J. (1985). Carte géologique du Maroc, scale 1: 1,000,000. *Serv. Carte géol. Maroc*. 260(2).

Howard, A. D., & Kerby, G. (1983). Channel changes in badlands. *Geological Society of America Bulletin*, *94*(6), 739-752. http://dx.doi.org/10.1130/0016-7606(1983)94<739:CCIB>2.0.CO;2.

Howard, A. D. (1994). A detachment-limited model of drainage basin evolution. *Water resources research*, *30*(7), 2261-2285. https://doi.org/10.1029/94WR00757

Hssaine, A. A., & Bridgland, D. (2009). Pliocene–Quaternary fluvial and aeolian records in the Souss Basin, southwest Morocco: A geomorphological model. *Global and Planetary Change*, 68, 288–296. https://doi.org/10.1016/j.gloplacha.2009.03.002

Jansen, J. D., Codilean, A. T., Bishop, P., & Hoey, T. B. (2010). Scale dependence of lithological control on topography: Bedrock channel geometry and catchment morphometry in western Scotland. *The Journal of geology*, *118*(3), 223-246. https://doi.org/10.1086/651273.

Kirby, E., & Whipple, K. (2001). Quantifying differential rock-uplift rates via stream profile analysis. *Geology*, *29*(5), 415-418. https://doi.org/10.1130/0091-7613(2001)029<0415:QDRURV>2.0.CO;2.

Kirby, E., Whipple, K. X., Tang, W., & Chen, Z. (2003). Distribution of active rock uplift along the eastern margin of the Tibetan Plateau: Inferences from bedrock channel longitudinal profiles. *Journal of Geophysical Research: Solid Earth*, *108*(B4). https://doi.org/10.1029/2001JB000861

Kirby, E., & Whipple, K. X. (2012). Expression of active tectonics in erosional landscapes. *Journal of Structural Geology*, *44*, 54-75. https://doi.org/10.1016/j.jsg.2012.07.009.

Korup, O. (2006). Effects of large deep-seated landslides on hillslope morphology, western Southern Alps, New Zealand. Journal of Geophysical Research: Earth Surface, 111(F1). https://doi.org/10.1029/2004JF000242

Lanari, R., Fellin, M. G., Faccenna, C., Balestrieri, M. L., Pazzaglia, F. J., Youbi, N., & Maden, C. (2020a). Exhumation and surface evolution of the western high atlas and surrounding regions as constrained by low-temperature thermochronology. *Tectonics*, *39*(3), e2019TC005562. https://doi.org/10.1029/2019TC005562

Lanari, R., Faccenna, C., Fellin, M. G., Essaifi, A., Nahid, A., Medina, F., & Youbi, N. (2020b). Tectonic evolution of the western high Atlas of Morocco: oblique convergence, reactivation, and transpression. *Tectonics*, *39*(3), e2019TC005563. https://doi.org/10.1029/2019TC005563

Leblanc, M. (1975). Ophiolites précambriennes et gites arseniés de cobalt: Bou Azzer (Maroc). *These Doctorat d'Etat, Faculte des Science Paris VI, Memoires Centre Geologique et Geophysique*.

Leprêtre, R., Missenard, Y., Barbarand, J., Gautheron, C., Jouvie, I., & Saddiqi, O. (2018). Polyphased inversions of an intracontinental rift: Case study of the Marrakech High Atlas, Morocco. *Tectonics*, 37(3), 818–841. https://doi.org/10.1002/2017TC004693

Ma, Z., Zhang, H., Wang, Y., Tao, Y., & Li, X. (2020). Inversion of Dadu River bedrock channels for the late cenozoic uplift history of the eastern Tibetan Plateau. *Geophysical Research Letters*, *47*(4), e2019GL086882. https://doi.org/10.1029/2019GL086882

Malusa, M. G., Polino, R., Feroni, A. C., Ellero, A., Ottria, G., Baidder, L., & Musumeci, G. (2007). Post-Variscan tectonics in eastern anti-atlas (Morocco). *Terra Nova*, *19*(6), 481-489. https://doi.org/10.1111/j.1365-3121.2007.00775.x

Mandal, S. K., Lupker, M., Burg, J. P., Valla, P. G., Haghipour, N., & Christl, M. (2015). Spatial variability of 10Be-derived erosion rates across the southern Peninsular Indian escarpment: A key to landscape evolution across passive margins. *Earth and Planetary Science Letters*, *425*, 154-167. https://doi.org/10.1016/j.epsl.2015.05.050.

Miller, S. R., Baldwin, S. L., & Fitzgerald, P. G. (2012). Transient fluvial incision and active surface uplift in the Woodlark Rift of eastern Papua New Guinea. *Lithosphere*, *4*(2), 131-149. https://doi.org/10.1130/L135.1

Miller, S. R., Sak, P. B., Kirby, E., & Bierman, P. R. (2013). Neogene rejuvenation of central Appalachian topography: Evidence for differential rock uplift from stream profiles and erosion rates. *Earth and Planetary Science Letters*, *369*, 1-12. https://doi.org/10.1016/j.epsl.2013.04.007

Miller, M. S., & Becker, T. W. (2014). Reactivated lithospheric-scale discontinuities localize dynamic uplift of the Moroccan Atlas Mountains. *Geology*, *42*(1), 35-38. https://doi.org/10.1130/G34959.1.

Miller, M. S., O'Driscoll, L. J., Butcher, A. J., & Thomas, C. (2015). Imaging Canary Island hotspot material beneath the lithosphere of Morocco and southern Spain. *Earth and Planetary Science Letters*, *431*, 186-194. https://doi.org/10.1016/j.epsl.2015.09.026

Missenard, Y., Zeyen, H., Frizon de Lamotte, D., Leturmy, P., Petit, C., Sébrier, M., & Saddiqi, O. (2006). Crustal versus asthenospheric origin of relief of the Atlas Mountains of Morocco. *Journal of Geophysical Research: Solid Earth*, *111*(B3). https://doi.org/10.1029/2005JB003708

Missenard, Y., Saddiqi, O., Barbarand, J., Leturmy, P., Ruiz, G., El Haimer, F. Z., & Frizon de Lamotte, D. (2008). Cenozoic denudation in the Marrakech High Atlas, Morocco: insight from apatite fission-track thermochronology. *Terra Nova*, *20*(3), 221-228. https://doi.org/10.1111/j.1365-3121.2008.00810.x.

Missenard, Y., & Cadoux, A. (2012). Can Moroccan Atlas lithospheric thinning and volcanism be induced by Edge-Driven Convection?. *Terra Nova*, *24*(1), 27-33. https://doi.org/10.1111/j.1365-3121.2011.01033.x

Molnar, P., & England, P. (1990). Late Cenozoic uplift of mountain ranges and global climate change: chicken or egg?. *Nature*, *346*(6279), 29-34. https://doi.org/10.1038/346029a0

Molnar, P. (2004). Late Cenozoic increase in accumulation rates of terrestrial sediment: How might climate change have affected erosion rates?. *Annu. Rev. Earth Planet. Sci.*, *32*, 67-89. https://doi.org/10.1146/annurev.earth.32.091003.143456

Montgomery, D. R., & Foufoula-Georgiou, E. (1993). Channel network source representation using digital elevation models. *Water Resources Research*, *29*(12), 3925-3934. https://doi.org/10.1029/93WR02463

Mudd, S. M., Attal, M., Milodowski, D. T., Grieve, S. W., & Valters, D. A. (2014). A statistical framework to quantify spatial variation in channel gradients using the integral method of channel profile analysis. *Journal of Geophysical Research: Earth Surface*, 119(2), 138-152. https://doi.org/10.1002/2013JF002981

Norton, K. P., von Blanckenburg, F., Schlunegger, F., Schwab, M., & Kubik, P. W. (2008). Cosmogenic nuclide-based investigation of spatial erosion and hillslope channel coupling in the transient foreland of the Swiss Alps. *Geomorphology*, 95(3-4), 474-486. https://doi.org/10.1016/j.geomorph.2007.07.013

Olivetti, V., Cyr, A. J., Molin, P., Faccenna, C., & Granger, D. E. (2012). Uplift history of the Sila Massif, southern Italy, deciphered from cosmogenic 10Be erosion rates and river longitudinal profile analysis. *Tectonics*, *31*(3). https://doi.org/10.1029/2011TC003037

Olivetti, V., Godard, V., Bellier, O., & ASTER team. (2016). Cenozoic rejuvenation events of Massif Central topography (France): Insights from cosmogenic denudation rates and river profiles. *Earth and Planetary Science Letters*, *444*, 179-191. https://doi.org/10.1016/j.epsl.2016.03.049.

Palomeras, I., Thurner, S., Levander, A., Liu, K., Villaseñor, A., Carbonell, R., & Harnafi, M. (2014). Finite-frequency Rayleigh wave tomography of the western Mediterranean: Mapping its lithospheric structure. *Geochemistry, Geophysics, Geosystems*, *15*(1), 140-160. https://doi.org/10.1002/2013GC004861

Pastor, A., Babault, J., Owen, L. A., Teixell, A., & Arboleya, M. L. (2015). Extracting dynamic topography from river profiles and cosmogenic nuclide geochronology in the Middle Atlas and the High Plateaus of Morocco. *Tectonophysics*, *663*, 95-109. https://doi.org/10.1016/j.tecto.2015.06.007

Perron, J. T., & Royden, L. (2013). An integral approach to bedrock river profile analysis. *Earth Surface Processes and Landforms*, *38*(6), 570-576. https://doi.org/10.1002/esp.3302.

Pique, A., & Michard, A. (1989). Moroccan Hercynides; a synopsis; the Paleozoic sedimentary and tectonic evolution at the northern margin of West Africa. *American Journal of science*, *289*(3), 286-330. https://doi.org/10.2475/ajs.289.3.286

Piqué, A., Bouabdelli, M., Soulaimani, A., Youbi, N., & Illiani, M. (1999). Les conglomérats du PIII (Protérozoïque terminal) de l'Anti-Atlas (Sud du Maroc): Molasses tardi-Panafricaines, ou marq n rifting fini-Protérozoïque. *Comptes Rendus Académie Sciences Paris*, *328*, 409-414.

Racano, S., Schildgen, T. F., Cosentino, D., & Miller, S. R. (2021). Temporal and spatial variations in rock uplift from river-profile inversions at the Central Anatolian Plateau southern margin. *Journal of Geophysical Research: Earth Surface*, *126*(8), e2020JF006027. https://doi.org/10.1029/2020JF006027

Rimi, A. (1999). Mantle heat flow and geotherms for the main geologic domains in Morocco. *International Journal of Earth Sciences*, *88*(3), 458-466. https://doi.org/10.1007/s005310050278

Royden, L., & Taylor Perron, J. (2013). Solutions of the stream power equation and application to the evolution of river longitudinal profiles. *Journal of Geophysical Research: Earth Surface*, *118*(2), 497-518. https://doi.org/10.1002/jgrf.20031

Safran, E. B., Bierman, P. R., Aalto, R., Dunne, T., Whipple, K. X., & Caffee, M. (2005). Erosion rates driven by channel network incision in the Bolivian Andes. *Earth Surface Processes and Landforms: The Journal of the British Geomorphological Research Group*, *30*(8), 1007-1024. https://doi.org/10.1002/esp.1259.

Saquaque, A., Admou, H., Karson, J., Hefferan, K., & Reuber, I. (1989). Precambrian accretionary tectonics in the Bou Azzer-El Graara region, Anti-Atlas, Morocco. *Geology*, *17*(12), 1107-1110. https://doi.org/10.1130/0091-7613(1989)017<1107:PATITB>2.3.CO;2

Scharf, T. E., Codilean, A. T., De Wit, M., Jansen, J. D., & Kubik, P. W. (2013). Strong rocks sustain ancient postorogenic topography in southern Africa. *Geology*, *41*(3), 331-334. https://doi.org/10.1130/G33806.1.

Schildgen, T. F., Cosentino, D., Bookhagen, B., Niedermann, S., Yıldırım, C., Echtler, H., ... & Strecker, M. R. (2012). Multi-phased uplift of the southern margin of the Central Anatolian plateau, Turkey: A record of tectonic and upper mantle processes. *Earth and Planetary Science Letters*, *317*, 85-95. https://doi.org/10.1016/j.epsl.2011.12.003

Schwanghart, W., & Scherler, D. (2014). TopoToolbox 2–MATLAB-based software for topographic analysis and modeling in Earth surface sciences. *Earth Surface Dynamics*, *2*(1), 1-7. https://doi.org/10.5194/esurf-2-1-2014.

Schwanghart, W., & Scherler, D. (2020). Divide mobility controls knickpoint migration on the Roan Plateau (Colorado, USA). *Geology*, *48*(7), 698-702. https://doi.org/10.1130/G47054.1

Seber, D., Barazangi, M., Tadili, B. A., Ramdani, M., Ibenbrahim, A., & Ben Sari, D. (1996). Three-dimensional upper mantle structure beneath the intraplate Atlas and interplate Rif mountains of Morocco. *Journal of Geophysical Research: Solid Earth*, *101*(B2), 3125-3138. https://doi.org/10.1029/95JB03112

Sébrier, M., Siame, L., Zouine, E. M., Winter, T., Missenard, Y., & Leturmy, P. (2006). Active tectonics in the moroccan high atlas. *Comptes Rendus Geoscience*, *338*(1-2), 65-79. https://doi.org/10.1016/j.crte.2005.12.001.

Sebti, S., Saddiqi, O., El Haimer, F. Z., Michard, A., Ruiz, G., Bousquet, R., Baidder, L., & de Lamotte, D. F. (2009). Vertical movements at the fringe of the West African Craton: First zircon fission track datings from the Anti-Atlas Precambrian basement, Morocco. *Comptes Rendus Geoscience*, *341*(1), 71-77. https://doi.org/10.1016/j.crte.2008.11.006

Sehrt, M., Glasmacher, U. A., Stockli, D. F., Jabour, H., & Kluth, O. (2018). The southern Moroccan passive continental margin: An example of differentiated long-term landscape evolution in Gondwana. *Gondwana Research*, *53*, 129-144. https://doi.org/10.1016/j.gr.2017.03.013

Sembroni, A., Molin, P., Pazzaglia, F. J., Faccenna, C., & Abebe, B. (2016). Evolution of continental-scale drainage in response to mantle dynamics and surface processes: An example from the

Ethiopian Highlands. *Geomorphology*, 261, 12-29. https://doi.org/10.1016/j.geomorph.2016.02.022

Siame, L. L., Sébrier, M., Bellier, O., Bourlès, D., Costa, C., Ahumada, E. A., ... & Cisneros, H. (2015). Active basement uplift of Sierra Pie de Palo (Northwestern Argentina): rates and inception from10Be cosmogenic nuclide concentrations. *Tectonics*, *34*(6), 1129-1153. https://doi.org/10.1002/2014TC003771

Singer, B. S., Le Mével, H., Licciardi, J. M., Córdova, L., Tikoff, B., Garibaldi, N., ... & Feigl, K. L. (2018). Geomorphic expression of rapid Holocene silicic magma reservoir growth beneath Laguna del Maule, Chile. *Science advances*, *4*(6), eaat1513. https://doi.org/10.1126/sciadv.aat1513

Snyder, N. P., Whipple, K. X., Tucker, G. E., & Merritts, D. J. (2000). Landscape response to tectonic forcing: Digital elevation model analysis of stream profiles in the Mendocino triple junction region, northern California. *Geological Society of America Bulletin*, *112*(8), 1250-1263. https://doi.org/10.1130/0016-7606(2000)112<1250:LRTTFD>2.0.CO;2

Soulaimani, A., Bouabdelli, M., & Piqué, A. (2003). L'extension continentale au Néo-Protérozoïque supérieur-Cambrien inférieur dans l'Anti-Atlas (Maroc). *Bulletin de la Société géologique de France*. http://hdl.handle.net/2042/244

Soulaimani, A., & Burkhard, M. (2008). The Anti-Atlas chain (Morocco): the southern margin of the Variscan belt along the edge of the West African Craton. *Geological Society, London, Special Publications*, *297*(1), 433-452. https://doi.org/10.1144/SP297.20

Soulaimani, A., Michard, A., Ouanaimi, H., Baidder, L., Raddi, Y., Saddiqi, O., & Rjimati, E. C. (2014). Late Ediacaran–Cambrian structures and their reactivation during the Variscan and Alpine cycles in the Anti-Atlas (Morocco). *Journal of African Earth Sciences*, *98*, 94-112. https://doi.org/10.1016/j.jafrearsci.2014.04.025.

Spieker, K., Wölbern, I., Thomas, C., Harnafi, M., & El Moudnib, L. (2014). Crustal and upper-mantle structure beneath the western Atlas Mountains in SW Morocco derived from receiver functions. *Geophysical Journal International*, *198*(3), 1474-1485. https://doi.org/10.1093/gji/ggu216

Stäblein, G. (1988). Geomorphological aspects of the Quaternary evolution of the Ouarzazate Basin, southern Morocco. In *The Atlas System of Morocco* (pp. 433-444). Springer, Berlin, Heidelberg. DOI: https://doi.org/10.1007/BFb0011603

Stock, J. D., & Montgomery, D. R. (1999). Geologic constraints on bedrock river incision using the stream power law. *Journal of Geophysical Research: Solid Earth*, *104*(B3), 4983-4993. https://doi.org/10.1029/98JB02139.

Stock, J., & Dietrich, W. E. (2003). Valley incision by debris flows: Evidence of a topographic signature. *Water Resources Research*, *39*(4). https://doi.org/10.1029/2001WR001057

Teixell, A., Arboleya, M. L., Julivert, M., & Charroud, M. (2003). Tectonic shortening and topography in the central High Atlas (Morocco). *Tectonics*, *22*(5). https://doi.org/10.1029/2002TC001460

Teson, E., & Teixell, A. (2006). Sequence of thrusting and syntectonic sedimentation in the eastern Sub-Atlas thrust belt (Dades and Mgoun valleys, Morocco). *International Journal of Earth Sciences*, *97*(1), 103-113. https://doi.org/10.1007/s00531-006-0151-1

Tesón, E., Pueyo, E. L., Teixell, A., Barnolas, A., Agustí, J., & Furió, M. (2010). Magnetostratigraphy of the Ouarzazate Basin: Implications for the timing of deformation and mountain building in the High Atlas Mountains of Morocco. *Geodinamica Acta*, *23*(4), 151-165. https://doi.org/10.3166/ga.23.151-165

Thomas, R. J., Chevallier, L. P., Gresse, P. G., Harmer, R. E., Eglington, B. M., Armstrong, R. A., de Beer, C.H., Martini, J. E. J., Kock, G. S., Macey, P. H:, & Ingram, B. A. (2002). Precambrian evolution of the Sirwa window, Anti-Atlas orogen, Morocco. *Precambrian Research*, *118*(1-2), 1-57. https://doi.org/10.1016/S0301-9268(02)00075-X

Torsvik, T. H., Rousse, S., Labails, C., & Smethurst, M. A. (2009). A new scheme for the opening of the South Atlantic Ocean and the dissection of an Aptian salt basin. *Geophysical Journal International*, *177*(3), 1315-1333. https://doi.org/10.1111/j.1365-246X.2009.04137.x

Townsend, M. (2022). Linking surface deformation to thermal and mechanical magma chamber processes. *Earth and Planetary Science Letters*, *577*, 117272. https://doi.org/10.1016/j.epsl.2021.117272

Tucker, G. E., & van Der Beek, P. (2013). A model for post-orogenic development of a mountain range and its foreland. *Basin Research*, *25*(3), 241-259. https://doi.org/10.1111/j.1365-2117.2012.00559.x

Walsh, G. J., Aleinikoff, J. N., Benziane, F., Yazidi, A., & Armstrong, T. R. (2002). U–Pb zircon geochronology of the Paleoproterozoic Tagragra de Tata inlier and its Neoproterozoic cover, western Anti-Atlas, Morocco. *Precambrian Research*, *117*(1-2), 1-20. https://doi.org/10.1016/S0301-9268(02)00044-X

West, A. J., Fox, M., Walker, R. T., Carter, A., Harris, T., Watts, A. B., & Gantulga, B. (2013). Links between climate, erosion, uplift, and topography during intracontinental mountain building of the Hangay Dome, Mongolia. *Geochemistry, Geophysics, Geosystems*, *14*(12), 5171-5193. https://doi.org/10.1002/2013GC004859

Whipple, K. X., & Tucker, G. E. (1999). Dynamics of the stream-power river incision model: Implications for height limits of mountain ranges, landscape response timescales, and research needs. *Journal of Geophysical Research: Solid Earth*, *104*(B8), 17661-17674. https://doi.org/10.1029/1999JB900120.

Whipple, K. X., DiBiase, R. A., Ouimet, W. B., & Forte, A. M. (2017). Preservation or piracy: Diagnosing low-relief, high-elevation surface formation mechanisms. *Geology*, *45*(1), 91-94. https://doi.org/10.1130/G38490.1

Whittaker, A. C. (2012). How do landscapes record tectonics and climate?. *Lithosphere*, *4*(2), 160-164. https://doi.org/10.1130/RF.L003.1

Willett, S. D., & Brandon, M. T. (2002). On steady states in mountain belts. *Geology*, *30*(2), 175-178. https://doi.org/10.1130/0091-7613(2002)030<0175:OSSIMB>2.0.CO;2

Willett, S. D., McCoy, S. W., Perron, J. T., Goren, L., & Chen, C. Y. (2014). Dynamic reorganization of river basins. *Science*, *343*(6175). https://doi.org/10.1126/science.1248765

Wobus, C., Whipple, K. X., Kirby, E., Snyder, N., Johnson, J., Spyropolou, K., Crosby, B., & Sheehan, D. (2006). Tectonics from topography: Procedures, promise, and pitfalls. *Special papers-Geological Society of America*, *398*, 55.https://doi.org/10.1130/2006.2398(04)

Wobus, C. W., Tucker, G. E., & Anderson, R. S. (2010). Does climate change create distinctive patterns of landscape incision?. *Journal of Geophysical Research: Earth Surface*, *115*(F4). https://doi.org/10.1029/2009JF001562

Wolson, M., & Downes, H. (1991). Tertiary—Quaternary extension-related alkaline magmatism in western and central Europe. *Journal of Petrology*, *32*(4), 811-849. https://doi.org/10.1093/petrology/32.4.811

Yang, R., Willett, S. D., & Goren, L. (2015). In situ low-relief landscape formation as a result of river network disruption. *Nature*, *520*(7548), 526-529. https://doi.org/10.1038/nature14354

Zeyen, H., Ayarza, P., Fernàndez, M., & Rimi, A. (2005). Lithospheric structure under the western African-European plate boundary: A transect across the Atlas Mountains and the Gulf of Cadiz. *Tectonics*, 24(2). https://doi.org/10.1029/2004TC001639

Zhang, Z., Ramstein, G., Schuster, M., Li, C., Contoux, C., & Yan, Q. (2014). Aridification of the Sahara desert caused by Tethys Sea shrinkage during the Late Miocene. *Nature*, *513*(7518), 401-404. https://doi.org/10.1038/nature13705.

Chapter 4. Erosional dynamics and surface uplift in a rejuvenated landscape: Insights from the Western Moroccan Meseta

Authors

Romano Clementucci[1,2*], Paolo Ballato[1], Lionel L. Siame[2], Claudio Faccenna[1,3], Giacomo Torreti[1], Ahmed Yaaqoub[4], Abderrahim Essaifi[4], Laëtitia Leanni[2], Valery Guillou[2]

Affiliations:

[1] Dipartimento di Scienze, Università Roma Tre, Largo San Leonardo Murialdo 1, 00146 Rome, Italy.

[2] Aix-Marseille Univ., CNRS, IRD, INRAE, Collège de France, CEREGE, Aix-en Provence, France.

[3] GFZ-German Research Centre for Geosciences, Potsdam, Germany.

[4] Département de Géologie, FSSM, B.P. 2390, Universite´ Cadi Ayyad, Marrakech, Morocco.

*Corrisponding author : romano.clementucci@uniroma3.it

Keywords

landscape evolution, cosmogenic nuclides, transient topography, quantitative geomorphology, Atlas-Meseta system, asthenospheric upwelling

4.1. Abstract

Transient topography represents an archive for extracting information on the combined effect of tectonics, lithology and climate across different temporal and spatial scales. Specifically, the geomorphic signature of transient conditions can be used to unravel the landscape evolution and to assess perturbations in uplift rates. The Western Moroccan Meseta represents a tectonically inactive region with a maximum elevation of 1500 m, characterized by deeply incised valleys and high-standing erosional surfaces (relict landscape). In this study, we determine denudation rates of selected watersheds and bedrock outcrops from cosmogenic nuclides concentrations and perform stream profiles, regional and basin-scale geomorphic analysis. Denudation rates of sampled watersheds and bedrocks range from 15 to 40 m/Myr and from 3 to 14 m/Myr, respectively, as observed worldwide in quiescent settings. Considering the whole dataset, we observe an apparent decoupling between topographic, channel metrics and denudation rates. However, the sensitivity strongly increases when discarding the lithological heterogenous catchments, indicating a spatial variability of denudation within the transient landscape. Moreover, the Western Moroccan Meseta topography is characterized by elevated non-lithological knickpoints, that delimit the uplifted relict landscape. Estimates from these relict portions together with the occurrence of Messinian uplifted marine sediments (1200 m) allow assessing a progressive increase in the magnitude of fluvial incision. This is interpreted to represent surface uplift, that varies from 400 to 800 and 1200 m from the Western Meseta to the Tabular Middle Atlas and the Folded Middle Atlas, respectively. These uplift data agree with estimates from the Folded Middle Atlas and the High Plateaus sector (eastern Moroccan Meseta). Overall, the spatial pattern of surface uplift describes a topographic swell with a wavelength of ~350 km. Such a swell, which is also well delimited by the warped relict landscape, is interpreted to represent a large wavelength, mantle-driven process such as astenospheric upwelling that must have occurred during the last 7 Ma (i.e., supposed age of the uplifted marine deposits). This agrees with the occurrence of ~ 3.7 to 0.6 Ma alkaline volcanics exposed in proximity of the center of the swell where the crust and the lithosphere is thinner. The top of the swell coincides with the Folded Middle Atlas where an additional short wavelength components, most likely associated with crustal shortening should have contributed to the construction of the observed topography. Overall, our approach provides insights into the erosional dynamics of quiescent tectonic settings and helps unravelling the long-term evolution of a rejuvenated landscape.

4.2. Introduction

The competition between tectonics (or deeper, mantle driven causes) and surface processes modulates the growth and the decay of topography across diverse temporal and spatial scales (Molnar and England, 1990; Braun, 2010; Champagnac et al., 2014; Faccenna and Becker, 2020). Analytical solutions and numerical models suggest that topography is in steady state when tectonics and surface processes are in balance (Whipple, 2001; Willet and Brandon, 2002; Mudd, 2017). Conversely, when such a balance is not respected, the landscapes attains a transient form marking disequilibrium conditions (*e.g.*, Olivetti et al., 2016; Godard et al., 2019; Chapter 2). Transient topography has been commonly observed in both stable and tectonically active regions across different spatial scales, from single hillslopes (*e.g.*, Hurst et al., 2013; Godard et al., 2019; 2021) to mountain ranges (*e.g.*, Miller et al., 2013; 2012; Olivetti et al., 2016; Calvet et al., 2015; Mudd, 2017; Chapter 3). There, topography is in a progressive state of adjustment to variations in uplift rates and/or climatic conditions, offering the possibility to extract first-order information that are usually not available in areas in topographic steady-state. This information include erosional dynamics and associated controlling factors as well as insights into the short- and long-term landscape evolution.

Transient landscapes results from a combination of different causes including base-level falls, drainage reorganizations, climate changes and/or variations in uplift rates (Hancock and Kirwan, 2007; Kirby and Whipple, 2012; Miller et al., 2013, Ballato et al., 2015). Therefore, topographic relief may result from the superimposition of processes acting at different rates, wavelength, and amplitude. Although diverse approaches and methods have been used to cope these problematics (*e.g.*, Matmon et al., 2003; Champagnac et al., 2014; Chapter 3), the relationships between denudation (surface processes) and topographic construction are still poorly constrained (*e.g.*, Champagnac et al., 2014; Harel et al., 2016), especially in areas subjected to large-scale uplift (Miller et al., 2013; Calvet et al., 2015; Chapter 3).

The Western Moroccan Meseta is a tectonically quiescent domain of the Atlas-Meseta system that includes elevated erosional surfaces that have not been disrupted by the widespread, regional Cenozoic tectonism. This configuration represents a transient topography with steep hillslope morphologies and extensive low-gradient, relict surfaces that are adjusting, through fluvial incision, to a relative change in the base level. These preserved relict surfaces document a long phase of hillslope lowering, as also suggested by low-temperature thermochronologic data indicating slow erosion and limited exhumation from the Triassic (*e.g.*, Barbero et al., 2010). These conditions provide a natural setting for investigating the mechanisms of topographic rejuvenation and quantify the erosional dynamics. Although the whole Atlas-Meseta system is characterized by the coexistence of different uplift components, our approach allows to decipher, the processes working at large wavelength and to isolate different signals from his morpho-structural domains.

In this work, we combine denudation rates derived from cosmogenic nuclides with regional and basin-scale geomorphic analysis. Specifically, we determine bedrock outcrops and basin-wide denudation rates from river-borne sediments to gauge them with basin-averaged metrics. Moreover, we estimate the magnitude of base-level fall by projecting the upper relict channels toward the present-day river mouth to unravel the long-term uplift history of the Western Moroccan Meseta and the surrounding Middle Atlas domains. Our results show a consistent linearity between channel steepness and basin-wide denudation rates in agreement with a detachment-limited setting and highlights the transient adjustment of hillslope and channels in response to a Cenozoic increase of rock uplift rates. Finally, we quantify fluvial incisions from different domains of Atlas-Meseta system to document the characteristics of the large wavelength surface uplift, so far attributed to mantle dynamics in agreement with geophysical and volcanological constrains (*e.g.*, Duggen et al., 2009; El Azzouzi et al., 2010; Miller and Becker, 2014).

4.3. Geological setting

The Atlas-Meseta is an intracontinental orographic system of Morocco (NW Africa) with highly diversified topographic features that include mountain ranges, elevated tabular and low-topographic relief areas, and sedimentary basins (Fig. 4.1A).

The ENE-trending Anti-Atlas domain represents the southernmost morpho-structural domain of the Atlas orographic system and consists of Precambrian basement and Paleozoic sedimentary rocks that experienced a complex geologic history including the Pan-African and the Variscan orogeny (Soulaimani et al., 2003; Gasquet et al., 2008). Although, the Anti-Atlas is a tectonically inactive orogen, its topography rises up to 2 km, as the result of topographic rejuvenation induced by large-scale uplift starting from the middle-late Miocene (Missenard et al., 2006; Frizon de Lamotte et al., 2009; Guimera et al., 2011; Chapter 3).

The High Atlas is subparallel to the Anti-Atlas and represents the most tectonically active and the highest mountain range of the Atlas-Meseta system. The oldest units exposed along the axial and in the western orogenic sectors include Precambrian basement and Paleozoic sedimentary rocks that were also deformed during the Pan-African and the Variscan orogeny. These rocks were subsequently covered by Mesozoic-Cenozoic syn- to post-rift deposits that started to be uplifted in the Eocene and the Miocene (Arboleya et al., 2004; Baudon et al., 2009; Lanari et al., 2020a).

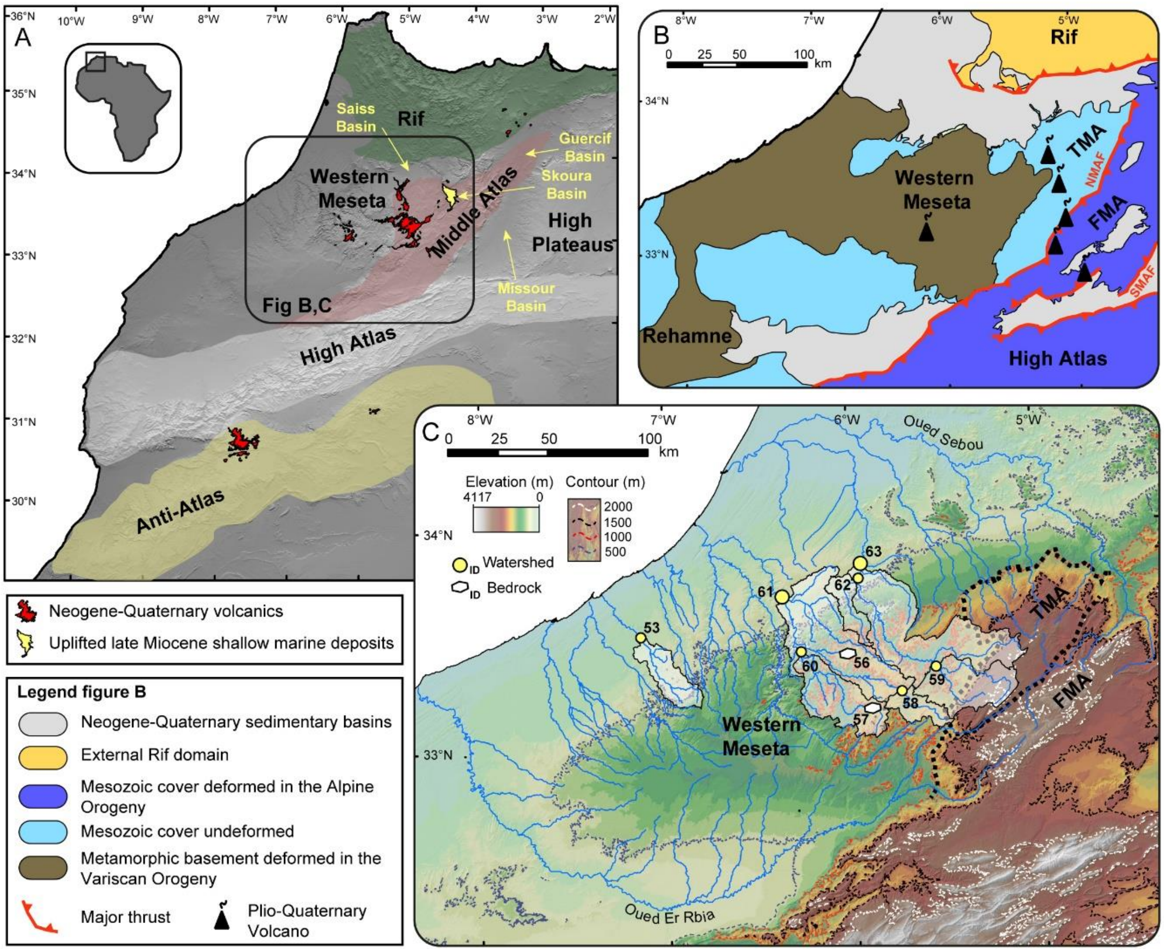

Figure 4.1. (A) Topographic hillshade of the Atlas-Meseta system and his morpho-structural domains. (B) Morpho-structural domains in the northern Morocco. FMA: Folded Middle Atlas. TMA: Tabular Middle Atlas. NMAF: North Middle Atlas fault. SMAF: South Middle Atlas fault. (C) DEM of the Western Moroccan Meseta. The white transparent areas show the sampled catchments while the dots show the location the sampling point. Note the occurrence of two major catchment and several sub-catchments. The white hexagons show the location of bedrock samples. The thick dashed line indicates the boundary between the TMA, the FMA and the Western Meseta.

The Middle Atlas belt is also composed of Meso-Cenozoic syn- to post-rift deposits that were deformed and eroded most likely from the late Miocene, although a few angular unconformities suggest a more complex history of deformation and sedimentation (Charriere, 1981). Topographically, it can be divided into two morpho-structural domains known as Tabular and Folded Middle Atlas (TMA and FMA; Fig. 4.1B), which are commonly interpreted as the flank (footwall) and the depocenter (hanging wall) of a Mesozoic rift, respectively (Gomez et al., 1996; 1998). The Folded Middle Atlas stretches NE-SW for approximately 200 km, with a width of 20 to 55 km. This domain is bounded to the northwest by the North Middle Atlas fault (NMAF) and to the southeast by the South Middle Atlas Fault (SMAF). The former is a north-east dipping steep fault, while the latter is a thrust that bounds the Missour-Guercif foreland basin (Gomez et al., 1996). The TMA domain is slightly deformed and tilted toward west. To the west and to the north, the boundary between the TMA and the Western Moroccan Meseta (WMM) is marked by a topographic escarpment that marks the stratigraphic contact between the Paleozoic basement and the undeformed Mesozoic rocks (Figs. 4.1B, 4.1C).

In this region, Quaternary alkali lava flows are commonly exposed in the TMA, the WMM (about 960 km^2), and to a lesser extent in the FMA (El Azzouzi et al., 2010). In the FMA and TMA sectors, strombolian volcanic cones are distributed along a NE-SW and E-W structural trend (Figs. 4.1A, 4.1B). The composition of these lava flows ranges from basanite to alkali basalt (Morel and Cabanis, 1993; El Azzouzi et al., 2010).

The Western and Eastern (or High Plateaus) Moroccan Meseta are elevated sectors of the Atlas-Meseta topographic system that haven’t experienced Cenozoic tectonic deformation. The High Plateaus is a ENE-WSW oriented, tabular region, composed of sub-horizontal Jurassic to Cretaceous carbonate rocks that stretches for more than 600 km over a width of ~200 km. The Western Moroccan Meseta is also oriented ENE-WSW and is separated from the High Plateaus by the Middle Atlas. It is characterized by a complex assemblage of Paleozoic rocks deformed during the Variscan orogeny (Hoepffner et al., 2005; Fig. 4.1B). This includes Ordovician, Silurian and Devonian shists, conglomerate and quartzites rocks, locally intruded by late Carboniferous granitoid that are exposed in the central area of the Western Moroccan Meseta (320 and 270 Ma; Mrini et al., 1992) and also late Carboniferous-Permian sedimentary rocks associated with volcanics (Youbi et al., 1995; Hoepffner et al., 2005). This domain is partially covered by undeformed Mesozoic sedimentary rocks (Fig. 4.1B).

In the Middle Atlas domain, the amount of Cenozoic shortening is less than 10% (Gomez et al., 1998; Arboleya et al., 2004) but is insufficient to explain the observed high topography of the orographic system. Moreover, geophysical studies highlight the presence of an anomalously thin lithosphere beneath the entire Atlas-Meseta system (Missenard et al., 2006; Duggen et al., 2009; Miller and Becker, 2014; Miller et al., 2015). The continental intraplate volcanism is also coeval with the main tectonic events that built the topography of the Atlas-Meseta (from Eocene/ middle Miocene to Quaternary, El Azzouzi et al., 1999; De Beer et al., 2000; Missenard et al., 2006; El Azzouzi et al., 2010), and has a geochemical affinity like the Canary mantle plume (Duggen et al., 2009). These data suggest a deep-seated, mantle driven contribution for the topography of the Atlas-Meseta system as also testified by the subaerial exposure of the Rifan Corridor, the occurrence of uplifted late Miocene

(Messinian) shallow-water marine deposits in the Skoura basin (TMA domain) at about 1200 m of elevation (Babault et al., 2008), and the progressive shallowing upward trend of the marine sediments deposited in the Taza-Guercif basin from 7.1-7.2 Ma (Krijgsman et al., 1999).

4.4. Methods

4.4.1. Topographic, stream profiles and knickpoints analysis

Regions characterized by recent changes in base levels retain a topographic signal in the upstream river network that provides the opportunity to evaluate the magnitude and the spatial variation of such perturbations. Here, we performed a regional and basin-scale topographic and a quantitative river network analyses to extract information on the recent uplift history of the Atlas-Meseta system. A Shuttle Radar Topography Mission Digital Elevation Model (SRTM DEM, pixel size of 90 m) was used to extract the drainage network. Hillslope metrics, such as slope and local relief with a circular sampling window of 2.5 km radius, as well as basin and channel morphometric characteristics were extracted using ArcGIS and the MATLAB software packages TopoToolbox (Schwanghart and Scherler, 2014) and TAK (Forte and Whipple, 2019), together with additional MATLAB functions (*e.g.*, Gallen, 2017).

The relationships between channel steepness and erosion/uplift rates have been demonstrated in various geological and structural settings (Safran et al., 2005; Cyr et al., 2010; Kirby and Whipple, 2012; Miller et al., 2013; Adams et al., 2020). In detachment-limited conditions, these relationships are modulated by the stream-power model (Howard, 1994; Whipple and Tucker, 1999) and can be expressed as:

$$E = KA^{m}S^{n} \qquad (1)$$

where E is the erosion rate (*i.e.*, change in elevation (z) of a stream with respect to time (t)), A is the upstream contributing drainage area, S is the local channel slope, K is the erosional efficiency (which is function of lithology and climate), and m and n are constant values (which depend on basin hydrology, channel geometry and erosional processes). Under steady-state conditions, erosion and rock uplift rates are balanced and *dz/dt* is equal to zero, therefore the power-law of equation (1) can be solved as (Flint et al., 1974):

$$S = \left(\frac{E}{K}\right)^{\frac{1}{n}} A^{-\left(\frac{m}{n}\right)} \qquad (2)$$

Equation (2) predicts a power relation between slope and drainage area and can be integrated, assuming E and K as spatially invariant (Perron and Royden, 2013):

$$z(x) = z(x_b) + \left(\frac{U}{KA_0^m}\right)^{\frac{1}{n}} \int_{xb}^{x} \left(\frac{A_0}{A(x)}\right)^{\frac{m}{n}} dx = z(x_b) + k_s\, A_0^{-\left(\frac{m}{n}\right)} \chi \qquad (3)$$

where:

$$\chi = \int_{xb}^{x} \left(\frac{A_0}{A(x')}\right)^{\frac{m}{n}} dx \qquad (4)$$

where x_b is the base level and χ is an integral quantity, A_0 is the reference drainage area (usually assumed to be 1) and m/n describes the concavity of the stream. Equation (3) allows transforming river longitudinal profiles to χ versus elevation plots (here and thereafter defined as χ - z plot, where z and χ are the dependent and independent variable, respectively). Consequently, $(E/K)^{1/n}$ is the slope in the χ space, where the slope is defined as steepness index (k_s). The steepness index (ks) and the concavity (m/n) can be determined by a linear regression in the log S - log A space by transforming equation (2) in a logarithmic function (Whipple, 2004; Wobus et al., 2006), and through the integral approach proposed by Perron and Royden, (2013). The ks parameter, however, presents a high variability among different river profiles, while empirical studies indicate that the concavity index typically falls within the relatively narrow range of 0.3 to 0.6 (Kirby and Whipple, 2012 and references therein). To compare ks values of longitudinal profiles with greatly varying drainage areas, a typical reference concavity index (θ_{ref}) of 0.45, is applied to derive normalized channel steepness indices (k_{sn}; Snyder et al., 2000; Wobus et al., 2006; Kirby and Whipple, 2012). This value also represents the best-fit concavity for all rivers of northern Atlas-Meseta system because it minimizes the scatter in the χ space (Perron and Royden, 2013; Goren et al., 2014; Fig. 4.3H).

Knickpoints were identified along the stream network based on the shape of the streams in the longitudinal profiles and in the χ - z plots and were discretized using available geological maps (1: 200.000, 100.000 and 50.000, Service Géologique du Maroc) and satellite imageries (Google Earth). Importantly, non-lithological, transient knickpoints cluster around similar χ values (Perron and Royden, 2013) and separate stream segments with different k_{sn} and θ values (Kirby and Whipple, 2012; Olivetti et al., 2016; Chapter 3). Conversely, knickpoints associated with heterogeneities along the profile and lithological contrasts are usually anchored in space and do not show a significant break in χ space (Fig. S4.1; Kirby and Whipple, 2012). Using this approach, the knickpoints were divided into four categories: transient knickpoints (non-lithological), minor, lithological and dam-related knickpoints.

Streams with knickpoints identified as transient (non-lithological) were used for reconstructing river projections to estimate the magnitude of fluvial incision. These profiles were reconstructed using the k_{sn} (θ_{ref} = 0.45) values of the river segments upstream of the non-lithological knickpoints in the χ space, and assuming that the paleo-river network remained approximately the same through time (Miller et al., 2012; Perron and Royden, 2013; Olivetti et al., 2016; Heidarzadeh et al., 2017; Fox et al., 2019; Chapter 3).

Finally, basin-averaged k_{sn} values, precipitation rates (as a proxy for the spatial climate variability), slope and local relief for the portions of the sampled catchments that include quartz-bearing lithologies were extracted for comparing ^{10}Be-derived denudation rates among different catchments (see next section; Supplementary Table S4.3).

4.4.2. ^{10}Be-derived denudation rates

We measured the concentration of in situ-produced cosmogenic ^{10}Be in quartz from seven river-born samples collected in active river channels and from four bedrock outcrops (location in Fig. 4.1C; Table 4.1). Catchments numbered as 58, 59, 60 and 62 are sub-catchments of two larger basins named 61 and 63 while, catchment 53 corresponds to the westernmost sampling location (Fig. 4.1C). All the selected catchments drain toward the Atlantic Ocean, with an upstream drainage area containing quartz-contributing lithologies varying from 40 to 1000 km^2 (for details see supplementary material Tables S4.3).

The sampled catchments drain different quartz-bearing rocks mainly including Lower Paleozoic basement (schists, conglomerate and quartzites), and late Carboniferous granitoid rocks. Thus, the basin-wide denudation rates were determined from these quartz-bearing rocks while rocks exposed in the catchments that do not contribute were filtered out for the area calculation (see similar approaches in Safran et al., 2005 and Carretier et al., 2015; Chapter 2).

Catchments 53, 58, 59, 62 and 63 are characterized by uniform quartz-bearing lithologies. Conversely, the contribution of quartz, in catchments 60 and 61, is mostly from two granite massifs exposed at the highest topography of the Moroccan Meseta region (Fig. 4.5A). To quantify the local denudation rates of the granite massifs forming the landscape of the western Meseta, we sampled four bedrock outcrops: two from the summit of an erosion surface (samples 56A, 56B, Fig. 4.5) and two from sub-horizontal ridge crests located close to the margin of the relict topography (samples 57A , 57B, Fig. 4.5).

All samples were analyzed following a protocol that includes crashing (only for bedrock samples), sieving and magnetic separation (three steps: 0.5 - 1 – 1.5 Ampere) to extract the 250 – 1000 μm sand fraction. This was followed by decarbonation of carbonate-rich samples through the reaction with HCl and leaching with HCl and H_2SiF_6 solution to remove all remaining minerals until pure quartz was obtained. To purify quartz grains, three sequential leaching in HF were performed for decontamination from atmospheric ^{10}Be. The quartz grains were totally dissolved after addition of 150 ml spike of an in-house carrier of ^{9}Be carrier solution (3025 ±9 mg/g) produced from a deep-mined phenakite crystal (Merchel et al., 2008). Beryllium was finally extracted using hydrofluoric and perchloric fuming to remove fluorides; cation and anion exchange chromatography was used to eliminate iron, aluminum, manganese and other elements. In situ-produced ^{10}Be concentrations were performed at the French Accelerator mass spectrometry (AMS) national facility ASTER (Aix-en Provence). The obtained $^{10}Be/^{9}Be$ ratios were corrected for procedural blanks and calibrated directly against the in-house STD-11 standard ($^{10}Be/^{9}Be = (1.191\pm0.013) \times 10^{-11}$; Braucher et al., 2015). Analytical uncertainties (1σ) are related to external uncertainties, variation of isotopic ratios of standards during the runs, and AMS counting statistics, and were propagated into the uncertainty of the calculated denudation rates.

In situ-produced ^{10}Be concentrations were converted to basin-wide denudation rates and bedrocks erosion rates using the MATLAB scripts by Balco et al. (2008), which are based on the time-dependent form of the Lal (1991) scaling model, and considering three different categories of particles responsible for the in-situ production of ^{10}Be (Braucher et al., 2011). The geomorphic shielding (Dunne et al., 1999), scaling factor of Stone (2000) and the mean elevation of sampled catchments were also determined for each pixel of digital elevation model (DEM), considering only the areas contributing with quartz-bearing lithologies. In the scaling model, λ describes the radioactive decay constant of ^{10}Be and 160, 1500 and 4320 g/cm^2 values were used for the effective neutron, slow muons and fast muons attenuation length (*e.g.*, Braucher et al., 2011).

Table 4.1. Denudation rates from cosmogenic ^{10}Be in river borne sand and bedrock samples

ID	Geomorphic position	Long.	Lat.	Elev.[a]	Quarz mass[b]	Carrier mass (^{9}Be)	10Be/9Be[c]		[^{10}Be][d] 10^3 (at./g)		Production rate[e] (at./g/yr)			Denudation (m/Myr)		Integration time[f] (yr)	
		°W	°N	(m)	(g)	(g)	Value (10^{-15})	Error (%)	Value	Error	Neutrons	Slow muons	Fast muons	Value	Error	Value	Error
53	Watershed	7.1500	33.5364	455	20.70	0.151	195.1	3.4	284.7	9.8	5.08	0.015	0.04	14.76	1.02	48081	3330.1
58	Watershed	5.7512	33.2640	1173	21.82	0.150	292.6	4.3	406.0	17.6	8.69	0.02	0.05	17.11	1.27	41624	3080.5
59	Watershed	5.5714	33.3807	1083	21.68	0.151	241.6	3.4	338.5	11.7	8.16	0.02	0.05	19.49	1.35	36639	2535.6
60	Watershed	6.2790	33.4496	914	21.20	0.150	238.8	3.4	339.4	11.8	7.28	0.02	0.05	17.36	1.20	41023	2845.5
62	Watershed	5.9743	33.7520	721	21.12	0.151	95.5	12.3	135.0	17.0	6.32	0.02	0.05	39.94	5.57	18044	2514.7
Blank							0.45	51.3									
61	Watershed	6.365	33.698	928	21.47	0.152	211.5	3.3	302.7	10.3	7.35	0.02	0.05	19.80	1.37	36076	2488.0
63	Watershed	5.931	33.829	1049	21.74	0.151	146.6	4.1	204.8	8.5	7.95	0.02	0.05	32.15	2.34	22369	1630.0
56A	Summit	6.0535	33.4123	1124	21.84	0.150	1055.6	3.1	1467.4	46.0	8.43	0.02	0.05	3.46	0.23	163446	11064.1
56B	Summit	6.0535	33.4123	1124	21.59	0.150	900.1	2.5	1259.7	31.2	8.43	0.02	0.05	4.11	0.27	139446	9053.0
57A	Ridge crest	5.8906	33.1922	1098	19.45	0.150	251.2	3.3	389.0	12.9	8.23	0.02	0.05	14.36	0.98	41958	2874.7
57B	Ridge crest	5.8913	33.1919	1099	17.24	0.151	239.1	3.5	423.6	14.9	8.24	0.02	0.05	13.13	0.91	45808	3185.9
Blank							0.788	23.05									

[a] Basin mean elevation.

[b] Mass of pure quartz dissolved.

[c] Isotopic ratio uncertainties include statistical error on counted ^{10}Be events (N) and analytical error correction.

[d] Uncertainties on ^{10}Be concentrations are calculated using the standard error propagation method using the quadratic sum of the relative errors associated to the counting statistics, AMS internal error (0.5% for ASTER), and error associated to the process blank.

[e] Production rate is the spatially averaged production rate over the river basin, scaled for elevation, latitude (Stone, 2000) and geomorphic shielding (Dunne et al., 1999). The values, relative to watersheds, are calculated for a non-uniform distribution of quartz-lithologies in the sample basins (*e.g.*, Safran et al., 2005; Carretier et al., 2015; Chapter 2).

[f] Integration times are calculated after Lal (1991) while their uncertainties are calculated propagating the error of the denudation rates.

4.5. Results

4.5.1. Topographic analysis

The study area is characterized by an elongated high-standing topography rising to more than 1500 m of elevation and plunging toward the Atlantic coast along its north-eastern and south-western sectors, respectively. Based on the geometry of the river network, the Western Meseta was divided into three different sectors: the Central Western Meseta (CWM), the Northern Western Meseta (NWM) and the Southern Western Meseta (SWM). The CWM is characterized by rivers draining directly into the ocean, while the NWM and SWM include the main tributaries of the Oued Sebou and Er Rbia, respectively (Fig. 4.1C). Overall, the WMM domain consists of a NE-SW striking topographic swell, with a low relief topography that locally has been deeply dissected by fluvial incisions (Fig. 4.2). Conversely, the adjacent Tabular (TMA) and Folded Middle Atlas (FMA) domains are characterized by a topography rising up to 2000 and 2500 m, respectively (Fig. 4.1C), with the TMA presenting a tabular, low relief topography and the FMA displaying and alternation and ridges and valleys with high values of topographic slope and relief (Figs. 4.2A, 4.2B and S4.2).

Importantly, a set of regionally widespread non-lithological knickpoints stand at different elevations in the three domains. They mark a sharp variation in the normalized channel steepness (k_{sn}), local relief and slope between the deep valleys and the upstream portions of the landscape (dashed line in Figs. 4.2A, 4.2B and S4.2). Particularly, high value of k_{sn} (> 80 $m^{0.9}$), local relief (> 500 m), and slope (> 25°) are found in the FMA domain and in the downstream portions of the non-lithological knickpoints in the WMM and the TMA domains (Figs. 4.2 and S4.2). A local increase in morphometric parameters occurs also along the boundary between the WMM and TMA domains, where high-standing lithological knickpoints are observed (bold dashed black line, Figs. 4.2B and S4.2). The lowest values of topographic and channel parameters are observed in the lower portions of the landscape, like the Er Rbia and Sebou basins toward the ocean, and upstream of the non-lithological knickpoints, especially within the WMM and the TMA domains (Figs. 4.2B and S4.2). A pattern of minor knickpoints is also observed at low elevation, mainly downstream of the non-lithological knickpoints (Figs. 4.2B and S4.2).

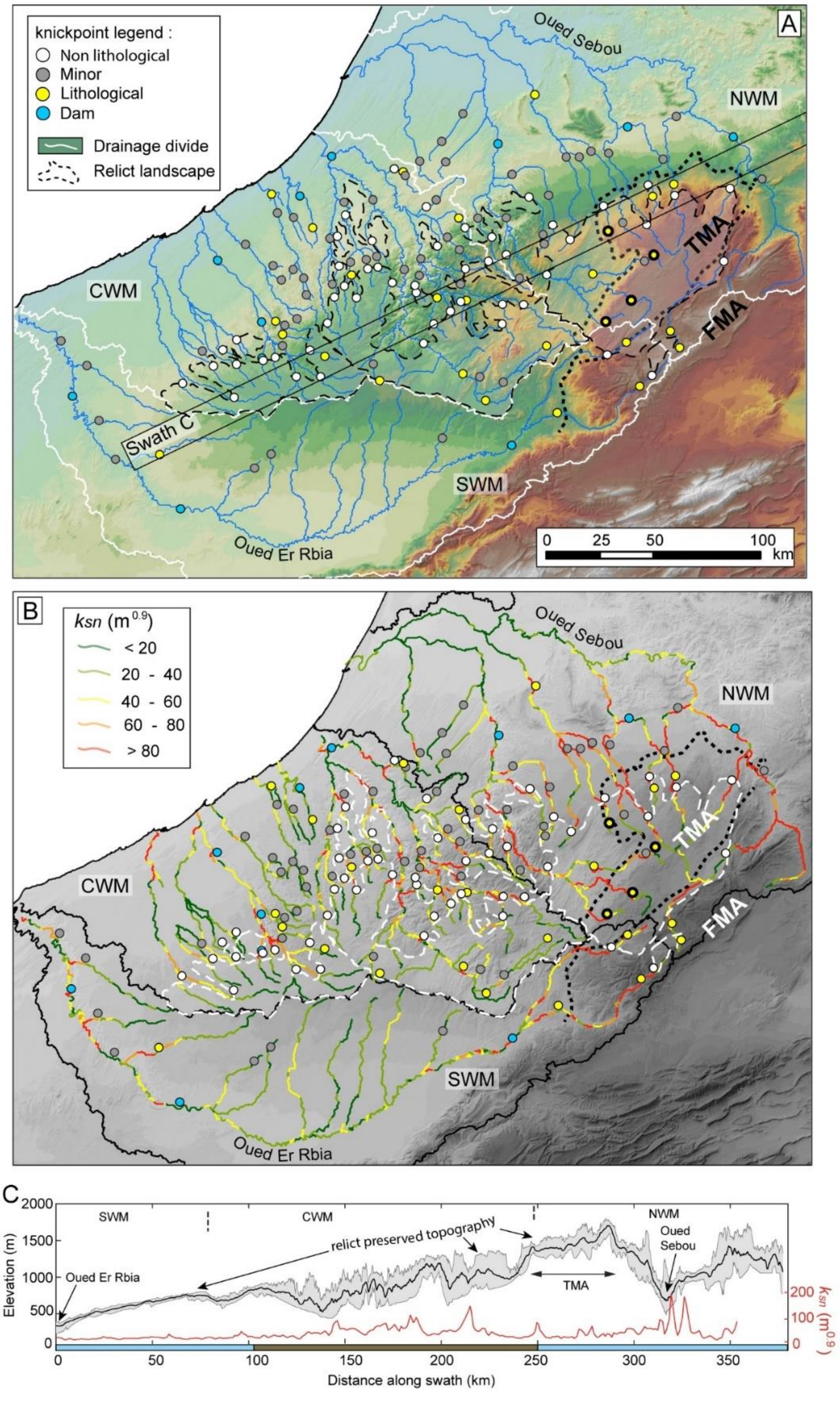

Figure 4.2. (A) Topographic (B) k_{sn} values with main knickpoints. The bold knickpoints describe the escarpment between the TMA and Moroccan Meseta, while the thick dashed line indicates the boundary between the main morpho-structural domains. The solid lines demarks the tributaries of the Oued El Rbia (South Western Meseta, SWM), of the Oued Sebou (North Western Meseta, NWM) and rivers draining directly from the Western Meseta to the Atlantic ocean (CWM: Central Western Meseta). TMA and FMA indicate the Tabular Middle Atlas and the Folded Middle Atlas, respectively. (C) Along-strike topographic swath profile and averaged k_{sn} values (see Fig. 4.1 for legend).

4.5.2. River morphology

The NWM sector is characterized by transient longitudinal profiles, showing minor, lithological, and non-lithological knickpoints. Most of the rivers flowing from the TMA and the WMM are characterized by lithological knickpoints located between 1500 and 2000 m of elevation at χ values of 20 to 25 (Figs. 4.3A and 4.3B). A pattern of widespread non-lithological knickpoints is located between 700 and 1500 m of elevation, and increases gradually from 200 to 450 km of distance from the river mouth (Fig. 3A; Supplementary Table S4.1). These non-lithological knickpoints cluster at χ values of 13 – 17 (Fig. 4.3B) and separate steep downstream from low-gradient upstream channel segments (Fig. 4.3B). Cluster of minor knickpoints are also located between 200 and 700 m of elevation at a χ value of approximately 10. With respect to the more elevated knickpoints, this cluster separates gentle downstream river segments from steeper upstream portions (Figs. 4.3A and 4.3B).

The rivers draining toward the Atlantic Ocean (CWM sector) present transient longitudinal profiles, with minor, lithological and non-lithological knickpoints (Fig. 4.3C). Rivers of the CWM sector show concave-up longitudinal profiles downstream of the main non-lithological knickpoints and straight low-gradient upper segments (Fig. 4.3C). These non-lithological knickpoints present a progressive increase in elevation from 300 m close to the river mouth, to ~1000 m toward the FMA. Most of these non-lithological knickpoints cluster at χ values of 10 – 15, and separate downstream steep segments from low-gradient upstream portions (Fig. 4.3D). Downstream of these non-lithological knickpoints, between 0 and 150 km from the river mouths, there are also several minor knickpoints that do not show any significant variation in the χ space (Figs. 4.3C and 4.3D).

The SWM sector is characterized by equilibrated and transient longitudinal profiles with several minor knickpoints and only two major non-lithological knickpoints (Fig. 4.3E). Rivers that are flowing from the FMA domain are characterized by concave-up longitudinal profiles. The main slope break is located at high elevation, where two non-lithological knickpoints lie (Figs. 4.3E and 4.3F). The average elevations of the knickpoints are 627 m (σ_m = 116), 1255 m (σ_m = 86) and 1724 m (σ_m = 135) for the WMM, TMA and FMA domains, respectively (Supplementary Table S4.1).

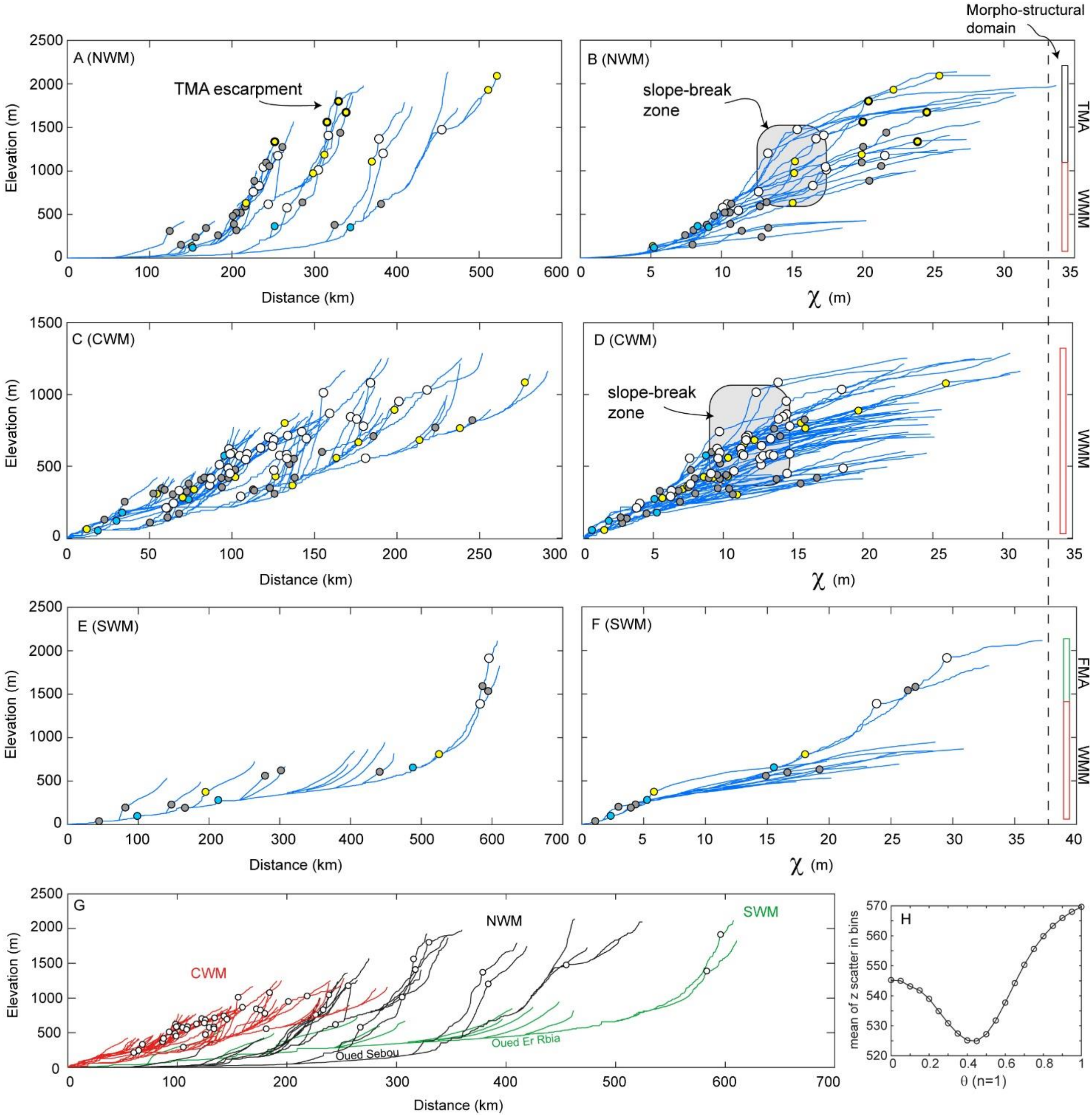

Figure 4.3. Longitudinal river profiles and χ - z plots with knickpoints for the NWM (A-B), CWM (C-D), and SWM (E-F). The knickpoints legend is in figure 4.2A. The non-lithological knickpoints are located at the slope-break zone separating segments with different k_{sn} value. (G) Longitudinal river profiles with the major non-lithological knickpoints. Red rivers: CWM sector; black rivers: NWM sector; green rivers: SWM sector. The non-lithological knickpoints mark the boundary between the downstream steep river profiles and the upstream low-gradient river segments, describing a paleo-surface margin. Note, the rivers of NWM and SWM sectors come mainly from the most elevated TMA and FMA domains, respectively. (H) Plot showing the best-fit concavity index for the rivers of the study area, which is ~0.45.

4.5.3. Transient incision

The magnitude of river incision can be estimated by the difference between the reconstructed river profiles projected from the non-lithological knickpoints and the modern base level. Estimates of fluvial incision for the NWM sector are variable because this region contains rivers draining both the WMM and TMA domains. Based on 12 river projections of the relict portion, the fluvial incision ranges from 265 (2σ = 27) to 1200 m (2σ = 18) (Fig. 4.4A and Table S4.2).

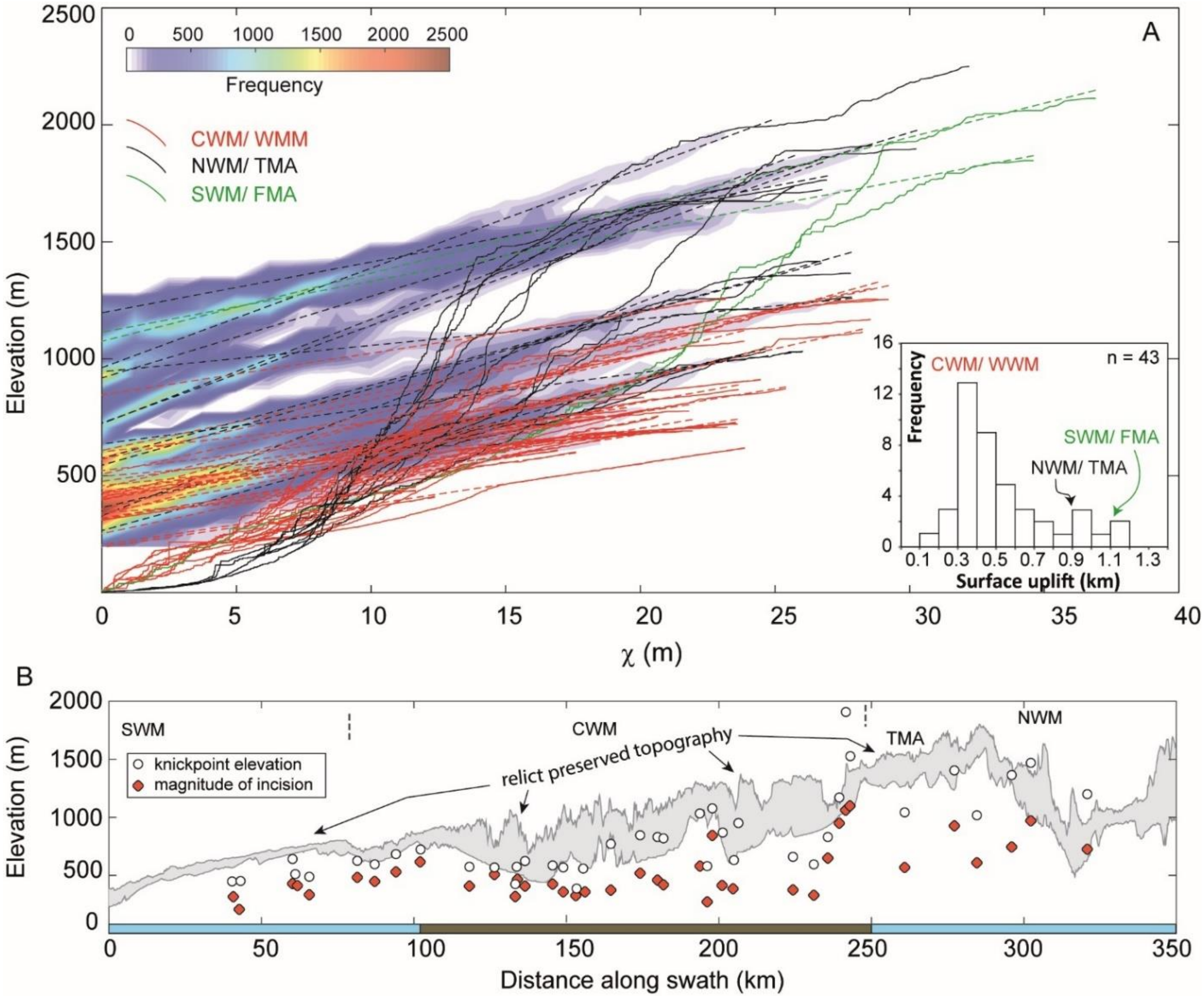

Figure 4.4. (A) Modern longitudinal profiles and projections of the relict landscape (black dashed segments) upstream of the highest knickpoints using $\theta_{ref} = 0.45$ and the k_{sn} of the relict portion in χ plot. The main peaks of fluvial incision are at ~400 m and ~800 m in the Western Moroccan Meseta and Tabular Middle Atlas domains, respectively (see details in Table S4.2). The density distribution legend is relative to the data point of the projected segments. Inset shows the frequency diagrams of the magnitude of surface uplift for the entire dataset (NWM, WMM, SWM). Note, the rivers of NWM and SWM sectors come mostly from the TMA and FMA domains, respectively. (B) Knickpoints elevation and magnitude of fluvial incision

obtained from the reconstructed river projections plotted along the topographic swath profile (see Fig. 4.1 for legend). The location of the swath profile is shown in figure 4.2A.

In the CWM sector, the magnitude of incision was estimated from 29 river profiles and fall in a narrow range of 200 ($2\sigma = 15$) to 610 m ($2\sigma = 10$) (Fig. 4.4A and Table S4.2). The river projections from the SWM sector show an average incision of 1086 ($\sigma_m = 64$) (Fig. 4.4A and Table S4.2). There, rivers flow directly from the FMA domain. Overall, rivers draining from the WMM domain (mainly from CWM and NWM sectors) show a mean vertical incision of 415 m ($\sigma_m = 55$) (Fig. 4.4A and Table S4.2). Conversely, mean values of incision from the TMA and FMA domains are 823 m ($\sigma_m = 66$) and 1086 ($\sigma_m = 64$), respectively (Fig. 4.4A and Table S4.2). Overall, both elevations of the non-lithological knickpoints and magnitude of vertical incision increase progressively from the SWM to the NWM sector (Fig. 4.4B).

4.5.4. ^{10}Be-derived denudation rates

^{10}Be concentrations from the largest catchments of the CWM yield denudation rates of 19.8 ± 1.4 and 32.2 ± 2.3 m/Myr, for samples 61 and 63, respectively (Table 4.1). Denudation rates from the sub-catchments forming the relict portion of the landscape, upstream of samples 61 and 63 are 17.1 ± 1.3 and 19.5 ± 1.4 m/Myr (samples 58 and 59), whereas the sub-catchments downstream of non-lithological knickpoints present rates of 17.4 ± 1.2 and 40.0 ± 5.6 m/Myr (samples 60 and 62; Table 4.1). In the western side of the Moroccan Meseta, sample 53 yields a denudation rate of 14.8 ± 1.0 m/Myr (Table 4.1). The sampled catchments are characterized by a uniform distribution of quartz, which is mostly sourced from the lower Paleozoic metamorphic basement, except for samples 60 and 61. These two basins are influenced by the occurrence of two granite massifs located in the high-standing low relief surface of the Western Moroccan Meseta (Fig. 4.5A), which may contribute more than the Paleozoic metamorphics. Local denudation rates of bare bedrock surfaces on the summit plateau (relict surface) and on the ridge crests of the granite massif vary from 3.5 ± 0.2 to 4.1 ± 0.3 m/Myr (samples 56A, 56B), and from 13.1 ± 0.9 to 14.4 ± 1.0 m/Myr (samples 57A, 57B), respectively (Table 4.1). It is worth noting that the steady denudation rates of granitic ridge crests: 1) are significantly higher than the rates of the flat summit surfaces (Figs. 4.5A, 4.5B and 4.5D), and 2) are close to the values determined for the watersheds of samples 60 and 61, where the same granite massifs are exposed and may provide most of the quartz that yielded the measured ^{10}Be concentration.

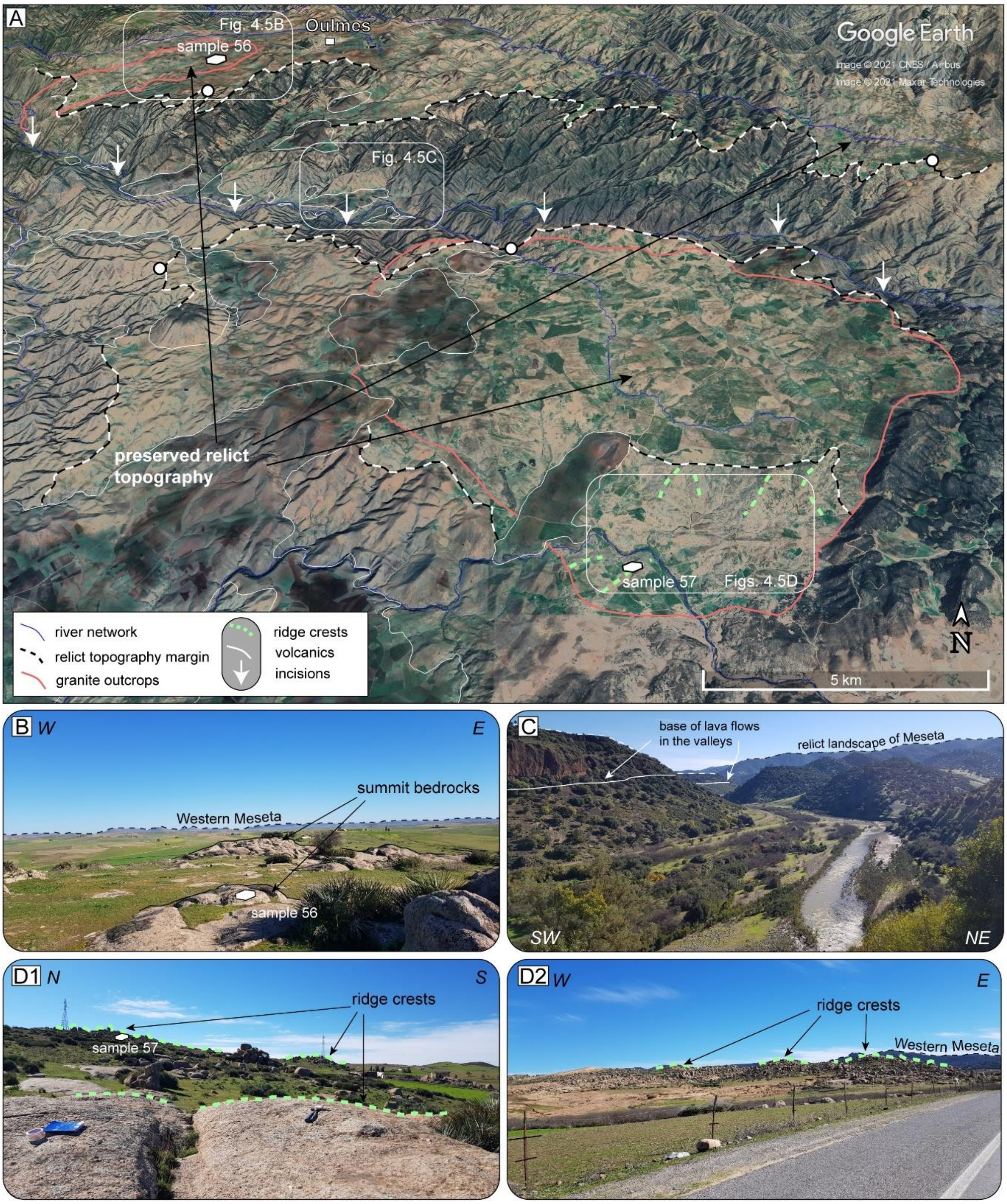

Figure 4.5. (A) Prospective Google Earth view of the Western Moroccan Meseta. Note that the landscape is characterized by a low-topographic relief, relict topography dissected by deep fluvial valleys. The granite rocks are located at the maximum topography over the summit erosional surface (i.e., relict landscape). The lava flows are located both in the deep incisions and above the remanence of relict topography. (B) View of the summit erosional surface of the Western Moroccan Meseta (see dashed black line) near the locality of Oulmes. The typical morphologies of the granite rocks lying at the maximum elevation are shown in the foreground (black lines). (C) View of the Aguennour River valley. Note the incision across

the lava flow deposits and basement rocks (~400 m from the summit erosional surface). (D1-D2) View of the granite outcrops close to the plateau margin. Note the rugged morphologies related to the granite incisions (green lines).

4.5.5. Basin-wide denudation rates versus topographic metrics

The basin-wide denudation rates from the Western Moroccan Meseta are plotted versus the basin-averaged k_{sn}, slope, local relief and precipitation, in order to assess the potential control on denudation rates (Figs. 4.6A, 4.6B, 4.6C, 4.6D and Table S4.3). Basin-averaged k_{sn} values range from 14.7 to 57.6 $m^{0.9}$ (Fig. 4.6A and Table S4.3), while basin-averaged slope values vary from 5.2 to 14.3° (Fig. 4.6B and Table S4.3) and basin-averaged local relief range from 222 to 454 m (Fig. 4.6C and Table S4.3).

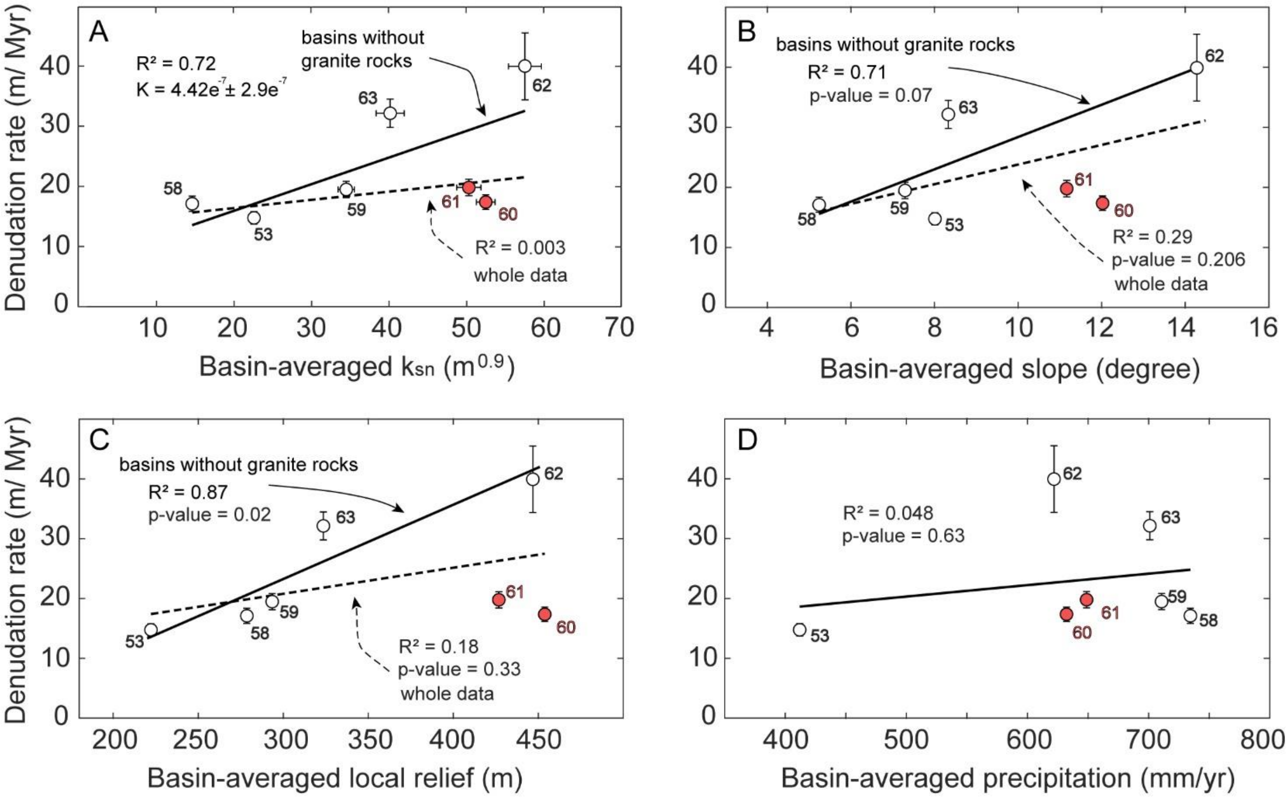

Figure 4.6. Relationships between topographic and channel metrics and basin-wide denudation rates. (A) Basin-averaged k_{sn} versus denudation rate. The solid line shows the bootstrap linear best-fit (R^2 = 0.72), and forced linear best-fit (0.95) without considering basins with exposed granite rocks. The gray best-fit (R^2 = 0) considere all the sampled basins. (B) Basin-averaged slope versus denudation rate. (C) Basin-averaged local relief (2.5 km radius) versus denudation rate. (D) Basin-averaged precipitation versus denudation rate of sampled basins. The red circles indicate catchments characterized by the contribution of quartz from granite massifs (details in fig. 4.5A).

The topographic and channel metrics do not exhibit a good correlation with the basin-wide denudation rates with R^2 of 0.003, 0.2 and 0.3 for k_{sn}, slope and local relief, respectively (dashed lines in Figs. 4.6A, 4.6B, 4.6C). Conversely, a stronger correlation between the metrics and basin-wide denudation considering the catchments characterized by homogeneous distribution of bearing-quartz lithologies (i.e., excluding samples 60 and 61) is observed. In this case, the coefficient of correlation is 0.72, 0.71 and 0.87 for the basin-averaged k_{sn}, slope and local relief, respectively (Figs. 4.6A, 4.6B, 4.6C). The lowest topographic and channel metrics are observed for the samples 53, 58 and 59, which represent the westernmost and the upstream sub-catchments of the study areas. Conversely, samples 60 and 62 (downstream of the non-lithological knickpoints) show the highest values of basin-averaged k_{sn}, slope and local relief, whereas samples 61 and 63, which are the larger catchments, show mixed values between the upstream and downstream catchments (Figs. 4.6A, 4.6B, 4.6C and Table S4.3). Finally, basins-wide denudation rates are independent from the basin-averaged precipitation (R^2=0.05; Fig. 4.6D).

4.6. Discussion

Our data documented the pervasiveness of the transience across the Western Moroccan Meseta (WMM) and the Middle Atlas domains (TMA, FMA). Similar disequilibrium topography has been observed also in the other domains of Atlas-Meseta system both in quiescent (Anti-Atlas, High Plateaus, Pastor et al., 2015; Chapter 2 and 3) and active domains (High Atlas, Middle Atlas; Pastor et al., 2015; Lanari et al., 2020a). Here, we discuss the state of landscape in the Western Moroccan Meseta, the rate of denudation and the magnitude of uplift to obtain insights into the topographic growth of the Atlas-Meseta domains.

4.6.1. Transient topography in Western Moroccan Meseta and Middle Atlas

The study area is characterized by a high-standing relict surfaces bounded by non-lithological knickpoints and deeply incised valleys downstream of these knickpoints. This elevated landscape consists of low-gradient surface, gently dipping from the FMA to the TMA and the WMM, and from the WMA toward the ocean (Fig. 4.3G). This surface represents a transient topography and is associated with low normalized channel steepness

(k_{sn}), topographic slopes and local reliefs (Figs. 4.2 and 4.4). A few knickpoints located at about 1500 m of elevation, however, are at the boundary between the WMM and TMA domains (see bold yellow points in Figs. 4.3A, 4.3B). There, the knickpoints coincide with local variations in k_{sn} values and in topographic metrics and hence reflect erodibility changes as also suggested by the occurrence of a ~500-m-high morphological escarpment representing the stratigraphic contact between the Paleozoic basement and undeformed Jurassic limestones forming a flat and elevated surface.

The disequilibrium state of a river network can be explained through several processes, such as drainage reorganization, climate change, eustatic sea level fall and tectonic uplift (Snyder et al., 2002; Hancock and Kirwan, 2007; Kirby and Whipple, 2012; Miller et al., 2013, Ballato et al., 2015). In the WMM, a base level fall due to eustatic forcing is unlikely to be the source of the observed non-lithological knickpoints, because it cannot explain the uniform increase in k_{sn} values in the same lithotype upstream of fluvial channels. Drainage reorganization could also explain the increase in fluvial incision downstream of the knickpoints due to a gain of drainage area and hence in water discharge (e g., Yang et al., 2015). The non-lithological knickpoints, however, are observed in the watersheds of all domains (WMM, TMA and FMA), even in small catchments where there is no evidence of drainage reorganization (*e.g.*, wind gaps, sudden changes in the river pattern, knickpoints due to capture processes among others). Furthermore, climate-driven faster erosion should produce a decrease in the channel slopes downstream of non-lithological knickpoints (Miller et al., 2013), conversely to what observed in the rivers of the Western Meseta. The main non-lithological knickpoints are characterized by a major upstream decrease in k_{sn} values even across the same lithology as documented in the χ space plots (Figs. 4.2 and 4.3), and also by changes in the topographic metrics at regional scale (Fig. S4.2). This indicate that these knickpoints separate portions of the landscape eroding at different rates (*e.g.*, Kirby and Whipple, 2012; Miller et al., 2013; Olivetti et al., 2016). Consequently, the portion with steep channels and deep incisions downstream of the knickpoints, records the response of the fluvial system to an increase in rock uplift rates, while the upstream low relief topography (relict landscape; Fig. 4.5A) records the pre-uplift conditions.

Overall, these observations indicate that the WMM experienced a recent topographic rejuvenation as documented in other regions exhibiting similar topographic patterns (Calvet et al., 2015; Olivetti et al., 2012; 2016; Miller et al., 2012; 2013; Chapter 2; 3). Although the exact timing of this event is unknown, available geological data summarized section 4.6.3 suggest that uplift must be younger than the Messinian.

4.6.2. Erosional dynamics in a rejuvenated landscape

The characterization of a transient landscape is critical for understanding the landscape dynamics because such a setting includes the coexistence of landscape portions that are in equilibrium with past and present uplift rates. In the Western Meseta the lowest bedrock denudation rates are from a granite exposed atop of the summit surfaces (3.5 ± 0.2 and 4.1 ± 0.3 m/Myr in Table 4.1) while the highest rates are from a similar granite exposed along small ridge crests (13.1 ± 0.9 to 14.4 ± 1.0 m/Myr in Table 4.1). This four-fold difference is presumably caused by different hillslope processes and by higher physical weathering considering the same exposure time and chemical weathering of the granite rocks (Kanamaru et al., 2018). This demonstrates the key role of hillslope topographic gradient and weathering process on the estimates of denudation from bedrocks, as observed elsewhere (Meyer et al., 2010; Godard et al., 2019; 2021). A similar order of magnitudes has been observed between the grus and bedrock from flat top in the granites of the Black Forest Mountains (Meyer et al., 2010). In our case, the faster denudations occur at the ridge morphologies, located to the margin of relict landscape, suggesting an abrupt increase in denudation and hillslope erosion at the transition between the rejuvenated and relict topography.

Interestingly, the rates of denudation from the ridge crests (samples 57A and 57B) are very similar to those from the watersheds of the same areas (samples 60 and 61 in Table 4.1). This may be due to the widespread exposure within the catchments of the relict surface sculptured on the granite rocks that contains a higher amount of quartz than the adjacent metamorphic rocks. These quartz-rich granite rocks erode at relatively low rates (~4 m/Myr versus few tens of meters for Millions of years for basin-wide denudation rates) and hence have a higher ^{10}Be concentration than the metamorphic basement exposed downstream of the non-lithological knickpoints in the deeply incised valleys. The greater amount of quartz sourced from the relict landscape influences (increases) the final ^{10}Be concentration for catchments 60 and 61, producing a decrease in the denudation rate estimates. This process is further corroborated by the poor sensitivity of these two watersheds to the linearity between basin-wide denudation rates and topographic metrics with the denudation rates that are systematically lower than expected (Figs. 4.6A, 4.6B, 4.6C).

Low denudation rates are also observed in watersheds 53, 58 and 59. This is consistent with the sampling location upstream of the non-lithological knickpoints within the relict portion of the WMM landscape, where values of basin-averaged k_{sn}, slope and relief are low (Figs. 4.6A, 4.6B, 4.6C). These low rates reflect the erosional decay of topography during a long period of relative base level stability (Champagnac er al., 2014; Calvet et al., 2015; Chapter 2). In particular, the relict topography of the WMM started to develop at least from the Triassic as suggested by the lack of Mesozoic and younger sediment in the axial Meseta zone and by old thermochronological cooling ages (*e.g.*, Frizon de Lamotte et al., 2009; Barbero et al., 2010; Charton et al., 2020).

Conversely, watersheds 62 and 63 present higher denudation rates because they receive most of the quartz from the deeply incised landscape downstream of the non-lithological knickpoints while the distribution of quartz-bearing rocks in the catchment is uniform (Figs. 4.6A, 4.6B, 4.6C). In this case higher denudation rates, reflect the recent increase in uplift rates as documented in other regions that experienced a topographic rejuvenation (Olivetti et al., 2012; 2016; Miller et al., 2013)

The relation between denudation rates, channel and topographic metrics are apparently poorly correlated when considering the entire dataset (dashed black trends in Figs. 4.6A, 4.6B, 4.6C and S4.2). In a setting characterized by topographic rejuvenation with a well-preserved relict landscape, this poor correlation has been attributed either to the lithological control on the landscape dynamics (*e.g.*, Scharf et al., 2013; Chapter 2) or to a decoupling between hillslope and channel incision (*e.g.*, Olivetti et al., 2016). In the studied area, the first hypothesis can be ruled out because there is not a clear correlation between the topographic relief, k_{sn} and exposed lithologies (both at regional and basin-scales). The second hypothesis can also be excluded because the denudation rates from the ridge crests (57A and 57B) and associated watersheds (60 and 61) are similar. Moreover, the topographic metrics and the k_{sn} values correlate well with the denudation rates when excluding the heterogeneous catchments indicating a transient adjustment of the hillslope and channels to the relative base level fall related to the Cenozoic increase in rock uplift rates (Figs. 4.6A, 4.6B, 4.6C). Moreover, the linearity of the relationship between basin-wide denudation and k_{sn}, for heterogeneous catchments, suggests that the n parameter of the stream power model (equation (1)) can be approximated to 1, as typically shown in slow tectonic or passive settings, where basin-averaged slope and k_{sn} are usually lower than 25° and 200 $m^{0.9}$, respectively (Fig. S4.3; *e.g.*, Miller et al., 2013; Mandal et al., 2015; Olivetti et al., 2016; Godard et al., 2019; Chapter 2). Therefore, for low ranges of denudation rates, the power-law and the linear trend are indistinguishable, not exceeding the critical threshold for bedrock detachment (Ouimet et al., 2009; DiBiase and Whipple, 2011). Finally, the basin-wide denudations are not sensitive to averaged annual precipitation rates, testifying the non-dependence of precipitation in the denudation of slow tectonic settings, as also observed in other settings characterized by different climatic conditions (Fig. 4.6D; Godard et al., 2019; Chapter 2).

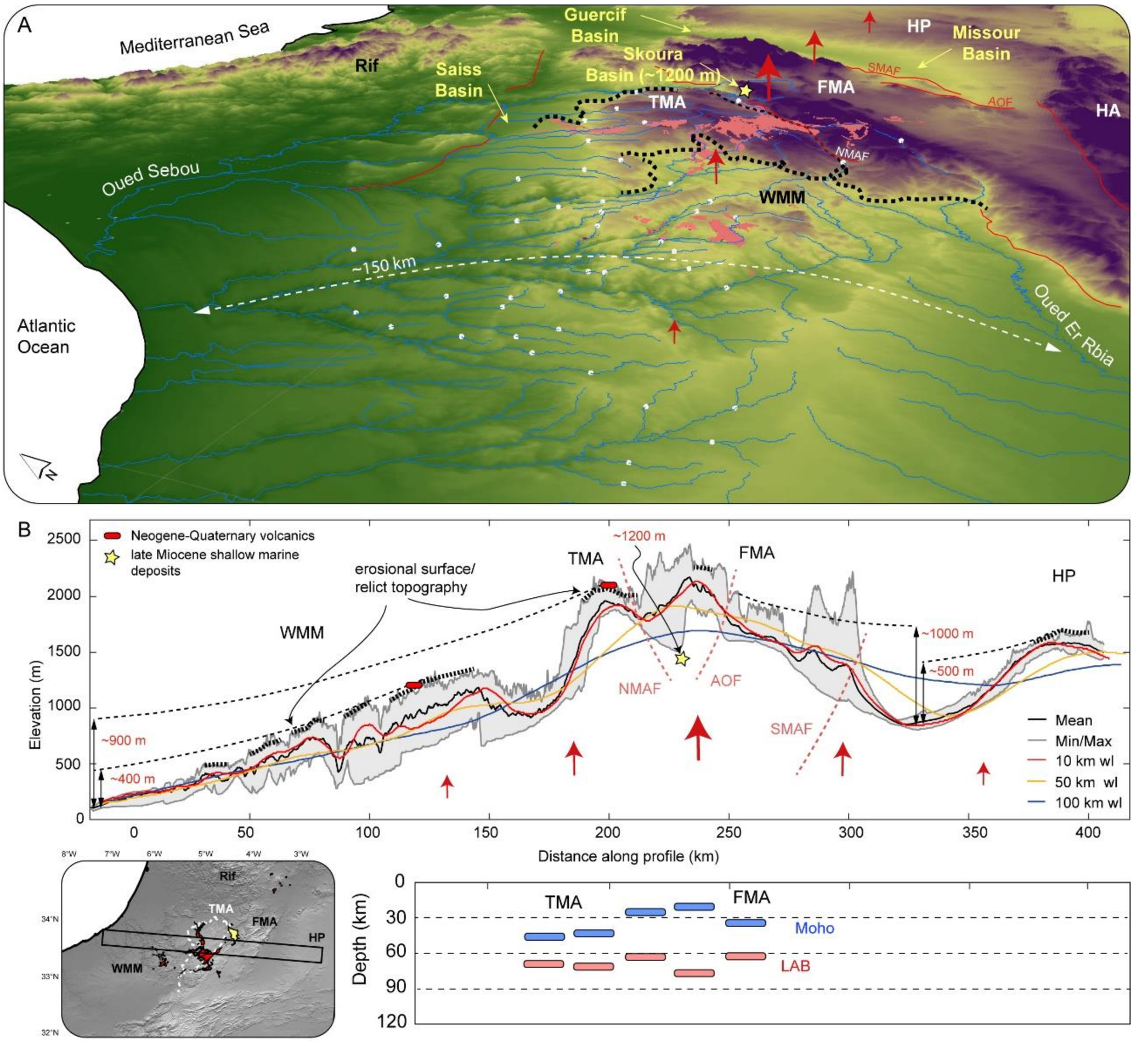

Figure 4.7. (A) Tridimensional view of the northern Atlas-Meseta system. (B) Swath profile (20 km of width) from west to east, showing the local relief and maximum elevation of Western Moroccan Meseta (WMM), Tabular (TMA) and Folded Middle Altas (FMA) and High Plateaus (HP) sectors of the Atlas-Meseta system. SMAF: South Middle Atlas Fault. AOF : Ait Oufella Fault; NMAF: North Middle Atlas Fault (after Gomez et al., 1996). Data of surface uplift indicate a 1000 m and 500 m in the eastern front of FMA and HP sectors (Pastor et al., 2015), whereas the uplifted shallow marine deposits of Skoura basin suggest an uplift up to 1200 m in the TMA and FMA domanis (Babault et al., 2008). Note, the Neogene-Quaternary volcanics are located above the regional erosional surface (red areas). Bottom panel indicate the position of Moho and lithosphere-asthenosphere boundary (LAB) beneath the Atlas-Meseta system from S-received functions (data from Miller and Becker, 2013).

4.6.3. Topographic evolution and surface uplift

The Atlas-Meseta system represents an intracontinental orographic system characterized by quiescent tectonic domains, such as the Western Moroccan Meseta and High Plateaus (HP) and tectonically active mountain belts like the Folded Middle Atlas or with limited activity like Tabular Middle Atlas (TMA) (Fig. 4.1A). The Middle Atlas includes elevated and steep mountain ridges that accommodated tectonic shortening mostly during the Cenozoic (up to 10%; Gomez et al., 1998; Arboleya et al., 2004). Conversely, the WMM and HP have not accommodated any deformation and includes NE-SW-striking topographic swells of ~150 x 300 km and ~100 x 250 km for the WMM and HP, respectively (Fig. 4.7A; Barbero et al., 2010; Pastor et al., 2015). Our new data indicate that the Atlas-Meseta system has undergone a recent topographic rejuvenation in agreement with available geological information such as the occurrence of Tortonian-Messinian shallow-water marine sediments (Skoura basin; western FMA margin) at an elevation of 1200 m (Babault et al., 2008), late Miocene deep-marine sediments (paleo-bathymetry of ~600 m) in the Taza-Guercif basin that started recording a shallowing-upward trend at ~7 Ma that culminated with terrestrial deposition from 6 Ma to the early Pliocene (Krijgsman et al., 1999) and high-standing river terraces in the eastern mountain front of the FMA (Fig. 4.7; Pastor et al., 2015).

Geophysical studies indicate that the crustal thickness and the depth of the lithosphere-asthenosphere boundary cannot isostatically compensate the observed high topography (Fig. 4.7; Missenard et al., 2006; Bezada et al., 2013; Miller and Becker, 2014; Miller et al., 2015). Importantly, intraplate volcanism occurred in the WMM and TMA/ FMA mostly between 3.7 and 0.6 Ma (El Azzouzi et al., 2010) with a geochemical signatures very similar to that one of the Canary Island suggesting a deep asthenospheric source (Duggen et al., 2009). Combined, these observations suggest that uplift of this portion of the Atlas-Meseta system must have started at ~7 Ma when the Skoura and basin became subaerially exposed (Babault et al. 2008) and the Guercif basins started recording a shallowing upward trend (Missenard et al., 2006; Krijgsman et al., 1999) and in part could have occurred during volcanism. Interestingly, the onset of uplift seems to coincide with (or slightly pre-date) the initiation of the Messinian salinity crisis (Krijgsman et al., 1999). Despite these geological constrains, the isolation of the large-scale uplift of the Atlas-Meseta system is complicated by the superimposed of smaller wavelength tectonic signals characterizing the different domains.

Topography filtered at 10 km is very similar to the topographic swath profile and highlights the occurrence of processes operating at crustal scale, such as tectonic shortening. This occurs mainly in the FMA domain. (Fig. 4.7) where the elevated zone with high topographic relief is delimited by a few high angle tectonic lineaments that have been interpreted, at least in part, to represent reverse fault possibly with a lateral components (NMAF, AOF in Fig. 4.7; Brede and Heinitz, 1989; Gomez et al., 1996). Topography filtered at 50 km provides a more uniform output, though undulated, that doesn’t allow distinguishing clearly the different domains of the WMA, TMA and FMA (Fig. 4.7B). Conversely, topography filtered at 100 km delineates a topographic swell with a wavelength of ~350 km and an amplitude of ~1600 m, peaking in the FMA domain (Fig. 4.7B) and centred in the area of recent volcanism, low upper mantle velocity, and thinned crust and lithosphere (Fig. 4.7B; El Azzouzi et al., 2010; Miller and Becker, 2013; Miller et al., 2015). The topographic swell reaches a minimum elevation of ~1300 m and then rises again toward the High Plateaus (Fig. 4.7B).

To a first approximation this swell coincides with the summit erosional surface that appears to be warped around its main axis (Fig 4.7A). Thus, the summit erosion can be used as a proxy for surface uplift. In the WMM, TMA and FMA domains, our data document a magnitude of surface uplift increasing progressively from 400 to 800 and 1100 m, respectively (Fig. 4.7) A similar magnitude of uplift has been described in the eastern flank of the Middle Atlas from the mountain front (1000 m) to the HP (500 m) domains (Pastor et al., 2015). The highest values are found in the FMA domain, where uplifted Messinian sediments are currently at 1200 m of elevation (Fig. 4.7; Babault et al., 2008; Pastor et al., 2015). Thus, the lower uplift values extracted from the WMM and HP and the maximum values for the Middle Atlas domains describe a large wavelength positive features (~350 km), most likely caused by a deep source (Fig. 4.7), similar to what has been observed in other orographic systems (Faccenna et al., 2011; Molin et al., 2012; Olivetti et al., 2016; Chapter 3). Therefore, the estimates from the WMM and HP (400 - 500 m) can be confidently attributed to mantle process, whereas the maximum magnitude of uplift in TMA (900 m) and FMA (1100 – 1200 m) can be explained by the superimposition of short wavelengths processes, such as local faulting induced by shortening, with a larger, longer wavelength, regional signal. Overall, these observations suggest that a deep-seated process, such as upwelling of hot asthenospheric mantle, could be responsible for the large wavelength topographic features centred in the Middle Atlas. This mechanism can reconcile the large-scale surface uplift that occurred during the last 7 Ma, the non-isostatically compensated topography, the anomalous thinning of the crust and lithosphere and the deep source of the 3.7- to 0.7-My-old alkaline volcanism.

4.7. Conclusion

Our study allows characterizing the erosional dynamics and the long-term topographic evolution of a the Western Moroccan Meseta domain. The preserved relict landscape standing at high elevation and the deeply incised valleys downstream of the major non-lithological knickpoints document a transience in topography and hence different stages of topographic evolution. Specifically, the ancient relict topography displays low topographic relief, slope and k_{sn} values in association with low rates of denudation on both bedrocks and watersheds (from 4 to 14 m/Myr). Conversely, the downstream portion of the landscape exhibits higher topographic metrics and denudation rates (up to 40 m/Myr) in response to a late Messinian increase in rock uplift rates that led to a topographic rejuvenation. Within this general trend a few exceptions emerge. These are interpreted to reflect hillslope topographic gradients and weathering processes as well as the uneven distribution of quartz-bearing lithologies in the sampled catchments. In certain catchments of the Western Meseta, the granite massifs exposed atop of the relict landscape provide a higher amount of quartz than the downstream metamorphics, resulting in a mixed signal of ^{10}Be concentration. Consequently, estimates of basin-wide denudation rates are lower than expected, where the prediction is based on correlations with the topographic metrics and k_{sn}. A linear correlation with basin-wide denudation rates for catchments not affected by such an uneven distribution, in fact, allows quantifying the transient adjustment of hillslope and channels to the base level perturbation. In addition, this correlation indicates that lithology and/ or decoupling processes between hillslope and channel, don’t play a role in controlling erosional dynamics in the study area. These findings highlight that the uneven distribution of quartz-bearing rocks in the sampled catchments and their relative location within the topographic sectors (*i.e.,* relict vs rejuvenated landscape) represents a critical issue for deriving basin-wide denudation rates.

Finally, our estimates of surface uplift for the Western Moroccan Meseta and the Tabular Middle Atlas allow deciphering a large wavelength positive feature (topographic swell) with a wavelength of ~350 km centred in the Middle Atlas where the highest uplift has been also recorded by uplifted Messinian marine deposits. This is consistent with values observed in the eastern side of the Folded Middle Atlas and High Plateaus by a previous study. Combined, these findings suggest that uplift in Western Moroccan Meseta is mainly related to a deep source like asthenosphere upwelling possibly acting on wavelength of ~100 km that culminate over the Tabular and Folded Middle Atlas where a shorter wavelength signal (10 – 50 km) of tectonic origin is also present. This interpretation agrees with the occurrence of alkaline Plio-Quaternary volcanism, a shallow lithosphere-asthenosphere boundary and Moho estimates. Furthermore it explains why the marine deposits of the Skoura and the Guercif sedimentary basins started to be uplifted at ~7 Ma, shortly before the Messinian salinity crisis. Overall, out results demonstrate the potential of topographic analysis to unravel uplift processes across different spatial wavelengths, including deep-seated, large wavelength signals, and hence provides a rigorous an approach for deciphering different uplift components.

4.8. Acknowledgments

This study is part of the PhD thesis of RC at the University of Roma Tre (PhD Cycle XXXIV). It was supported by the PhD School of Roma Tre and grant “Vinci 2020” awarded to RC (Number : C2- 1403). PB was supported by the MIUR (Ministry of Education University and Research), Excellence Department Initiative, Art. 1, com. 314-337, Low 232/2016. The ASTER (CEREGE, Aix-en-Provence) AMS national facility, is supported by the INSU/CNRS, the ANR (Projets thématiques d’excellence programme for the Equipements d’Excellence) and the IRD. We thank G. Aumaître and K. Keddadouche for their expertise in AMS measurements, S. Racano, R. Lanari, N. Youbi and R. Braucher for the stimulating discussions.

4.9. References

Adams, B. A., Whipple, K. X., Forte, A. M., Heimsath, A. M., Hodges, K. V. (2020). Climate controls on erosion in tectonically active landscapes. *Sci. adv.* 6(42), eaaz3166. https://www.science.org/doi/10.1126/sciadv.aaz3166.

Arboleya, M. L., Teixell, A., Charroud, M., & Julivert, M. (2004). A structural transect through the High and Middle Atlas of Morocco. *Journal of African Earth Sciences*, 39(3‑5), 319‑327. https://doi.org/10.1016/j.jafrearsci.2004.07.036

Babault, J., Teixell, A., Arboleya, M. L., & Charroud, M. (2008). A Late Cenozoic age for long-wavelength surface uplift of the Atlas Mountains of Morocco. *Terra nova*, *20*(2), 102-107. https://doi.org/10.1111/j.1365-3121.2008.00794.x

Balco, G., Stone, J. O., Lifton, N. A., Dunai, T. J., (2008). A complete and easily accessible means of calculating surface exposure ages or erosion rates from 10Be and 26Al measurements. *Quat. Geochronol*. 3(3), 174-195. https://doi.org/10.1016/j.quageo.2007.12.001.

Ballato, P., Landgraf, A., Schildgen, T. F., Stockli, D. F., Fox, M., Ghassemi, M. R., Kirby, E., & Strecker, M. R. (2015). The growth of a mountain belt forced by base-level fall: Tectonics and surface processes during the evolution of the Alborz Mountains, N Iran. *Earth and Planetary Science Letters*, *425*, 204-218. https://doi.org/10.1016/j.epsl.2015.05.051

Barbero, L., Jabaloy, A., Gómez-Ortiz, D., Pérez-Peña, J. V., Rodríguez-Peces, M. J., Tejero, R., Estupinan, J., Azdimousa, A., & Asebriy, L. (2011). Evidence for surface uplift of the Atlas Mountains and the surrounding peripheral plateaux: Combining apatite fission-track results and geomorphic indicators in the Western Moroccan Meseta (coastal Variscan Paleozoic basement). *Tectonophysics*, 502(1-2), 90-104. https://doi.org/10.1016/j.tecto.2010.01.005

Baudon, C., Fabuel ‐ Perez, I., & Redfern, J. (2009). Structural style and evolution of a Late Triassic rift basin in the central High Atlas, Morocco: Controls on sediment deposition. *Geological Journal*, 44(6), 677‐691. https://doi.org/10.1002/gj.1195

Bezada, M. J., Humphreys, E. D., Davila, J. M., Carbonell, R., Harnafi, M., Palomeras, I., & Levander, A. (2014). Piecewise delamination of Moroccan lithosphere from beneath the Atlas Mountains. *Geochemistry, Geophysics, Geosystems*, *15*(4), 975-985. https://doi.org/10.1002/2013GC005059

Bishop, P., Hoey, T. B., Jansen, J. D., & Artza, I. L. (2005). Knickpoint recession rate and catchment area: the case of uplifted rivers in Eastern Scotland. *Earth Surface Processes and Landforms: The Journal of the British Geomorphological Research Group*, *30*(6), 767-778. https://doi.org/10.1002/esp.1191

Braucher, R., Merchel, S., Borgomano, J., Bourlès, D. L., (2011). Production of cosmogenic radionuclides at great depth: A multi element approach. *Earth Planet. Sci. Lett*. 309(1-2), 1-9. https://doi.org/10.1016/j.epsl.2011.06.036.

Braucher, R., Guillou, V., Bourlès, D. L., Arnold, M., Aumaître, G., Keddadouche, K., Nottoli, E., (2015). Preparation of ASTER in-house ^{10}Be/^{9}Be standard solutions. *Nucl. Instrum. Methods Phys. Res., Sect. Beam Interactions with Materials and Atoms*. 361, 335-340. https://doi.org/10.1016/j.nimb.2015.06.012.

Braun, J. (2010). The many surface expressions of mantle dynamics. Nature Geoscience, 3(12), 825-833. https://doi.org/10.1038/ngeo1020

Brede, R., & Heinitz, W. (1989). Durchgepauste tektonik im Mittleren Atlas Marokkos. *Zeitschrift der Deutschen Geologischen Gesellschaft*, 161-171. https://doi.org/10.1127/zdgg/140/1989/161

Calvet, M., Gunnell, Y., & Farines, B. (2015). Flat-topped mountain ranges: Their global distribution and value for understanding the evolution of mountain topography. *Geomorphology*, *241*, 255-291. https://doi.org/10.1016/j.geomorph.2015.04.015

Carretier, S., Regard, V., Vassallo, R., Martinod, J., Christophoul, F., Gayer, E., Audin, L., & Lagane, C. (2015). A note on 10Be-derived mean erosion rates in catchments with heterogeneous lithology: Examples from the western Central Andes. *Earth Surface Processes and Landforms*, *40*(13), 1719-1729. https://doi.org/10.1002/esp.3748

Champagnac, J. D., Valla, P. G., & Herman, F. (2014). Late-Cenozoic relief evolution under evolving climate: A review. *Tectonophysics*, *614*, 44-65. https://doi.org/10.1016/j.tecto.2013.11.037

Charriere, A. (1984). Évolution néogène de bassins continentaux et marins dans le Moyen Atlas central (Maroc). *Bulletin de la Société Géologique de France*, *7*(6), 1127-1136. https://doi.org/10.2113/gssgfbull.S7-XXVI.6.1127

Cyr, A. J., Granger, D. E., Olivetti, V., & Molin, P. (2010). Quantifying rock uplift rates using channel steepness and cosmogenic nuclide–determined erosion rates: Examples from northern and southern Italy. *Lithosphere,* 2(3), 188-198. https://doi.org/10.1130/L96.1

De Beer, C. H., Chevallier, L. P., De Kock, G. S., Gresse, P. G., & Thomas, R. J. (2000). Mémoire explicatif de la carte géologique du Maroc au 1/50 000, Feuille Sirwa. *Notes Mem. Serv. Geol. Maroc*, *395*, 86.

DiBiase, R. A., & Whipple, K. X. (2011). The influence of erosion thresholds and runoff variability on the relationships among topography, climate, and erosion rate. *Journal of Geophysical Research: Earth Surface*, *116*(F4). https://doi.org/10.1029/2011JF002095

Duggen, S., Hoernle, K. A., Hauff, F., Kluegel, A., Bouabdellah, M., & Thirlwall, M. F. (2009). Flow of Canary mantle plume material through a subcontinental lithospheric corridor beneath Africa to the Mediterranean. *Geology*, *37*(3), 283-286. https://doi.org/10.1130/G25426A.1

Dunne, J., Elmore, D., Muzikar, P., (1999). Scaling factors for the rates of production of cosmogenic nuclides for geometric shielding and attenuation at depth on sloped surfaces. *Geomorphology*. 27(1-2), 3-11. https://doi.org/10.1016/S0169-555X(98)00086-5.

El Azzouzi, M., Bellon, H., Maury, R. C., Pique, A., Cotten, J., Griffiths, J. B., ... & Hernandez, J. (1999). Evolution of the sources of Moroccan volcanism during the Neogene. *Comptes Rendus de l'Academie des Sciences. Serie 2, Sciences de la Terre et des Planetes*, 95-102.

El Azzouzi, M. H., Maury, R. C., Bellon, H., Youbi, N., Cotten, J., & Kharbouch, F. (2010). Petrology and K-Ar chronology of the Neogene-quaternary Middle Atlas basaltic province, Morocco. *Bulletin de la société géologique de France*, *181*(3), 243-257. https://doi.org/10.2113/gssgfbull.181.3.243

Faccenna, C., Molin, P., Orecchio, B., Olivetti, V., Bellier, O., Funiciello, F., Minelli, L., Piromallo, C., & Billi, A. (2011). Topography of the Calabria subduction zone (southern Italy): Clues for the origin of Mt. Etna. *Tectonics*, 30(1). https://doi.org/10.1029/2010TC002694

Faccenna, C., & Becker, T. W. (2020). Topographic expressions of mantle dynamics in the Mediterranean. *Earth-Science Reviews*, 103327. https://doi.org/10.1016/j.earscirev.2020.103327

Flint, J. J. (1974). Stream gradient as a function of order, magnitude, and discharge. *Water Resources Research*, 10, 969‑973.

Forte, A. M., & Whipple, K. X. (2019). Short communication: The Topographic Analysis Kit (TAK) for TopoToolbox, *Earth Surface Dynamics*. 7, 87–95. https://doi.org/10.5194/esurf-7-87-2019.

Fox, M. (2019). A linear inverse method to reconstruct paleo-topography. *Geomorphology*, *337*, 151-164. https://doi.org/10.1016/j.geomorph.2019.03.034

Frizon de Lamotte, D., Leturmy, P., Missenard, Y., Khomsi, S., Ruiz, G., Saddiqi, O., Guillocheau F., & Michard A. (2009). Mesozoic and Cenozoic vertical movements in the Atlas system (Algeria, Morocco, Tunisia). An overview: *Tectonophysics*. 475, 9‑28. https://doi.org/10.1016/j.tecto.2008.10.024.

Gallen, S. F., & Wegmann, K. W. (2017). River profile response to normal fault growth and linkage: An example from the Hellenic forearc of south-central Crete, Greece. *Earth Surface Dynamics*, *5*(1), 161-186. https://doi.org/10.5194/esurf-5-161-2017

Gallen, S. F. (2018). Lithologic controls on landscape dynamics and aquatic species evolution in post-orogenic mountains. *Earth and Planetary Science Letters*, *493*, 150-160. https://doi.org/10.1016/j.epsl.2018.04.029.

Gasquet, D., Ennih, N., Liégeois, J. P., Soulaimani, A., & Michard, A. (2008). The pan-african belt. In *Continental evolution: the geology of Morocco* (pp. 33-64). Springer, Berlin, Heidelberg. https://doi.org/10.1007/978-3-540-77076-3_2

Godard, V., Dosseto, A., Fleury, J., Bellier, O., Siame, L., & ASTER Team. (2019). Transient landscape dynamics across the Southeastern Australian Escarpment. *Earth and Planetary Science Letters*, *506*, 397-406. https://doi.org/10.1016/j.epsl.2018.11.017

Godard, V., Salgado, A., Siame, L., Fleury, J., & Team, A. (2021). Transient hillslope erosion in slow evolution landscapes. *Earth Surface Processes and Landforms*, *46*(12), 2485-2500. https://doi.org/10.1002/esp.5190

Gomez, F., Barazangi, M., & Bensaid, M. (1996). Active tectonism in the intracontinental Middle Atlas Mountains of Morocco: synchronous crustal shortening and extension. *Journal of the Geological Society*, *153*(3), 389-402. https://doi.org/10.1144/gsjgs.153.3.0389

Gomez, F., Allmendinger, R., Barazangi, M., Er-Raji, A., & Dahmani, M. (1998). Crustal shortening and vertical strain partitioning in the Middle Atlas Mountains of Morocco. *Tectonics*, *17*(4), 520-533. https://doi.org/10.1029/98TC01439

Goren, L., Fox, M., & Willett, S. D. (2014). Tectonics from fluvial topography using formal linear inversion: Theory and applications to the Inyo Mountains, California. *Journal of Geophysical Research: Earth Surface*, *119*(8), 1651-1681. https://doi.org/10.1002/2014JF003079

Guimerà, J., Arboleya, M. L., & Teixell, A. (2011). Structural control on present-day topography of a basement massif: the Central and Eastern Anti-Atlas (Morocco). *Geologica Acta: an international earth science journal*, *9*(1), 55-65. https://doi.org/10.1344/105.00 0001643.

Hancock, G., & Kirwan, M. (2007). Summit erosion rates deduced from 10Be: Implications for relief production in the central Appalachians. *Geology*, 35(1), 89-92. https://doi.org/10.1130/G23147A.1

Harel, M. A., Mudd, S. M., & Attal, M. (2016). Global analysis of the stream power law parameters based on worldwide 10Be denudation rates. *Geomorphology*, 268, 184-196. https://doi.org/10.1016/j.geomorph.2016.05.035

Heidarzadeh, G., Ballato, P., Hassanzadeh, J., Ghassemi, M. R., & Strecker, M. R. (2017). Lake overspill and onset of fluvial incision in the Iranian Plateau: Insights from the Mianeh Basin. *Earth and Planetary Science Letters*, 469, 135-147. https://doi.org/10.1016/j.epsl.2017.04.019

Hoepffner, C., Soulaimani, A., & Piqué, A. (2005). The moroccan hercynides. *Journal of African Earth Sciences*, 43(1-3), 144-165. https://doi.org/10.1016/j.jafrearsci.2005.09.002

Hollard, H., Choubert, G., Bronner, G., Marchand, J., Sougy, J. (1985). Carte géologique du Maroc, scale 1: 1,000,000. *Serv. Carte géol. Maroc*. 260(2).

Howard, A. D. (1994). A detachment-limited model of drainage basin evolution. Water resources research, 30(7), 2261-2285. https://doi.org/10.1029/94WR00757

Hurst, M. D., Mudd, S. M., Attal, M., & Hilley, G. (2013). Hillslopes record the growth and decay of landscapes. *Science*, *341*(6148), 868-871. https://doi.org/10.1126/science.1241791

Kanamaru, T., Suganuma, Y., Oiwane, H., Miura, H., Miura, M., Okuno, J. I., Hayakawa, H. (2018). The weathering of granitic rocks in a hyper-arid and hypothermal environment: A case study from the Sør-Rondane Mountains, East Antarctica. *Geomorphology*. 317, 62-74. https://doi.org/10.1016/j.geomorph.2018.05.015.

Kirby, E., & Whipple, K. X. (2012). Expression of active tectonics in erosional landscapes. *Journal of Structural Geology*, *44*, 54-75. https://doi.org/10.1016/j.jsg.2012.07.009.

Krijgsman, W., Langereis, C. G., Zachariasse, W. J., Boccaletti, M., Moratti, G., Gelati, R., Iaccarino, F., Papani, G., & Villa, G. (1999). Late Neogene evolution of the Taza–Guercif Basin (Rifian Corridor, Morocco) and implications for the Messinian salinity crisis. Marine Geology, 153(1-4), 147-160.

Lal, D., (1991). Cosmic ray labeling of erosion surfaces: in situ nuclide production rates and erosion models. *Earth Planet. Sci. Lett*.104, 424–439. http://dx.doi.org/10.1016/0012-821X(91)90220-C.

Lanari, R., Fellin, M. G., Faccenna, C., Balestrieri, M. L., Pazzaglia, F. J., Youbi, N., & Maden, C. (2020a). Exhumation and surface evolution of the western high atlas and surrounding regions as constrained by low-temperature thermochronology. *Tectonics*, *39*(3), e2019TC005562. https://doi.org/10.1029/2019TC005562

Lanari, R., Faccenna, C., Fellin, M. G., Essaifi, A., Nahid, A., Medina, F., & Youbi, N. (2020b). Tectonic evolution of the western high Atlas of Morocco: oblique convergence, reactivation, and transpression. *Tectonics*, *39*(3), e2019TC005563. https://doi.org/10.1029/2019TC005563

Mandal, S. K., Lupker, M., Burg, J. P., Valla, P. G., Haghipour, N., & Christl, M. (2015). Spatial variability of 10Be-derived erosion rates across the southern Peninsular Indian escarpment: A key to landscape evolution across passive margins. *Earth and Planetary Science Letters*, 425, 154-167. https://doi.org/10.1016/j.epsl.2015.05.050.

Matmon, A., Bierman, P. R., Larsen, J., Southworth, S., Pavich, M., & Caffee, M. (2003). Temporally and spatially uniform rates of erosion in the southern Appalachian Great Smoky Mountains. *Geology*, 31(2), 155-158. https://doi.org/10.1130/0091-7613(2003)031<0155:TASURO>2.0.CO;2

Merchel, S., Arnold, M., Aumaître, G., Benedetti, L., Bourlès, D. L., Braucher, R., Alfimov V., Freeman S.P.H.T., Steier P., Wallner, A., (2008). Towards more precise ^{10}Be and ^{36}Cl data from measurements at the 10− 14 level: Influence of sample preparation. *Nucl. Instrum. Methods Phys. Res., Sect. Beam Interactions with Materials and Atoms*. 266(22), 4921-4926. https://doi.org/10.1016/j.nimb.2008.07.031.

Meyer, H., Hetzel, R., Fügenschuh, B., & Strauss, H. (2010). Determining the growth rate of topographic relief using in situ-produced 10Be: a case study in the Black Forest, Germany. *Earth and Planetary Science Letters*, 290(3-4), 391-402. https://doi.org/10.1016/j.epsl.2009.12.034

Miller, S. R., Baldwin, S. L., & Fitzgerald, P. G. (2012). Transient fluvial incision and active surface uplift in the Woodlark Rift of eastern Papua New Guinea. *Lithosphere*, *4*(2), 131-149. https://doi.org/10.1130/L135.1

Miller, S. R., Sak, P. B., Kirby, E., & Bierman, P. R. (2013). Neogene rejuvenation of central Appalachian topography: Evidence for differential rock uplift from stream profiles and erosion rates. *Earth and Planetary Science Letters*, *369*, 1-12. https://doi.org/10.1016/j.epsl.2013.04.007

Miller, M. S., & Becker, T. W. (2014). Reactivated lithospheric-scale discontinuities localize dynamic uplift of the Moroccan Atlas Mountains. *Geology*, *42*(1), 35-38. https://doi.org/10.1130/G34959.1.

Miller, M. S., O'Driscoll, L. J., Butcher, A. J., & Thomas, C. (2015). Imaging Canary Island hotspot material beneath the lithosphere of Morocco and southern Spain. *Earth and Planetary Science Letters, 431*, 186-194. https://doi.org/10.1016/j.epsl.2015.09.026

Missenard, Y., Zeyen, H., Frizon de Lamotte, D., Leturmy, P., Petit, C., Sébrier, M., & Saddiqi, O. (2006). Crustal versus asthenospheric origin of relief of the Atlas Mountains of Morocco. *Journal of Geophysical Research: Solid Earth*, *111*(B3). https://doi.org/10.1029/2005JB003708

Molin, P., Fubelli, G., Nocentini, M., Sperini, S., Ignat, P., Grecu, F., & Dramis, F. (2012). Interaction of mantle dynamics, crustal tectonics, and surface processes in the topography of the Romanian Carpathians: A geomorphological approach. *Global and Planetary Change*, *90*, 58-72. https://doi.org/10.1016/j.gloplacha.2011.05.005

Molnar, P., & England, P. (1990). Late Cenozoic uplift of mountain ranges and global climate change: chicken or egg?. *Nature*, *346*(6279), 29-34. https://doi.org/10.1038/346029a0

Morel, J. M., & Cabanis, B. (1993). Mise en évidence d'une association magmatique dans le volcanisme plio-quaternaire du Moyen-Atlas marocain. *Comptes rendus de l'Académie des sciences. Série 2, Mécanique, Physique, Chimie, Sciences de l'univers, Sciences de la Terre*, *316*(3), 357-362.

Mrini, Z., Rafi, A., Duthou, J. L., & Vidal, P. (1992). Chronologie Rb-Sr des granitoides hercyniens du Maroc; consequences. Bulletin de la Société géologique de France, 163(3), 281-291.

Mudd, S. M. (2017). Detection of transience in eroding landscapes. Earth Surface Processes and Landforms, 42(1), 24-41. https://doi.org/10.1002/esp.3923

Ouimet, W. B., Whipple, K. X., & Granger, D. E. (2009). Beyond threshold hillslopes: Channel adjustment to base-level fall in tectonically active mountain ranges. *Geology*, 37(7), 579-582. https://doi.org/10.1130/G30013A.1

Olivetti, V., Cyr, A. J., Molin, P., Faccenna, C., & Granger, D. E. (2012). Uplift history of the Sila Massif, southern Italy, deciphered from cosmogenic 10Be erosion rates and river longitudinal profile analysis. *Tectonics*, *31*(3). https://doi.org/10.1029/2011TC003037

Olivetti, V., Godard, V., Bellier, O., & ASTER team. (2016). Cenozoic rejuvenation events of Massif Central topography (France): Insights from cosmogenic denudation rates and river profiles. *Earth and Planetary Science Letters*, *444*, 179-191. https://doi.org/10.1016/j.epsl.2016.03.049.

Pastor, A., Babault, J., Owen, L. A., Teixell, A., & Arboleya, M. L. (2015). Extracting dynamic topography from river profiles and cosmogenic nuclide geochronology in the Middle Atlas and the High Plateaus of Morocco. *Tectonophysics*, *663*, 95-109. https://doi.org/10.1016/j.tecto.2015.06.007

Perron, J. T., & Royden, L. (2013). An integral approach to bedrock river profile analysis. *Earth Surface Processes and Landforms*, *38*(6), 570-576. https://doi.org/10.1002/esp.3302.

Safran, E. B., Bierman, P. R., Aalto, R., Dunne, T., Whipple, K. X., Caffee, M., (2005). Erosion rates driven by channel network incision in the Bolivian Andes. *Earth Surf. Processes Landforms,* 30(8), 1007-1024. https://doi.org/10.1002/esp.1259.

Scharf, T. E., Codilean, A. T., De Wit, M., Jansen, J. D., & Kubik, P. W. (2013). Strong rocks sustain ancient postorogenic topography in southern Africa. *Geology*, *41*(3), 331-334. https://doi.org/10.1130/G33806.1.

Schwanghart, W., & Scherler, D. (2014). TopoToolbox 2–MATLAB-based software for topographic analysis and modeling in Earth surface sciences. *Earth Surface Dynamics*, *2*(1), 1-7. https://doi.org/10.5194/esurf-2-1-2014.

Snyder, N. P., Whipple, K. X., Tucker, G. E., & Merritts, D. J. (2000). Landscape response to tectonic forcing: Digital elevation model analysis of stream profiles in the Mendocino triple junction region, northern California. *Geological Society of America Bulletin*, *112*(8), 1250-1263. https://doi.org/10.1130/0016-7606(2000)112<1250:LRTTFD>2.0.CO;2

Soulaimani, A., Bouabdelli, M., & Piqué, A. (2003). L'extension continentale au Néo-Protérozoïque supérieur-Cambrien inférieur dans l'Anti-Atlas (Maroc). *Bulletin de la Société géologique de France*. http://hdl.handle.net/2042/244

Stone, J. O., (2000). Air pressure and cosmogenic isotope production. *J. Geophys. Res., Solid Earth*. 105(B10), 23753-23759. https://doi.org/10.1029/2000JB900181.

Willett, S. D., & Brandon, M. T. (2002). On steady states in mountain belts. *Geology*, *30*(2), 175-178. https://doi.org/10.1130/0091-7613(2002)030<0175:OSSIMB>2.0.CO;2

Whipple, K. X., & Tucker, G. E. (1999). Dynamics of the stream-power river incision model: Implications for height limits of mountain ranges, landscape response timescales, and research needs. *Journal of Geophysical Research: Solid Earth*, 104(B8), 17661-17674. https://doi.org/10.1029/1999JB900120.

Whipple, K. X. (2001). Fluvial landscape response time: How plausible is steady-state denudation?. *American Journal of Science*, *301*(4-5), 313-325. https://doi.org/10.2475/ajs.301.4-5.313

Whipple, K. X. (2004). Bedrock rivers and the geomorphology of active orogens. *Annu. Rev. Earth Planet. Sci.*, *32*, 151-185. https://doi.org/10.1146/annurev.earth.32.101802.120356

Wobus, C., Whipple, K. X., Kirby, E., Snyder, N., Johnson, J., Spyropolou, K., Crosby, B., & Sheehan, D. (2006). Tectonics from topography: Procedures, promise, and pitfalls. *Special papers-Geological Society of America*, *398*, 55.https://doi.org/10.1130/2006.2398(04)

Yang, R., Willett, S. D., & Goren, L. (2015). In situ low-relief landscape formation as a result of river network disruption. *Nature*, *520*(7548), 526-529. https://doi.org/10.1038/nature14354

Youbi, N., Cabanis, B., Chalot-Prat, F., & Cailleux, Y. (1995). Histoire volcano-tectonique du massif permien de Khénifra (Sud-Est du Maroc Central). *Geodinamica Acta*, 8(3), 158-172. https://doi.org/10.1080/09853111.1995.11105387

Chapter 5. General conclusions

The results of this Ph.D. thesis provide first-order constrains to understand the topographic evolution of the Atlas-Meseta orographic system. Although several questions are still open, the combination of geomorphic data and denudation rates from watersheds and bedrocks cosmogenic nuclide concentration, allow concluding that:

- The tectonically inactive sectors of the Atlas-Meseta system (Anti-Atlas and Western Mesetas) consist of uplifted, low-topographic relief, relict landscapes located upstream of major non-lithological knickpoints. These regions document erosional conditions predating the recent increase in uplift rates that led to a topographic resurgence. The coincidence in the relict landscape between short-term, ^{10}Be erosion rates, and long-term rates from low temperature thermochronology suggests steady state conditions at least since the late Cretaceous. Instead, the downstream portions of the landscape record the recently established erosional setting associated with the increase in uplift rates. There, erosion rates are five times higher. This configuration suggests that the entire landscape is in a transient state and is progressively adjusting to new uplift/erosion conditions.
- In the Anti-Atlas, the relict landscape shows a clear lithological control on the erosional dynamics and topographic relief production. In particular, the erodibility parameter ranges from $1.4 \pm 0.9 \times 10^{-7}$ to $3.8 \pm 0.4 \times 10^{-7}$ $m^{0.1}$/ yr for quartzite and granitic dominated basins. This agrees with estimates from other slow tectonic regions located in different climatic zones, demonstrating the critical role of bedrock erodibility on the development of topographic relief of the relict landscape.
- The surface uplift estimates for the Anti-Atlas vary from 500 to more than 1100 m, from the western to the central Anti-Atlas sectors and 1150 m in the Siroua Massif (Fig. 5.2). Surface uplift occurred over a wavelength of ~600 x 100 km with a maximum amplitude of ~1150 m and started most likely during middle-late Miocene (10±4 Ma) together with magmatism. The peak of uplift is documented in the Siroua area where additional uplift mechanisms are superimposed onto the large wavelength signal. These uplift mechanisms include local faulting and most likely magma injection within the crust.

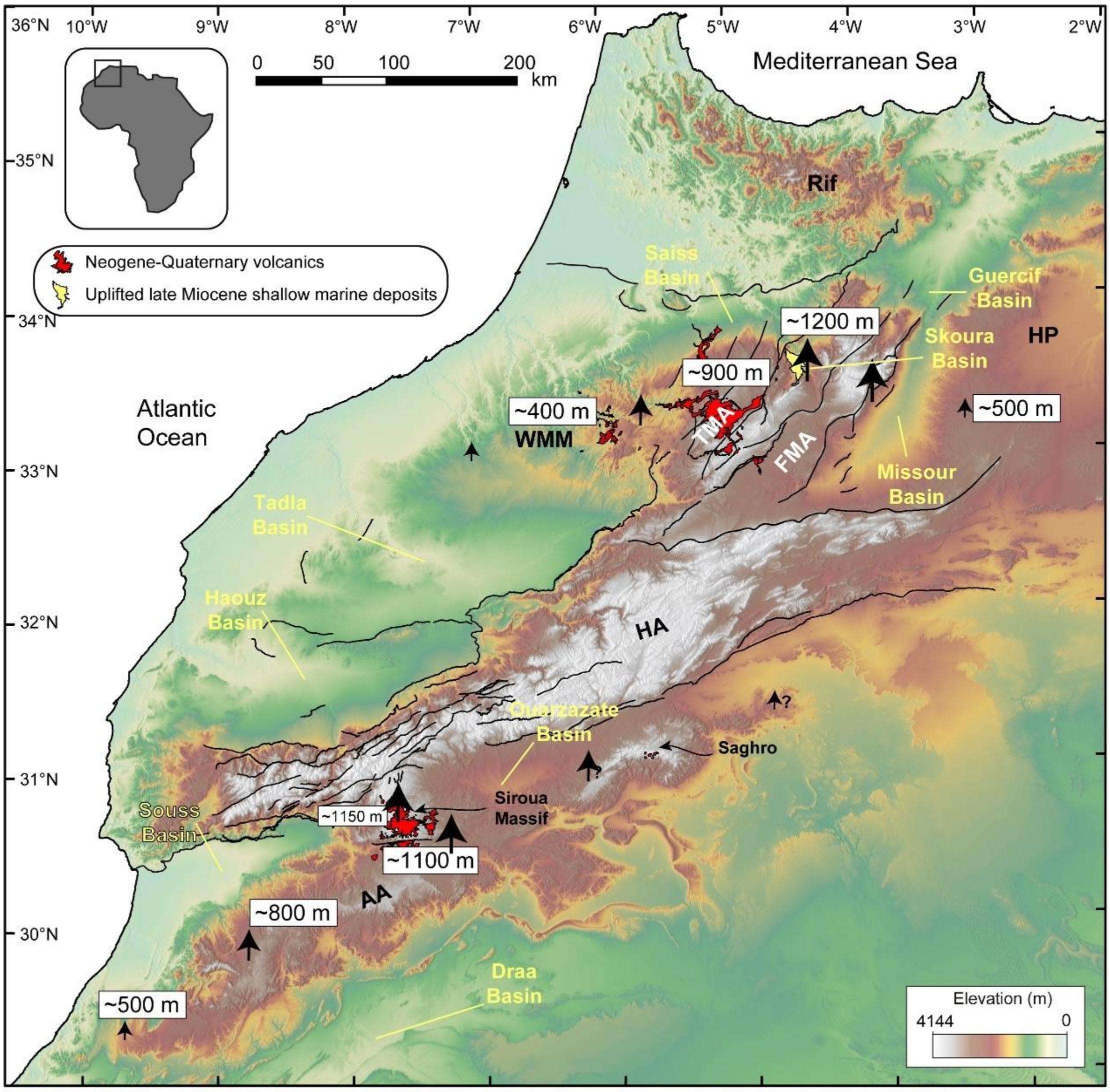

Figure 5.1. Topographic map of the Atlas-Meseta system and his morpho-structural domains. FMA: Folded Middle Atlas. TMA: Tabular Middle Atlas. HP: High Plateaus. WMM: Western Moroccan Meseta. AA : Anti-Atlas. HA : High Atlas. Black arrows and values indicate the magnitude of surface uplift estimates from this work. Black lines indicate the main faults.

- The Western Moroccan Meseta is also characterized by a rejuvenated topography, with a transient adjustment of hillslopes and fluvial channels to the new uplift conditions. The magnitude of surface uplift increases progressively from 400 to 900 and 1100/1200 m from the Western Moroccan Meseta, to the Tabular Middle Atlas and the Folded Middle Atlas, respectively. These estimates are consistent with data from the surrounding domains and describe a large wavelength signal from the Weastern Meseta to the High Plateaus, with a peak beneath the Folded Middle Atlas domain where tectonic deformation occurs (Fig. 5.1). Our data are in agreement with available geological and volcanological data, such as uplifted shallow marine deposits in the Taza-Guercif and Skoura basins, which indicates a shallowing-upward trend at ~7 Ma, representing an important marker to constrain the timing of uplift in this sector. Moreover, the ^{10}Be concentrations from catchments and bedrocks highlight the importance of considering uneven distribution of quartz-bearing rocks. Indeed, linear correlation between the estimates of denudation and metrics are observed when considered only the catchments characterized by uniform distribution of quartz-bearing rocks, documenting the transient adjustment of hillslope and channels to the base level perturbation.

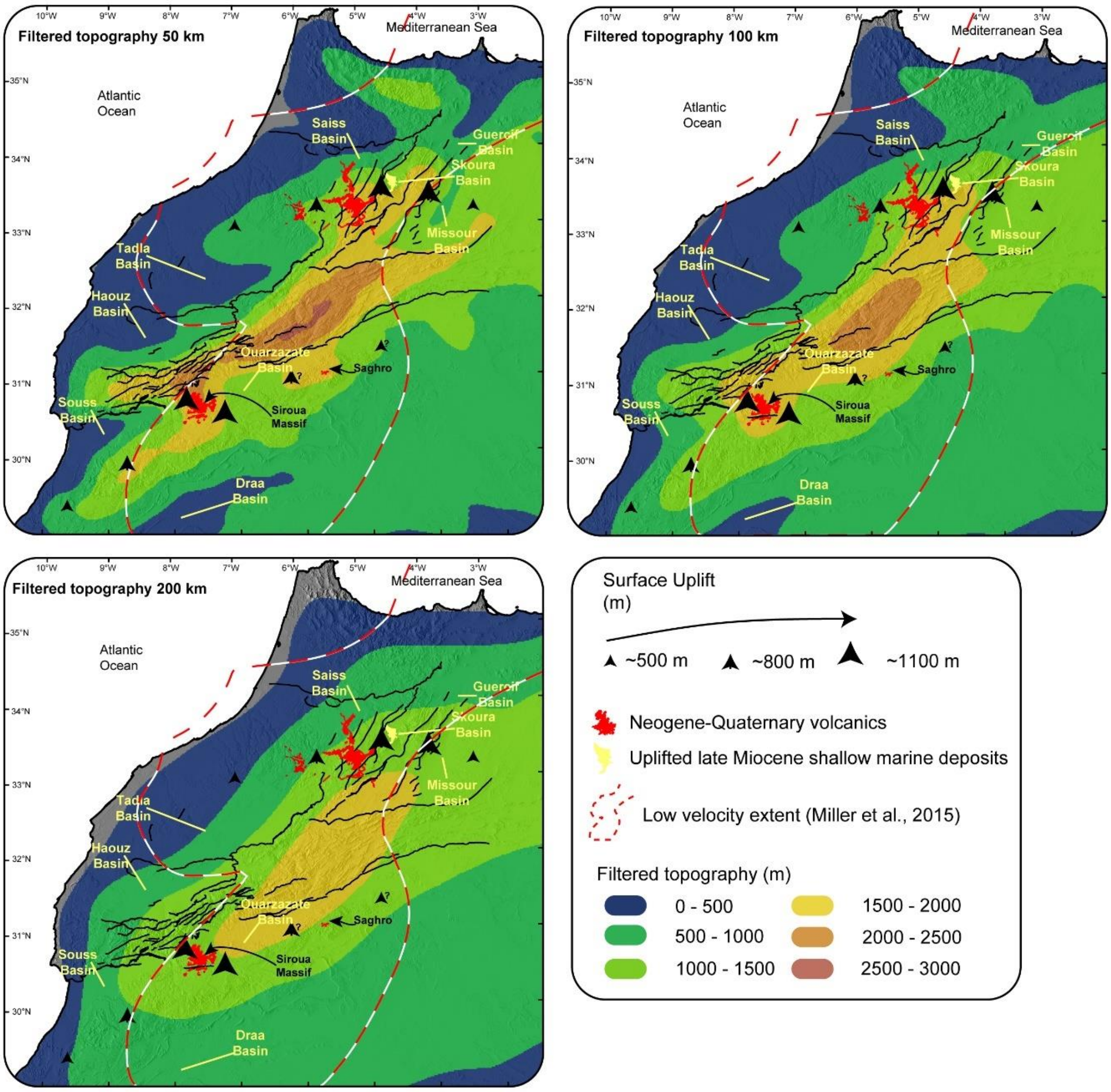

Figure 5.2. Filtered topographic maps of the Atlas-Meseta system at 50, 100 and 200 km radius, with major tectonic structures, late Cenozoic lava flows and magnitude of surface uplift.

- The sedimentary basins, in between the main topographic high can be still distinguished at lower filtered windows (e.g., 50 km). However, the signal becomes unique at a wavelength of ca. 200 km. This indicates that the different domains of the Atlas-Meseta system can be described as a single, larger swell (Fig. 5.2). Importantly our surface uplift estimates agree with the elevation extracted from the filtered topography suggesting that the mechanisms that created the modern topography must be controlled by processes operating at large wavelength (200 km). These observations, combined with the lack of recent tectonic deformation, at least in the quiescent Anti-Atlas and the Meseta, indicate that the topographic growth was controlled by deep-mantle processes.
- The agreement between the distribution of modern and filtered (averaged radius of 200 km) topography, the occurrence of recent (Miocene-Quaternary) volcanism in the peripheral, tectonically inactive zones of the Atlas-Meseta system, and the rough coincidence between the 200km filtered topography and the low velocity anomaly at 200 km of depth (Sun et al., 2014; Miller et al., 2015). suggest that these deep-seated processes where most likely characterized by astenospheric upwelling. Such a magmatism seems to have occurred in areas of the Atlas-Meseta system, where strike-slip faulting occurs, possibly favoring the rise of magma. Additional processes such as shortening (see the High-Atlas, Middle-Atlas) and magmatic addition (see the Siroua, Western Meseta and Tabular Middle Atlas) may have produced local shorter wavelength uplift.

Overall, in this work, I quantified the timing, magnitudes and rates of mantle-driven uplift from the inactive tectonically domains of the Atlas-Meseta system. The combined approach of traditional and innovative techniques, together with compilations of published data, allowed to characterize the topographic growth of this intracontinental and elevated belt. This approach provides new inspiration for exploring settings affected by recent topographic rejuvenation, especially when the geomorphic markers are the unique available archive because stratigraphic evidence are scarce.

Appendix Chapter 2.

Table S2.1. Basin-wide denudation rates from cosmogenic ^{10}Be in river borne sand samples

Sample	Long.	Lat.	Elev.[a]	Quarz mass[b]	Carrier mass (^{9}Be)	^{10}Be/^{9}Be[c]		[^{10}Be][d] 10^3 (at./ g)		Production rate[e] (at./ g/ yr)			Denudation (m/ Myr)		Integration time[f] (yr)	
ID	°W	°N	(m)	(g)	(g)	Value (10^{-15})	Error (%)	Value	Error	Neutrons	Slow muons	Fast muons	Value	Error	Value	Error
4	6.8746	30.1248	964	21.25	0.151	413.9	3.6	593.6	22	8.29	0.02	0.05	9.25	0.65	75651	5307
11	9.1448	30.1667	1601	20.84	0.148	753.3	3.0	1083.8	34	9.03	0.02	0.05	7.53	0.51	92079	6225
7	7.8442	30.2851	1835	21.25	0.152	632.7	2.8	914.3	26	12.91	0.03	0.06	10.72	0.71	65592	4347
2	6.0539	30.2815	1275	21.05	0.150	539.5	3.4	775.6	27	8.62	0.02	0.05	8.67	0.60	80497	5595
10	8.3909	30.3910	1525	20.50	0.149	658.2	3.1	970.4	31	9.70	0.02	0.05	8.10	0.55	85962	5845
12	8.9737	29.2456	1538	21.29	0.151	456.1	4.7	652.6	31	9.49	0.02	0.05	12.46	0.95	56700	4326
1	5.3260	30.628	1135	20.92	0.147	858.4	1.9	1221.0	23	8.73	0.02	0.05	4.85	0.31	139378	8774
5	7.1218	30.625	1573	20.65	0.149	607.3	3.2	883.7	29	11.55	0.02	0.06	9.38	0.64	74627	5092
8	7.7955	30.0064	1863	20.52	0.150	326.1	3.3	480.7	16	10.97	0.02	0.06	21.32	1.47	33542	2312
13	8.5513	29.2479	715	20.77	0.150	450.3	3.0	657.3	20	6.18	0.02	0.05	6.72	0.45	102600	6929
3	6.4668	30.6868	1248	20.90	0.152	754.0	2.9	1105.8	33	9.03	0.02	0.05	5.78	0.39	118351	7948
9	8.0042	29.8237	1334	21.05	0.151	432.1	3.0	623.9	19	9.71	0.02	0.05	11.34	0.77	62160	4201
6	7.9521	30.7082	1836	20.66	0.151	175.8	5.7	257.4	15	13.45	0.03	0.06	40.96	3.42	17599	1469
Process blank						0.447	51.2									

[a] Basin mean elevation.

[b] Mass of pure quartz dissolved.

[c] Isotopic ratio uncertainties include statistical error on counted ^{10}Be events (N) and analytical error correction.

[d] Uncertainties on ^{10}Be concentrations are calculated using the standard error propagation method using the quadratic sum of the relative errors associated to the counting statistics, AMS internal error (0.5% for ASTER), and error associated to the process blank.

[e] Production rate is the spatially averaged production rate over the river basin, scaled for elevation, latitude (Stone, 2000) and geomorphic shielding (Dunne et al., 1999). The values are calculated for a non-uniform distribution of quartz-lithologies in the sample basins (*e.g.*, Safran et al., 2005; Carretier et al., 2015).

[f] Integration times are calculated after Lal (1991) while their uncertainties are calculated propagating the error of the denudation rates.

Table S2.2. Knickpoint and river profile data

Stream[a]	Long.	Lat.	Elevation	DFD[b]	DFM[c]	Drainage area	Stream parameters			
							Downstream		Upstream	
	°W	°N	(m)	(m)	(m)	(km^2)	k_{sn} ($m^{0.9}$)	θ	k_{sn} ($m^{0.9}$)	θ
NAA1	637465.1	3379132.5	1731	20354.6	280487.6	157.7	114.6 ± 0.2	0.42	15 ± 0.3	0
NAA2	613556.8	3372613.8	1424	56831.3	257482.3	432.6	118.5± 0.4	0.58	42.6 ± 0.78	0
NAA3	608426.8	3354013.8	1565	23537.1	266134.2	141.6	108.5 ± 0.4	0.43	35.5 ± 0.5	0.25
NAA4	596666.8	3351313.8	1492	18508.4	257691	103.2	111.5 ± 0.43	0.41	43 ± 0.4	0.3
NAA5	589316.8	3345523.8	1529	11566.5	266422.9	26.4	90.4 ± 0.5	0.28	30 ± 0.3	0.34
NAA6	561056.8	3341233.8	1506	13041.2	185763.1	35.2	102 ± 0.55	0.49	46 ± 0.7	0.2
NAA7	555176.8	3340753.8	1324	16987.9	185931.6	47.3	105 ± 0.42	0.35	63.7 ± 1	0.38
NAA8	550076.8	3341713.8	1387	20427.4	187603.8	46.9	103 ± 0.43	0.34	39 ± 0.9	-0.1
NAA9	543836.8	3339913.8	1334	21396.4	162843.2	69.5	99.5 ± 0.47	0.56	45.2 ± 1.2	-0.18
NAA10	525536.8	3328513.8	1175	24446.5	128875.8	81.0	136.8 ± 0.44	0.46	57 ± 0.56	0.27
WAA1	497197.4	3309532.6	1111	15696.8	137453.2	54.8	61.5 ± 0.2	0.6	37.5 ± 1.17	0.86
WAA2	443907.4	3255074.6	857	25669.3	106609.4	148.6	72.16 ± 0.6	0.8	49 ± 1.1	0.1
WAA3	433249.4	3252884.6	849	29224.3	62967.29	111.3	79.9 ± 0.4	0.63	35.3 ± 0.75	-0.1
WAA4	422883.4	3241277.6	854	11251.1	115444.2	12.5	62.7 ± 0.3	0.33	30.7 ± 0.43	0.02
WAA5	428504.4	3236605.6	1012	12228.2	128546.6	22.5	67.8 ± 0.37	0.39	20.24 ± 0.6	-0.18
WAA6	445513.4	3233028.6	982	14909.3	143614.5	29.4	66.2 ± 0.37	0.63	45.4 ± 3.44	-0.90
WAA7	471939.4	3246752.6	1272	10221.8	206751.6	30.9	66.86 ± 0.17	0.37	25.3 ± 0.85	-0.10
WAA8	482670.4	3251424.6	1294	11699.5	208687.2	33.5	68.8 ± 0.14	0.36	18.1 ± 0.47	0.08
WAA9	483765.4	3234050.6	971	43222.3	187564.6	254.9	72.5 ± 0.21	0.42	33.6 ±	0.02

									0.43	
SAA1	497927.4	3246825.6	1181	27564.3	430725.4	162.0	82.56 ± 0.21	0.51	25.9 ± 0.57	0.76
SAA2	520922.4	3281573.6	1628	14831.1	482538.4	39.3	79.58 ± 0.1	0.38	24 ± 0.38	0.04
SAA5	549465.4	3322015.6	1580	12837.2	592340.5	32.3	86.4 ± 0.1	0.43	27.9 ± 0.23	0.47
SAA6	564284.4	3324643.6	1448	17885.5	608379.3	151.3	79.85 ± 0.26	0.52	49.1 ± 0.35	0.37
SAA7	618961.4	3336542.6	1773	13358.6	685609.1	21.4	89.76 ± 0.67	0.63	15.7 ± 0.5	-0.03
SAA8	636992.4	3343550.6	1476	22859.9	672273.4	86.1	70.85 ± 0.3	0.63	46.17 ± 0.6	0.20
Mean							87.9 ± 4.07	0.47 ± 0.02	36.0 ± 2.5	0.12 ± 0.07

[a] NAA : rivers draining the northern flank of Anti-Atlas; WAA : rivers draining the western flank of Anti-Atlas; SAA : rivers draining the southern flank of Anti-Atlas.

[b] Distance from divide.

[c] Distance from river mouth.

Table S2.3. Denudation rates estimates from the volume of early Miocene volcanic rocks eroded from the Siroua relict landscape.

Stream	Eroded material[a]	Basin area[b]	V / A[c] (m)	Basalt age[d] (Myr)		Denudation rate[e] (m/ Myr)	
	(km^3)	(km^2)	Value	Value	Error	Value	Error
1	0.875	12.77	68.4	4.2	0.2	16.3	0.7
2	3.231	35.87	90.0	6.4	-	14.1	-
3	1.402	13.71	102.2	4.3	0.2	23.8	1
4	3.935	48.03	81.9	6.4	-	12.8	-
5	0.684	10.11	67.6	6.4	-	10.6	-

[a] Estimated missing volume of eroded material between a smooth surface fitting the preserved summit of the flat basaltic flows and the present-day topography.
[b] Basin area extracted from ArcGIS.
[c] Ratio between volume of eroded material and basin area (e.g., Siame et al., 2015).
[d] Age of the Siroua volcanics from Berrahma and Delaloye, (1989); De Beer et al., (2000).
[e] Ratio between eroded material from the river basin and the volcanic age.

Table S2.4. Distribution of quartz- bearing lithologies in the river basins of the study area

Sample	Basin area	Quartz-bearing area	Quartz-bearing area	Lithology of quartz-bearing areas (%)				
ID	(km^2)	(km^2)	(%)	Quartzite	Conglomerate	Granite	Shist	Sedimentary
4	1828.07	270.25	15	0.0	0.0	19.1	0.0	80.9
11	1200.60	132.42	11	72.7	27.3	0.0	0.0	0.0
7	74.07	42.51	58	18.4	0.0	79.9	1.7	0.0
2	367.23	87.80	24	0.0	9.3	0.0	0.0	90.7
10	480.059	146.35	31	52.9	47.1	0.0	0.0	0.0
12	842.711	102.57	12	0.0	5.7	88.6	5.7	0.0
1	3427.21	2008.77	59	0.0	6.3	2.2	0.0	91.0
5	1438.89	933.20	65	3.0	0.0	97.0	0.0	0.0
8	195.75	29.64	15	0.0	0.0	9.5	0.0	90.5
13	73.76	13.83	19	0.0	26.4	0.0	0.0	73.6
3	558.25	234.39	42	0.0	0.0	0.0	0.0	100.0
9	1905.07	219.24	12	31.2	49.3	1.6	17.9	0.0
6	286.74	171.73	60	2.2	0.0	65.5	32.2	0.0

Table S2.5. Averaged denudation rate, channel steepness, topographic slope, local relief, precipitation rate and main rock-type of the quartz-bearing lithologies exposed in the sampled basins.

Sample	Denudation rate (m/ Myr)		k_{sn} ($m^{0.9}$)[a]		Slope[b]	Local Relief (2.5 km radius)[c]	Precipitation rate[d]	Main quartz-bearing lithology[e]
ID	Value	Error	Value	Error	(°)	(m)	(mm/ yr)	Type
4	9.25	0.65	32.9	0.8	7.9	320.1	143.3	Sedimentary
11	7.53	0.51	58.8	2.8	12.6	598.93	334.2	Quartzite
7	10.72	0.71	30.6	1.5	8.1	394.9	406.6	Granite
2	8.67	0.60	36.0	0.9	9.5	299	109.8	Sedimentary
10	8.10	0.55	62.5	3.0	10.8	488.64	370.7	Quartzite
12	12.46	0.95	35.3	2.2	5.5	286.15	284.7	Granite
1	4.85	0.31	26.6	0.3	7.2	283.4	89.6	Sedimentary
5	9.38	0.64	22.7	0.6	3.8	213.4	363.5	Granite
8	21.32	1.47	66.8	3.2	11.1	375.8	339.1	Sedimentary
13	6.72	0.45	34.8	3.3	7.3	312.07	149.1	Sedimentary
3	5.78	0.39	28.5	0.6	5.5	320.6	139.6	Sedimentary
9	11.34	0.77	64.0	3.2	12.8	586.9	288.3	Quartzite
6	40.96	3.42	105.4	4.3	13.6	606.67	452.1	Granite

[a] Basin-averaged k_{sn} of quartz-bearing lithologies in the sampled basins.

[b] Basin-averaged slope of quartz-bearing lithologies in the sampled basins.

[c] Basin-averaged local relief (2.5 km radius) of quartz-bearing lithologies in the sampled basins.

[d] Averaged precipitation rate for the quartz-bearing lithologies areas exposed in the sampled basins.

[e] Sedimentary : mainly encompasses the Paleozoic sedimentary cover (mostly Cambrian and Ordovician). Quartzite : mainly encompasses the Precambrian quartzite and conglomerate of the basement. Granite : mainly encompasses the Precambrian granite of the basement. More details in Figure S2.5 and Table S2.4.

Table S2.6. Best-fit values of data plotted in figure 2.7B.

K ($m^{0.1}$ yr^{-1})[a] ($x\ 10^{-7}$)	1 σ	R^2	p-value	n° points	Study area	Main quartz-bearing lithology	Reference
3.769	0.436	0.99	0.013	4	Anti-Atlas	Granite	This study
2.203	0.32	0.99	0.002	6	Anti-Atlas	Sedimentary	This study
1.412	0.963	0.82	0.381	3	Anti-Atlas	Quartzite	This study
8.833	1.944	0.04	0.02	5	SE Brazil	Granite	Peifer et al., 2021
0.188	0.048	-0.71	0.007	8	SE Brazil	Quartzite	Peifer et al., 2021
0.377	0.039	0.83	1.1E-05	10	Cape Mountains	Quartzite	Scharf et al., 2013
5.821	0.155	0.82	0.0	38	Peninsular Indian	Granite	Mandal et al., 2015
9.204	0.539	0.52	3.0E-11	17	Massif Central	Granite	Olivetti et al., 2016
6.217	0.35	0.90	1.9E-10	15	SE Australian	Granite	Godard et al., 2019

[a] slope of forced-origin linear regression for n=1.

Table S2.7. Best-fit values of data plotted in figure S2.8.

K ($m^{0.8}$ yr^{-1})[a] ($x\ 10^{-8}$)	1 σ	R^2	n° points	Study area	Main quartz-bearing lithology	Reference
0.372	0.1	0.89	4	Anti-Atlas	Granite	This study
0.496	0.08	0.91	6	Anti-Atlas	Sedimentary	This study
0.242	0.1	0.47	3	Anti-Atlas	Quartzite	This study
7.848	5.3	-3.07	5	SE Brazil	Granite	Peifer et al., 2021
0.033	0.022	-0.71	8	SE Brazil	Quartzite	Peifer et al., 2021
0.017	0.007	-1.69	10	Cape Mountains	Quartzite	Scharf et al., 2013
0.44	0.085	-0.64	38	Peninsular Indian	Granite	Mandal et al., 2015
0.80	0.29	-6.05	17	Massif Central	Granite	Olivetti et al., 2016
0.86	0.26	-1.60	15	SE Australia	Granite	Godard et al., 2019

[a] slope of forced-origin power law regression for n=2.

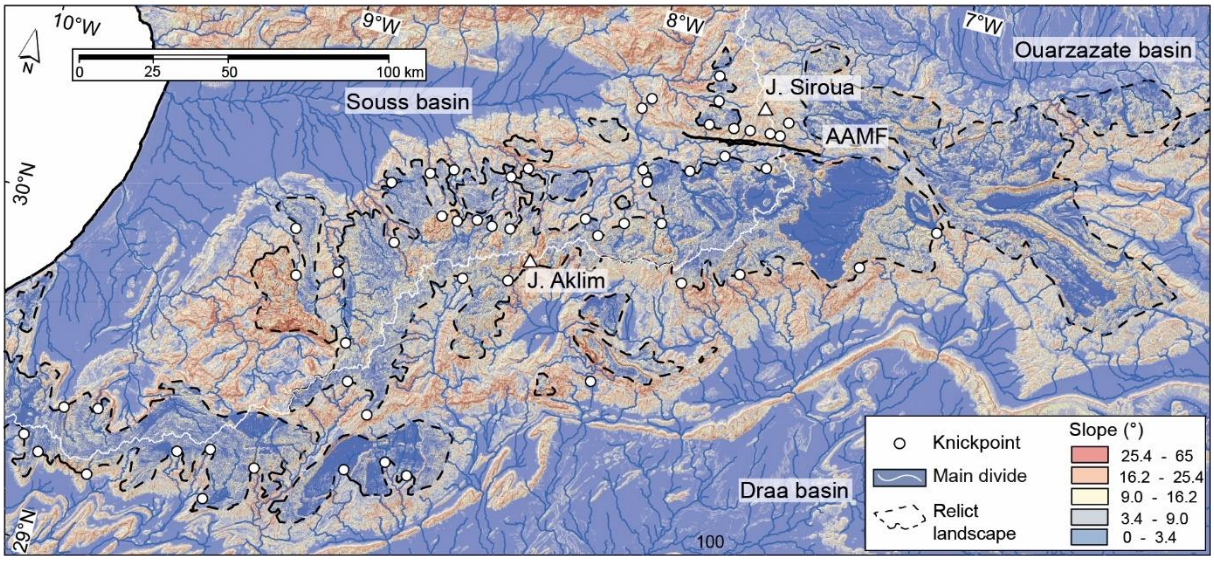

Figure S2.1. Slope map with main non-lithological knickpoints. The dashed black lines delineate the low slope, elevated, relict landscape of the Anti-Atlas. AAMF : Anti-Atlas Major Fault.

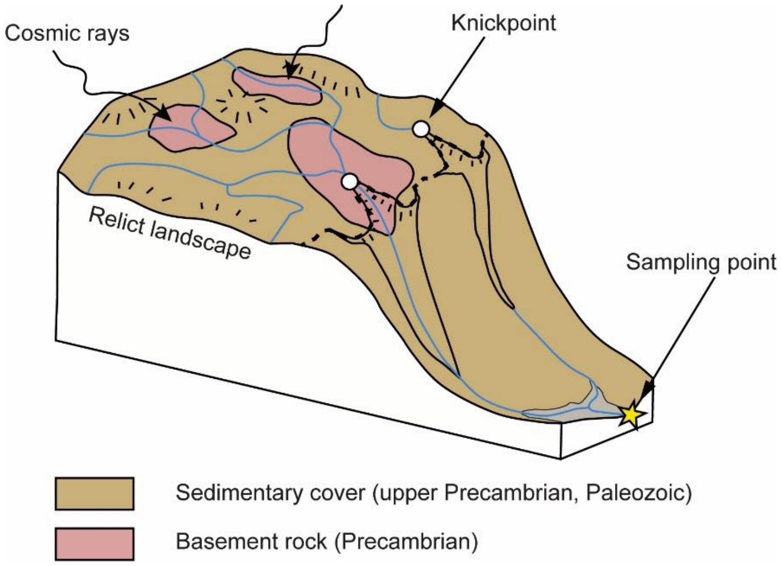

Figure S2.2. Cartoon of the Anti-Atlas topography. The major lithological variation is located between the crystalline basement and the late Precambrian/Paleozoic sedimentary cover. It is noteworthy that the main quartz contributing patches are the basement rocks, in the high-standing relict landscape.

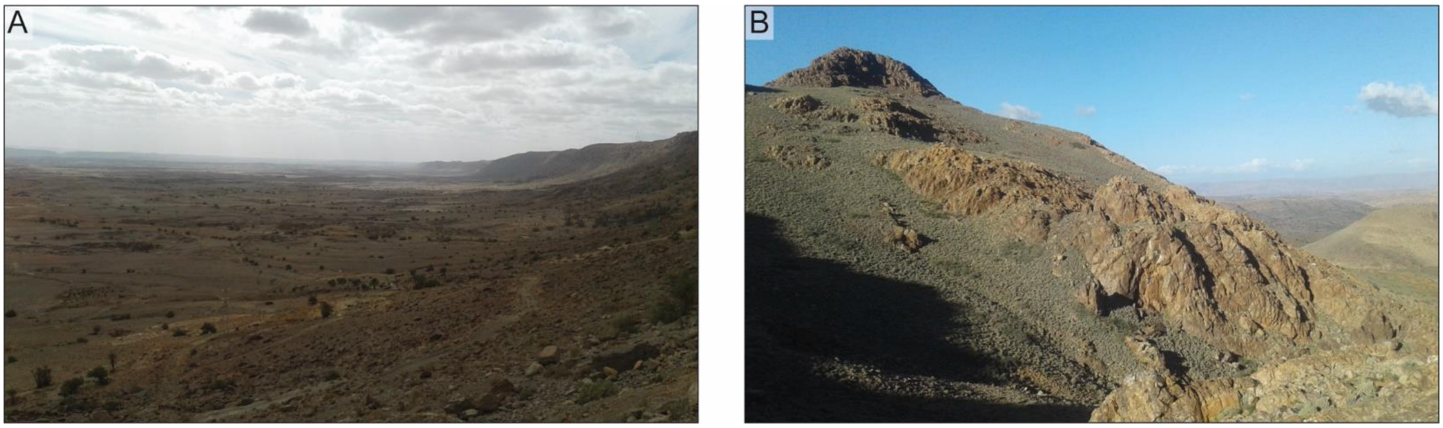

Figure S2.3. Field photos from the Anti-Atlas. A) Typical granite topography forming a very low-relief landscape. B) Typical quartzite topography forming a rugged, high-relief landscape.

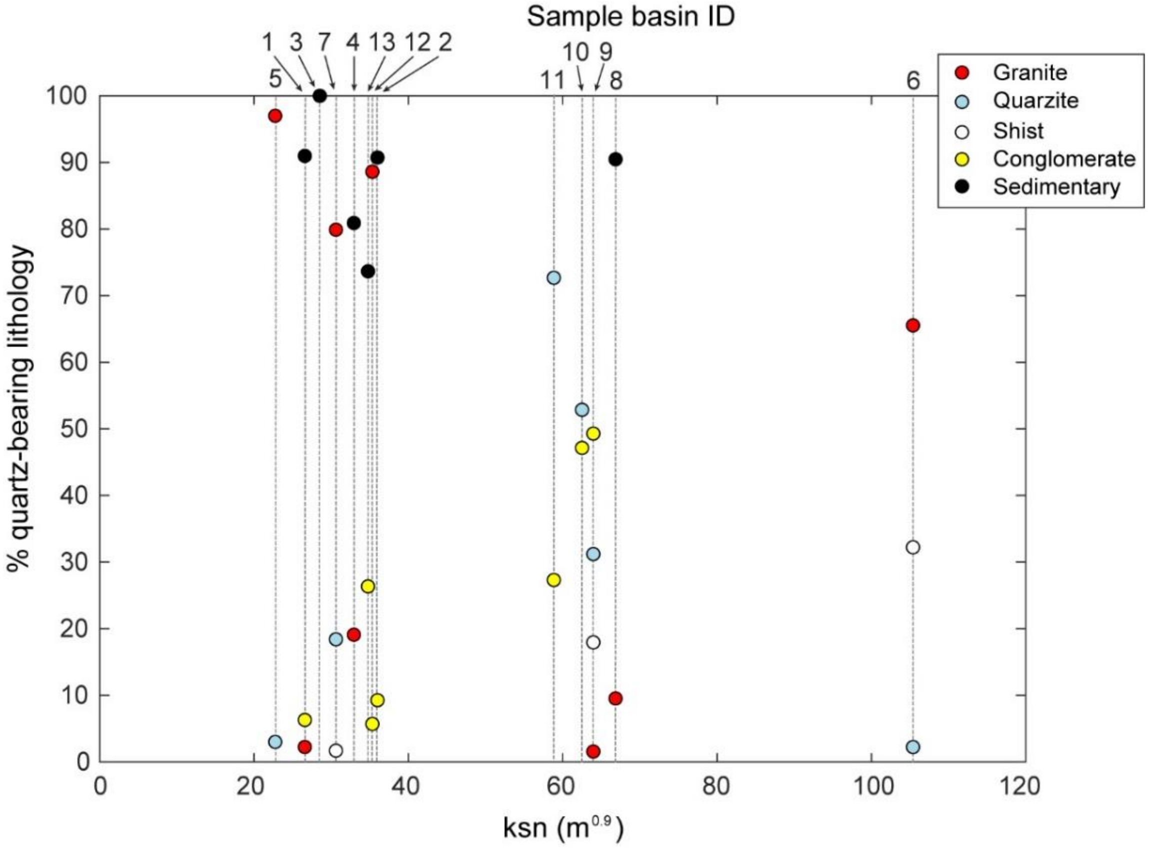

Figure S2.4. Averaged basin k_{sn} values versus percentage of quartz-bearing lithology for each sampled basin. Basins with lower k_{sn} values are characterized by a high percentage of granite and sedimentary cover rocks. Conversely, basins with higher k_{sn} values are characterized by a high percentage of Precambrian quartzite and conglomerate.

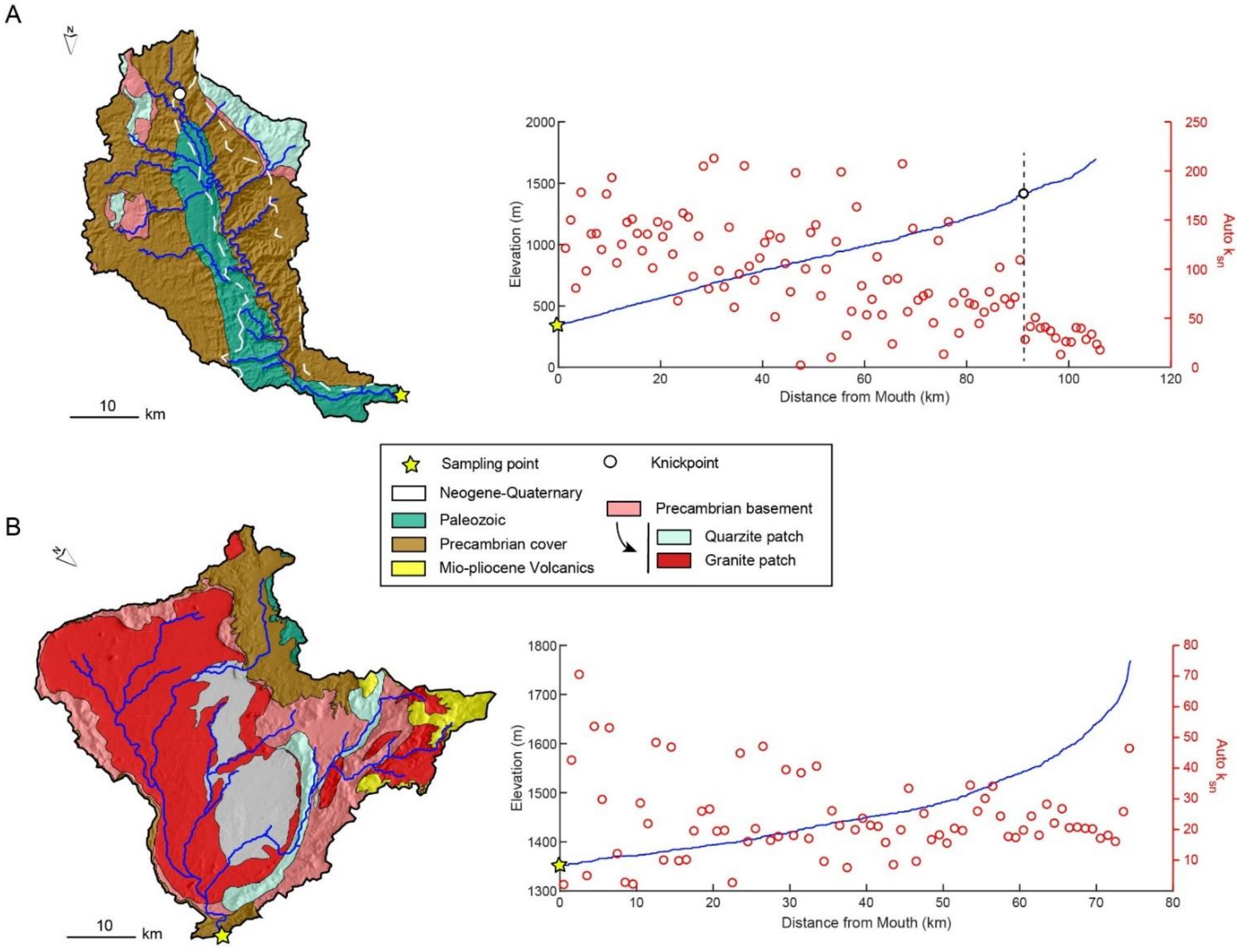

Figure S2.5. Longitudinal river profiles and relative geological map of basins 11 and 5 (location in figure 1). A) Basin 11 presents a widespread relict portion in the catchment bounded by dashed white line. Note the main quartz contributing lithologies are quartzite located within the relict landscape. The longitudinal river profile is characterized by a significative decrease of k_{sn} upstream of the non-lithological knickpoint. B) Basin 5 is entirely located within the relict portion of landscape. Note that the longitudinal profile shows a typical equilibrium condition.

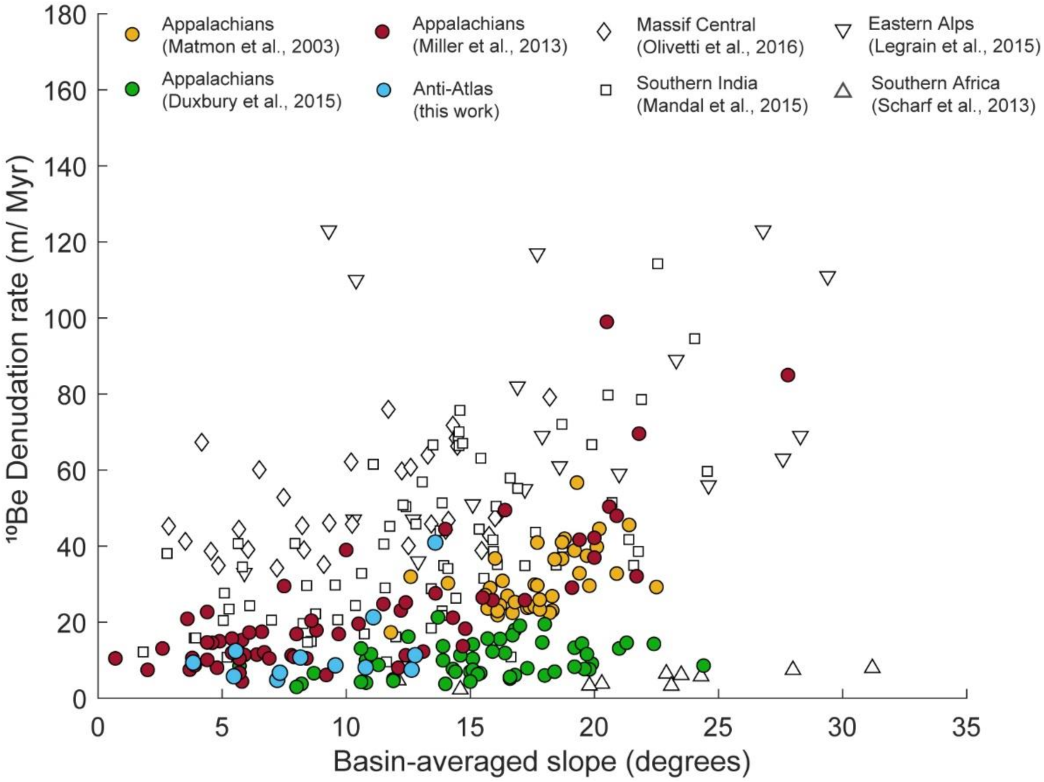

Figure S2.6. Relationship between ^{10}Be denudation rate versus basin-averaged slope for slow tectonic regions (modified from Olivetti et al., 2016). Note that the Anti-Atlas distribution is similar to the Appalachians Mountains (compare green and red with blue points).

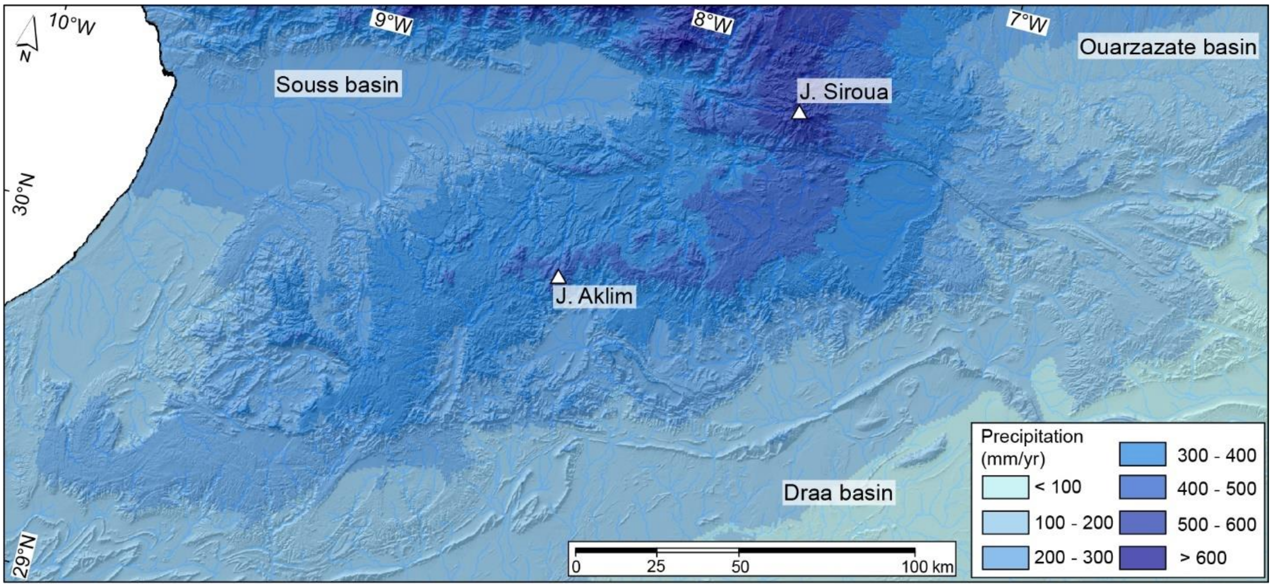

Figure S2.7. Averaged annual precipitation of the study area, database from WorldClim (Hijmans et al., 2005; http://www.worldclim.org/bioclim).

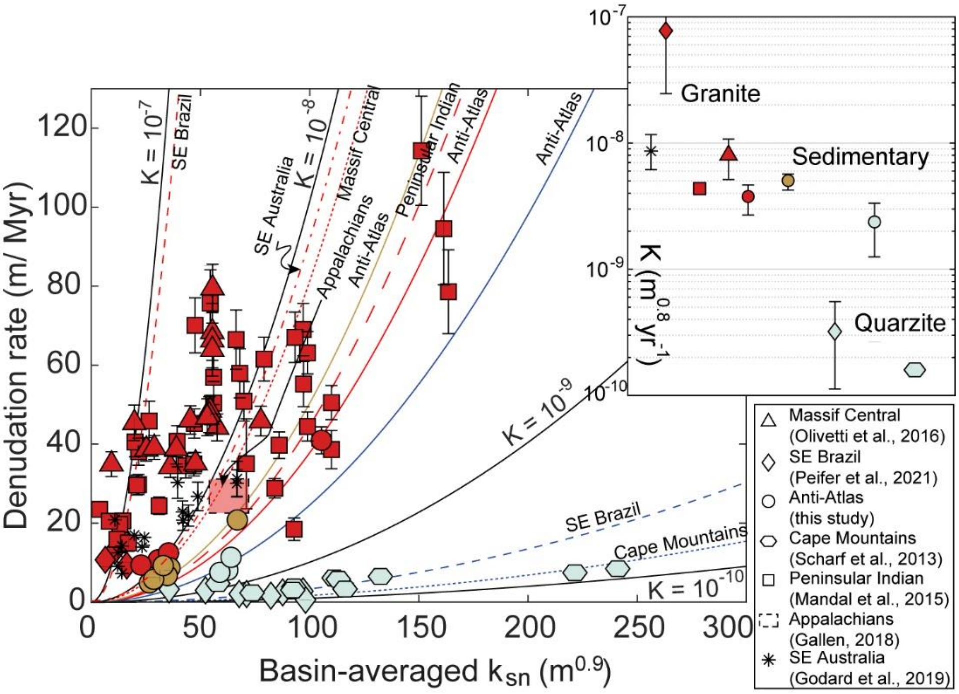

Figure S2.8. Comparison of basin-averaged k_{sn} value versus denudation rate for different rock-types (red: granitic rocks, brown: sedimentary rocks, light blue: quartzite) in tectonically inactive settings. The solid lines show the forced power best-fit for n=2 (see Table S2.7 for details).

References appendix Chapter 2.

Berrahma, M., Delaloye, M., 1989. Données géochronologiques nouvelles sur le massif volcanique du Siroua (Anti-Atlas, Maroc). J. Afr. Earth. Sci. 9(3-4), 651-656, https://doi.org/10.1016/0899-5362(89)90049-3.

Carretier, S., Regard, V., Vassallo, R., Martinod, J., Christophoul, F., Gayer, E., Audin L., Lagane, C., 2015. A note on 10Be-derived mean erosion rates in catchments with heterogeneous lithology: Examples from the western Central Andes. Earth Surf. Processes Landforms. 40(13), 1719-1729. https://doi.org/10.1002/esp.3748.

De Beer, C. H., Chevallier, L. P., De Kock, G. S., Gresse, P. G., & Thomas, R. J., 2000. Mémoire explicatif de la carte géologique du Maroc au 1/50 000, Feuille Sirwa. Notes Mem. Serv. Geol. Maroc, 395, 86.

Dunne, J., Elmore, D., & Muzikar, P., 1999. Scaling factors for the rates of production of cosmogenic nuclides for geometric shielding and attenuation at depth on sloped surfaces. Geomorphology. 27(1-2), 3-11. https://doi.org/10.1016/S0169-555X(98)00086-5.

Duxbury, J., Bierman, P. R., Portenga, E. W., Pavich, M. J., Southworth, S., Freeman, S. P. 2015. Erosion rates in and around Shenandoah National Park, Virginia, determined using analysis of cosmogenic 10Be. American Journal of Science. 315(1), 46-76. https://doi.org/10.2475/01.2015.02

Hijmans, R. J., Cameron, S. E., Parra, J. L., Jones, P. G., Jarvis, A., 2005. Very high resolution interpolated climate surfaces for global land areas. International Journal of Climatology. Q. J. R. Meteorolog. Soc. 25(15), 1965-1978. https://doi.org/10.1002/joc.1276.

Lal, D., 1991. Cosmic ray labeling of erosion surfaces: in situ nuclide production rates and erosion models. Earth Planet. Sci. Lett.104, 424–439. http://dx.doi.org/10.1016/0012-821X(91)90220-C.

Legrain, N., Dixon, J., Stüwe, K., von Blanckenburg, F., Kubik, P. 2015. Post-Miocene landscape rejuvenation at the eastern end of the Alps. Lithosphere. 7(1), 3-13. https://doi.org/10.1130/L391.1

Mandal, S. K., Lupker, M., Burg, J. P., Valla, P. G., Haghipour, N., and Christl, M., 2015. Spatial variability of 10Be-derived erosion rates across the southern Peninsular Indian escarpment: A key to landscape evolution across passive margins. Earth and Planet. Sci. Lett. 425, 154-167. https://doi.org/10.1016/j.epsl.2015.05.050.

Matmon, A., Bierman, P. R., Larsen, J., Southworth, S., Pavich, M., Caffee, M. 2003. Temporally and spatially uniform rates of erosion in the southern Appalachian Great Smoky Mountains. Geology. 31(2), 155-158. https://doi.org/10.1130/0091-7613(2003)031<0155:TASURO>2.0.CO;2

Miller, S. R., Sak, P. B., Kirby, E., & Bierman, P. R. 2013. Neogene rejuvenation of central Appalachian topography: Evidence for differential rock uplift from stream profiles and erosion rates. Earth and Planet. Sci. Lett. 369, 1-12.

Olivetti, V., Godard, V., Bellier, O., & ASTER team., 2016. Cenozoic rejuvenation events of Massif Central topography (France): Insights from cosmogenic denudation rates and river profiles. Earth and Planet. Sci. Lett. 444, 179-191. https://doi.org/10.1016/j.epsl.2016.03.049.

Peifer, D., Persano, C., Hurst, M. D., Bishop, P., and Fabel, D., 2021. Growing topography due to contrasting rock types in a tectonically dead landscape. Earth Surf. Dyn. 9(2), 167-181. https://doi.org/10.5194/esurf-9-167-2021.

Safran, E. B., Bierman, P. R., Aalto, R., Dunne, T., Whipple, K. X., Caffee, M., 2005. Erosion rates driven by channel network incision in the Bolivian Andes. Earth Surf. Processes Landforms. 30(8), 1007-1024. https://doi.org/10.1002/esp.1259.

Scharf, T. E., Codilean, A. T., De Wit, M., Jansen, J. D., and Kubik, P. W., 2013. Strong rocks sustain ancient postorogenic topography in southern Africa. Geology. 41(3), 331-334. https://doi.org/10.1130/G33806.1.

Siame, L. L., Sébrier, M., Bellier, O., Bourlès, D., Costa, C., Ahumada, E. A., Gardini C. E., Cisneros, H., 2015. Active basement uplift of Sierra Pie de Palo (Northwestern Argentina): rates and inception from10Be cosmogenic nuclide concentrations. Tectonics. 34(6), 1129-1153. https://doi.org/10.1002/2014TC003771.

Stone, J. O., 2000. Air pressure and cosmogenic isotope production. J. Geophys. Res., Solid Earth. 105(B10), 23753-23759. https://doi.org/10.1029/2000JB900181.

Appendix Chapter 3.

Table S3.1. Knickpoint and river profile data from log-log of channel slope vs. drainage area

Stream[a]	Long.	Lat.	Elevation	DFD[b]	DFM[c]	Drainage area	Stream parameters			
							Downstream		Upstream	
	°W	°N	(m)	(m)	(m)	(m^2)	k_{sn} (m$^{0.9}$)	θ	k_{sn} (m$^{0.9}$)	θ
NAA1	637465.1	3379132.5	1731	20354	280487	1.58E+08	108 ± 2	0.45 ± 0.15	11.5 ± 2.4	0.27 ± 0.09
NAA2	613556.8	3372613.8	1424	56831	257482	4.33E+08	113 ± 3	0.47 ± 0.18	32.6 ± 2.9	0.056 ± 0.14
NAA3	608426.8	3354013.8	1565	23537	266134	1.42E+08	99.8 ± 2.8	0.51 ± 0.13	28.7 ± 1.5	0.32 ± 0.084
NAA4	596666.8	3351313.8	1492	18508	257691	1.03E+08	104 ± 3	0.42 ± 0.11	44.5 ± 1.2	0.38 ± 0.17
NAA5	589316.8	3345523.8	1529	11566	266423	2.64E+07	76.5 ± 8	0.28 ± 0.085	34.7 ± 2.6	0.096 ± 0.13
NAA6	561056.8	3341233.8	1506	13041	185763	3.52E+07	96.4 ± 2.4	0.52 ± 0.092	37.1 ± 2.5	0.25 ± 0.13
NAA7	555176.8	3340753.8	1324	16987	185931	4.73E+07	98.4 ±1.6	0.38 ± 0.093	39.7 ± 4.3	0.083 ± 0.11
NAA8	550076.8	3341713.8	1387	20427	187603	4.69E+07	96.9 ± .7	0.4 ± 0.089	21.8 ± 2.2	0.28 ± 0.11
NAA9	543836.8	3339913.8	1334	21396	162843	69549300	97.9 ±2.8	0.53 ± 0.39	30.8 ± 4.8	-0.084 ± 0.14
NAA10	525536.8	3328513.8	1175	24446	128875	80991900	135 ± 5	0.45 ± 0.34	50.7 ± 3.7	0.15 ± 0.11
Mean NCAA							102.6 ± 4.7	0.44 ± 0.02	33.2 ± 3.5	0.18 ± 0.04
WAA1	497197.4	3309532.6	1111	15696	137453	54819423	70.1 ± 3.8	1.1 ± 0.3	75.6 ± 3.2	0.55 ± 0.077
WAA2	443907.4	3255074.6	857	25669	106609	1.49E+08	71.7 ± 6.4	0.91 ± 0.3	42.9 ± 4.6	-0.065 ± 0.19
WAA3	433249.4	3252884.6	849	29224	62967	1.11E+08	78.6 ± 2.3	1.1 ± 0.78	19.9 ± 2.8	0.098 ± 0.094
WAA4	422883.4	3241277.6	854	11251	115444	12464531	49.8 ± 1.4	0.6 ± 0.079	25.9 ± 1.2	0.38 ± 0.31
WAA5	428504.4	3236605.6	1012	12228	128546	22472393	55.3 ± 4.1	1.1 ± 0.17	12.9 ± 1.3	0.28 ± 0.2
WAA6	445513.4	3233028.6	982	14909	143614	29352132	74.8 ± 1.1	0.49 ± 0.087	39.8 ± 7.9	0.055 ± 0.13
WAA7	471939.4	3246752.6	1272	10221	206751	30897542	59.7 ± 0.7	0.41 ± 0.037	25 ± 5.6	-0.24 ± 0.41
WAA8	482670.4	3251424.6	1294	11699	208687	33460791	62.5 ± 0.7	0.45 ± 0.057	33.6 ± 5	0.019 ± 0.15
WAA9	483765.4	3234050.6	971	43222	187564	2.55E+08	63.2 ± 0.8	0.63 ± 0.18	23.5 ± 1.8	0.14 ± 0.11
Mean WAA							65.07 ± 3.1	0.75 ± 0.1	33.23 ± 6.1	0.14 +. 0.07
SAA1	497927.4	3246825.6	1181	27564	430725	1.62E+08	81 ±1.6	0.61 ± 0.19	15.6 ± 2.4	0.22 ± 0.091
SAA2	520922.4	3281573.6	1628	14831	482538	39338678	79.2 ± 0.8	0.5 ± 0.066	18.5 ± 2.9	0.036 ± 0.19
SAA4	529390.4	3272156.6	1588	6291	485819	9485620	75.3 ± 2.2	0.66 ± 0.12	8.44 ± 3.8	0.041 ± 0.4
SAA5	549465.4	3322015.6	1580	12837	592340	32309727	94.3 ± 0.9	0.41 ± 0.065	17.3 ± 1.2	0.41 ± 0.073

SAA6	564284.4	3324643.6	1448	17885	608379	1.51E+08	83.5 ± 2.2	0.6 ± 0.13	43.7 ± 1.5	0.5 ± 0.1
SAA7	618961.4	3336542.6	1773	13358	685609	21443896	88.5 ± 2	0.61 ± 0.089	15.4 ± 3.8	0.065 ± 0.17
SAA8	636992.4	3343550.6	1476	22860	672273	86074008	74.1 ± 2	0.65 ± 0.13	39.9 ± 3.8	0.091 ± 0.11
Mean SCAA							82.2 ± 2.7	0.57 ± 0.03	22.7 ± 5.1	0.17 ± 0.07
Mean tot							84.1 ± 3.8	0.58 ± 0.04	30.4 ± 2.9	0.17 ± 0.03

[a] NAA : rivers draining the northern flank of Anti-Atlas; WAA : rivers draining the western flank of Anti-Atlas; SAA : rivers draining the southern flank of Anti-Atlas.

[b] Distance from divide.

[c] Distance from river mouth.

Table S3.2. Knickpoint and river profile data from χ-plot

Stream[a]	Long.	Lat.	Elevation	DFD[b]	DFM[c]	Drainage area	Stream parameters			
							Downstream		Upstream	
	°W	°N	(m)	(m)	(m)	(m^2)	k_{sn} ($m^{0.9}$)	θ	k_{sn} ($m^{0.9}$)	θ
NAA1	637465.1	3379132.5	1731	20354	280487	1.58E+08	114.6 ± 0.2	0.42	15 ± 0.3	0
NAA2	613556.8	3372613.8	1424	56831	257482	4.33E+08	118.5± 0.4	0.58	42.6 ± 0.78	0
NAA3	608426.8	3354013.8	1565	23537	266134	1.42E+08	108.5 ± 0.4	0.43	35.5 ± 0.5	0.25
NAA4	596666.8	3351313.8	1492	18508	257691	1.03E+08	111.5 ± 0.43	0.41	43 ± 0.4	0.3
NAA5	589316.8	3345523.8	1529	11566	266423	2.64E+07	90.4 ± 0.5	0.28	30 ± 0.3	0.34
NAA6	561056.8	3341233.8	1506	13041	185763	3.52E+07	102 ± 0.55	0.49	46 ± 0.7	0.2
NAA7	555176.8	3340753.8	1324	16987	185931	4.73E+07	105 ± 0.42	0.35	63.7 ± 1	0.38
NAA8	550076.8	3341713.8	1387	20427	187603	4.69E+07	103 ± 0.43	0.34	39 ± 0.9	-0.1
NAA9	543836.8	3339913.8	1334	21396	162843	69549300	99.5 ± 0.47	0.56	45.2 ± 1.2	-0.18
NAA10	525536.8	3328513.8	1175	24446	128875	80991900	136.8 ± 0.44	0.46	57 ± 0.56	0.27
Mean NCAA							109 ± 3.9	0.43 ± 0.03	41.7 ± 4.2	0.15 ± 0.06

WAA1	497197.4	3309532.6	1111	15696	137453	54819423	61.5 ± 0.2	0.6	37.5 ± 1.17	0.86
WAA2	443907.4	3255074.6	857	25669	106609	1.49E+08	72.16 ± 0.6	0.8	49 ± 1.1	0.1
WAA3	433249.4	3252884.6	849	29224	62967	1.11E+08	79.9 ± 0.4	0.63	35.3 ± 0.75	-0.1
WAA4	422883.4	3241277.6	854	11251	115444	12464531	62.7 ± 0.3	0.33	30.7 ± 0.43	0.02
WAA5	428504.4	3236605.6	1012	12228	128546	22472393	67.8 ± 0.37	0.39	20.24 ± 0.6	-0.18
WAA6	445513.4	3233028.6	982	14909	143614	29352132	66.2 ± 0.37	0.63	45.4 ± 3.44	-0.90
WAA7	471939.4	3246752.6	1272	10221	206751	30897542	66.86 ± 0.17	0.37	25.26 ± 0.85	-0.10
WAA8	482670.4	3251424.6	1294	11699	208687	33460791	68.8 ± 0.14	0.36	18.1 ± 0.47	0.08
WAA9	483765.4	3234050.6	971	43222	187564	2.55E+08	72.5 ± 0.21	0.42	33.6 ± 0.43	0.02
Mean WAA							68.7 ± 1.8	0.5 ± 0.05	32.7 ± 3.5	0 ± 0.14
SAA1	497927.4	3246825.6	1181	27564	430725	1.62E+08	82.56 ± 0.21	0.51	25.9 ± 0.57	0.76
SAA2	520922.4	3281573.6	1628	14831	482538	39338678	79.58 ± 0.1	0.38	24 ± 0.38	0.04
SAA4	-	-	-	-	-	-	-	-	-	-
SAA5	549465.4	3322015.6	1580	12837	592340	32309727	86.4 ± 0.1	0.43	27.86 ± 0.23	0.47
SAA6	564284.4	3324643.6	1448	17885	608379	1.51E+08	79.85 ± 0.26	0.52	49.15 ± 0.35	0.37
SAA7	618961.4	3336542.6	1773	13358	685609	21443896	89.76 ± 0.67	0.63	15.7 ± 0.5	-0.03
SAA8	636992.4	3343550.6	1476	22860	672273	86074008	70.85 ± 0.3	0.63	46.17 ± 0.6	0.20
Mean SCAA							81.5 ± 2.4	0.51 ± 0.03	31.4 ± 5	0.30 ± 0.1
Mean tot							87.9 ± 4.07	0.47 ± 0.02	36.01 ± 2.5	0.12 ± 0.07

[a] NAA : rivers draining the northern flank of Anti-Atlas; WAA : rivers draining the western flank of Anti-Atlas; SAA : rivers draining the southern flank of Anti-Atlas.

[b] Distance from divide.

[c] Distance from river mouth

Table S3.3. Reconstructed relict stream profile and 95% confidence interval.

Stream[a]	m/n	Drainage divide elevation [b]	Paleo-relief [c]	Elevation knickpoint	ΔZ [d]	Error (2σ)
		(m)	(m)	(m)	(m)	(m)
NAA1	0.45	1900	738.2	1731	1161.8	18.3
NAA2	0.45	1900	916.1	1424	983.9	22.3
NAA3	0.45	1900	1047.1	1565	852.9	17.4
NAA4	0.45	1900	782.7	1492	1117.3	8.4
NAA5	0.45	1900	903.2	1529	996.8	11.1
NAA6	0.45	1900	1055.1	1506	844.9	42.5
NAA7	0.45	1900	1024.1	1324	875.9	28.3
NAA8	0.45	1900	1139.8	1387	760.2	38.4
NAA9	0.45	1900	1054.2	1334	845.8	29.1
NAA11	0.45	1900	1077.4	1175	822.6	36.5
Mean			973.8		926.2	42.1
WAA1	0.45	1400	879.5	1111	520.5	31.8
WAA3	0.45	1400	846.8	849	553.2	15.1
WAA4	0.45	1400	941.2	854	458.8	9.1
WAA5	0.45	1400	644.9	1012	755.1	15.7
WAA6	0.45	1400	760.1	982	639.9	13.9
WAA7	0.45	1400	527.9	1272	872.1	28.8
WAA9	0.45	1400	808.6	971	591.4	10.0
Mean			772.7		627.3	54.1
SAA1	0.45	1900	1025.8	1181	874.2	5.9
SAA2	0.45	1900	783.3	1628	1116.7	18.3
SAA4	0.45	1900	1089.1	1588	810.9	117.7
SAA6	0.45	1900	822.9	1448	1077.1	12.7
SAA7	0.45	1900	824.3	1773	1075.7	58.4
SAA8	0.45	1900	806.9	1476	1093.1	20.9
Mean			892		1008.0	53.3

[a] NAA : rivers draining the northern flank of Anti-Atlas; WAA : rivers draining the western flank of Anti-Atlas; SAA : rivers draining the southern flank of Anti-Atlas.

[b] Mean drainage divide elevation.

[c] Difference between mean drainage divide elevation and surface elevation (ΔZ).

[d] Estimated surface uplift from reconstructed relict stream profiles

Table S3.4. Maximum excavation time estimated from basin-wide denudation rates of Anti-Atlas watersheds.

Stream	Basin area[a]	Eroded material[b]	Ratio V/A [c]	Denudation rate[d] (m/Myr)		Excavation time[e] (Myr)	
	(km^2)	(km^3)	(km)	Value	Error	Value	Error
11	1200.6	148.1	0.12	7.53	0.51	16.37	0.64
10	480.1	58.6	0.12	8.10	0.55	15.07	0.59
12	842.7	117.4	0.14	12.46	0.95	11.18	0.50
9	1905.1	260.0	0.14	11.34	0.77	12.04	0.47
7	74.1	7.0	0.09	10.72	0.71	8.79	0.34
8	195.8	15.9	0.08	21.32	1.47	3.81	0.15
4	1828.1	314.7	0.17	9.25	0.65	18.61	0.76
3	558.3	56.0	0.10	5.78	0.39	17.36	0.68
5	1438.9	229.5	0.16	9.38	0.64	17.00	0.67

[a] Basin area extracted from ArcGIS.

[b] Estimated missing volume of eroded material between a smooth surface fitting the preserved summit and present-day topography (e.g., Siame et al., 2015).

[c] Ratio between volume of eroded material and basin area.

[d] Denudation rate from Chapter 2 (^{10}Be - derived denudation rate).

[e] Ratio between eroded material from river basin and denudation rate. The values are maximum time using the denudation relative only to the relict portion of the landscape, which providing quartz grains (Chapter 2).

Table S3.5. Celerity model of non-lithological knickpoints in the NCAA, WAA and SCAA sectors.

Stream[a]	Elevation	DFD	DFM	Drainage area	Model constrains						Model results					
					K		m		Time (Ma)		K	m	Time (Ma)		Model DFM	RMSE
	(m)	(m)	(m)	(m^2)	Min	Max	Min	Max	Min	Max	Value	Value	Value	Error	(m)	
NCAA1	1731	20354	280487	1.58E+08	10^{-7}	10^{-4}	0	0.75	3.8	18.6	5.29E-05	0.66	10.1	4.2	280488	0.198181
NCAA3	1565	23537	266134	1.42E+08	10^{-7}	10^{-4}	0	0.75	3.8	18.6	6.14E-05	0.69	9.9	4.4	266254	0.065654
NCAA6	1506	13041	185763	3.52E+07	10^{-7}	10^{-4}	0	0.75	3.8	18.6	6.33E-05	0.69	9.8	4.3	185763	0.031449
NCAA9	1334	21396	162843	6.95E+07	10^{-7}	10^{-4}	0	0.75	3.8	18.6	5.84E-05	0.69	10.7	4.3	163048	0.012972
NCAA10	1175	24446	128875	8.10E+07	10^{-7}	10^{-4}	0	0.75	3.8	18.6	6.04E-05	0.67	9.3	4.1	129128	0.066367
Mean											5.93E-05	0.68	9.9	4.3		
WAA1	1111	15696	137453	5.48E+07	10^{-7}	10^{-4}	0	0.75	3.8	18.6	5.91E-05	0.64	9.2	4.1	137453	0.051899
WAA2	857	25669	106609	1.49E+08	10^{-7}	10^{-4}	0	0.75	3.8	18.6	5.22E-05	0.61	9.2	4.0	106609	0.138172
WAA3	849	29224	62967	1.11E+08	10^{-7}	10^{-4}	0	0.75	3.8	18.6	5.48E-05	0.58	9.8	4.5	62967	0.090955
WAA5	1012	12228	128546	2.25E+07	10^{-7}	10^{-4}	0	0.75	3.8	18.6	5.53E-05	0.65	9.1	3.9	128547	0.20324
WAA7	1272	10221	206751	3.09E+07	10^{-7}	10^{-4}	0	0.75	3.8	18.6	5.34E-05	0.68	9.0	4.2	206752	0.186591
Mean											5.50E-05	0.63	9.2	4.1		
SCAA1	1181	27564	430725	1.62E+08	10^{-7}	10^{-4}	0	0.75	3.8	18.6	5.47E-05	0.68	10.2	4.2	430725	0.128857
SCAA2	1628	14831	482538	3.93E+07	10^{-7}	10^{-4}	0	0.75	3.8	18.6	6.69E-05	0.71	10.8	4.0	482538	0.11664
SCAA4	1588	6291	485819	9.49E+06	10^{-7}	10^{-4}	0	0.75	3.8	18.6	7.00E-05	0.72	11.0	3.8	485819	0.022455
SCAA5	1580	12837	592340	3.23E+07	10^{-7}	10^{-4}	0	0.75	3.8	18.6	6.63E-05	0.71	9.8	3.8	592340	0.147208
SCAA6	1448	17885	608379	1.51E+08	10^{-7}	10^{-4}	0	0.75	3.8	18.6	6.42E-05	0.70	10.2	4.3	608379	0.109103
Mean											6.44E-05	0.70	10.4	4.0		
Mean tot											5.96E-05	0.67	9.9	4.1		

[a] NAA : rivers draining the northern flank of Anti-Atlas; WAA : rivers draining the western flank of Anti-Atlas; SAA : rivers draining the southern flank of Anti-Atlas.

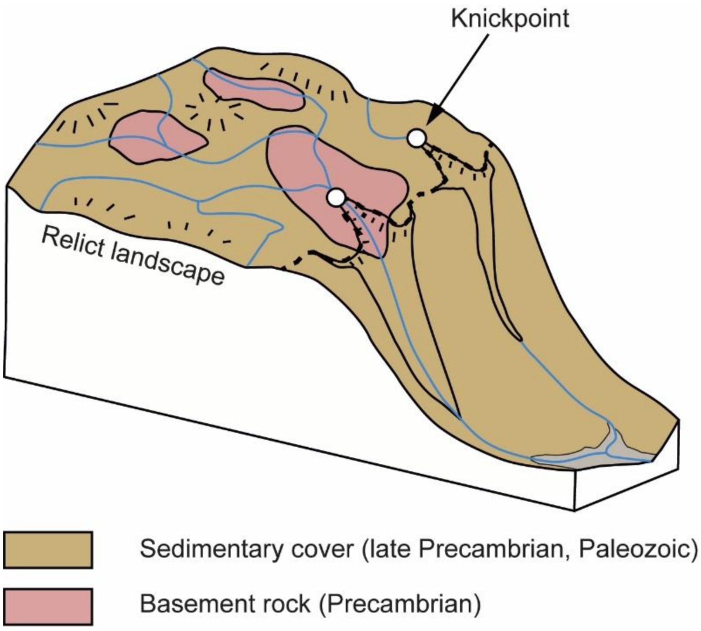

Figure S3.1. Cartoon of the Anti-Atlas topography. The major lithological contrast is between crystalline/ methamorphic Precambrian rock and late Precambrian/ Paleozoic sedimentary cover.

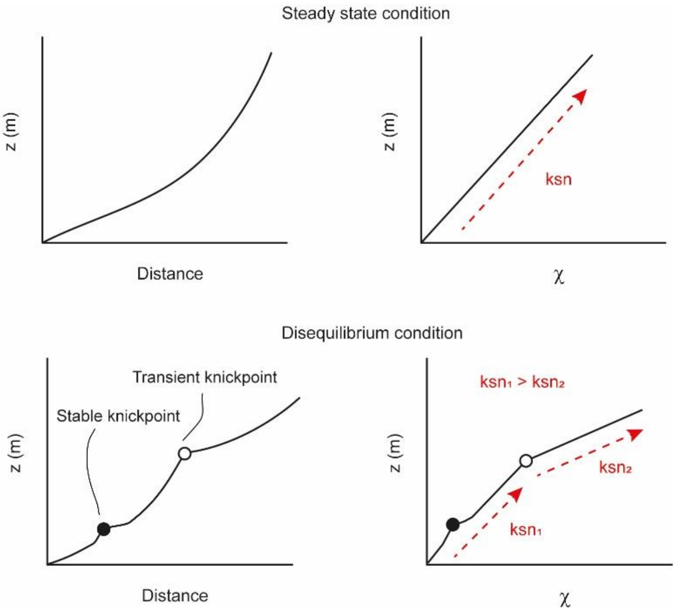

Figure S3.2. The simplified sketch of longitudinal river profiles (to the left) and χ-plot (to the right) in a steady-state condition and disequilibrium state. In a steady-state condition, the river can be well explain by a single value of k_{sn}, thus a straight line in a chi space (top). In a disequilibrium condition, the river is characterized by knickpoints. The transient knickpoints show an abrupt break in the χ-plot reflected the variation of rock uplift. Whereas, the stable knickpoints (lithological, dam, landslide, local heterogeneities or climate related) is not characterized by k_{sn} variation in along the profile.

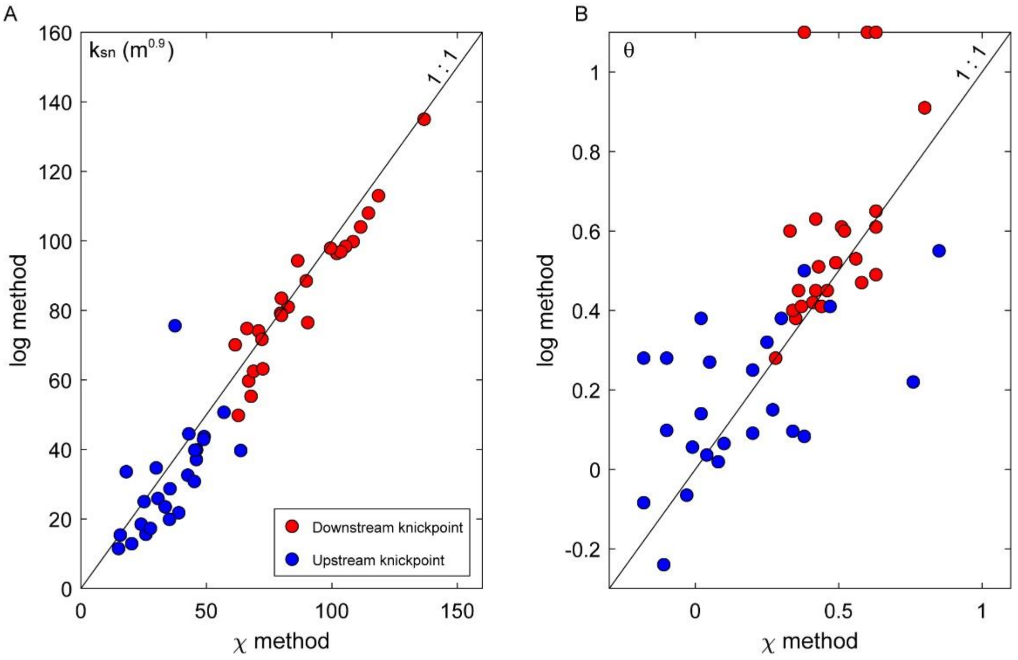

Figure S3.3. Comparison normalized channel steepness (k_{sn}) and concavity values (θ) using the logS-logA method and integration method (χ). Note the ksn values approximately follow the 1:1 line (plot to left), whereas the concavity values are more scattered (plot to right).

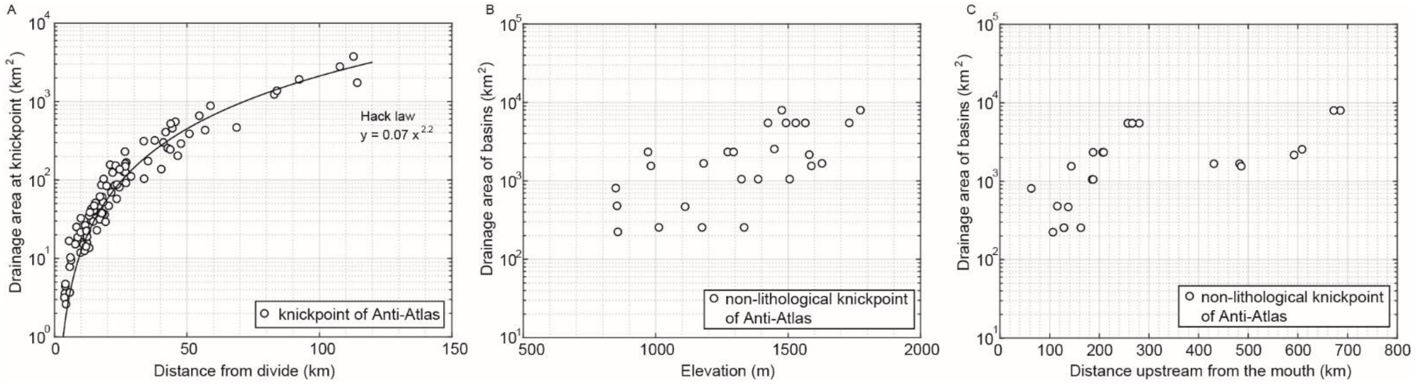

Figure S3.4. (A) Distance from divide versus upstream area at knickpoints location. Best-fit regression confirm the power law relation of Hack law for knickpoints in the study area. (B) Elevation of knickpoints versus drainage area of basins calculating at 500 m of elevation. (C) Distance from mouth of knickpoints versus drainage area of basins calculating at 500 m of elevation.

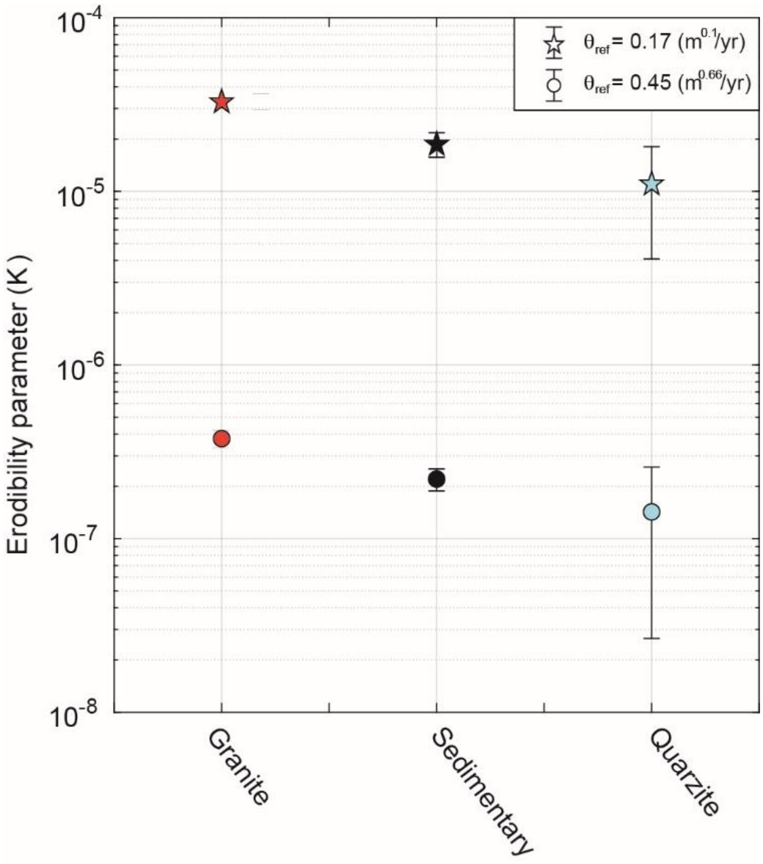

Figure S3.5. Rock-type versus erodibility parameter. Erodibility values were estimate from the forced linear regression between basin-wide denudation rates and basin-averaged k_{sn} using θ_{ref} of 0.45 and 0.17 (mean value of concavity relative to uplifted relict landscape, Table S3.1), assuming n = 1.

References appendix Chapter 3.

Siame, L. L., Sébrier, M., Bellier, O., Bourlès, D., Costa, C., Ahumada, E. A., Gardini C. E., & Cisneros, H., (2015). Active basement uplift of Sierra Pie de Palo (Northwestern Argentina): rates and inception from10Be cosmogenic nuclide concentrations. *Tectonics*, 34(6), 1129-1153. https://doi.org/10.1002/2014TC003771.

Appendix Chapter 4.

Table S4.1. Non-lithological knickpoints and river profile data

Stream[a]	Long.	Lat.	Elevation	DFM[b]	DFD[c]	Drainage area	Location[d]
	°W	°N	(m)	(m)	(m)	(m^2)	
cwm1	798790.6	3686682.0	952	201102	53510	4.03E+08	Meseta
cwm2	789008.6	3686828.0	1080	183894	13154	23133189	Meseta
cwm3	782292.6	3707195.0	870	158744	34061	1.3E+08	Meseta
cwm4	771342.6	3723036.0	579	133132	9464	10119771	Meseta
cwm5	788862.6	3677776.0	1036	218149	23205	91632155	Meseta
cwm6	769298.6	3688215.0	829	175387	13766	22765488	Meseta
cwm7	764407.6	3683616.0	846	171845	9950	19514798	Meseta
cwm8	756596.6	3677849.0	780	179567	12641	34062968	Meseta
cwm9	788643.6	3651058.0	821	245553	48319	4.2E+08	Meseta
cwm 10	737178.6	3697121.0	558	180842	113029	1.66E+09	Meseta
cwm 11	720242.6	3689894.0	624	117302	30969	1.51E+08	Meseta
cwm 12	725571.6	3703691.0	587	99210	13761	24588006	Meseta
cwm 13	730316.6	3704348.0	570	104676	10108	31057412	Meseta
cwm 14	727615.6	3716685.0	372	86589	16312	64187805	Meseta
cwm 15	714694.6	3695588.0	575	109394	16581	32629467	Meseta
cwm 16	709949.6	3690259.0	550	108052	19479	68285806	Meseta
cwm 17	711993.6	3704932.0	417	87228	10624	16525229	Meseta
cwm 18	711190.6	3718875.0	380	68009	10914	16871614	Meseta
cwm 19	706737.6	3678141.0	573	128930	28522	1.97E+08	Meseta
cwm 20	699656.6	3723255.0	309	64177	14033	28920483	Meseta
cwm 21	703379.6	3652810.0	715	133855	27291	1.77E+08	Meseta
cwm 22	691918.6	3652883.0	683	125310	18694	1.1E+08	Meseta
cwm 23	682063.6	3662008.0	594	100791	15438	48595151	Meseta
cwm 24	676369.6	3660548.0	625	98177	20559	84757745	Meseta
cwm 25	664032.6	3670330.0	450	98742	37468	1.88E+08	Meseta
cwm 26	657389.6	3665585.0	486	97543	8084	9650819	Meseta
cwm 27	652936.6	3657920.0	510	92406	23132	69106472	Meseta
cwm 28	662791.6	3643247.0	641	124468	30872	2.15E+08	Meseta
cwm 29	638628.6	3649817.0	450	97603	14434	42861147	Meseta
cwm 30	663813.6	3658869.0	586	109108	17521	84661823	Meseta
cwm 31	698415.6	3665439.0	702	122126	20191	65541371	Meseta
cwm 32	715059.6	3728876.0	208	60653	87617	7.66E+08	Meseta
cwm 33	748347.6	3692522.0	742	142194	9300	18454327	Meseta
cwm 34	737178.6	3697121.0	558	133229	28759	1.25E+08	Meseta
cwm 35	747836.6	3695880.0	695	145047	9453	16653125	Meseta
cwm 36	771561.6	3703691.0	1012	155344	15274	33604674	Meseta
cwm 37	753092.6	3732745.0	290	105407	33158	1.76E+08	Meseta
cwm 38	742945.6	3747564.0	331	72907	14934	42941082	Meseta
Mean wmm			621 ± 121				
nwm1	800323.6	3705808.0	618	243974	118616	2.1E+09	Meseta
nwm2	892887.6	3707268.0	1475	454628	84775	1.35E+09	TMA
nwm3	895734.6	3741505.0	1202	383385	48155	2.9E+08	TMA
nwm4	869965.6	3738074.0	1369	378393	33778	1.99E+08	TMA
nwm5	857336.6	3743038.0	1013	304827	20068	76364570	TMA
nwm6	856752.6	3724350.0	1408	316886	31219	1.49E+08	TMA
nwm7	820544.6	3717415.0	1175	255613	10791	35347257	TMA
nwm8	836385.6	3733110.0	1045	237996	19018	59407692	TMA
nwm9	783898.6	3718510.0	632	217020	15622	45099327	Meseta
nwm10	928949.6	3707560.0	1348	441636574215	49221738281	4.1E+08	TMA
nwm11	812514.6	3724131.0	830	232775	19436	1.06E+08	Meseta
nwm12	801272.6	3737344.0	545	201537	31106	1.04E+08	Meseta
nwm13	790687.6	3710261.0	761	225872	21699	64560835	Meseta

Mean nwm			1032 ± 188				
swm1	859161.6	3653467.0	1915	595726	13296	57745044	FMA
swm2	847262.6	3670914.0	1532	595711	19902	84938931	FMA
Mean swm	798790.6	3686682.0	1724 ± 135				
Mean Meseta			627 ± 116				
Mean TMA			1255 ± 86				
Mean FMA			1724 ± 135				

[a] cwm : river draining directly to the ocean; nwm : river draining into the Oued Sebou; swm : river draining into the Oued Er Rbia.

[b] Distance from divide.

[c] Distance from river mouth

[d] Meseta : rivers draining the Western Moroccan Meseta sectors (WMM); TMA: rivers draining the Tabular Middle Atlas (NWM sector). FMA: rivers draining the Folded Middle Atlas (SWM sector).

Table S4.2. Reconstructed relict stream profile and 95% confidence interval

Stream[a]	m/n	Elevation knickpoint	ΔZ[b]	Error (2σ)	Location[b]
		(m)	(m)	(m)	
cwm1	0.45	952	608.2	10.1	Meseta
cwm2	0.45	1080	845.3	2.7	Meseta
cwm3	0.45	870	404.8	6.3	Meseta
cwm4	0.45	579	252.3	11.8	Meseta
cwm5	0.45	1036	570.8	14.2	Meseta
cwm6	0.45	829	447.0	15.7	Meseta
cwm7	0.45	846	506.5	6.9	Meseta
cwm8	0.45	780	356.8	9.5	Meseta
cwm9	0.45	821	396.7	3.8	Meseta
cwm 10	0.45	558	332.5	6.5	Meseta
cwm 11	0.45	624	396.6	4.1	Meseta
cwm 12	0.45	587	423.5	4.7	Meseta
cwm 13	0.45	570	341.5	13.1	Meseta
cwm 14	0.45	372	310.7	14.1	Meseta
cwm 15	0.45	575	457.8	4.1	Meseta
cwm 16	0.45	550	497.4	7.0	Meseta
cwm 17	0.45	417	309.5	13.9	Meseta
cwm 18	0.45	380	341.4	4.1	Meseta
cwm 19	0.45	573	399.0	22.0	Meseta
cwm 20	0.45	309	193.7	14.8	Meseta
cwm 21	0.45	715	602.0	1.1	Meseta
cwm 22	0.45	683	521.9	1.3	Meseta
cwm 23	0.45	594	430.3	6.8	Meseta
cwm 24	0.45	625	475.9	2.5	Meseta
cwm 25	0.45	450	203.9	1.4	Meseta
cwm 26	0.45	486	319.2	9.0	Meseta
cwm 27	0.45	510	413.5	8.7	Meseta
cwm 28	0.45	641	428.1	4.6	Meseta
cwm 29	0.45	450	313.6	4.9	Meseta
Mean wmm			417.3	54.9	
nwm1	0.45	618	328.4	17.8	Meseta
nwm2	0.45	1475	961.3	26.9	TMA
nwm3	0.45	1202	722.4	22.6	TMA
nwm4	0.45	1369	725.1	23.8	TMA
nwm5	0.45	1013	574.3	41.3	TMA
nwm6	0.45	1408	917.7	23.3	TMA
nwm7	0.45	1175	944.3	12.6	TMA
nwm8	0.45	1045	544.8	28.1	TMA
nwm9	0.45	632	363.1	24.6	Meseta
nwm10	0.45	1348	1196.1	17.6	TMA
nwm11	0.45	830	635.6	24.1	Meseta
nwm12	0.45	545	265.1	27.1	Meseta
Mean nwm			681.5	86.4	
swm1	0.45	1915	1067.0	37.8	FMA
swm2	0.45	1532	1105.4	89.6	FMA
Mean swm			1086.2	63.7	
Mean Meseta			414.9	54.9	
Mean TMA			823.2	66.5	
Mean FMA			1086.2	63.7	

[a] cwm : river draining directly to the ocean; nwm : river draining into the Oued Sebou; swm : river draining into the Oued Er Rbia.

[b] Estimated surface uplift from reconstructed relict stream profiles.

[c] Meseta domains : rivers draining the Western Moroccan Meseta domain (mostly from cwm and nwm sector); TMA: rivers draining the Tabular Middle Atlas (mostly nwm sectors); FMA: rivers draining the Folded Middle Atlas (from swm sector).

Table S4.3. Averaged denudation rate, channel steepness, topographic slope, local relief, precipitation rate of the quartz-bearing areas exposed in the sampled basins

Sample	Basin area	Quartz-bearing area	Quartz-bearing area	Denudation rate (m/ Myr)		k_{sn} (m$^{0.9}$) [a]		Slope [b]	Local Relief [c]	Precipitation rate [d]
ID	(m2)	(m2)	(%)	Value	Error	Value	Error	(°)	(m)	(m/ yr)
53	5.35E+08	2E+08	42.57	14.76	1.02	22.7	0.5	8.011	222.2	411.9
58	3.39E+08	1E+08	35.85	17.11	1.27	14.7	0.7	5.24	278.6	734.5
59	9.70E+08	2E+08	20.66	19.49	1.35	34.6	1.0	7.296	293.5	710.7
60	1.01E+09	5E+08	52.72	17.36	1.20	52.5	1.2	12.023	453.8	632.2
62	3.54E+08	4E+07	12.50	39.94	5.57	57.6	2.1	14.277	446.8	621.9
61	3.20E+09	1E+09	36.24	19.80	1.37	50.3	1.6	11.164	426.8	648.8
63	3.46E+09	3E+08	8.19	32.15	2.34	40.2	1.8	8.331	323.6	701

[a] Basin-averaged k_{sn} of quartz-bearing lithologies in the sampled basins.

[b] Basin-averaged slope of quartz-bearing lithologies in the sampled basins.

[c] Basin-averaged local relief (2.5 km radius) of quartz-bearing lithologies in the sampled basins.

[d] Averaged precipitation rate for the quartz-bearing lithologies areas exposed in the sampled basins.

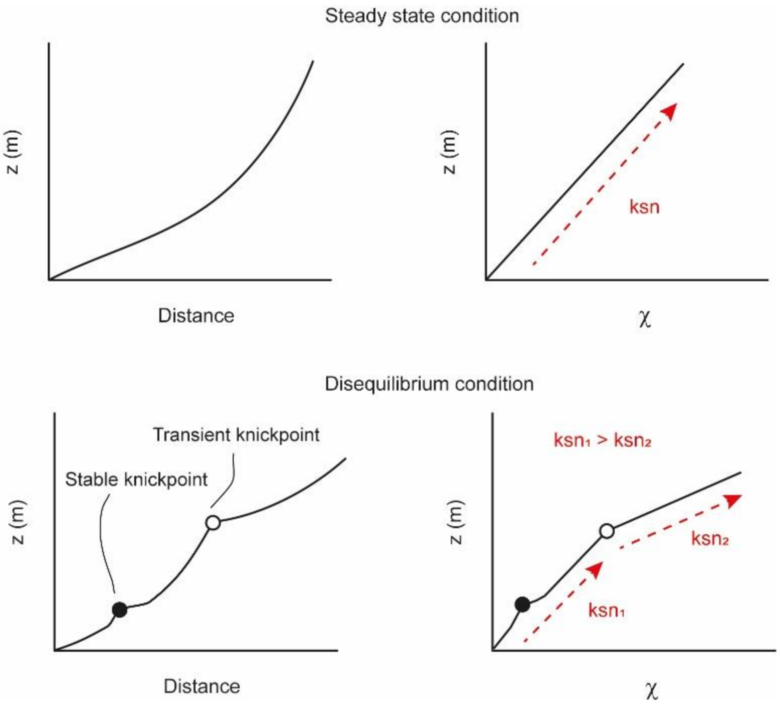

Figure S4.1. The simplified sketch of longitudinal river profiles (to the left) and χ-plot (to the right) in a steady-state condition and disequilibrium state. In a steady-state condition, the river can be well explain by a single value of k_{sn}, thus a straight line in a chi space (top). In a disequilibrium condition, the river is characterized by knickpoints. The transient knickpoints show an abrupt break in the χ-plot reflected the variation of rock uplift. Whereas, the stable knickpoints (lithological, dam, landslide, local heterogeneities or climate related) is not characterized by k_{sn} variation in along the profile.

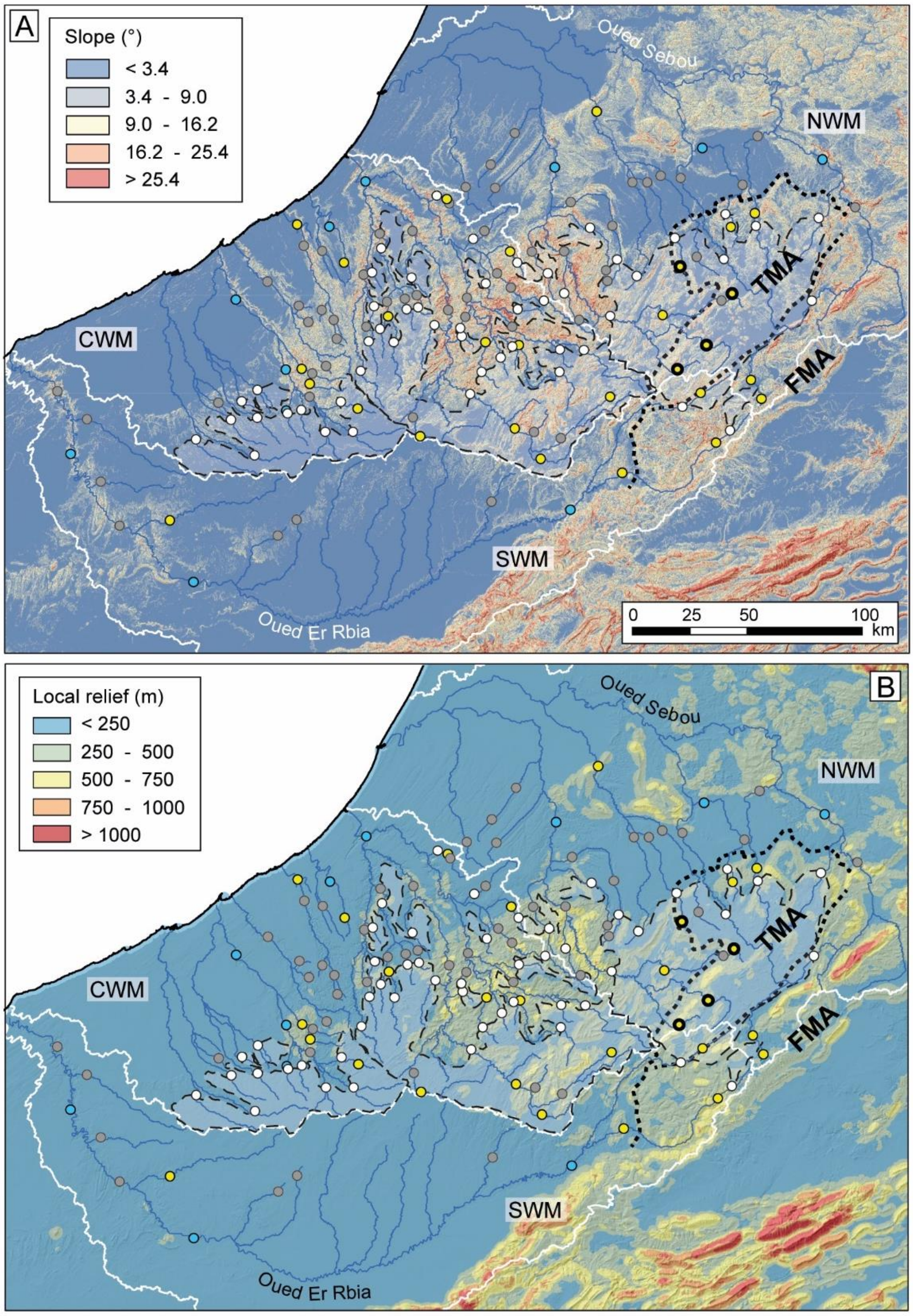

Figure S4.2. The slope and D) local relief(2.5 km radius) maps with main knickpoints. The bold knickpoints describe the escarpment between the TMA and Moroccan Meseta, while the thick dashed line indicates the boundary between the main morpho-structural domains. The white solid lines demarks the tributaries of the Oued El Rbia (South Western Meseta, SWM), of the Oued Sebou (North Western Meseta, NWM) and rivers draining directly from the Western Meseta to the Atlantic ocean (CWM: Central Western Meseta). TMA and FMA indicate the Tabular Middle Atlas and the Folded Middle Atlas, respectively.

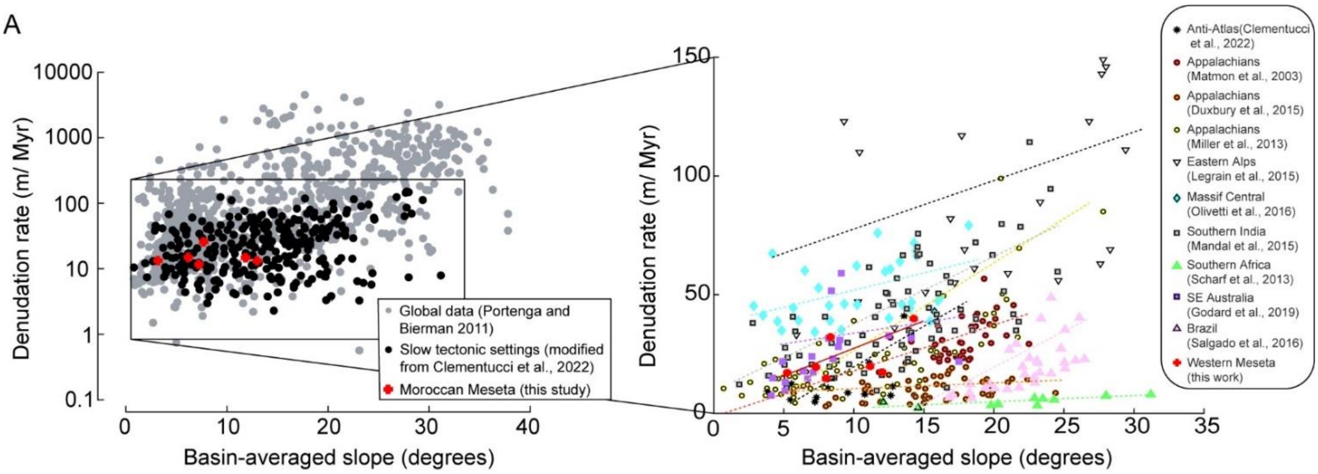

Figure S4.3. Global compilation of basin-averaged slope versus basin-wide denudation rates for slow tectonic settings (modified from Olivetti et al., 2016; Chapter 2).

References appendix Chapter 4.

Duxbury, J., Bierman, P. R., Portenga, E. W., Pavich, M. J., Southworth, S., Freeman, S. P. (2015). Erosion rates in and around Shenandoah National Park, Virginia, determined using analysis of cosmogenic 10Be. *American Journal of Science*, 315(1), 46-76. https://doi.org/10.2475/01.2015.02

Godard, V., Dosseto, A., Fleury, J., Bellier, O., Siame, L., & ASTER Team. (2019). Transient landscape dynamics across the Southeastern Australian Escarpment. *Earth and Planet. Sci. Lett*., 506, 397-406. https://doi.org/10.1016/j.epsl.2018.11.017

Legrain, N., Dixon, J., Stüwe, K., von Blanckenburg, F., Kubik, P. (2015). Post-Miocene landscape rejuvenation at the eastern end of the Alps. *Lithosphere*, 7(1), 3-13. https://doi.org/10.1130/L391.1

Mandal, S. K., Lupker, M., Burg, J. P., Valla, P. G., Haghipour, N., and Christl, M., (2015). Spatial variability of 10Be-derived erosion rates across the southern Peninsular Indian escarpment: A key to landscape evolution across passive margins. *Earth and Planet. Sci. Lett*., 425, 154-167. https://doi.org/10.1016/j.epsl.2015.05.050.

Matmon, A., Bierman, P. R., Larsen, J., Southworth, S., Pavich, M., Caffee, M. (2003). Temporally and spatially uniform rates of erosion in the southern Appalachian Great Smoky Mountains. *Geology*, 31(2), 155-158. https://doi.org/10.1130/0091-7613(2003)031<0155:TASURO>2.0.CO;2

Miller, S. R., Sak, P. B., Kirby, E., & Bierman, P. R. (2013). Neogene rejuvenation of central Appalachian topography: Evidence for differential rock uplift from stream profiles and erosion rates. *Earth and Planet. Sci. Lett*., 369, 1-12.

Olivetti, V., Godard, V., Bellier, O., & ASTER team., (2016). Cenozoic rejuvenation events of Massif Central topography (France): Insights from cosmogenic denudation rates and river profiles. *Earth and Planet. Sci. Lett*., 444, 179-191. https://doi.org/10.1016/j.epsl.2016.03.049.

Salgado, A. A. R., de Andrade Rezende, E., Bourles, D., Braucher, R., da Silva, J. R., & Garcia, R. A. (2016). Relief evolution of the Continental Rift of Southeast Brazil revealed by in situ-produced 10Be concentrations in river-borne sediments. *Journal of South American Earth Sciences*, *67*, 89-99. https://doi.org/10.1016/j.jsames.2016.02.002

Scharf, T. E., Codilean, A. T., De Wit, M., Jansen, J. D., and Kubik, P. W., (2013). Strong rocks sustain ancient postorogenic topography in southern Africa. *Geology*, 41(3), 331-334. https://doi.org/10.1130/G33806.1.